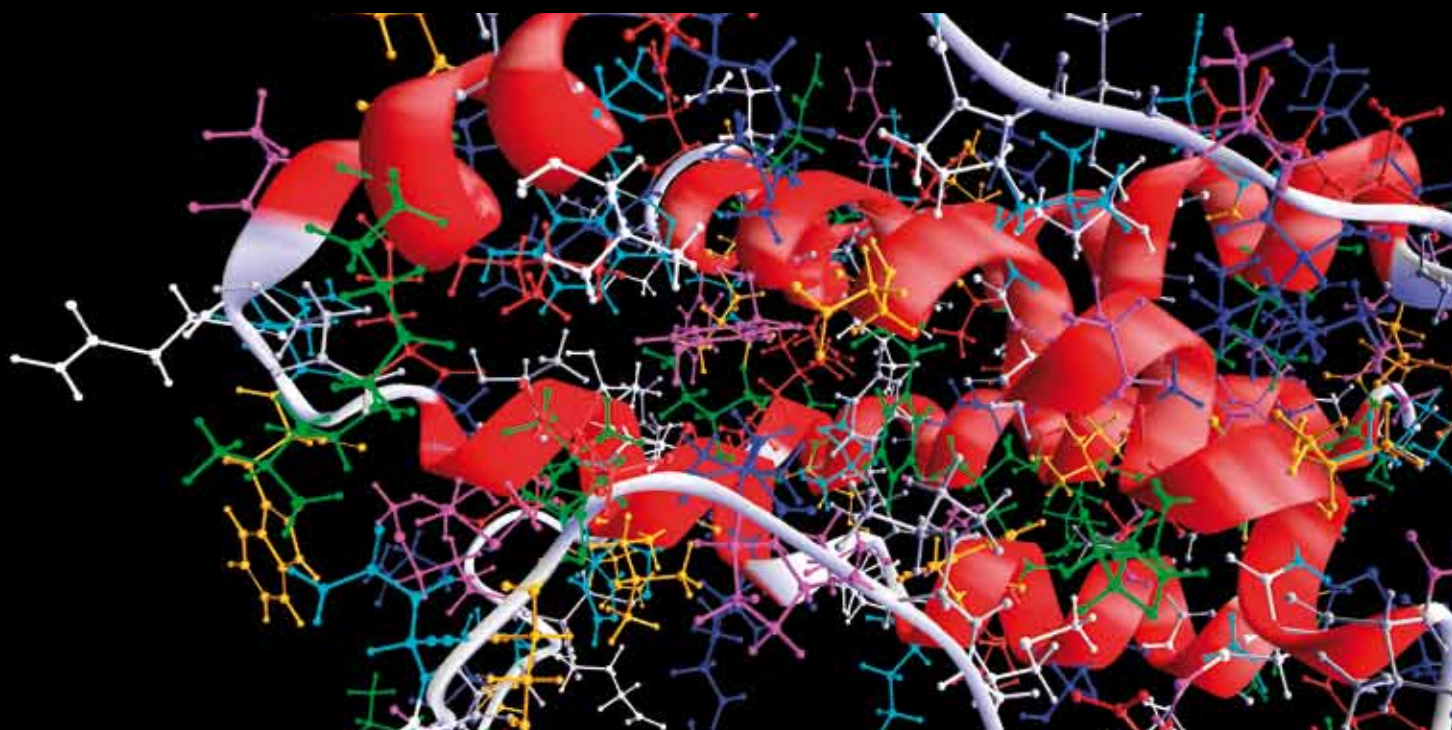
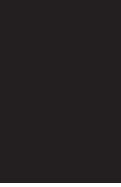


COMPUTATIONAL AND MATHEMATICAL MODELING OF TUMOR KINETICS AND RESPONSE TO RADIATION AND CHEMOTHERAPY

GUEST EDITORS: EVA BEZAK, LOREDANA MARCU, AND SCOTT PENFOLD





**Computational and Mathematical Modeling
of Tumor Kinetics and Response to Radiation
and Chemotherapy**

Computational and Mathematical Methods in Medicine

**Computational and Mathematical Modeling
of Tumor Kinetics and Response to Radiation
and Chemotherapy**

Guest Editors: Eva Bezak, Loredana Marcu,
and Scott Penfold



Copyright © 2012 Hindawi Publishing Corporation. All rights reserved.

This is a special issue published in “Computational and Mathematical Methods in Medicine.” All articles are open access articles distributed under the Creative Commons Attribution License, which permits unrestricted use, distribution, and reproduction in any medium, provided the original work is properly cited.

Editorial Board

Zvia Agur, Israel
Emil Alexov, USA
Gary C. An, USA
Georgios Archontis, Cyprus
Pascal Auffinger, France
Facundo Ballester, Spain
Dimos Baltas, Germany
Chris Bauch, Canada
Maxim Bazhenov, USA
Niko Beerenwinkel, Switzerland
Philip Biggin, UK
Michael Breakspear, Australia
Thierry Busso, France
Carlo Cattani, Italy
Bill Crum, UK
Timothy David, New Zealand
Gustavo Deco, Spain
Carmen Domene, UK
Wim Van Drongelen, USA
Frank Emmert-Streib, UK
Ricardo Femat, Mexico
Alfonso T. García-Sosa, Estonia
Kannan Gunasekaran, USA

Damien R. Hall, Japan
William F. Harris, South Africa
Vassily Hatzimanikatis, USA
Tasawar Hayat, Pakistan
Volkhard Helms, Germany
J.-H. S. Hofmeyr, South Africa
Seiya Imoto, Japan
Bleddyn Jones, UK
Lawrence A. Kelley, UK
Lev Klebanov, Czech Republic
Ina Koch, Germany
David Liley, Australia
Quan Long, UK
Yoram Louzoun, Israel
Jianpeng Ma, USA
C.-M. C. Ma, USA
Reinoud Maex, France
Francois Major, Canada
Simeone Marino, USA
Ali Masoudi-Nejad, Iran
Ramit Mehr, Israel
Seth Michelson, USA
Michele Migliore, Italy

Karol Miller, Australia
Ernst Niebur, USA
Kazuhisa Nishizawa, Japan
Martin Nowak, USA
Markus Owen, UK
Hugo Palmans, UK
Lech S. Papiez, USA
Jean Pierre Rospars, France
David James Sherman, France
Sivabal Sivaloganathan, Canada
Elisabeth Tillier, Canada
Nestor V. Torres, Spain
Anna Tramontano, Italy
Nelson J. Trujillo-Barreto, Cuba
Kutlu O. Ulgen, Turkey
Nagarajan Vaidehi, USA
Edelmira Valero, Spain
Jinliang Wang, UK
Jacek Waniewski, Poland
Guang Wu, China
X. George Xu, USA
Henggui Zhang, UK

Contents

Computational and Mathematical Modeling of Tumor Kinetics and Response to Radiation and Chemotherapy, Eva Bezak, Loredana Marcu, and Scott Penfold

Volume 2012, Article ID 702675, 2 pages

Modelling Tumour Oxygenation, Reoxygenation and Implications on Treatment Outcome, Iuliana Toma-Dasu and Alexandru Dasu

Volume 2013, Article ID 141087, 9 pages

Assessing the Effects of Estrogen on the Dynamics of Breast Cancer, Chipo Mufudza, Walter Sorofa, and Edward T. Chiyaka

Volume 2012, Article ID 473572, 14 pages

A Simulation Study of the Radiation-Induced Bystander Effect: Modeling with Stochastically Defined Signal Reemission, Kohei Sasaki, Kosuke Wakui, Kaori Tsutsumi, Akio Itoh, and Hiroyuki Date

Volume 2012, Article ID 389095, 5 pages

(Radio)Biological Optimization of External-Beam Radiotherapy, Alan E. Nahum and Julien Uzan

Volume 2012, Article ID 329214, 13 pages

Microdosimetry for Targeted Alpha Therapy of Cancer, Chen-Yu Huang, Susanna Guatelli, Bradley M. Oborn, and Barry J. Allen

Volume 2012, Article ID 153212, 6 pages

Study of Tumor Growth under Hyperthermia Condition, Qing Zhu, Aili Zhang, Ping Liu, and Lisa X. Xu

Volume 2012, Article ID 198145, 9 pages

Atomic Radiations in the Decay of Medical Radioisotopes: A Physics Perspective, B. Q. Lee, T. Kibédi, A. E. Stuchbery, and K. A. Robertson

Volume 2012, Article ID 651475, 14 pages

***In Silico* Modelling of Treatment-Induced Tumour Cell Kill: Developments and Advances**,

Loredana G. Marcu and Wendy M. Harriss-Phillips

Volume 2012, Article ID 960256, 16 pages

***In Silico* Modelling of Tumour Margin Diffusion and Infiltration: Review of Current Status**,

Fatemeh Leyla Moghaddasi, Eva Bezak, and Loredana Marcu

Volume 2012, Article ID 672895, 16 pages

Risk-Adaptive Volumetric Modulated Arc Therapy Using Biological Objective Functions for Subvolume Boosting in Radiotherapy, Nicholas Hardcastle and Wolfgang A. Tome

Volume 2012, Article ID 348471, 7 pages

The HYP-RT Hypoxic Tumour Radiotherapy Algorithm and Accelerated Repopulation Dose per Fraction Study, W. M. Harriss-Phillips, E. Bezak, and E. Yeoh

Volume 2012, Article ID 363564, 13 pages



***In Silico* Nanodosimetry: New Insights into Nontargeted Biological Responses to Radiation,**
Zdenka Kuncic, Hilary L. Byrne, Aimee L. McNamara, Susanna Guatelli, Westa Domanova,
and Sébastien Incerti
Volume 2012, Article ID 147252, 9 pages

Editorial

Computational and Mathematical Modeling of Tumor Kinetics and Response to Radiation and Chemotherapy

Eva Bezak,^{1,2} Loredana Marcu,^{1,2,3} and Scott Penfold^{1,2}

¹Department of Medical Physics Royal Adelaide Hospital, Adelaide, SA 5000, Australia

²School of Chemistry and Physics, The University of Adelaide, Adelaide, SA 5005, Australia

³Faculty of Science, University of Oradea, Universitatii str., Oradea, Romania

Correspondence should be addressed to Eva Bezak, eva.bezak@health.sa.gov.au

Received 28 November 2012; Accepted 28 November 2012

Copyright © 2012 Eva Bezak et al. This is an open access article distributed under the Creative Commons Attribution License, which permits unrestricted use, distribution, and reproduction in any medium, provided the original work is properly cited.

The AACR Cancer Progress Report (2011) shows that in the USA from 1990 to 2007, death rates from all cancers dropped to 22% in men and 14% in women. More than 68% of adults live five years or more after diagnosis, up from 50% in 1975. For all paediatric cancers, the five-year survival rate is 80%, compared with 52% in 1975. However, the poor survival rates from most deadly cancers, pancreatic, ovarian and glioblastoma multiforme (GBM), have not changed to this date.

Despite many technological and clinical advances, cancer death rates are still high. Patient death arises from the failure to detect primary tumors before they spread their micrometastases around the body, as in pancreatic and ovarian cancers, the inability to control primary tumors, as in GBM, or the inability to eliminate micrometastases before they form new lesions. Disseminated disease is the primary cause of cancer death.

On top of this is the rapidly developing cost of the management of cancer. Cancer causes the highest economic loss of all of the 15 leading causes of death worldwide. The World Health Organisation (WHO) notes that the economic toll from cancer is nearly 20% higher than heart disease, the second leading cause of economic loss (\$895 billion and \$753 billion, resp.). Health budgets in developed countries are continually expanding and constrained by limited resources. But cost/benefit analyses to determine whether the increased cost of treatment achieves improved outcomes remain unknown.

Approaches to understanding the causes and treatment of cancer are numerous, involving chemistry, physics, biology, genetics, medicine, pharmacology, and experiments

based on *in vivo* or *in vitro* setups, using animal models and/or human trials. Among the plethora of experimental and research activities, mathematical models of cancer growth, behaviour, and response of tumors to agents like chemotherapy and radiotherapy have been the subject of intensive research and development since the middle of the last century. Just like all other cancer research, cancer modeling requires a multidisciplinary approach, involving physicists, mathematicians, molecular biologists, medical specialists, and many others. At present, the rapid growth of computational power allows us to build complex mathematical models that can investigate different aspects of the disease and can be used to investigate the role of complex tumor behaviour and its response to various therapeutic protocols.

In general, modeling methods can be divided into analytical methods and stochastic methods. Analytical methods are based on deterministic equations in order to model evolution of a biological system. A set of differential equations with multiple parameters is often used to model complex tumor kinetics under various conditions. On the other hand, stochastic methods use random number generators and probability distributions to simulate evolution of the system from a set of initial conditions and parameter values (also known as *in silico* models). These methods are particularly useful as they can take into account the high degree of complexity and multifaceted nature of cellular proliferation, communication, and interactions with reagents that cannot be easily described by a set of equations.

Pros for modeling in cancer research are as follows.

- (i) Modeling significantly reduces the time needed for an outcome as compared to *in vivo* techniques; it also

reduces the costs involved in the research and, very importantly, reduces the risks, which, for example, in a clinical trial are unavoidable.

- (ii) Modeling allows the easy investigation of the “what if?” scenarios; that is, models have predictive power.
- (iii) Modeling allows for the quantitative assessment of qualitative processes.
- (iv) Because of the low costs involved, modeling allows researchers with modest infrastructure to contribute with valuable ideas to the field.
- (v) Modeling enables to quantify and interpret experimental results, including data obtained from clinical trials.

Cons are as follows.

- (i) It is very difficult, if not impossible, to model the entirety of a biological process.
- (ii) There is always a compromise in a modeling process as only a certain number of known biological processes/parameters can be accounted for within the model. This known compromise exists on top of the unknown compromise represented by the obvious omission of the unknown processes that happen in the modeled biological system.
- (iii) The results of an *in silico* model should be considered clinically only after the credibility of the model has been validated by several *in vivo* results.

Models can also allow for individualization of treatments. It is therefore possible that in near future a patient can receive individualized treatment based on their specific biological/genetic parameters rather than undergoing a treatment protocol that is based on population averages.

In this special issue we will explore the topic of computational and mathematical modeling of tumor kinetics and response to radiation and chemotherapy. The papers in this issue have been contributed by eminent researchers and research groups in the area of cancer modeling, radiation biology modeling, microdosimetry, and many others. Several papers offer comprehensive reviews of current status of cancer modeling in specific areas (e.g., hypoxia, glioblastoma multiforme models, etc.). We trust that the readers will find this issue both useful and practical as well as a good source of reference material and a stimulating read.

*Eva Bezak
Loredana Marcu
Scott Penfold*

Review Article

Modelling Tumour Oxygenation, Reoxygenation and Implications on Treatment Outcome

Iuliana Toma-Dasu¹ and Alexandru Dasu²

¹ *Medical Radiation Physics, Stockholm University and Karolinska Institutet, 171 76 Stockholm, Sweden*

² *Department of Radiation Physics UHL, County Council of Östergötland, Radiation Physics and Department of Medical and Health Sciences, Faculty of Health Sciences, Linköping University, 581 83 Linköping, Sweden*

Correspondence should be addressed to Iuliana Toma-Dasu; iuliana.livia.dasu@ki.se

Received 11 December 2012; Accepted 26 December 2012

Academic Editor: Eva Bezak

Copyright © 2013 I. Toma-Dasu and A. Dasu. This is an open access article distributed under the Creative Commons Attribution License, which permits unrestricted use, distribution, and reproduction in any medium, provided the original work is properly cited.

Oxygenation is an important component of the tumour microenvironment, having a significant impact on the progression and management of cancer. Theoretical determination of tissue oxygenation through simulations of the oxygen transport process is a powerful tool to characterise the spatial distribution of oxygen on the microscopic scale and its dynamics and to study its impact on the response to radiation. Accurate modelling of tumour oxygenation must take into account important aspects that are specific to tumours, making the quantitative characterisation of oxygenation rather difficult. This paper aims to discuss the important aspects of modelling tumour oxygenation, reoxygenation, and implications for treatment.

1. Introduction

Oxygenation is an important component of the tumour microenvironment and has a significant impact on the progression and management of cancer. Hypoxia, or reduced oxygenation, has been associated with restrained proliferation, apoptosis, necrosis, angiogenesis, the development of an aggressive phenotype, and resistance to treatment [1]. These aspects make the quantification of tumour oxygenation and the study of its impact on treatment approaches highly relevant topics in oncology research. Consequently, several methods have been proposed for measuring tissue oxygenation, employing polarographic, fluorescent, radionuclide, or magnetic resonance techniques [2]. The results of such measurements have generally been used for qualitative correlations with treatment outcome [3–9]. However, many of these methods are invasive or suffer from sampling or

resolution limitations and these aspects may reduce the significance of the results. From this perspective, theoretical determination of tissue oxygenation through simulations of the oxygen transport process might be a practical alternative to characterise the spatial distribution of oxygen on the microscopic scale and its dynamics and to study its impact on the response to radiation. This paper aims to discuss the important aspects of modelling tumour oxygenation, reoxygenation, and implications for treatment.

2. Origins of Tumour Hypoxia

One of the most striking features of solid tumours in comparison to normal tissues is their architecture of vascular networks. In normal tissues, the vasculature has developed to provide adequate supply of oxygen to all of the cells,

while in tumours, the vascular network is inadequate, almost chaotic and the quality of the blood flowing in it can be quite poor [10, 11]. This is the result of the generally high proliferation rates of tumour cells in comparison to normal cells that allow the tumours to quickly outgrow the existing blood and nutrient supply. As sustained angiogenesis is one of the hallmarks of cancer [12], oxygen supply is restored in tumours through the formation of new blood vessels. This is a relatively slow process [13] and newly formed vessels are also outgrown by the proliferating cells. Furthermore, newly formed vessels in tumours usually originate on the venous side of the vasculature [10]. Newly formed vessels in most solid tumours are often dilated, tortuous and have incomplete or missing endothelial lining resulting in an increased vascular permeability [14]. They are also unable to respond to local or systemic signals for vasodilatation or vasoconstriction [11]. In addition, tumour vasculature is not accompanied by a lymphatic system hampering the drainage of interstitial fluid and by-products of cell metabolism which can further influence vascular flow. Indeed, changes in interstitial pressure are thought to be responsible for the temporary cessation or resumption of flow through tumour microvessels. Further, the preference of tumour cells to glucose metabolism leading to the formation of lactic acid as a by-product leads to an acidification of the extracellular fluid in tumours [14]. All of these effects lead to a unique microenvironment in tumours characterised by poor supply and steep gradients of oxygen and other nutrients.

Depending on the underlying mechanisms and their duration, two main types of hypoxia have been identified in tumours, chronic and acute. Limitations in oxygen diffusion from the blood vessels into the tissue lead to the development of diffusion-limited or chronic hypoxia, first described by Thomlinson and Gray [15]. In contrast, local disturbances in vessel perfusion lead to the appearance of perfusion-limited or acute hypoxia, described by Brown [16] and verified experimentally by Chaplin et al. [17]. This has also been referred to as cyclic or fluctuating hypoxia due to the temporary character of the disturbances and the restoration of the perfusion through the affected vessels. Further subtypes of hypoxia have been identified depending on the mechanisms behind the development of hypoxic regions in tumours [18]. An important feature of tumour oxygenation is that it is not static and that several mechanisms determine its dynamics on timescales ranging from a few minutes for acute hypoxia to several days for chronic hypoxia. Accurate modelling of tumour oxygenation would have to take into account all of these aspects. However, their underlying complexity makes the study of oxygen transport to tumours quite difficult, especially when the aim is to accurately quantify the oxygen distribution.

3. Intravascular Oxygen Transport

In vertebrates, oxygen transport from the lungs to tissues takes place through the circulatory system. Most oxygen is transported bound to the heme groups of the haemoglobin (Hb) molecule in red blood cells (RBCs). The binding of the

oxygen to haemoglobin takes place in 4 steps corresponding to the 4 heme groups of the metalloprotein, since binding one oxygen molecule determines a conformational change of the Hb molecule that influences its ability to further bind other molecules. From this perspective, the kinetics of the oxygen-haemoglobin reaction is described by the Adair equation [19] giving the equilibrium relationship between the saturation of the Hb molecule and the oxygen tension. However, the Adair equation is seldom used for the mathematical modelling of oxygen transport since it cannot be inverted analytically to give the oxygen tension as a function of the saturation of the haemoglobin. Instead, the simpler Hill equation [20] is used:

$$S = \frac{(p/p_{50,\text{Hb}})^n}{1 + (p/p_{50,\text{Hb}})^n}, \quad (1)$$

where S is the fractional haemoglobin saturation, p is the local partial pressure of oxygen (or $p\text{O}_2$), $p_{50,\text{Hb}}$ is the $p\text{O}_2$ value at which the haemoglobin is 50% saturated, and n is the Hill parameter.

The sigmoid relationship described by the Adair and Hill equations is usually known as the oxyhaemoglobin dissociation curve or the oxygen-haemoglobin equilibrium curve. This curve is affected by a number of factors including temperature, pH, and CO_2 concentration [21]. Given the unique microenvironment of tumours with a low pH, the oxygen-haemoglobin equilibrium may be achieved at different oxygen tensions in tumours compared to normal tissues and there may also be differences between various normal tissues. In light of these expected differences, caution is advised at the generalisation of parameters determined for a particular tissue or during the extrapolation of the results achieved using these parameters.

Besides the bound component, modelled oxygen transport would also have to account for the free and dissolved oxygen in the red blood cells and blood plasma. Unbound oxygen represents only 1.5% of the total oxygen content of the blood in normal tissues, provided Hb is completely saturated [21]. However, this fraction might be higher for tumours, where vessels often originate on the venous side of the vasculature containing desaturated blood. The association between anaemia and cancer would further decrease the relative importance of the bound component.

Modelling of intravascular transport has to account for both the free and the Hb-bound oxygen, as well as for the transport of oxygen through the membrane of the red blood cells. Popel [21] provided a comprehensive review of the earlier theoretical work on the particulate nature of RBC-plasma transport of oxygen. More recent approaches, however, have incorporated RBC-plasma transport into intravascular transport models accounting for intracapillary O_2 gradients and giving the average flux of oxygen through the capillary wall [22]. These models have mainly been used for studying the oxygen delivery to muscles and have found that blood-tissue transport encounters an effective intravascular resistance (IVR) that could be quantified as a mass transfer coefficient. This is influenced by the assumptions for intravascular transport, the shape of the RBC or vessel permeability. This suggests that care has to be employed when extrapolating

normal tissue models to tumours, as the poor endothelial lining of tumour microvessels increases their permeability, while the acidic tumour microenvironment could influence the shape of the RBC as well as the Hb dissociation curve.

4. Tissue Transport Models

The first attempts to theoretically describe the oxygen transport into tissue date from the beginning of the 20th century [23, 24] and were based on systems with simple geometries for which an analytical solution could be obtained. One of these early models, the Krogh tissue cylinder model, has been particularly important as it has served as the foundation for many subsequent studies. Its main assumptions were the following.

- (i) pO_2 distribution in tissue has a cylindrical symmetry and axial diffusion is not significant;
- (ii) tissue pO_2 at capillary wall equals capillary pO_2 (no intravascular resistance);
- (iii) oxygen transport in tissue takes place through passive diffusion;
- (iv) tissue diffusivity is independent of spatial position;
- (v) transport phenomena are steady state.

Many models derived from the Krogh model have focused on the study of oxygenation in normal tissues as reviewed by Popel [21] and Goldman [22]. However, the assumptions of the Krogh tissue cylinder model have also been used by Thomlinson and Gray [15] and by Tannock [25] to describe theoretically the spatial distribution of tumour hypoxia. Later developments saw the introduction of models with more realistic vascular geometries to reflect the complexity of tumour vasculature, using Green functions or numerical methods to describe the tissue oxygenation [2, 26–31].

A general expression for the reaction-diffusion equation describing the oxygen transport in homogeneous tissues is shown in

$$\frac{\partial p}{\partial t} = \nabla \cdot (D \nabla p) - \nabla \cdot (\vec{u} p) - q + s, \quad (2)$$

where p is the local pO_2 , D is the diffusion coefficient, \vec{u} is the flow velocity, q represents the local consumption, and s is a source term.

In (2), the term $\nabla \cdot (D \nabla p)$ describes the movement of oxygen through diffusion and the term $\nabla \cdot (\vec{u} p)$ describes the movement through convection. The convection term is usually neglected as the convective currents in the interstitial compartment of the normal tissues are estimated to represent only about 0.5–1% of the plasma flow. This may, however, not be the case of tumours, where the convective compartment could reach up to 15% [14]. The impact of neglecting the convective compartment in modelling tumour oxygenation is yet to be studied.

The rate of oxygen consumption in tissues, q , is thought to follow the Michaelis-Menten kinetics (3) as originally

proposed by Tang [32], although variations of the equation have also been considered [33]:

$$q = q_{\max} \frac{P}{p + p_{50,MM}}, \quad (3)$$

where q_{\max} is the maximum consumption rate, p is the local pO_2 , and $p_{50,MM}$ is a parameter describing the pO_2 at which the consumption rate halves. Equation (3) predicts an almost constant consumption rate at high oxygen tensions that is in agreement with the zero-order kinetics assumed by some of the earlier models [23, 25, 28, 34]. The Michaelis-Menten kinetics has, however, the advantage of more accurately describing the consumption at low pO_2 and has been used in recent models [2, 27, 29, 31, 35–38].

The source term, s , in (2) has been used in different ways in various models. Some models assume that the source term could be set to zero since cells do not produce oxygen [29, 37–40], while others implement a different approach where the oxygen supply from the capillaries is described as a distributed source throughout the tissue with localised spikes at the vessel positions [30, 40].

Most of the studies have focused on a steady state of the system where $\partial p / \partial t = 0$. This is in agreement with the observations by Hill [24], that the nonstationary evolution of the system is very short. Changes of oxygenation patterns due to perfusion limitations have time scales of minutes [16], while the formation of new blood vessels through angiogenesis takes place over several days [13] and therefore the steady state solution would apply in most situations. However, there might be some cases where the time-dependent oxygen transport would have to be considered, such as the onset of acute hypoxia after the cessation of blood flow, its disappearance following the reperfusion of capillaries, or cases when the oxygen supply through tumour capillaries has variations for longer time periods.

Solving (2) to determine tissue oxygenation requires setting boundary conditions for the limits of the modelled domain and even in this case various approaches have been used. For the interface between capillaries and tissue, one could neglect the intravascular resistance and use a Dirichlet boundary condition assuming that the pO_2 value at the capillary wall equals the capillary pO_2 [23, 29]. Alternatively, one could use a Robin boundary condition, assuming that the oxygen flux across the interface, that is, the vessel wall, must be continuous [37, 39, 40]. Assuming cylindrical symmetry for a capillary with radius R and thickness w , the diffusive flux on the tissue side of the vessel wall could be written as

$$F = -D_{\text{wall}} \int_0^{2\pi} \frac{\partial p}{\partial r} r d\theta = \frac{D_{\text{wall}}}{R} \frac{p_{\text{cap}} - p}{\ln(1 - w/R)}, \quad (4)$$

where D_{wall} is the diffusivity in the wall and p_{cap} is the capillary pO_2 . Assuming that the wall thickness w is much smaller than the external radius R , (4) becomes

$$F = \frac{D_{\text{wall}}}{w} (p_{\text{cap}} - p) = P_m (p_{\text{cap}} - p), \quad (5)$$

where P_m is the vessel permeability.

The expression in (5) could be integrated over the surface of the capillary to obtain the net rate of oxygen entering the tissue. Thus, the source term in (2) could be written for each point representing the capillary as

$$s = \frac{1}{V} \int_0^{2\pi} F \cdot RL d\theta = \frac{1}{V} S \cdot P_m (p_{\text{cap}} - p), \quad (6)$$

where V is the capillary volume and S is its area. Explicitly writing the volume and area of a cylinder, (6) becomes

$$s = \frac{1}{\pi R^2 L} 2\pi RL \cdot P_m (p_{\text{cap}} - p) = \frac{2P_m}{R} (p_{\text{cap}} - p). \quad (7)$$

As expected, different boundary conditions would lead to different solutions of the reaction-diffusion equation, especially in the regions close to the vessels. However, Skeldon et al. [40] showed that for vessels with very high permeability, the Robin boundary condition leads to similar results as the Dirichlet boundary condition. If this is the case of tumour capillaries with increased permeability, it could provide an advantage when solving (2), since Dirichlet boundary conditions are easier to program.

Similarly, different approaches may be used for the outer boundaries of the simulated domain. These include Neuman boundary conditions setting the flux through the outer boundaries to zero, imposing periodic boundary conditions or other approaches [23, 29, 37]. The choice of the border conditions for the outer boundaries could also influence the amount of calculated hypoxia in the tissue as shown by Secomb et al. [37] who discussed the advantages and disadvantages of these approaches.

5. Modelling Parameters

An important aspect for the theoretical modelling of tissue oxygenation is the choice of parameters in (1)–(7). Experimental determination of these parameters is rather challenging and in many cases it involves the assumption of a model relating a measured quantity to the quantity to be determined. This highlights the importance of using parameters in the limit of the models for which they have been determined.

The least debated parameter in the literature is the average diffusivity of oxygen into tissue, with most authors agreeing on $D = 2 \times 10^{-5} \text{ cm}^2 \text{ s}^{-1}$ [25, 28]. This could be explained from the point of view of the passive transport of oxygen through tissue and the relative homogeneity of soft tissues in the body.

In contrast, a relatively large range of values have been proposed for the maximum consumption rate, q_{max} , in (3) [10, 41–43], predominantly explained by the variability of the metabolic characteristics of tissues. As early as the beginning of the 20th century, Hill [24] observed significant differences in the consumption rates in active versus inactive muscle, while more recently Kallinowski et al. [44] showed that oxygen consumption in tumour cells decreases as cell quiescence develops. These are key observations because oxygen consumption is an important determinant of tissue oxygenation as shown by Secomb et al. [35], who found

that a relatively modest reduction of tissue consumption may abolish tissue hypoxia, while a considerable increase of capillary oxygen content would be required for the same purpose. These results illustrate the difficulties in selecting the relevant consumption parameter for modelling. Indeed, significant differences may appear between tumour types or individuals depending on their metabolic activity, and intratumour heterogeneity could also be expected. Further confounding factors when determining the tissue consumption rate may reside in the method used for the determination and the assumptions made with respect to the oxygen supply rate or the invasiveness of the method used. Nevertheless, a relevant value for the maximum oxygen consumption rate in tumours that has been used in many studies is 15 mmHg s^{-1} [15, 25, 29].

Another parameter that is needed for the Robin boundary conditions (5) or for the distributed source models (7) is the permeability of tumour capillaries. Most of the permeability values available are relevant for normal tissue capillaries and these values have been used in studies investigating the oxygenation of tumours [30, 39, 40]. However, it has to be borne in mind that tumour vasculature has poor endothelial lining resulting in increased vascular permeability [14] and that normal tissue values may lead to an overestimation of the intravascular resistance of tumour capillaries.

Simulations of tumour oxygenation also require vascular oxygenation for the boundary conditions. Given the venous origin of newly formed vessels in tumours [10], a common assumption is that vascular $p\text{O}_2$ in tumours is rather low [15, 25, 29, 37] and this is in agreement with experimental determinations of vascular oxygenations [45, 46]. Some studies have assumed a uniform oxygenation of the vessels [29, 30, 37, 39], while others have considered distributions of values [2, 28, 31]. Comparisons between simulations with the two assumptions have shown microscale differences between the resulting distributions, but no significant differences in the global characterisation of tissue oxygenation [2].

The vascular geometry is another important factor that has to be taken into account when simulating tumour oxygenation. Given the complexity of tumour vasculature, three-dimensional (3D) data would be required for the full characterisation of tumour oxygenation, but such images are difficult to obtain with existing *in vivo* imaging modalities due to their limited spatial resolution. Skin flap window chambers could be a solution to provide 3D geometries [35], but the thickness of the tissue in this model is much smaller than the chamber diameter. Alternatively, two-dimensional (2D) sections of *ex vivo* tissue samples could be used for the characterisation of vasculature and oxygenation. This approach was originally used by Thomlinson and Gray [15] for comparing the appearance of necrotic regions in lung tumours with calculations of tumour oxygenation and also in more recent studies employing tissue sections as input for simulations [28, 39]. An alternative approach is to use generated 2D maps of capillaries, either reflecting measured distributions of intervascular distances [2, 29, 31] or randomly generated distributions [30, 38, 40]. The former approach should be preferred as it has been shown that a full

description of tissue vasculature is required for an accurate characterisation of tissue oxygenation. Average intervascular distance or the related quantity mean vascular density giving the number of vessels per unit area is one determinant of tissue oxygenation, the other being the shape of the distribution of intravascular distances [29].

Oxygen transport has also been coupled with the transport of other substances. Kirkpatrick et al. [47] used a mathematical model of oxygen and glucose mass transport in tumours to study the influence of kinetic and physical factors on metabolism. Other models are concerned with the transport and metabolism of tracers used in advanced imaging methods capable of visualising tumour hypoxia [30, 39, 40].

6. Modelling the Dynamics of Hypoxia

The dynamics of tumour hypoxia is an important aspect that has to be taken into consideration for many modelling studies. Indeed, angiogenesis and fluctuations in the perfusion of the blood vessels supplying the tumours have the potential to alter the oxygenation pattern, even in the absence of a therapeutic action upon the tumour cell population. These changes could in principle be modelled by assuming different spatial distributions of blood vessels over time, as the impaired perfusion of some vessels considered responsible for acute hypoxia would be equivalent to a decrease of the effective vascular density, while the appearance of new vessels would increase it. In this context it is important to note that even if the resulting distributions from repeated simulations are similar, in the case of acute hypoxia, different cells will be in different hypoxic subcompartments at each modelled time point and this dynamic process needs to be reflected in the modelled radiosensitivity of the cells.

Besides fluctuations in perfusion that are responsible for the cycling variation of the acutely hypoxic compartment, there are other mechanisms that may lead to changes in oxygenation during the course of a treatment. Radiation and other cytotoxic agents may induce growth inhibition in the irradiated cells that would subsequently lead to a decreased oxygen consumption in the surviving tumour cells [44] and thus improved oxygenation for previously hypoxic cells [35, 48]. On a longer timescale, the removal of the doomed cells near the blood vessels damaged by the cytotoxic agents might also improve the oxygenation of cells situated further away.

Another important aspect related to the timescale of hypoxia is the radiosensitivity of the affected cells. It is rather well known that decreased oxygen availability could lead to increased radioresistance of the hypoxic cells. Less known, however, is the effect of nutrient starvation that often accompanies chronic hypoxia, but not acute hypoxia. Indeed, it has been suggested [49, 50] that the two types of hypoxia might have different radiosensitivities due to changes in the repair capacity of the chronically hypoxic cells starved of oxygen and nutrients [51–55]. Consequently, differentiating between the two types of hypoxia as well as the time-dependent variation of the oxygen and nutrient availability might be needed for studies aiming to quantify the impact of certain treatment approaches on tumour containing both

types of hypoxic cells. In this case, simulations would have to account for the perfusion status of the blood vessels in the tumour at various time points during the treatment and the impact on cellular radiosensitivity [56].

7. Tumour Oxygenation and Treatment Modelling

Theoretical simulations of oxygen transport to tumours have played a key role in understanding many aspects of tumour microenvironment that could influence treatment outcome. For example, theoretical modelling has allowed the characterisation of the gradients that may appear around the blood vessels, the study of the impact of the temporary closure of some capillaries, the radiobiological distinction between the two hypoxic compartments, or the effectiveness of various measurements methods. Comparisons between the maximum diffusion distance of oxygen into tissue and size of the viable rims of tumour cells around stroma or individual blood vessels led to the first descriptions of the appearance of chronic hypoxia in tumours [15, 25]. Simulations have also shown that several factors influence the relationship between tumour vasculature and oxygenation, indicating that there is an equivocal relationship between tissue oxygenation and vascular oxygenation, mean intravascular distance, or the number of unperfused vessels. Thus, mean vascular density is an important determinant of tumour oxygenation, but the relationship is modulated by the shape of the distribution of intervascular distances, the vascular oxygen content, and the number of closed capillaries [2, 29, 31]. This explains the failure to find in experimental studies a direct correlation between tumour oxygenation and vascular density [57].

Calculating the expected response from cell populations with different oxygenation requires a cell survival model with parameters that could be modified according to the radiation sensitivity of each compartment. According to the linear quadratic LQ model [58, 59], cell survival in a fully oxic population after a single radiation dose d is given by

$$SF_{\text{ox}} = \exp(-\alpha d - \beta d^2), \quad (8)$$

where α and β are model parameters for oxic conditions. The modification of radiosensitivity in hypoxia could be accounted for through the use of modifying factors (OMFs) that are dependent on the local oxygen tension and the duration of hypoxia as in

$$SF_{\text{hyp}} = \exp \left[-\frac{\alpha}{\text{OMF}_{\alpha}(p\text{O}_2, t)} d - \frac{\beta}{\text{OMF}_{\beta}^2(p\text{O}_2, t)} d^2 \right]. \quad (9)$$

A noteworthy expression for the oxygen modification factors has been proposed by Alper and Howard-Flanders [60]:

$$\text{OMF}(p\text{O}_2) = \text{OER}_{\text{max}} \frac{k + p\text{O}_2}{k + \text{OER}_{\text{max}} p\text{O}_2}, \quad (10)$$

where OER_{max} is the maximum protection achieved in the absence of oxygen and k is a reaction constant around 2.5–3 mmHg [61, 62].

Cell survival for populations of cells characterised by a distribution of oxygenations could be obtained as the weighted sum of cell survival for each compartment:

$$SF_{\text{distr}}(d) = \sum_i w_i SF_{\text{hyp},i}(d), \quad (11)$$

where w_i is the relative weight of each oxygenation compartment.

For fractionated treatments delivering n fractions of size d , different equations may be employed depending on the interfraction dynamics of oxygenation in the assumed population. Thus, for populations with static oxygenations, the cell survival is given by

$$SF_{\text{distr}}^{\text{static}}(n, d) = \sum_i w_i [SF_{\text{hyp},i}(d)]^n, \quad (12)$$

while for populations with full dynamics of the oxygenation, cell survival is given by

$$SF_{\text{distr}}^{\text{dynamic}}(n, d) = \left[\sum_i w_i SF_{\text{hyp},i}(d) \right]^n. \quad (13)$$

Cell survival for other frequencies of oxygenations could be obtained by combining (12) and (13).

Theoretical simulations using (9)–(13) have shown significant differences in the predicted response depending on the assumed oxygenation of the tissue and these results indicate that full distributions of pO_2 values, not only the hypoxic fraction, are needed for modelling [25, 56, 63]. This is particularly important in light of the equivocal relationship between tumour oxygenation and the above-mentioned parameters.

Equally interesting have been the results of simulations taking into account the possible radiobiological differences between acute and chronic hypoxic cells. Experimental studies have shown that chronically hypoxic cells may have low or depleted energy reserves which would impair their repair mechanisms [52–55], in contrast with acutely hypoxic cells that are repair competent. Correlating these findings with calculated oxygen distributions in tumours has suggested that the added biochemical sensitisation of chronically hypoxic cells could provide an explanation for the success of radiotherapy, as the chemical radioresistance conferred by hypoxia in general would otherwise require unrealistically high doses to control tumours containing hypoxic cells [49, 50, 56]. This comes as a confirmation of studies showing an improvement of control in experimental systems in the presence of chronically hypoxic cells [64]. In contrast, the presence of acute hypoxia in tumours leads to a worsening of the response to radiation therapy [56, 65, 66]. However, while the fluctuating character of the perfusion disturbances in tumour capillaries does not lead to a full “washout” of the radioresistance of acutely hypoxic cells, the fluctuations are essential for the success of fractionated therapy. Indeed, treatment schedules employing too few fractions (5 or fewer) might not allow enough interfraction reoxygenation opportunities to change the sensitivity of the hypoxic cells in tumours which would in turn lead to poor outcome [67]. This could have significant implications for stereotactic radiotherapy where extremely

hypofractionated schedules should be pursued with caution [68].

Theoretical simulations have also been used to study the effectiveness of polarographic electrodes used to characterise tissue oxygenation [65, 69–72] or imaging with hypoxia-specific tracers [30, 39, 73–75]. It has thus been shown that averaging characteristic both to polarographic methods and to imaging methods with finite spatial resolution as well as differences in sensitivity of the measurement probes could lead to measured oxygenations that would be quite different from the tissue oxygenation [70, 73, 76], that in turn would translate into different predictions regarding tissue responsiveness to radiation therapy. This highlights the importance of carefully extrapolating measurements of tissue oxygenation to quantitative assessments of the expected response from radiation therapy.

In vivo imaging of hypoxia with dedicated tracers has received considerable attention in recent years as it could be used to quantify the spatial distribution and the severity of hypoxic areas in tumours for individualising or adapting the treatment according to biological factors [67, 77, 78]. In this context it has been shown that the dynamic character of hypoxia observed in clinical and experimental studies [79–84] has important implications for radiation therapy and it needs to be taken into account for treatment simulations. Indeed, neglecting it for prescriptions of highly heterogeneous dose distributions could lead to mismatches between planned dose hotspots and radioresistant hypoxic domains in tumours that would lead to poor outcome [67]. Furthermore, the limited spatial resolution of imaging methods could lead to poor rendering of the small hypoxic regions [76] that would translate into an underestimation of their radiosensitivity. However, this might be less of a problem for rapid interfraction reoxygenation that might ensure the success of dose painting techniques that do not take into account the microscale heterogeneity of hypoxia [85].

Besides these direct applications, theoretical modelling has proven a valuable tool in supplementing experimental data and for understanding the effects of factors that could not be studied individually or experimentally, in spite of uncertainties regarding tissue geometry, vascular O_2 distributions, and *in vivo* parameters such as oxygen consumption rate [21, 22, 40]. It could also be used for more complex models studying the interplay between tissue oxygenation and cell growth and the macroscopic dynamics of tumours [86–88].

Far from being exhaustive, this review illustrates the importance of simulating the many complex facets tumour oxygenation. Considerable amount of work remains to be performed, both in updating the models of oxygen transport into tissue according to new findings and validations regarding the involved mechanisms and parameters and in terms of new opportunities for simulating treatments. Therefore, the increased interest in light of ion therapy [89] with its included potential of reducing the hypoxic radioresistance opens up new directions for research in terms of studying the impact of hypoxia on radiation treatment. New models for taking into account the response of hypoxic cells to high LET radiation are being developed [90] and will be tested with

the ultimate aim to counteract hypoxic radioresistance and achieve maximum clinical benefit for patients.

Conflict of Interests

The authors declare that they have no conflict of interests.

References

- [1] P. Vaupel and A. Mayer, "Hypoxia in cancer: significance and impact on clinical outcome," *Cancer and Metastasis Reviews*, vol. 26, no. 2, pp. 225–239, 2007.
- [2] A. Daşu and I. Toma-Daşu, "Vascular oxygen content and the tissue oxygenation—a theoretical analysis," *Medical Physics*, vol. 35, no. 2, pp. 539–545, 2008.
- [3] M. Hockel, C. Knoop, K. Schlenger et al., "Intratumoral pO₂ predicts survival in advanced cancer of the uterine cervix," *Radiotherapy and Oncology*, vol. 26, no. 1, pp. 45–50, 1993.
- [4] D. M. Brizel, R. K. Dodge, R. W. Clough, and M. W. Dewhirst, "Oxygenation of head and neck cancer: changes during radiotherapy and impact on treatment outcome," *Radiotherapy and Oncology*, vol. 53, no. 2, pp. 113–117, 1999.
- [5] J. Bussink, J. H. A. M. Kaanders, A. M. Strik, and A. J. Van Der Kogel, "Effects of nicotinamide and carbogen on oxygenation in human tumor xenografts measured with luminescence based fiber-optic probes," *Radiotherapy and Oncology*, vol. 57, no. 1, pp. 21–30, 2000.
- [6] N. A. Mayr, W. T. Yuh, J. C. Arnholt et al., "Pixel analysis of MR perfusion imaging in predicting radiation therapy outcome in cervical cancer," *Journal of Magnetic Resonance Imaging*, vol. 12, no. 6, pp. 1027–1033, 2000.
- [7] J. H. A. M. Kaanders, K. I. E. M. Wiffels, H. A. M. Marres et al., "Pimonidazole binding and tumor vascularity predict for treatment outcome in head and neck cancer," *Cancer Research*, vol. 62, no. 23, pp. 7066–7074, 2002.
- [8] M. Kikuchi, T. Yamane, S. Shinohara et al., "¹⁸F-fluoromisonidazole positron emission tomography before treatment is a predictor of radiotherapy outcome and survival prognosis in patients with head and neck squamous cell carcinoma," *Annals of Nuclear Medicine*, vol. 25, no. 9, pp. 625–633, 2011.
- [9] A. Sun, S. Johansson, I. Turesson, A. Daşu, and J. Sörensen, "Imaging tumor perfusion and oxidative metabolism in patients with head-and-neck cancer using 1- [¹¹C]-acetate PET during radiotherapy: preliminary results," *International Journal of Radiation Oncology, Biology, Physics*, vol. 82, no. 2, pp. 554–560, 2012.
- [10] P. Vaupel, F. Kallinowski, and P. Okunieff, "Blood flow, oxygen and nutrient supply, and metabolic microenvironment of human tumors: a review," *Cancer Research*, vol. 49, no. 23, pp. 6449–6465, 1989.
- [11] J. Denekamp, A. Daşu, and A. Waites, "Vasculature and microenvironmental gradients: the missing links in novel approaches to cancer therapy?" *Advances in Enzyme Regulation*, vol. 38, no. 1, pp. 281–299, 1998.
- [12] D. Hanahan and R. A. Weinberg, "The hallmarks of cancer," *Cell*, vol. 100, no. 1, pp. 57–70, 2000.
- [13] J. Folkman, "The vascularization of tumors," *Scientific American*, vol. 234, no. 5, pp. 58–73, 1976.
- [14] P. Vaupel, "Tumor microenvironmental physiology and its implications for radiation oncology," *Seminars in Radiation Oncology*, vol. 14, no. 3, pp. 198–206, 2004.
- [15] R. H. Thomlinson and L. H. Gray, "The histological structure of some human lung cancers and the possible implications for radiotherapy," *British Journal of Cancer*, vol. 9, no. 4, pp. 539–549, 1955.
- [16] J. M. Brown, "Evidence for acutely hypoxic cells in mouse tumours, and a possible mechanism of reoxygenation," *British Journal of Radiology*, vol. 52, no. 620, pp. 650–656, 1979.
- [17] D. J. Chaplin, R. E. Durand, and P. L. Olive, "Acute hypoxia in tumors: implications for modifiers of radiation effects," *International Journal of Radiation Oncology Biology Physics*, vol. 12, no. 8, pp. 1279–1282, 1986.
- [18] C. Bayer, K. Shi, S. T. Astner, C. A. Maftei, and P. Vaupel, "Acute versus chronic hypoxia: why a simplified classification is simply not enough," *International Journal of Radiation Oncology Biology Physics*, vol. 80, no. 4, pp. 965–968, 2011.
- [19] G. S. Adair, "The hemoglobin system. VI. The oxygen dissociation curve of hemoglobin," *Journal of Biological Chemistry*, vol. 63, pp. 529–545, 1925.
- [20] A. V. Hill, "The possible effects of the aggregation of the molecules of haemoglobin on its disassociation curve," *Journal of Physiology*, vol. 41, pp. 4–7, 1910.
- [21] A. S. Popel, "Theory of oxygen transport to tissue," *Critical Reviews in Biomedical Engineering*, vol. 17, no. 3, pp. 257–321, 1989.
- [22] D. Goldman, "Theoretical models of microvascular oxygen transport to tissue," *Microcirculation*, vol. 15, no. 8, pp. 795–811, 2008.
- [23] A. Krogh, "The number and distribution of capillaries in muscles with calculations of the oxygen pressure head necessary for supplying the tissue," *Journal of Physiology*, vol. 52, no. 6, pp. 409–415, 1919.
- [24] A. V. Hill, "The diffusion of oxygen and lactic acid through tissues," *Proceedings of the Royal Society B*, vol. 104, pp. 39–96, 1928.
- [25] I. F. Tannock, "Oxygen diffusion and the distribution of cellular radiosensitivity in tumours," *British Journal of Radiology*, vol. 45, no. 535, pp. 515–524, 1972.
- [26] T. W. Secomb and R. Hsu, "Analysis of oxygen delivery to tissue by microvascular networks," *Advances in Experimental Medicine and Biology*, vol. 222, pp. 95–103, 1988.
- [27] T. W. Secomb, R. Hsu, M. W. Dewhirst, B. Klitzman, and J. F. Gross, "Analysis of oxygen transport to tumor tissue by microvascular networks," *International Journal of Radiation Oncology Biology Physics*, vol. 25, no. 3, pp. 481–489, 1993.
- [28] B. W. Pogue, J. A. O'Hara, C. M. Wilmot, K. D. Paulsen, and H. M. Swartz, "Estimation of oxygen distribution in RIF-1 tumors by diffusion model-based interpretation of pimonidazole hypoxia and eppendorf measurements," *Radiation Research*, vol. 155, no. 1, pp. 15–25, 2001.
- [29] A. Daşu, I. Toma-Daşu, and M. Karlsson, "Theoretical simulation of tumour oxygenation and results from acute and chronic hypoxia," *Physics in Medicine and Biology*, vol. 48, no. 17, pp. 2829–2842, 2003.
- [30] C. J. Kelly and M. Brady, "A model to simulate tumour oxygenation and dynamic [¹⁸F]-Fmiso PET data," *Physics in Medicine and Biology*, vol. 51, no. 22, pp. 5859–5873, 2006.
- [31] A. Daşu and I. Toma-Daşu, "The relationship between vascular oxygen distribution and tissue oxygenation," *Advances in Experimental Medicine and Biology*, vol. 645, pp. 255–260, 2009.
- [32] P. S. Tang, "On the rate of oxygen consumption by tissues and lower organisms as a function of oxygen tension," *Quarterly Review of Biology*, vol. 8, pp. 260–274, 1933.

- [33] P. K. Nair, D. G. Buerk, and W. J. Whalen, "Cat carotid body oxygen metabolism and chemoreception described by a two-cytochrome model," *American Journal of Physiology*, vol. 250, no. 2, pp. H202–H207, 1986.
- [34] R. Hsu and T. W. Secomb, "A green's function method for analysis of oxygen delivery to tissue by microvascular networks," *Mathematical Biosciences*, vol. 96, no. 1, pp. 61–78, 1989.
- [35] T. W. Secomb, R. Hsu, E. T. Ong, J. F. Gross, and M. W. Dewhirst, "Analysis of the effects of oxygen supply and demand on hypoxic fraction in tumors," *Acta Oncologica*, vol. 34, no. 3, pp. 313–316, 1995.
- [36] A. P. Bassom, A. Ilchmann, and H. Voss, "Oxygen diffusion in tissue preparations with Michaelis-Menten kinetics," *Journal of Theoretical Biology*, vol. 185, no. 1, pp. 119–127, 1997.
- [37] T. W. Secomb, R. Hsu, E. Y. H. Park, and M. W. Dewhirst, "Green's function methods for analysis of oxygen delivery to tissue by microvascular networks," *Annals of Biomedical Engineering*, vol. 32, no. 11, pp. 1519–1529, 2004.
- [38] S. F. Petit, A. L. A. J. Dekker, R. Seigneuric et al., "Intra-voxel heterogeneity influences the dose prescription for dose-painting with radiotherapy: a modelling study," *Physics in Medicine and Biology*, vol. 54, no. 7, pp. 2179–2196, 2009.
- [39] D. Mönnich, E. G. C. Troost, J. H. A. M. Kaanders, W. J. G. Oyen, M. Alber, and D. Thorwarth, "Modelling and simulation of [¹⁸F]fluoromisonidazole dynamics based on histology-derived microvessel maps," *Physics in Medicine and Biology*, vol. 56, no. 7, pp. 2045–2057, 2011.
- [40] A. C. Skeldon, G. Chaffey, D. J. Lloyd, V. Mohan, D. A. Bradley, and A. Nisbet, "Modelling and detecting tumour oxygenation levels," *PLoS ONE*, vol. 7, no. 6, Article ID e38597, 2012.
- [41] P. M. Gullino, F. H. Grantham, and A. H. Courtney, "Utilization of oxygen by transplanted tumors in vivo," *Cancer Research*, vol. 27, no. 6, pp. 1020–1030, 1967.
- [42] P. L. Olive, C. Vikse, and M. J. Trotter, "Measurement of oxygen diffusion distance in tumor cubes using a fluorescent hypoxia probe," *International Journal of Radiation Oncology Biology Physics*, vol. 22, no. 3, pp. 397–402, 1992.
- [43] M. W. Dewhirst, T. W. Secomb, E. T. Ong, R. Hsu, and J. F. Gross, "Determination of local oxygen consumption rates in tumors," *Cancer Research*, vol. 54, no. 13, pp. 3333–3336, 1994.
- [44] F. Kallinowski, G. Tyler, W. Mueller-Klieser, and P. Vaupel, "Growth-related changes of oxygen consumption rates of tumor cells grown in vitro and in vivo," *Journal of Cellular Physiology*, vol. 138, no. 1, pp. 183–191, 1989.
- [45] D. F. Wilson, S. A. Vinogradov, B. W. Dugan, D. Biruski, L. Waldron, and S. A. Evans, "Measurement of tumor oxygenation using new frequency domain phosphorimeters," *Comparative Biochemistry and Physiology*, vol. 132, no. 1, pp. 153–159, 2002.
- [46] L. S. Ziemer, W. M. F. Lee, S. A. Vinogradov, C. Sehgal, and D. F. Wilson, "Oxygen distribution in murine tumors: characterization using oxygen-dependent quenching of phosphorescence," *Journal of Applied Physiology*, vol. 98, no. 4, pp. 1503–1510, 2005.
- [47] J. P. Kirkpatrick, D. M. Brizel, and M. W. Dewhirst, "A mathematical model of tumor oxygen and glucose mass transport and metabolism with complex reaction kinetics," *Radiation Research*, vol. 159, no. 3, pp. 336–344, 2003.
- [48] B. M. Fenton, E. M. Lord, and S. F. Paoni, "Effects of radiation on tumor intravascular oxygenation, vascular configuration, development of hypoxia, and clonogenic survival," *Radiation Research*, vol. 155, no. 2, pp. 360–368, 2001.
- [49] J. Denekamp and A. Dau, "Inducible repair and the two forms of tumour hypoxia—time for a paradigm shift," *Acta Oncologica*, vol. 38, no. 7, pp. 903–918, 1999.
- [50] A. Daşu and J. Denekamp, "The impact of tissue microenvironment on treatment simulation," *Advances in Experimental Medicine and Biology*, vol. 510, pp. 63–67, 2003.
- [51] E. J. Hall, J. S. Bedford, and R. Oliver, "Extreme hypoxia; its effect on the survival of mammalian cells irradiated at high and low dose-rates," *British Journal of Radiology*, vol. 39, no. 460, pp. 302–307, 1966.
- [52] I. J. Spiro, K. A. Kennedy, R. Stickler, and C. C. Ling, "Cellular and molecular repair of X-ray-induced damage: dependence on oxygen tension and nutritional status," *Radiation Research*, vol. 101, no. 1, pp. 144–155, 1985.
- [53] C. C. Ling, E. Robinson, and D. C. Shrieve, "Repair of radiation induced damage—dependence on oxygen and energy status," *International Journal of Radiation Oncology Biology Physics*, vol. 15, no. 5, pp. 1179–1186, 1988.
- [54] F. Zölzer and C. Streffer, "Increased radiosensitivity with chronic hypoxia in four human tumor cell lines," *International Journal of Radiation Oncology Biology Physics*, vol. 54, no. 3, pp. 910–920, 2002.
- [55] N. Chan, M. Koritzinsky, H. Zhao et al., "Chronic hypoxia decreases synthesis of homologous recombination proteins to offset chemoresistance and radioresistance," *Cancer Research*, vol. 68, no. 2, pp. 605–614, 2008.
- [56] A. Daşu and I. Toma-Daşu, "Treatment modelling: the influence of micro-environmental conditions," *Acta Oncologica*, vol. 47, no. 5, pp. 896–905, 2008.
- [57] K. I. E. M. Wýffels, J. H. A. M. Kaanders, P. F. J. W. Rijken et al., "Vascular architecture and hypoxic profiles in human head and neck squamous cell carcinomas," *British Journal of Cancer*, vol. 83, no. 5, pp. 674–683, 2000.
- [58] G. W. Barendsen, "Dose fraction, dose rate and iso-effect relationships for normal tissue responses," *International Journal of Radiation Oncology Biology Physics*, vol. 8, no. 11, pp. 1981–1997, 1982.
- [59] J. F. Fowler, "The linear-quadratic formula and progress in fractionated radiotherapy," *British Journal of Radiology*, vol. 62, no. 740, pp. 679–694, 1989.
- [60] T. Alper and P. Howard-Flanders, "Role of oxygen in modifying the radiosensitivity of *E. coli* B," *Nature*, vol. 178, no. 4540, pp. 978–979, 1956.
- [61] T. Alper, *Cellular Radiobiology*, Cambridge University Press, Cambridge, UK, 1979.
- [62] E. J. Hall and A. J. Giaccia, *Radiobiology For the Radiologist*, Lippincott Williams & Wilkins, Philadelphia, Pa, USA, 6th edition, 2006.
- [63] B. G. Wouters and J. M. Brown, "Cells at intermediate oxygen levels can be more important than the 'hypoxic fraction' in determining tumor response to fractionated radiotherapy," *Radiation Research*, vol. 147, no. 5, pp. 541–550, 1997.
- [64] F. M. Buffa, C. West, K. Byrne, J. V. Moore, and A. E. Nahum, "Radiation response and cure rate of human colon adenocarcinoma spheroids of different size: the significance of hypoxia on tumor control modelling," *International Journal of Radiation Oncology Biology Physics*, vol. 49, no. 4, pp. 1109–1118, 2001.
- [65] I. Toma-Daşu, A. Daşu, and M. Karsoon, "The relationship between temporal variation of hypoxia, polarographic measurements and predictions of tumour response to radiation," *Physics in Medicine and Biology*, vol. 49, no. 19, pp. 4463–4475, 2004.

- [66] I. Toma-Dașu, A. Dasu, and A. Brahme, "Influence of acute hypoxia on radiation therapy outcome," in *Physical, Chemical and Biological Targeting in Radiatio Oncology*, M. Mehta, B. R. Paliwal, and S. Bentzen, Eds., vol. 14 of *AAPM Symposium Proceedings*, pp. 111–117, Medical Physics Publishing, Madison, Wis, USA, 2005.
- [67] I. Toma-Dașu, A. Dașu, and A. Brahme, "Dose prescription and optimisation based on tumour hypoxia," *Acta Oncologica*, vol. 48, no. 8, pp. 1181–1192, 2009.
- [68] E. Lindblom, *The impact of hypoxia on tumour control probability in the high-dose range used in stereotactic body radiation therapy [M.S. thesis]*, Stockholm University, 2012.
- [69] I. Toma-Dașu, A. Waites, A. Dașu, and J. Denekamp, "Theoretical simulation of oxygen tension measurement in tissues using a microelectrode: I. The response function of the electrode," *Physiological Measurement*, vol. 22, no. 4, pp. 713–725, 2001.
- [70] I. Toma-Dașu, A. Dașu, A. Waites, J. Denekamp, and J. F. Fowler, "Theoretical simulation of oxygen tension measurement in the tissue using a microelectrode: II. Simulated measurements in tissues," *Radiotherapy and Oncology*, vol. 64, no. 1, pp. 109–118, 2002.
- [71] I. Toma-Dașu, A. Dașu, A. Waites, and J. Denekamp, "Computer simulation of oxygen microelectrode measurements in tissues," *Advances in Experimental Medicine and Biology*, vol. 510, pp. 157–161, 2003.
- [72] G. Powathil, M. Kohandel, M. Milosevic, and S. Sivaloganathan, "Modeling the spatial distribution of chronic tumor hypoxia: implications for experimental and clinical studies," *Computational and Mathematical Methods in Medicine*, vol. 2012, Article ID 410602, 11 pages, 2012.
- [73] I. Toma-Dașu, A. Dașu, and A. Brahme, "Quantifying tumour hypoxia by PET imaging—a theoretical analysis," *Advances in Experimental Medicine and Biology*, vol. 645, pp. 267–272, 2009.
- [74] I. Toma-Dașu, J. Uhrdin, A. Dașu, and A. Brahme, "Therapy optimization based on non-linear uptake of PET tracers versus "linear dose painting"" in *World Congress on Medical Physics and Biomedical Engineering: Radiation Oncology*, vol. 25/1 of *IFMBE Proceedings*, pp. 221–224, September 2009.
- [75] I. Toma-Dașu and A. Dasu, "Biologically-optimised IMRT based on molecular imaging of tumour hypoxia—the impact of the tracer used," in *World Congress on Medical Physics and Biomedical Engineering*, vol. 39 of *IFMBE Proceedings*, pp. 1742–1745.
- [76] M. Busk, M. R. Horsman, and J. Overgaard, "Resolution in PET hypoxia imaging: voxel size matters," *Acta Oncologica*, vol. 47, no. 7, pp. 1201–1210, 2008.
- [77] C. C. Ling, J. Humm, S. Larson et al., "Towards multidimensional radiotherapy (MD-CRT): biological imaging and biological conformality," *International Journal of Radiation Oncology Biology Physics*, vol. 47, no. 3, pp. 551–560, 2000.
- [78] A. Brahme, "Biologically optimized 3-dimensional in vivo predictive assay-based radiation therapy using positron emission tomography-computerized tomography imaging," *Acta Oncologica*, vol. 42, no. 2, pp. 123–136, 2003.
- [79] D. J. Chaplin, P. L. Olive, and R. E. Durand, "Intermittent blood flow in a murine tumor: radiobiological effects," *Cancer Research*, vol. 47, no. 2, pp. 597–601, 1987.
- [80] J. Bussink, J. H. A. M. Kaanders, P. F. J. W. Rijken et al., "Vascular architecture and microenvironmental parameters in human squamous cell carcinoma xenografts: effects of carbogen and nicotinamide," *Radiotherapy and Oncology*, vol. 50, no. 2, pp. 173–184, 1999.
- [81] P. F. J. W. Rijken, H. J. J. A. Bernsen, J. P. W. Peters, R. J. Hodgkiss, J. A. Raleigh, and A. J. Van Der Kogel, "Spatial relationship between hypoxia and the (perfused) vascular network in a human glioma xenograft: a quantitative multi-parameter analysis," *International Journal of Radiation Oncology Biology Physics*, vol. 48, no. 2, pp. 571–582, 2000.
- [82] W. J. Koh, K. S. Bergman, J. S. Rasey et al., "Evaluation of oxygenation status during fractionated radiotherapy in human nonsmall cell lung cancers using [F-18]fluoromisonidazole positron emission tomography," *International Journal of Radiation Oncology Biology Physics*, vol. 33, no. 2, pp. 391–398, 1995.
- [83] S. M. Eschmann, F. Paulsen, C. Bedeshem et al., "Hypoxia-imaging with ¹⁸F-Misonidazole and PET: changes of kinetics during radiotherapy of head-and-neck cancer," *Radiotherapy and Oncology*, vol. 83, no. 3, pp. 406–410, 2007.
- [84] S. Roels, P. Slagmolen, J. Nuyts et al., "Biological image-guided radiotherapy in rectal cancer: is there a role for FMISO or FLT, next to FDG?" *Acta Oncologica*, vol. 47, no. 7, pp. 1237–1248, 2008.
- [85] A. Dasu and I. Toma-Dașu, "Dose painting by numbers—do the practical limitations of the technique decrease or increase the probability of controlling tumours?" in *World Congress on Medical Physics and Biomedical Engineering*, vol. 39 of *IFMBE Proceedings*, pp. 1731–1734, 2012.
- [86] M. Kohandel, M. Kardar, M. Milosevic, and S. Sivaloganathan, "Dynamics of tumor growth and combination of anti-angiogenic and cytotoxic therapies," *Physics in Medicine and Biology*, vol. 52, no. 13, pp. 3665–3677, 2007.
- [87] C. Harting, P. Peschke, K. Borkenstein, and C. P. Karger, "Single-cell-based computer simulation of the oxygen-dependent tumour response to irradiation," *Physics in Medicine and Biology*, vol. 52, no. 16, pp. 4775–4789, 2007.
- [88] W. Tuckwell, E. Bezak, E. Yeoh, and L. Marcu, "Efficient Monte Carlo modelling of individual tumour cell propagation for hypoxic head and neck cancer," *Physics in Medicine and Biology*, vol. 53, no. 17, pp. 4489–4507, 2008.
- [89] A. Brahme, "Recent advances in light ion radiation therapy," *International Journal of Radiation Oncology Biology Physics*, vol. 58, no. 2, pp. 603–616, 2004.
- [90] L. Antonovic, A. Brahme, Y. Furusawa, and I. Toma-Dașu, "Radiobiological description of the LET dependence of the cell survival of oxic and anoxic cells irradiated by carbon ions," *Journal of Radiation Research*. In press.

Research Article

Assessing the Effects of Estrogen on the Dynamics of Breast Cancer

Chipo Mufudza, Walter Sorofa, and Edward T. Chiyaka

Modelling Biomedical Systems Research Group, Department of Applied Mathematics, National University of Science and Technology, P.O. Box AC 939, Ascot, Bulawayo, Zimbabwe

Correspondence should be addressed to Chipo Mufudza, chipmuf@gmail.com

Received 8 August 2012; Revised 2 November 2012; Accepted 12 November 2012

Academic Editor: Scott Penfold

Copyright © 2012 Chipo Mufudza et al. This is an open access article distributed under the Creative Commons Attribution License, which permits unrestricted use, distribution, and reproduction in any medium, provided the original work is properly cited.

Worldwide, breast cancer has become the second most common cancer in women. The disease has currently been named the most deadly cancer in women but little is known on what causes the disease. We present the effects of estrogen as a risk factor on the dynamics of breast cancer. We develop a deterministic mathematical model showing general dynamics of breast cancer with immune response. This is a four-population model that includes tumor cells, host cells, immune cells, and estrogen. The effects of estrogen are then incorporated in the model. The results show that the presence of extra estrogen increases the risk of developing breast cancer.

1. Introduction

Among many cancer types, breast cancer is the second most common cancer in women, exceeded only by skin cancers. The chance of developing invasive breast cancer at some time in a woman's life is a little less than about 12% [1]. Being exceeded only by lung cancer, breast cancer is the second leading cause of cancer deaths in women. The chance that breast cancer will be responsible for a woman's death is about 1 in 36 [1]. The disease has been more pronounced in the developed world in the past but has soon crossed boundaries into the developing world of Africa and Asia. In Zimbabwe, breast cancer is currently the third leading cancer responsible for deaths of women of all ages with crude mortality rate of 5.6 per 100 000, exceeded only by Cervical cancer and Kaposi sarcoma [2]. Breast cancer is a malignant (cancerous) tumor that starts in the cells of the breast, that is, a group of cancer cells that can grow into (invade) surrounding tissues or spread (metastasize) to distant areas of the body. It begins when breast cells start to grow out of control due to DNA damage which controls all cell actions in the body tissues. When DNA is damaged, normal cells will repair the damage or the cell dies but in cancer cells, damaged DNA is not

repaired and does not die like it should. Instead the cell goes on making new abnormal cells with the same damaged DNA which the body does not need. A single genetically altered cell then grows into a tumor in a stepwise progression.

There are several types of breast cancer, but some of them are quite rare. In some cases a single breast tumor can be a combination of these types or be a mixture of invasive and *in situ* cancer. Ductal carcinoma *in situ* (DCIS) is the most common type of noninvasive breast cancer. DCIS means that the cancer cells are inside the ducts but have not spread through the walls of the ducts into the surrounding breast tissue. However, after starting in a milk passage (duct) of the breast, it can break through the wall of the duct and grow into the fatty tissue of the breast. At this point, it may be able to spread (metastasize) to other parts of the body through the lymphatic system and bloodstream and will now be referred to as invasive ductal carcinoma (IDC). Lobular carcinoma *in situ* (LCIS) is another type of noninvasive breast cancer which begins in the milk-producing glands and does not grow through the wall of the lobules. This can become invasive and spread to other parts of the body as invasive lobular carcinoma (ILC), a state which is harder to detect by a mammogram.

2. Risk Factors and Vulnerable Groups

There are many factors that affect the chance of an individual developing breast cancer, some of which one can change and some cannot be changed. Having a risk factor, or even several, does not mean that one will automatically develop the disease. Women have a higher risk of developing breast cancer although in men it has been discovered too [3]. Some of these factors include use of alcohol with the risk increasing relative to the amount of alcohol consumed, overweight or obese, especially for women after menopause. Obesity increases estrogen levels due to fat tissue producing small amounts of estrogen [1]. High doses of radiation are also known to increase breast cancer risk, where exposure to radiation from the atomic bomb at Hiroshima caused increased breast cancer incidence, especially in women exposed as teenagers, when their breast cells were very immature [4]. Repeated X-ray exposure for treatment of tuberculosis, postpartum mastitis, chest acne, and monitoring treatment for scoliosis increases risk [5]. A woman may become pregnant after a cancer cell has formed in her breast, a cell which may have been dormant for many years. However, with pregnancy, estrogen levels rise stimulating the dormant cancer cell to grow into a clinically detectable cancer [6].

Breast cancer incidence rates are higher in non-Hispanic white women compared to African American women for most age groups. Incidence and death rates for breast cancer are lower among women of other racial and ethnic groups like Asian, African, and Hispanic white than among non-Hispanic white and African American women [1]. However, in women under 45 years of age, breast cancer is more common in African American women. There is higher risk among women whose close blood relatives have this disease. Having one first-degree relative (mother, sister, or daughter) with breast cancer approximately doubles a woman's risk. Having 2 first-degree relatives increases her risk about 3-fold. The exact risk is not known, but women with a family history of breast cancer in a father or brother also have an increased risk of breast cancer. Altogether, less than 15% of women with breast cancer have a family member with the disease. This means that most (over 85%) women who get breast cancer do not have a family history of this disease [7]. A woman with cancer in one breast has a 3- to 4-fold increased risk of developing breast cancer in the other breast or in another part of the same breast [8]. Certain inherited DNA changes can increase the risk for developing cancer and are responsible for the cancers that run in families. For example, the breast cancer genes one and two (BRCA1 and BRCA2) are tumor suppressor genes. Mutations in these genes can be inherited from parents. When they are mutated, they no longer suppress abnormal growth and cancer is more likely to develop [9].

2.1. Estrogen as a Risk Factor. The hormone estrogen works as a chemical messenger in the body. It is essential for normal sexual development and functioning of female organs important for childbearing like the ovaries, uterus, and breasts. Estrogen also helps regulate a woman's menstrual cycles. It is necessary for the normal development

of the breast. It also helps maintain the heart and healthy bones. However, during each monthly menstrual cycle, a woman is exposed to increased estrogen levels, especially just before an egg is produced by her ovaries (ovulation). Also during pregnancy, women have prolonged exposure to high levels of estrogen. If a woman gives birth before 32 weeks or has an induced abortion, she will have an increased estrogen exposure without the protective effect of lobule differentiation. Estrogen can cause cancer in two ways. It acts as a "mitogen"; that is, it stimulates breast tissue to increase cell divisions (mitosis). This sometimes results in cancers due to errors in cell division (mutation). Secondly, certain metabolites of estrogen also act as carcinogens or genotoxins, by directly damaging DNA, thereby causing cancer cells to form [10]. Estrogen exposure can be in the form of environmental estrogens termed "xenoestrogens" which are naturally occurring like phytoestrogens in plants or synthetic chemicals that can act like human estrogen made by the ovary. Xenoestrogens can mimic the effect of human estrogen as they have a chemical structure that allows them to fit into the estrogen receptor the way a key fits into a lock.

The presence of estrogens can also activate hormones like relaxin to stimulate cell division. In fact, relaxin (RLX) has been shown to have a powerful effect on growth and differentiation of breast cancer (MCF-7) cells [14]. However, the effect of RLX is induced by estrogen probably by inducing RLX receptors as in myometrial cells [15]. Therefore, in general, it may be implicated in breast cancer risk because of its role in stimulating breast cell division, work during the critical periods of breast growth and development, effect on other hormones like relaxin that stimulate breast cell division, and support of the growth of estrogen-responsive tumors. Other studies have also shown that there is a positive relationship between endogenous hormone levels in postmenopausal women and risk of breast cancer [16]. In hormonal birth control mechanisms, there are two hormones involved, estrogen and progesterin. Hormonal birth control mechanisms involve the oral contraceptives, minipill, Depo-Provera, and implants. These prevent pregnancy by releasing synthetic hormones to prevent the release of eggs from the ovaries (ovulation) and by thickening the cervical mucus, which helps block sperm from entering the uterus and by making it hard for an egg to attach and grow in the uterus.

2.2. Researches on Other Risk Factors. In the search for the actual cause of this deadly disease, many risk factors have been studied. Oral contraceptives use has undergone many discussions as a risk factor of breast cancer. A meta-analysis was performed of case control studies that addressed whether prior oral contraceptive use is associated with breast cancer. MEDLINE and PubMed databases and bibliography reviews were searched to identify related material published in or after 1980. Thirty-four studies were identified that met inclusion criteria. Two reviewers extracted data from original research articles or data provided by study authors. The DerSimonian-Laird method was used to compute pooled odds ratios (ORs) and confidence intervals (CIs). The Mantel-Haenszel test was then used to assess association between

OC use and breast cancer. Results showed that the use of OCs was associated with an increased risk of premenopausal breast cancer in general with an OR (1.19) and 95% CI (1.09–1.29) and across various patterns used. It was associated with breast cancer risk in both parous (OR, 1.29; 95% CI, 1.20–1.40) and nulliparous women (OR, 1.24; 95% CI, 0.92–1.67) [17]. It was however not specific on whether the oral contraceptive investigated had estrogen, progesterone, or both. Other researchers have argued that estrogen level is increased in women receiving exogenous estrogens in form of OC or HRT [18]. Moreover, there is general agreement that the risk associated with OC and HRT depends on the duration of exposure, being lowest in women who never used OC or HRT [19].

Abortion and fertility have also been investigated as risk factors on breast cancer. In a research, modelling and forecasts based on abortion and other risk factors were done. They used the national cancer registration data for female breast cancer incidence in eight European countries: England and Wales, Scotland, Northern Ireland, the Irish Republic, Sweden, the Czech Republic, Finland and Denmark which were chosen because of their comprehensive data on abortion incidence. Relaxin has also been discovered to promote differentiation of breast cancer cells *in vitro*, more specifically, the MCF-7 breast adenocarcinoma cells. MCF-7 cells can be induced to progress in the differentiation pathway under the influence of relaxin (RLX), a peptide hormone that has been shown to have a powerful effect on growth and differentiation of epithelial and myoepithelial cells of the mouse mammary ducts *in vivo* [20]. Estrogen involvement has also been suggested. In fact, as shown for normal mammary gland, estrogens are needed to allow relaxin to produce its effect [14], probably by inducing relaxin receptors, as occurs in myo-metrial cells [15].

Association of metal exposure with breast cancer risk is a topic currently under discussions. An experiment was done to review the scientific evidence with respect to the *in vitro* and *in vivo* studies and epidemiological evidence for links between breast cancer and exposure to metals. It was found that there is growing evidence that environmental contaminants such as metals play a role in breast cancer [21]. Based on a relatively small number of studies, this literature review uncovered important deficiencies and gaps in the current literature that assesses the link of the incidence of breast cancer to metal exposure.

Several studies suggest that selective estrogen-receptor modulators (SERMs) like tamoxifen and raloxifene may lower breast cancer risk in women with certain breast cancer risk factors. But so far, many women are reluctant to take these medicines because they are concerned about possible side effects. Newer studies are looking at whether aromatase inhibitors; and drugs such as anastrozole, letrozole, and exemestane can reduce the risk of developing breast cancer in postmenopausal women. These drugs are already being used as adjuvant hormone therapy to help prevent breast cancer recurrences, but none of them is approved for reducing breast cancer risk at this time. One of these drugs, exemestane, has recently been shown to lower the risk of invasive breast cancer by 65% in women at increased risk.

Fenretinide, a retinoid (drugs related to vitamin A), is also being studied as a way to reduce the risk of breast cancer. In a small study, this drug reduced breast cancer risk as much as tamoxifen. Other drugs are also being studied to reduce the risk of breast cancer [1].

Studies continue to uncover lifestyle factors and habits that alter breast cancer risk. Ongoing studies are looking at the effect of exercise, weight gain or loss, and diet on breast cancer risk. Studies on the best use of genetic testing for BRCA1 and BRCA2 mutations continue at a rapid pace. Scientists are also exploring how common gene variations may affect breast cancer risk. Each gene variant has only a modest effect in risk (10 to 20%), but when taken together they may potentially have a large impact. Potential causes of breast cancer in the environment have also received more attention in recent years. While much of the science on this topic is still in its earliest stages, this is an area of active research [3].

3. Treatment of Breast Cancer

Treatment of breast cancer can be classified into broad groups, based on how they work and when they are used. These include surgery, chemotherapy, radiation therapy, and hormone therapy. Surgery is when the breast tumor is removed as partial mastectomy/breast-conserving surgery and mastectomy. Partial mastectomy surgery only removes a part of the affected breast, but how much is removed depends on the size and location of the tumor and other factors whilst mastectomy surgery removes the entire breast. The whole breast tissue is removed, and sometimes along with other nearby tissues. This can be in the form of a simple mastectomy or skin-sparing mastectomy depending on whether there is need for immediate reconstruction of the breast.

Radiation therapy, as the name implies, is treatment with high energy rays or particles that destroy cancer cells. This is also used to treat cancer that has spread to other areas, for example, to the bones or brain. It can be administered in two ways, external beam radiation and internal radiation. External beam radiation is when the radiation is focused from a machine outside the body on the area affected by the cancer. This procedure is more like getting an X-ray, but here the radiation is more intense. Brachytherapy, also called internal radiation, is when instead of aiming radiation beams from outside the body, radioactive seeds or pellets are placed directly into the breast tissue next to the cancer. Its administration is limited by tumor size, location of tumor, and other factors relating to the patient's medical condition. Systematic therapy refers to drugs which can be given by mouth or directly into the bloodstream to reach cancer cells anywhere in the body. chemotherapy, hormone therapy, and targeted therapy are examples.

Chemotherapy is treatment with cancer-killing drugs that can be given intravenously (injected into a vein) or by mouth. It is given in cycles, with each period of treatment followed by a recovery period. Treatment usually lasts for several months when chemotreatment is given to patients with

no evidence of cancer after surgery. This is known as adjuvant therapy. When the treatment is given before surgery, chemotherapy is called neoadjuvant therapy. Hormone therapy hormonal therapy is often used as an adjuvant therapy to help reduce the risk of the cancer coming back after surgery although it can also be used as neoadjuvant treatment as well. This is when several approaches to blocking the effect of estrogen or lowering estrogen levels are used to treat hormone receptor-positive breast cancers. However, hormonal therapy does not help patients whose tumors are both estrogen receptor (er) negative and progesterin receptor (PR) negative.

4. Models Done on Tumor Growth

Several mathematical techniques have been applied in the study of breast cancer [11, 22–24]. Delay differential equations were used to model the interaction of breast cancer cells with the immune system. A developed model with delay differential equations modelling breast cancer accounted for different cell cycles and included terms to evaluate drug treatments, but ignored quiescent tumor cells [11]. Another related model included quiescent cells but ignored immune response and drug treatments in which there was consideration of the interconnected growth patterns of both proliferating and quiescent cells [22]. In a bid to improve the researches done by [11, 22], an integrated model in form of delay differential equations was developed accounting for quiescent cells, immune cells and included drug intervention terms. They included additional terms to account for the impact of Paclitaxel on the quiescent cells [25].

In one of the studies on the relationship between Body Mass Index (BMI), menopausal status, estrogen replacement therapy (ERT), and breast cancer risk, a mathematical model was developed and results showed that estrogen levels are responsible for the relationship between BMI, ERT, menopausal status, and breast cancer risk [23]. Statistical analysis and stochastic modelling have also been applied to investigate breast cancer and tumor growth [26]. They dealt with aspects of probability and statistics applied to breast cancer research. From *in vitro* experiments, breast cancer cells, the MCF-7 cells' behaviour in different types of substrates was noted. More specifically, it is how the stiffness of the different substrates affects the cell that is of most interest. The effect on aggregate counts and morphological parameters of the cells by surrounding (simulated) tissue's stiffness was analysed using methods from linear Mixed Models theory. The analysis indicated that certain parameters are significantly different for different tissue stiffness. Stochastic modelling related to initial tumor growth was studied and certain types of randomness were introduced in it. They numerically investigated how the model responds to stochastic behaviour of the parameters defining mutation characteristics. The model for tumor growth was rather stable with respect to small random perturbations. For the case of significant parameter randomness, the average number of cells (normal and mutant) at a time T was highly dependent on the expected value of the stochastic

process representing the corresponding parameter value. This suggested a stable state for *in vitro* experiments and since *in vivo* experiments are known to be unstable, the presence of risk factors had aided in tumor behaviour.

A mathematical model of immune response to tumor invasion was also developed using competition models. Tumor cells population, CD8⁺T cell population, and Natural Killer cell population competed in a way almost similar to that suggested by Lotka-Volterra's competition models [24]. This carries a fundamental aspect on the interaction between immune cells and tumor cells. The presence of tumor cells stimulates the immune response, represented by the positive nonlinear growth term for the immune cells. This type of response term is of the same form as the terms used in the respective model of [27].

Cell populations have also been known to compete for nutrients and natural cell requirements resulting in nutrient consumption models. Burton [28] first proposed that diffusion and nutrient consumption might be limiting solid tumor, and since then a large number of studies have described the spatiotemporal interactions between tumor cell populations and nutrients. Early models of nutrient-limited tumor growth calculated the nutrient concentration profiles as a function of tumor spheroid radius that was changing due to the rate of cell proliferation [29]. The later models have incorporated differing degrees of complexity for cell movement. Tumor cell proliferation and death are considered to be dependent on only one generic nutrient (most often oxygen). However, some consider the effect of several nutrients and pH on the cell population [30].

The Gail model is also one of the widely used models and established models for predicting breast cancer risk in women. It was developed from a nested case control study conducted on a cohort of white women who were receiving regular screening mammograms in order to calculate multivariate relative risks of breast cancer based on age at menarche, age at first live birth, number of first-degree relatives (mother and sisters) with breast cancer, number of breast biopsies, and whether or not a typical hyperplasia was present on any biopsy specimen [31]. However, this widely used model does not predict breast cancer risk in young women generally and should not be used for that purpose [32]. It also underestimates genetically inherited breast cancer because it does not take into account paternal history. The model was also not intended to predict risk in women under age 40, nor in African American women of all ages [33].

Cell-DEVS, an extension of the DEVS formalism, has been used to model tumor-immune systems that involve growing tumors interacting with immune cells [34]. This has an advantage in that it facilitates the formal specification and reuse of cellular models. A Cell-DEVS model was implemented and tested using the CD++ toolkit and simulation results indicated that the model captured the intended qualitative aspects of tumor growth and immune system response [35]. Simulation-based parameter estimation offers a powerful means of estimating parameters in complex stochastic models. The use of simulation for computing the maximum likelihood estimator in the natural history of

breast cancer was discussed. From the analysis, simulation provided a straight forward means of computing such estimators for models of substantial complexity [36].

A commonly proposed model for tumor growth assumes that the rate of growth is proportional to the number of malignant cells [37]. But currently, the hardest challenge in modelling tumor growth and treatment is estimating parameters in models that are mathematically simple and broadly applicable [38]. Most of the risk factors have shown an association with estrogen as emphasised so we seek to develop Lotka-Volterra's competition model of the tumor cells and the immune response in order to assess the impact of estrogen on the dynamics of breast cancer tumor.

5. The Estrogen-Free Model

Based on many previous useful models done on tumor growth we here consider a model which subdivides the total population $N(t)$ of cells of the breast tissue at any given time t into three groups which include normal or host cells, tumor cells and immune cells classes. The normal cells class, denoted by $H(t)$ is in form of epithelial cells that make up the breast tissue. The cells differentiate and die normally as they have unaltered DNA which controls all cell actions. We assumed that the normal and tumor cells compete for space and resources in a small volume and therefore assumed a competition model used by Gatenby [39]. The normal cells grow exponentially at a *per capita* growth rate of α_1 as a result of DNA initiation [39]. β_1 is the depletion rate resulting from competition for resources such as nutrients and oxygen or the accumulation of substances released from cell metabolism within themselves.

Tumor cells, denoted by $T(t)$ at any time t , represent a class of breast cancer cells with damaged DNA. There are about 51 breast cancer cell lines which mirror the 145 primary breast tumors [40]. These can be classified into 2 major branches, the luminal, which has estrogen receptors (ESR1 positive), and basal-like, without estrogen receptors (ESR1 negative). We then assume a homogeneous luminal type of cancer cells in form of MCF-7, MDAMB361, BT474, T47D, and ZR75 cell lines. Several tumor growth laws have been proposed which include an exponential growth, Gompertz growth and logistic growth. We assume the presence of a small tumor mass, that is, a tumor size that is close to zero relative to carrying capacity, and therefore the choice of growth law does not significantly affect the qualitative behaviour of the model since they only differ for large tumor sizes. We therefore assume an exponential growth of tumor cells with *per capita* rate of α_2 which results from the damaged DNA. Analogously β_2 is a factor restricting their growth competition for space and food within themselves. The normal cells $H(t)$ and tumor cells $T(t)$ also compete for space and natural cell requirements like oxygen as they are supplied by the blood vessels. We assume cancer cells have uncontrolled cycle than the normal cells due to changed DNA which makes them fail to regulate a cell cycle [12] and thus their interaction with normal cells results in an inhibitory effect on normal cells at rate δ_1 [41].

The model includes an immune cells class, $I(t)$, in form of Natural Killer (NK) cells and CD8⁺ T cells. Their growth may be stimulated by the presence of the tumor and they can destroy tumor cells through a kinetics process. We also assume that the presence of a detectable tumor in a system does not necessarily imply that the tumor has completely escaped active immunosurveillance. Although a tumor is immunogenic, it is possible that the immune response may not be sufficient on its own to completely combat the rapid growth of the tumor cell population and the eventual development into a tumor.

The population of immune cells is considered to be outside of the system and we assume a background level of NK cells, even in the absence of tumor with CD8⁺ T cells only present as a result of activation. It is therefore reasonable to assume a constant source, s , of the immune cells from the thymus gland [27]. Furthermore, in the absence of any tumor, the cells will die off naturally at a *per capita* rate of μ . The presence of tumor cells stimulates the immune response resulting in growth of immune cells. This is represented by a positive nonlinear growth term for immune cells which as a function of $T(t)$, is positive, increasing and concave with the form $\rho I(t)T(t)/(\omega + T(t))$, where ρ is the immune response rate and ω is the immune threshold rate, which is inversely proportional to the steepness of the immune response curve. This type of response term is of the same form as the terms used in respective models of [13, 27]. Thus immune cell proliferation is controlled and will never result in immune crowding which might in turn be detected as a threat. Furthermore, the reaction of immune cells and tumor cells can result in either the death of tumor cells at a rate γ_2 or the inactivation of the immune cells, with γ_3 as the interaction coefficient.

After considering all these aspects, we present the following system of Lotka-Volterra type of differential equations to determine the dynamics of breast cancer cells:

$$\begin{aligned}\frac{dH}{dt} &= H(\alpha_1 - \beta_1 H - \delta_1 T), \\ \frac{dT}{dt} &= T(\alpha_2 - \beta_2 T) - \gamma_2 IT, \\ \frac{dI}{dt} &= s + \frac{\rho IT}{\omega + T} - \gamma_3 IT - \mu I.\end{aligned}\tag{1}$$

Initial values of variables are $H(0) = 1$, $T(0) = 10^{-5}$ and $I(0) = s/\mu = 1.379310345$ adopted from [11, 13].

5.1. Equilibrium Points and Positivity of Solutions. An equilibrium point is a stable condition that does not change over time, or in which change in one direction is continually balanced by change in another. The variables H , T , and I represent subpopulations of breast cells and therefore, should be positive or zero for all $t \geq 0$. One can easily show that all the variables are greater than or equal to zero. If this condition is not met, the model should be discarded as it violates a basic aspect of scientific reality. The steady

states occur where the ordinary differential equations are simultaneously zero, that is, where

$$\frac{dH}{dt} = \frac{dT}{dt} = \frac{dI}{dt} = 0. \quad (2)$$

The model system admits four steady states in which there are two dead equilibria, one tumor-free equilibrium points and one coexisting equilibrium point.

5.1.1. Tumor-Free Equilibrium- ξ_t . The first equilibrium point as the tumor-free equilibrium as this is when only tumor cell population has been forced to extinction as a result of the competition with normal and immune cells. This is given by

$$\xi_t = (H^*, T^*, I^*) = \left(\frac{\alpha_1}{\beta_1}, 0, \frac{s}{\mu} \right). \quad (3)$$

We define a feasible region as a set of nonnegative and real solutions of our variables (H, T, I) since cell populations are nonnegative and real. The equilibrium state ξ_t exists since $\alpha_1 > 0$, $\beta_1 > 0$, $\mu > 0$, and $s > 0$, we have all solutions in the neighbourhood of ξ_t as positive and real and hence in the feasible region.

5.1.2. Type 1 Dead Equilibrium- ξ_d^1 . The dead equilibrium point is when normal cells only have died off leaving the tumor cells surviving. We classify this as a “dead” in the sense that there is no recovery of damaged normal cells since they have been forced to extinction. This is given by

$$\begin{aligned} \xi_d^1 &= (H^*, T^*, I^*) \\ &= \left(0, \frac{\alpha_2 - \gamma_2 I^*}{\beta_2}, \frac{s}{\mu - \rho T^*/(\omega + T^*) + \gamma_3 T^*} \right), \end{aligned} \quad (4)$$

where ξ_d^1 represents the type 1 dead equilibrium value of the normal cells, tumor cells, and immune cells, respectively.

The tumor cell population will increase with a decrease in tumor cell death rate, β_2 , and an increase in tumor growth rate, α_2 . An increase in immune cells also reduces tumor cell population as a result of predation on tumor cells by immune cells. We know that $\beta_2 > 0$. So we need $\alpha_2 \geq \gamma_2 I^*$ which implies $I^* \leq \alpha_2/\gamma_2$ so that T^* can be in the feasible region. That is, the net growth rate of tumor cells must be more than or equal to immune cells at any time t in order for the competition to drive normal cells to extinction.

The immune cells are inversely proportional to tumor dynamics such that an increase in tumor dynamics reduces immune cells as more immune cells are deactivated by tumor cells. This exists when

$$\mu - \frac{\rho T^*}{\omega + T^*} + \gamma_3 T^* > 0, \quad (5)$$

which when expanded will give

$$\gamma_3 T^{*2} + (\mu + \omega\gamma_3 - \rho)T^* + \mu\omega > 0. \quad (6)$$

By letting $u_1 = \gamma_3$, $u_2 = \mu + \omega\gamma_3 - \rho$ and $u_3 = \mu\omega$, we get

$$T^* = \frac{-u_2 + \sqrt{u_2^2 - 4u_1u_3}}{2u_1}. \quad (7)$$

We know that $u_1 > 0$ and $u_3 > 0$ and thus we need $u_2 < 0$, that is, $\mu + \omega\gamma_3 < \rho$. This implies that the immune response rate should be greater than the rate at which they are reduced. We also have $u_2^2 - 4u_1u_3 > 0$ for T^* to be real, that is, $(\mu + \omega\gamma_3 - \rho)^2 > 4\gamma_3\omega\mu$ for solutions of our system around the type 1 dead equilibrium to be real and nonnegative. This implies that the difference in the rates of immune cell initiation and reduction should be greater than the rate at which they are lost. Also

$$\sqrt{u_2^2 - 4u_1u_3} \geq u_2 \implies 4\mu\omega\gamma_3 \leq 0, \quad (8)$$

which means one or more of the parameters μ , ω , γ_3 is zero. This explains that ξ_d^1 only exists when there are totally no immune dynamics which is a rare scenario, hence it is very rare to reach to such an equilibrium point unless someone is dead.

5.1.3. Type 2 Dead Equilibrium- ξ_d^2 . Type 2 dead equilibrium exists when both normal cells and tumor cell population have died off, given by

$$\xi_d^2 = (H^*, T^*, I^*) = \left(0, 0, \frac{s}{\mu} \right), \quad (9)$$

where ξ_d^2 represents the type 2 dead equilibrium values for the normal cells, tumor cells and immune cells, respectively. Since $s > 0$ and $\mu > 0$ it implies that all the solutions around the dead equilibrium of type 2, ξ_d^2 are in the feasible region. This state is feasible but however no fixed tissue is present which can be as a result of whole breast tissue removal maybe by a mastectomy surgery or death.

5.1.4. Coexisting Equilibrium- ξ_c . The coexisting equilibrium point ξ_c is a state in which all cell populations have survived the competition and they coexist and is given by

$$\xi_c = (H^*, T^*, I^*) = \left(\frac{\alpha_1}{\beta_1} - \frac{\delta_1(\alpha_2 - \gamma_2 I^*)}{\beta_1\beta_2}, \frac{\alpha_2 - \gamma_2 I^*}{\beta_2}, \frac{s}{\mu - \rho T^*/(\omega + T^*) + \gamma_3 T^*} \right), \quad (10)$$

where ξ_c represent the coexisting equilibrium values of the normal cells, tumor cells and immune cells, respectively.

This exists when $\beta_1, \beta_2 > 0$ and

$$\begin{aligned} \alpha_1 - \frac{\delta_1(\alpha_2 - \gamma_2 I^*)}{\beta_2} &\geq 0, \\ \Rightarrow \frac{\alpha_2 \delta_1 - \alpha_1 \beta_2}{\gamma_2 \delta_1} &\leq I^*. \end{aligned} \quad (11)$$

This implies that the combination of the net growth of tumor cells as a result of competition due to normal cells must always be less than the equilibrium value of the immune cells for the cells to coexist. $I^* > 0$ when $\alpha_2 \delta_1 \geq \alpha_1 \beta_2$ which implies $\alpha_2/\beta_2 \geq \alpha_1/\delta_1$. That is, the net growth of tumor cells must be greater than that of normal cells for a nonnegative solution to exist at ξ_c . The equilibrium values for the tumor cells and immune cells are given as the same as the ones at the type 1 dead equilibrium.

5.2. Stability Analysis of Equilibria. We analyse the equilibrium points in terms of their stability by means of eigenvalues. We apply the Hartman Grobman Theorem which states that in the neighbourhood of a hyperbolic equilibrium point, a nonlinear dynamical system is topologically equivalent to its linearisation.

5.2.1. Local Stability of the Tumor-Free Equilibrium Point. We now evaluate the stability of the tumor-free equilibrium point, that is at ξ_t in which the Jacobian is given by

$$J_{\xi_t} = \begin{pmatrix} -\alpha_1 & -\frac{\alpha_1 \delta_1}{\beta_1} & 0 \\ 0 & \alpha_2 - \frac{\gamma_2 s}{\mu} & 0 \\ 0 & \frac{s}{\mu} \left(\frac{\rho}{\omega} - \gamma_3 \right) & -\mu \end{pmatrix}. \quad (12)$$

Therefore the system gives three eigenvalues (λ_i) which are, $\lambda_1 = -\alpha_1$, $\lambda_2 = \alpha_2 - \gamma_2 s/\mu$, and $\lambda_3 = -\mu$. Since $\lambda_1, \lambda_3 < 0$, we have the tumor-free equilibrium point being stable as long as $\alpha_2 < s\gamma_2/\mu$. This implies that the system is stable at tumor-free if and only if the resistance coefficient $s\gamma_2/\mu$ is greater than the *per capita* growth rate of the tumor cells, α_2 . This measures how the immune system competes with the tumor cells and since we assumed that the immune cells are capable of destroying cancer cells at some rate, we have λ_2 being negative and therefore ξ_t is always a stable equilibrium point.

5.2.2. Local Stability of Type 1 Dead Equilibrium. Evaluating the Jacobian at the ξ_d^1 gives the first eigenvalue as

$$\Rightarrow \lambda_1 = \frac{\alpha_1 \beta_2 - \alpha_2 \delta_1 + \delta_1 \gamma_2 I^*}{\beta_2}. \quad (13)$$

We know from Section 5.1.4 that $\alpha_1 \beta_2 - \alpha_2 \delta_1 + \delta_1 \gamma_2 I^* \geq 0$, thus λ_1 is a nonnegative eigenvalue and thus the type 1 dead equilibrium is always unstable. This is in fact the case suggested by De Pillis and Radunskaya [13] that the dead equilibria are always unstable in host dynamics. This implies that once interactions among these cells drives them to the death of normal cells, there is no recovery and no form of intervention or parameter adjustment that will stabilise it. That is, once normal cells' DNA is damaged, the cell can never recover.

5.2.3. Local Stability of Type 2 Dead Equilibrium. Evaluating the Jacobian at the point ξ_d^2 gives

$$J_{\xi_d^2} = \begin{pmatrix} \alpha_1 & 0 & 0 \\ 0 & \alpha_2 - \frac{\gamma_2 s}{\mu} & 0 \\ 0 & \frac{s}{\mu} \left(\frac{\rho}{\omega} - \gamma_3 \right) & -\mu \end{pmatrix}. \quad (14)$$

The system has three eigenvalues (λ_i) which are $\lambda_1 = \alpha_1$, $\lambda_2 = \alpha_2 - \gamma_2 s/\mu$, and $\lambda_3 = -\mu$ and since $\alpha_1 > 0$ and $-\mu < 0$, this implies that whatever value of λ_2 , the type 2 dead equilibrium is a saddle point which is always unstable.

5.2.4. Local Stability of the Coexisting Equilibrium Point. We would want to analyse how the system behaves around the coexisting equilibrium point, ξ_c . For simplicity, we introduce parameters $f(h), f(t), f(i)$ where,

$$\begin{aligned} f(t) &= \frac{\alpha_2 - \gamma_2 I^*}{\beta_2}, \\ f(h) &= \frac{\alpha_1}{\beta_1} - \frac{\delta_1(\alpha_2 - \gamma_2 I^*)}{\beta_1 \beta_2}, \\ f(i) &= \frac{s}{\mu - \rho T^*/(\omega + T^*) + \gamma_3 T^*}. \end{aligned} \quad (15)$$

We need $f(h) \geq 0, f(t) \geq 0$ and $f(i) \geq 0$, for feasibility of solutions, and therefore these parameters are nonnegative as shown in the previous sections. Thus computing the Jacobian matrix at this point gives

$$J_{\xi_c} = \begin{pmatrix} \alpha_1 - 2\beta_1 f(h) - \delta_1 f(t) & -\delta_1 f(h) & 0 \\ 0 & \alpha_2 - 2\beta_2 f(t) - \gamma_2 f(m) & -\gamma_2 f(t) \\ 0 & \frac{-\rho \omega f(i)}{(f(t) + \omega)^2} - f(i) \gamma_3 & -\mu + \frac{\rho f(t)}{\omega + f(t)} - \gamma_3 f(t) \end{pmatrix}. \quad (16)$$

This results in one of the eigenvalues

$$\lambda_1 = \alpha_1 - 2f(h)\beta_1 - f(t)\delta_1. \quad (17)$$

Substituting for $f(t)$ and $f(h)$, then solve we have

$$\lambda_1 = -\alpha_1 + \delta_1 \left(\frac{\alpha_2 - \gamma_2 I^*}{\beta_2} \right). \quad (18)$$

However, since H^* exist at ξ_c when

$$\alpha_1 - \frac{\delta_1(\alpha_2 - \gamma_2 I^*)}{\beta_2} \geq 0, \quad (19)$$

this implies that λ_1 is negative and thus the stability of the system can be determined by the state of eigenvalues λ_2 and λ_3 . These are obtained from the remaining 2×2 matrix below:

$$\tau = \begin{pmatrix} \alpha_2 - 2\beta_2 f(t) - \gamma_2 f(i) & -\gamma_2 f(t) \\ \frac{-\rho\omega f(i)}{(f(t) + \omega)^2} - f(i)\gamma_3 & -\mu + \frac{\rho f(t)}{\omega + f(t)} - \gamma_3 f(t) \end{pmatrix}. \quad (20)$$

For the system to be stable, we need the trace to be negative and the determinant to be positive. The trace (τ) can be written as

Trace (τ) = $-\alpha_2 + 2\gamma_2 I^* - \gamma_2 f(i) - \mu + \rho f(t)/(\omega + f(t)) - \gamma_3 f(t)$.

For stability, we need trace $\tau < 0$,

$$\Rightarrow 2\gamma_2 I^* - \gamma_3 f(t) + \frac{\rho f(t)}{\omega + f(t)} - \mu < \alpha_2 + \gamma_2 f(i). \quad (21)$$

That is, for us to have a stable system, tumor cell dynamics should be less than that of immune cell population. Also we need the determinant (Δ) of the 2×2 matrix to be positive for the system to be stable. The determinant Δ for the system is also given by

$$\begin{aligned} \Delta &= f(i)\gamma_2(f(t))^2(\mu - \rho) \\ &+ 2f(t)\mu\omega + \mu\omega^2 - \gamma_2(f(t) + \omega)f(t)(\mu - \rho) \\ &+ \mu\omega + f(t)(f(t) + \omega)\gamma_3 \\ &+ 2f(t)\beta_2(f(t) + \omega)(f(t)(\mu - \rho)) \\ &+ \mu\omega + f(t)\gamma_3(f(t) + \omega). \end{aligned} \quad (22)$$

For $\Delta > 0$

$$\begin{aligned} &f(i)\gamma_2(f(t))^2(\mu - \rho) + 2f(t)\mu\omega \\ &+ \mu\omega^2 + \mu\omega + f(t)\gamma_3(f(t) + \omega) \\ &> \gamma_2(f(t) + \omega)f(t)(\mu - \rho). \end{aligned} \quad (23)$$

We know that $f(t)$ is a function of I^* and $f(i)$ is a function of T^* , therefore we generally have the growth of immune cells being greater than that of tumor cells for us to have a stable system.

5.2.5. Global Stability of Equilibria. To establish the global asymptotic stability of the equilibrium points, we adopt the method of Castillo-Chavez [42]. We rewrite system (1) as

$$\begin{aligned} \frac{dX}{dt} &= F(X, Z), \\ \frac{dZ}{dt} &= G(X, Z), \end{aligned} \quad (24)$$

where $G(X, 0) = 0$, $X \in \mathfrak{R}^2$ denotes the undamaged cell compartments, ($H(t)$ and $I(t)$) and $Z \in \mathfrak{R}^1$ is comprised of the damaged cell compartment, $T(t)$.

The conditions below must be satisfied to guarantee global stability.

H1: For $dX/dt = F(X, 0)$, X^* is globally asymptotically stable.

H2: $G(X, Z) = AZ - G^*(X, Z)$, $G(X, Z) \geq 0$ for $(X, Z) \in \Omega$ where $A = D_Z G(X^*, 0)$ is an M -matrix (with off diagonal elements as nonnegative) and Ω is the region where the model makes biological sense.

In our case,

$$F(X, 0) = \begin{pmatrix} \alpha_1 H - \beta_1 H^2 \\ s - \mu I \end{pmatrix} \quad (25)$$

and A is a 1×1 matrix given by

$$\begin{aligned} A &= D_Z G(X^*, 0) = \alpha_2 - 2\beta_2 T^* - \gamma_2 I^*, \\ G^*(X, Z) &= -\beta_2 T^*. \end{aligned} \quad (26)$$

We therefore conclude that the tumor-free equilibrium, ξ_t is the only state that is globally asymptotically stable since $G^*(X, Z) \geq 0$. All the other equilibrium states are globally unstable since $G^*(X, Z) < 0$.

Hence, the system can only be stable when the immune system can efficiently compete with the cancer cells, that is, the efficiency in CD8+ activation and NK cell supply from the thymus. As shown by both equilibria, immune resistance to tumor growth is the only factor that determines stability of the system. The general necessary condition for stability of our system is that the growth rate of immune cells α_2 must be greater than the immune cell resistance coefficient $s\gamma_2/\mu$. The global stability of the system is only dependant on the natural exponential death of tumor cells. That is, as the number of tumor cells dies naturally, the system approaches a stable state.

6. Model with Estrogen

We introduce another class of estrogen, $E(t)$, in the form of 17- β estradiol to the dynamics of breast cancer cells. Over and above the estrogen produced by the ovaries, there is more estrogen introduced into the system as part of some oral contraceptives, in hormone replacement therapy or in estrogen replacement therapy. The assumption here is that as

women take hormonal birth control methods they increase a constant level of the estrogen hormonal level. We therefore assume a constant source, π of 17- β estradiol, the primary biologically most active estrogen which is all the estrogen in the system at any given time.

Human breast cells, the epithelial cells, contain estrogen receptors termed estrogen receptor-1 (ER- α) and estrogen receptor-2 (ER- β). These are intracellular receptors, which when activated by ligand binding, translocate to the nucleus and act as transcription factors by binding to DNA in the promoter regions of target genes. Both ER- α and ER- β bind 17- β estradiol in the nucleus of the cell with similar affinity (0.1–1 nM) and act as transcription factors to regulate gene expression. This will lead to gene transactivation which may also result from tethering of estrogen receptors to nuclear transcription factors such as NFYB and SPI [43]. It is also consistent to assume that the estrogen modulation of the inflammatory response is a contributing factor in estrogen-stimulated growth of breast tumor [43] which also has an effect on the host innate immune response. This can however result in damage to DNA primary structure of the double helix as a result of estrogen oxidation products, the 2-OH and 4-OH catechol estrogens, and how it stimulates cell proliferation and gene expression via the ER. Therefore, normal cell population, $H(t)$ will be reduced as some of the normal cells are being converted into tumor cells by a factor $\sigma_1 HE$, where σ_1 is the rate of tumor formation as a result of DNA damage by estrogen. Damaged normal cells will now form the class of tumor cells and therefore tumor cell population will also increase at a rate σ_2 resulting in a growth factor of $\sigma_2 HE$ on tumor cell population. Here $\sigma_2 < \sigma_1$ since some of the damaged cells can be destroyed as a result of antitumor immunity from Natural Killer cells.

Estrogen is oxidised to catechol estrogens by recombinant phase 1 enzymes (CYP1A1 and CYP1B1) which also die naturally at a rate θ represented by the death factor θE . The molecule 17- β estradiol stimulates growth in estrogen-responsive breast cancer cells. As shown by [44] in a series of experiments, ER-positive cells can stimulate surrounding benign cells to proliferate through similar paracrine effects involving stromal-epithelial cell interactions. ER-positive breast cancer cells are themselves stimulated to grow by estrogen through autocrine effects, and they are Ki67 positive [45]. We therefore introduce a growth factor $\alpha_3 T$ of tumor cells where α_3 is the *per capita* growth of $T(t)$ cells which is greater than α_2 , the growth factor from the estrogen-free model. α_3 is greater than α_2 as a result of combined natural growth rate plus growth due to autocrine effects.

The presence of estrogen has also been shown to reduce immune cell proliferation. A process known as ovariectomy which involves removal of one or both ovaries upregulates T cell Tumor Necrosis Factor (TNF) production by increasing the number of TNF producing T cells without altering the amount of TNF produced by each T cell [46]. We therefore assume that if estrogen deficiency increases immune cell proliferation and lifespan, then its presence will inhibit immune

cell proliferation. We can therefore represent this by a decay factor

$$\frac{\sigma_3 IE}{v + E} \quad (27)$$

on immune cells with σ_3 as the rate of immune suppression due to estrogen presence and v is the estrogen threshold rate. Incorporating these effects of estrogen on system (1) will result in the following system of equations:

$$\begin{aligned} \frac{dH}{dt} &= H(\alpha_1 - \beta_1 H - \delta_1 T) - \sigma_1 HE, \\ \frac{dT}{dt} &= T(\alpha_3 - \beta_2 T) - \gamma_2 IT + \sigma_2 HE, \\ \frac{dI}{dt} &= s + \frac{\rho IT}{\omega + T} - \gamma_3 IT - \mu I - \frac{\sigma_3 IE}{v + E}, \\ \frac{dE}{dt} &= \pi - \theta E, \end{aligned} \quad (28)$$

where $H(0) = 1$, $T(0) = 10$, $I(0) = 1.379310345$, and $E(0) = 2$.

6.1. Equilibrium Points and Positivity of Solutions. The model system admits three steady states which are the dead equilibrium, tumor-free equilibrium, and coexisting equilibrium points.

6.1.1. Tumor-Free Equilibrium ψ_t . The tumor-free equilibrium is when only the tumor cell population has died due to the competition with the other cells. This is given by

$$\begin{aligned} \psi_t &= (H^*, T^*, I^*, E^*) \\ &= \left(\frac{\alpha_1 - \sigma_1 E^*}{\beta_1}, 0, \frac{s(E^* + v)}{\mu(E^* + v) + \sigma_3 E^*}, \frac{\pi}{\theta} \right), \end{aligned} \quad (29)$$

where H^* , T^* , I^* , E^* represent the tumor free equilibrium values for the normal cells, tumor cells, immune cells, and the estrogen hormone, respectively. We have $I^* > 0$ and $E^* > 0$ since all parameters s , v , μ , σ_3 , θ , π , σ_1 , α_1 , and β_1 are positive. I^* now depends on estrogen suppression unlike in the estrogen-free model, where it only depends on natural dynamics.

H^* will be nonnegative at ψ_t when $(\alpha_1 - \sigma_1 E^*)/\beta_1 \geq 0$,

$$\implies E^* \leq \frac{\alpha_1}{\sigma_1}. \quad (30)$$

This implies that estrogen cells at any given time t should be less than the growth coefficient of normal cells. We also noted earlier on that E^* is nonnegative. Therefore, the existence of a tumor-free equilibrium in this case depends on the estrogen levels and (30) whilst on the estrogen-free model it depends on the natural dynamics only.

6.1.2. Dead Equilibrium ψ_d . An equilibrium point is referred to as dead if the host cell population is zero. There are two dead equilibria where the first one is as a result of breast tissue

removal characterised with both normal cells and tumor cell population having died off. This is feasible as the competition has led to exclusion of both normal and tumor cells but

$$\psi_d = (H^*, T^*, I^*, E^*) = \left(0, \frac{\gamma_2 I^* - \alpha_3}{\beta_2}, \frac{s}{\mu + \delta_3 E^*/(v + E^*) + \gamma_3 T^* - \rho T^*/(\omega + T^*)}, \frac{\pi}{\theta} \right), \quad (31)$$

where (H^*, T^*, I^*, E^*) represents the equilibrium values of the normal cells, tumor cells, immune cells and estrogen levels, respectively. This dead equilibrium is a situation where the normal cells have been out competed by the tumor cells and as a result the whole breast tissue is a tumor. It exist when $I^* < \alpha_3/\gamma_2$ and $\mu + \delta_3 E^*/(v + E^*) > (\rho T^*/(\omega + T^*) - \gamma_3 T^*)$. Which implies the net growth of the tumor cells must be more than the immune cell value in order to have the tumor cells outgrowing the normal cells as the reactivation of the immune cells due to estrogen effects is greater than the reactivation of the immune cells due to tumor effect.

6.1.3. Coexisting Equilibrium- ψ_c . The coexisting equilibrium state exists when all cell populations would have survived the competition. This is given by $\psi_c = (H^*, T^*, I^*, E^*)$ where H^* , T^* , I^* , and E^* represent the coexisting equilibrium values for the normal cells, tumor cells, immune cells and the estrogen hormone, respectively, and are given by,

$$\begin{aligned} H^* &= \frac{\alpha_1 - \delta_1 T^* - \sigma_1 E^*}{\beta_1}, \\ T^* &= \frac{1}{2\beta_1\beta_2} \left(-B + \sqrt{B^2 - 4\beta_1\beta_2(-\alpha_1\sigma_2 E^* + \sigma_1\sigma_2 E^{*2})} \right), \\ I^* &= \frac{s}{\mu - \rho T^*/(\omega + T^*) + \gamma_3 T^* + \sigma_3 E^*/(v + E^*)}, \\ E^* &= \frac{\pi}{\theta}, \end{aligned} \quad (32)$$

where $B = -\alpha_3\beta_1 + \beta_1\gamma_2 I^* + \delta_1\sigma_2 E^*$. Since π and θ are positive parameters, we have $E^* \geq 0$. We also need $\alpha_1 \geq \delta_1 T^* + \sigma_1 E^*$ for H^* to be feasible at this equilibrium state. That is, the rate of normal cell growth must be greater than the rate at which they are lost as a result of interactions with tumor and presence of more estrogen. The value of $T^* > 0$ at the ψ_c when

$$E^*(\sigma_1\sigma_2 E^* - \alpha_1\sigma_2) \geq 0. \quad (33)$$

Therefore we have either $E^* = 0$ resulting in estrogen-free model or $E^* \geq \alpha_1/\sigma_1$ which implies that the estrogen levels must be greater than the net growth rate of normal cells for cells to coexist an opposite case with the tumor-free state equation (30).

I^* exists at ψ_c when

$$\mu + \frac{\sigma_3 E^*}{v + E^*} > \frac{\rho T^*}{\omega + T^*} - \gamma_3 T^*. \quad (34)$$

however not of importance since it does not give us anything to analyse the effects of estrogen on the dynamics of breast cancer. The second dead equilibrium is given by

Therefore activation of immune response as a result of tumor presence should be lower than the rate at which they are lost due to estrogen effects plus natural death.

6.2. Stability Analysis of Equilibria. Linearising the system at different equilibrium values gives the following.

6.2.1. Local Stability of the Tumor-Free Equilibria. We would want to check how the system at the tumor-free equilibrium point will now behave in terms of stability given the incorporated effects of estrogen. The system has four eigenvalues (λ_i) which will determine the stability of the system, with the first two eigenvalues both negative and given as

$$\lambda_1 = -\theta, \quad \lambda_2 = -\frac{\mu(\pi + \theta v) + \sigma_3 \pi}{\pi + \theta v}. \quad (35)$$

The remaining eigenvalues are given by the characteristic equation:

$$\begin{aligned} \lambda^2 - \lambda(\alpha_3 + 3\sigma_1 E^* + \gamma_2 g(i) - \alpha_1) \\ + \alpha_1 \alpha_3 - 2g(h)\alpha_3\beta_1 - \alpha_1 \alpha_2 g(i) \\ + 2g(i)g(h)\beta_1\gamma_2 - \alpha_3\sigma_1 \frac{\pi}{\theta} \\ + g(i)\gamma_2\sigma_1 \frac{\pi}{\theta} + g(h)\delta_1\sigma_2 \frac{\pi}{\theta} = 0, \end{aligned} \quad (36)$$

where

$$\begin{aligned} g(h) &= \frac{\alpha_1 - \sigma_1 E^*}{\beta_1}, \\ g(i) &= \frac{s(E^* + v)}{\mu(E^* + v) + \sigma_3 E^*}. \end{aligned} \quad (37)$$

Since $(\alpha_3 - \alpha_1 + 3\sigma_1 E^* + \gamma_2 g(i))$ is positive due to the fact that the rate of tumor growth is greater than that of normal cells, that is, $\alpha_2 > \alpha_1$, this implies $-(\alpha_3 - \alpha_1 + 3\sigma_1 E^* + \gamma_2 g(i))$ is negative and by Routh Hurwitz criterion the system cannot be stable. Thus the tumor-free equilibrium point is always unstable implying the existence of estrogen has caused instability in the tumor free state.

6.2.2. Local Stability of the Coexisting Equilibrium Point. We linearise the system of differential equations (28) at $\psi_c = (H^*, T^*, I^*, E^*) = (p(h), p(t), p(i), \pi/\theta)$, where from the previous section, $p(h)$, $p(t)$ and $p(i)$ are nonnegative and real parameters. This results in the following eigenvalues

TABLE 1: Model parameters and their interpretations.

Parameter	Symbol	Value	Units	Reference
Per capita growth rate of normal cells	α_1	0.70	(day) ⁻¹	est
Per capita growth rate of tumor cells	α_2	0.98	(day) ⁻¹	[11]
Natural death rate of normal cells	β_1	0.30	(day) ⁻¹	est
Natural death rate of tumor cells	β_2	0.40	(day) ⁻¹	[12]
Normal cell death rate due to competition	δ_1	1.0	(day) ⁻¹	[12]
Tumor death rate due to immune response	γ_2	0.9	(day) ⁻¹	[12]
Source rate of immune cells	s	0.4	(day) ⁻¹	[13]
Immune response rate	ρ	0.2	(day) ⁻¹	[13]
Immune threshold rate	ω	0.3	(day) ⁻¹	[13]
Natural death rate of immune cells	μ	0.29	(day) ⁻¹	[12]

with $\lambda_1 = -\theta$ which is negative. The other eigenvalues are obtained from the following characteristic equation:

$$\lambda^3 + \lambda^2 \left(\alpha_1 + \alpha_3 - 2p(h)\beta_1 - 2p(t)\beta_2 - p(i)\gamma_2 - p(t)\delta_1 - 2p(t)^2\beta_2\delta_1 - \sigma_1 E^* - \frac{s}{I^*} \right) + \dots = 0. \quad (38)$$

By Routh-Hurwitz criteria the system is stable only if

$$\alpha_1 + \alpha_3 > 2p(h)\beta_1 + 2p(t)\beta_2 + p(i)\gamma_2 + p(t)\delta_1 + 2p(t)^2\beta_2\delta_1 + \sigma_1 E^* + \frac{s}{I^*} \quad (39)$$

It is ideal when we have the growth of the tumor and normal cells being greater than their depreciation if they have to survive competition and coexist regardless of the interactions. Otherwise if the rate of growth of these normal and tumor cells is lower than the rate at which they die due to either interaction or naturally, this will lead to competitive exclusion and hence the dead equilibria. We therefore conclude that it is ideal to have

$$\alpha_1 + \alpha_3 < 2p(h)\beta_1 + 2p(t)\beta_2 + p(i)\gamma_2 + p(t)\delta_1 + 2p(t)^2\beta_2\delta_1 + \sigma_1 E^* + \frac{s}{I^*}, \quad (40)$$

which implies a negative coefficient for λ_2 ; hence the system is unstable if cells coexist.

6.2.3. Global Stability of Equilibria. Global stability of the equilibrium points here is done using Castillo-Chavez method [42]. We rewrite system (1) as

$$\begin{aligned} \frac{dX}{dt} &= F(X, Z), \\ \frac{dZ}{dt} &= G(X, Z), \end{aligned} \quad (41)$$

where $G(X, 0) = 0$, $X \in \mathfrak{R}^3$ denotes the undamaged cell compartments ($H(t)$, $I(t)$ and $E(t)$), and $Z \in \mathfrak{R}^1$ is comprised of the damaged cell compartment; $T(t)$.

The conditions below must be satisfied to guarantee global stability.

H1: For $dX/dt = F(X, 0)$, X^* is globally stable.

H2: $G(X, Z) = AZ - G^*(X, Z)$, $G(X, Z) \geq 0$ for $(X, Z) \in \Omega$.

where $A = D_Z G(X^*, 0)$ is an M -matrix (with off diagonal elements as nonnegative) and Ω is the region where the model makes biological sense. In our case,

$$F(X, 0) = \begin{pmatrix} \alpha_1 H - \beta_1 H^2 - \sigma_1 H E \\ s - \mu I - \frac{\sigma_3 I E}{v + E} \\ \pi - \theta E \end{pmatrix}, \quad (42)$$

and A is a 1×1 matrix given $A = D_Z G(X^*, 0) = \alpha_2 - 2\beta_2 T^* - \gamma_2 I^*$ and $G^*(X, Z) = -(\beta_2 T^* + \sigma_2 H^* E^*)$.

The conditions H1 and H2 have not been satisfied. We therefore conclude that the tumor-free equilibrium, ψ_t is globally unstable since $G^*(X, Z) < 0$. The coexisting equilibrium point ψ_c likewise is globally unstable since $G^*(X, Z) < 0$ for all nonnegative values of coexisting equilibrium points. The global stability of the system now depends for the presence of estrogen levels

7. Numerical Simulations

Matlab 6.5 version was used for all our simulations for both models using ODE45 solver. Simulations on this model give us a portrait of the general behaviour of breast cancer cells in the presence of normal cells and immune cells. We are also concerned on the parameters which are of importance in stabilising the model and the ranges in which the system is stable and unstable. Initial values of variables are $H(0) = 1$, $T(0) = 10^{-5}$, and $I(0) = s/\mu = 1.379310345$ adopted from [13]. All parameter values used for the numerical simulations are as shown in Table 1. The numerical solutions generally show that in the presence of excess estrogen, tumor cells grow as shown by Figure 1(a) while immune cells and normal cells decrease with normal cells being the most affected (Figure 1(b)).

8. Conclusions

The general dynamics of breast cancer have been presented in form of a system of differential equations. Conditions of

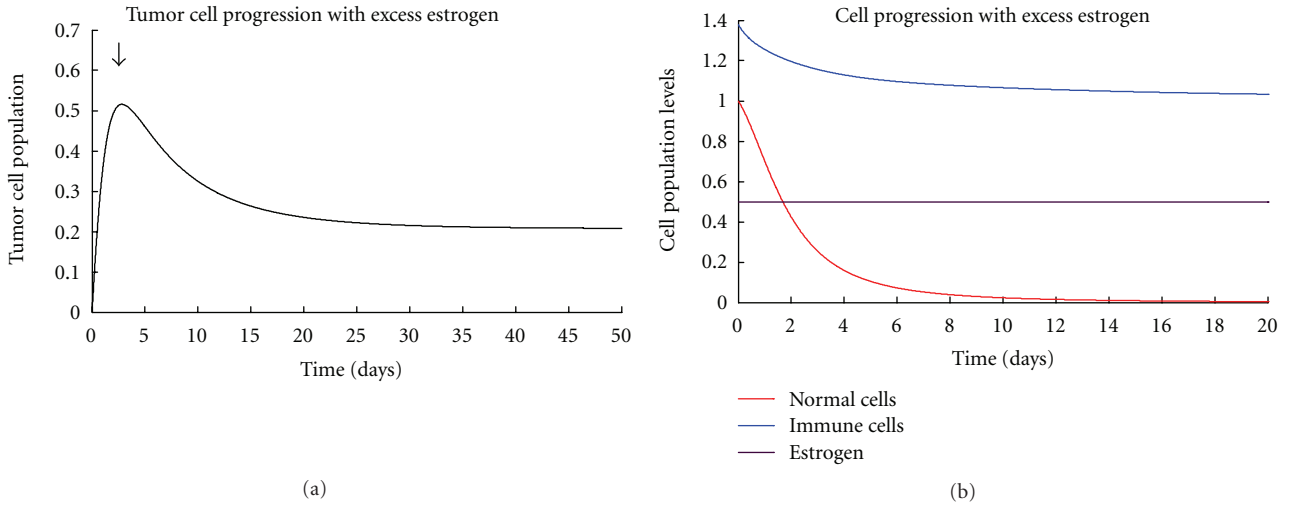


FIGURE 1: (a) Showing the general result tumor progression with excess estrogen. (b) Showing the general normal, immune, and estrogen levels in the presence of excess estrogen.

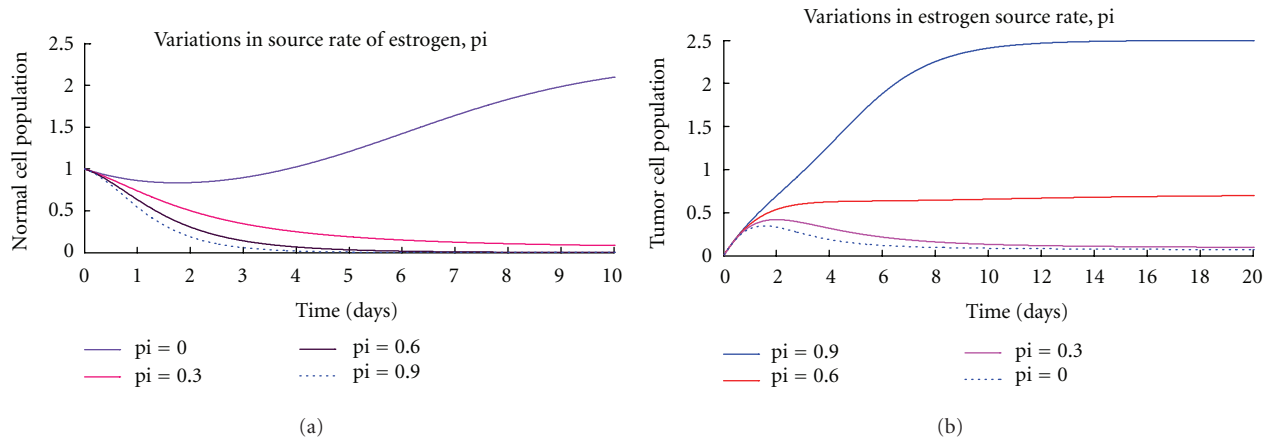


FIGURE 2: (a), (b) are graphs of numerical solutions showing the propagation of normal cells and tumor cells, respectively, with estrogen variations.

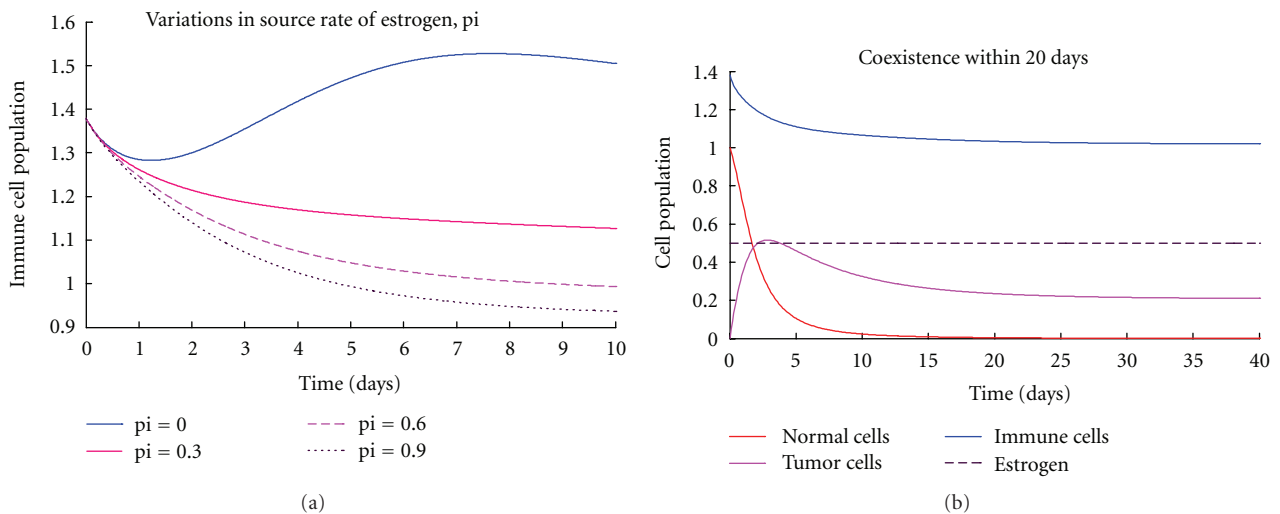


FIGURE 3: (a) The propagation of immune cells with estrogen variations. (b) The coexistence state of normal, tumor, and immune cells in the presence of excess estrogen.

stability of the tumor-free equilibria were established. The system is only stable if and only if the immune resistance is greater than tumor growth rate. That is, the chance of an individual developing breast cancer depends on the ability of the immunity to combat tumor cells. We have also deduced that the presence of excess estrogen in the system makes it unstable. This implies that additional estrogen quantity introduced increases rate of tumor development hence the development of breast cancer. This is supported by Figure 2(a) which shows that the normal cells grow normally without excess estrogen levels ($\pi = 0$). However, their growth is affected negatively in the presence of excess estrogen as they decrease with increase in estrogen amounts. The excess estrogen is however, a favorable condition to the tumor growth. When $\pi = 0$ tumor cells can be controlled to minimum levels by the immune system but rises to uncontrollable levels as the estrogen amount increases bringing the instability as shown by Figure 2(b). This is so because excess estrogen increases the rate of tumor formation and also suppresses immune growth. Figure 3(a) shows that immune levels are reduced with increase in estrogen levels hence weakening the immune system. Therefore the immune system will not be able to compete effectively with the cancer cells and thus will fail to control the disease. The estrogen-free model is always stable in the absence of any tumor but as we introduced estrogen, the system became unstable as shown on the global stability. Thus, the presence of excess estrogen will lead into a situation in which the disease is uncontrollable. No form of control measure or intervention can stabilise the system since it is always unstable in the presence of excess estrogen. Therefore, abnormal estrogen levels increase the chances of an individual developing breast cancer. This can also imply that the use of estrogen hormone as a birth control method has a negative impact since it can cause breast cancer. The global stability of the model system (28) shows that as estrogen levels approach zero, the tumor-free equilibrium becomes stable. This brings us to another aspect that increasing estrogen levels will increase the chance of an individual developing breast cancer.

Numerical simulations have also shown that tumor population increases as estrogen source rate increases in excess estrogen (Figure 2(b)). That is, as estrogen levels increase, the risk of developing breast cancer also increases. Normal and immune cells also decreased with an increase in estrogen levels. This implies that in the long run, the whole breast tissue will be infested with tumor cells in the presence of excess estrogen. We have also found out that any estrogen amount above normal has a negative impact on the dynamics of normal and immune cells. We therefore conclude that taking extra estrogen levels either as hormonal birth control or beauty enhancing practices will increase risk of breast cancer development.

9. Discussion

The results clearly show a negative relationship of estrogen amounts and tumor cell development. The development of tumor cells depends on the ability of the normal cells

(immune system) to combat tumor cells in the absence of excess estrogen and on estrogen levels plus immune compatibility in case of excess estrogen levels. However, it must be noted that it may also depend on genetics of an individual like the ability of DNA to resist change in structure and amount of estrogen released during natural biological processes like menopause and premenopause stages. Exposure periods to radioactive material, for example, are other external factors which have not also been incorporated in the model which might result in a difference of the results.

References

- [1] American Cancer Society, *Cancer Facts and Figures 2011*.
- [2] International Agency for Research on Cancer, *Cancer Survival in Africa, Asia, the Caribbean and Central America*, 2011, Edited by R. Sankaranarayanan, R. Swaminathan, K. Jayant, and H. Brenner.
- [3] American Cancer Society, *Cancer Facts and Figures 2012*.
- [4] M. Tokunaga, C. E. Land, S. Tokuoka, I. Nishimori, M. Soda, and S. Akiba, "Incidence of female breast cancer among atomic bomb survivors, 1950–1985," *Radiation Research*, vol. 138, no. 2, pp. 209–223, 1994.
- [5] A. B. Miller, G. R. Howe, G. J. Sherman et al., "Mortality from breast cancer after irradiation during fluoroscopic examinations in patients being treated for tuberculosis," *The New England Journal of Medicine*, vol. 321, no. 19, pp. 1285–1289, 1989.
- [6] A. Lanfranchi and J. Brind, *Breast Cancer: Risks and Prevention*, Breast Cancer Prevention Institute, 4th edition, 2007.
- [7] D. Thompson, D. Easton, and The Breast cancer linkage consortium, "Cancer incidence in BCR1-mutation carriers," *Journal of the National Cancer Institute*, vol. 94, no. 18, pp. 1358–1365, 2002.
- [8] N. Avis, S. Crawford, and J. Manuel, "Quality of life among younger women with breast cancer," *Journal of Clinical Oncology*, vol. 23, no. 15, pp. 3322–3330, 2005.
- [9] National Cancer Institute, "Breast Cancer Risk Increased in BRCA2 Carriers in Iceland," *NCI Cancer Bulletin*, vol. 3, no. 4, 2006.
- [10] J. D. Yager and N. E. Davidson, "Estrogen carcinogenesis in breast cancer," *The New England Journal of Medicine*, vol. 354, no. 3, pp. 270–282, 2006.
- [11] M. Villasana, *A delay differential equation model for tumor growth [Ph.D. dissertation]*, Claremont University, 2001.
- [12] M. Villasana and A. Radunskaya, "A delay differential equation model for tumor growth," *Journal of Mathematical Biology*, vol. 47, no. 3, pp. 270–294, 2003.
- [13] L. G. De Pillis and A. Radunskaya, "A mathematical tumor model with immune resistance and drug therapy. An optimal control approach," *Journal of Theoretical Medicine*, vol. 3, no. 2, pp. 79–100, 2001.
- [14] G. Bani, M. Biggazi, and T. Sacchi, "Relaxin as a mammatrophic hormone," *Experimental and Clinical Endocrinology*, vol. 10, pp. 143–150, 1991.
- [15] R. C. Mercado-Simmen, G. D. Bryant-Greenwood, and F. C. Greenwood, "Relaxin receptor in the rat myometrium: regulation by estrogen and relaxin," *Endocrinology*, vol. 110, no. 1, pp. 220–226, 1982.
- [16] G. A. Colditz, "Relationship between estrogen levels, use of hormone replacement therapy, and breast cancer," *Journal of*

- the National Cancer Institute*, vol. 90, no. 11, pp. 814–823, 1998.
- [17] C. Kahlenborn, F. Modugno, D. M. Potter, and W. B. Severs, “Oral contraceptive use as a risk factor for premenopausal breast cancer: a meta-analysis,” *Mayo Clinic Proceedings*, vol. 81, no. 10, pp. 1290–1302, 2006.
- [18] P. S. Crooke, C. Justenhoven, H. Brauch et al., “Estrogen metabolism and exposure in a genotypic-phenotypic model for breast cancer risk prediction,” *Cancer Epidemiology Biomarkers and Prevention*, vol. 20, no. 7, pp. 1502–1515, 2011.
- [19] Collaborative Group on Hormonal Factors in Breast Cancer, “Breast cancer and hormone replacement therapy: collaborative reanalysis of data from 51 epidemiological studies of 52 705 women with breast cancer and 108 411 women without breast cancer,” *The Lancet*, vol. 350, no. 9084, pp. 1047–1059, 1997.
- [20] T. Sacchi, “Relaxin influences the growth of MCF-7 breast cancer cells,” *Cancer*, vol. 70, no. 3, pp. 639–643, 1992.
- [21] S. Yaghoubi, J. Barlow, and P. H. Kass, *Breast cancer and metals: a literature review, zero breast cancer [Ph.D. thesis]*, University of California, Davis, Calif, USA, 2007.
- [22] R. Yafia, “Dynamics analysis and limit cycle in a delayed model for tumor growth with quiescence,” *Nonlinear Analysis: Modelling and Control*, vol. 11, no. 1, pp. 95–110, 2006.
- [23] L. E. Green, T. A. Dinh, and R. A. Smith, “An estrogen model: the relationship between body mass index, menopausal status, estrogen replacement therapy, and breast cancer risk,” *Computational and Mathematical Methods in Medicine*, vol. 2012, Article ID 792375, 8 pages, 2012.
- [24] L. G. DePillis and A. Radunskaya, “A mathematical model of immune response to tumor invasion, Computational fluid and solid mechanics,” in *Proceedings of the 2nd MIT Conference on Computational Fluid and Solid Mechanics*, pp. 1661–1668, June 2003.
- [25] G. Newbury, *A numerical study of a delay differential equation model for breast cancer [M.S. thesis]*, Faculty of the Virginia Polytechnic Institute and State University, 2007.
- [26] H. A. Mattsson and K. U. Nyquist, *A mathematical investigation of breast cancer and tumor growth. Statistical analysis and stochastic modelling2009 [M.S. thesis]*, Department of Mathematical Statistics, Chalmers University of Technology, University of Gothenburg, Gothenburg, Sweden, 2009.
- [27] V. A. Kuznetsov, I. A. Makalkin, M. A. Taylor, and A. S. Perelson, “Nonlinear dynamics of immunogenic tumors. Parameter estimation and global bifurcation analysis,” *Bulletin of Mathematical Biology*, vol. 56, no. 2, pp. 295–321, 1994.
- [28] A. C. Burton, “Rate of growth of solid tumours as a problem of diffusion,” *Growth, Development and Aging*, vol. 30, no. 2, pp. 157–176, 1966.
- [29] J. A. Adam, “A simplified mathematical model of tumor growth,” *Mathematical Biosciences*, vol. 81, no. 2, pp. 229–244, 1986.
- [30] J. J. Casciari, S. V. Sotirchos, and R. M. Sutherland, “Mathematical modelling of microenvironment and growth in EMT6/Ro multicellular tumour spheroids,” *Cell Proliferation*, vol. 25, no. 1, pp. 1–22, 1992.
- [31] M. H. Gail, L. A. Brinton, D. P. Byar et al., “Projecting individualized probabilities of developing breast cancer for white females who are being examined annually,” *Journal of the National Cancer Institute*, vol. 81, no. 24, pp. 1879–1886, 1989.
- [32] J. D. Boice and R. W. Miller, “Childhood and adult cancer after intrauterine exposure to ionizing radiation,” *Teratology*, vol. 59, no. 4, pp. 227–233, 1999.
- [33] M. Donovan, C. M. Tiwary, D. Axelrod et al., “Personal care products that contain estrogens or xeno-estrogens may increase breast cancer risk,” *Medical Hypotheses*, vol. 68, no. 4, pp. 756–766, 2007.
- [34] B. Zeigler, T. Kim, and H. Praehofer, *Theory of Modelling and Simulation. Integrating Discrete Event and Continuous Complex Dynamic System*, Academic press, 2000.
- [35] R. Goldstein and G. Wainer, “Modelling tumor-immune systems with Cell-DEVS,” in *Proceedings of the European Conference on Modelling and Simulation (ECMS '08)*, Nicosia, Cyprus, June 2008.
- [36] Y. L. Chia, P. Salzman, S. K. Plevritis, and P. W. Glynn, “Simulation-based parameter estimation for complex models: a breast cancer natural history modelling illustration,” *Statistical Methods in Medical Research*, vol. 13, no. 6, pp. 507–524, 2004.
- [37] G. G. Steel, *Growth Kinetics of Tumours*, Clarendon Press, 1977.
- [38] R. K. Sachs, L. R. Hlatky, and P. Hahnfeldt, “Simple ODE models of tumor growth and anti-angiogenic or radiation treatment,” *Mathematical and Computer Modelling*, vol. 33, no. 12-13, pp. 1297–1305, 2001.
- [39] R. A. Gatenby, “The potential role of transformation-induced metabolic changes in tumor-host interaction,” *Cancer Research*, vol. 55, no. 18, pp. 4151–4156, 1995.
- [40] A. A. Neves and K. M. Brindle, “Assessing responses to cancer therapy using molecular imaging,” *Biochimica et Biophysica Acta*, vol. 1766, no. 2, pp. 242–261, 2006.
- [41] R. P. Jimenez and E. O. Hernandez, “Tumor host dynamics under radiotherapy,” *Chaos, Solitons & Fractals*, vol. 44, no. 9, pp. 685–692, 2011.
- [42] C. Castillo-Chavez, Z. Feng, and W. Haug, “On the computation of R_0 and its role on global stability,” in *Mathematical Approaches for Emerging and Reemerging Infectious Diseases: An Introduction*, C. Castillo-Chavez, S. Blower, P. van den Driessche et al., Eds., vol. 125 of *IMA*, pp. 229–250, 2002.
- [43] E. M. Curran, B. M. Judy, N. A. Duru et al., “Estrogenic regulation of host immunity against an estrogen receptor—negative human breast cancer,” *Clinical Cancer Research*, vol. 12, no. 19, pp. 5641–5647, 2006.
- [44] S. Paruthiyil, H. Parmar, V. Kerekatte, G. R. Cunha, G. L. Firestone, and D. C. Leitman, “Estrogen receptor β inhibits human breast cancer cell proliferation and tumor formation by causing a G_2 cell cycle arrest,” *Cancer Research*, vol. 64, no. 1, pp. 423–428, 2004.
- [45] N. Heldring, A. Pike, S. Andersson et al., “Estrogen receptors: how do they signal and what are their targets,” *Physiological Reviews*, vol. 87, no. 3, pp. 905–931, 2007.
- [46] C. Roggia, Y. Gao, S. Cenci et al., “Up-regulation of TNF-producing T cells in the bone marrow: a key mechanism by which estrogen deficiency induces bone loss in vivo,” *Proceedings of the National Academy of Sciences of the United States of America*, vol. 98, no. 24, pp. 13960–13965, 2001.

Research Article

A Simulation Study of the Radiation-Induced Bystander Effect: Modeling with Stochastically Defined Signal Reemission

Kohei Sasaki,¹ Kosuke Wakui,² Kaori Tsutsumi,³ Akio Itoh,¹ and Hiroyuki Date³

¹ Graduate School of Engineering, Kyoto University, Kyoto 606-8501, Japan

² Graduate School of Health Sciences, Hokkaido University, Sapporo 060-0812, Japan

³ Faculty of Health Sciences, Hokkaido University, Sapporo 060-0812, Japan

Correspondence should be addressed to Hiroyuki Date, date@hs.hokudai.ac.jp

Received 17 March 2012; Revised 2 May 2012; Accepted 21 May 2012

Academic Editor: Loredana Marcu

Copyright © 2012 Kohei Sasaki et al. This is an open access article distributed under the Creative Commons Attribution License, which permits unrestricted use, distribution, and reproduction in any medium, provided the original work is properly cited.

The radiation-induced bystander effect (RIBE) has been experimentally observed for different types of radiation, cell types, and cell culture conditions. However, the behavior of signal transmission between unirradiated and irradiated cells is not well known. In this study, we have developed a new model for RIBE based on the diffusion of soluble factors in cell cultures using a Monte Carlo technique. The model involves the signal emission probability from bystander cells following Poisson statistics. Simulations with this model show that the spatial configuration of the bystander cells agrees well with that of corresponding experiments, where the optimal emission probability is estimated through a large number of simulation runs. It was suggested that the most likely probability falls within 0.63–0.92 for mean number of the emission signals ranging from 1.0 to 2.5.

1. Introduction

The radiation-induced bystander effect (RIBE) was initially reported by Nagasawa and Little [1]. Since then, this phenomenon has been observed for different radiation types such as α particles, photons, and carbon beams [2–5], and new experimental techniques have been applied to investigate the effect and associated processes [6]. Particularly, the microbeam technique has demonstrated RIBE clearly and precisely in experiments [7–10]. Some of the experiments indicate that the bystander effect is independent of dose, number of irradiated cells, and the linear energy transfer (LET) of the radiation [11, 12].

Currently, it is presumed that the signal transmission from irradiated cells to unirradiated cells is realized via several molecules secreted by the irradiated cells, such as interleukins, growth factors, and nitric oxide [13–15]. Facchetti et al. [16] have measured Interleukin-8 (IL-8) and Interleukin-6 (IL-6), as candidates of the bystander signals, and evaluated the influence of experimental conditions (e.g., cell density and medium volume) on the presence and release of these molecules in the medium. On another front, the

mechanism of RIBE focusing on the intercellular signal transmission has been investigated by simulation studies considering the geometry of *in vitro* experiments. Brenner et al. have proposed a mathematical model for RIBE, the Bystander and Direct (BaD) model, based on a binary phenomenon in a small sensitive subpopulation of cells and suggested that the bystander effect is important only at small doses [17]. Khvostunov and Nikjoo [18] have developed a biophysical model taking account of the bystander signal molecules with a certain probability of emission from the irradiated cells (bystander diffusion modeling: BSDM), and some researchers have simulated the RIBE in different ways such as a fully Monte Carlo procedure [19–24]. However, the underlying mechanisms of the molecules have not been clearly shown. The information on the number of original signals and the emitting probabilities of the signals from bystander cells is scarce, while the model itself still remains to be validated through a variety of means to examine this effect.

In this study, we present a simulation model of RIBE focusing on the signal number, in which the behavior of the bystander signal molecules is analyzed with a Monte Carlo

technique. The model involves the signal emission probability from the bystander cells following Poisson statistics.

2. Methods and Modeling

The current investigations are based on experiments and computer simulations to make clear the biological characteristics and reactive properties of RIBE. Recently, Xia et al. simulated RIBE with a Monte Carlo technique aimed at studying how bystander cells react at different distances from the irradiated cell [22]. However, the parameters were arbitrary in their model, making it difficult to determine them uniquely.

2.1. Modeling of RIBE with Signal-Emission Probability following Poisson Statistics. Our simulation algorithm is constructed for demonstrating the clonogenic assays of V79 cells which were randomly seeded as described in Schettino et al. [25]. In Schettino's experiment, individual V79 cells were exposed to a focused carbon K-shell X-ray microbeam (278 eV) in the 0–2 Gy range. The V79 cells were randomly allocated in a circle with radius 3 mm in the dish corresponding to the experimental condition. The assumptions underlying this simulation are described as follows.

- (1) At the beginning, the original bystander signals are generated by the irradiated cell and diffuse in cell culture medium through Brownian motion with a mean square displacement (r) of

$$\langle r^2(t) \rangle = 4Dt. \quad (1)$$

Here, D is the diffusion coefficient (constant) of the molecule considered as the bystander signal, and t is the time. In order to estimate the spread pattern of the bystander signals in the culture medium, the two-dimensional (2D) motion of the signal molecules is considered as in (1). The simulation is performed on the assumption that the signaling molecules are cytokines, such as IL-8 or IL-6, which have a mass of about 10 kDa. Thus, the diffusion coefficient of cytokine in the cell culture medium can be estimated to be around $10^8 \text{ nm}^2\text{s}^{-1}$ [26], while the unit time step Δt is set to be 1 s.

- (2) When a signal comes in the sphere of $5 \mu\text{m}$ radius about the center of an unirradiated cell, the unirradiated cell is transformed into a so-called "bystander cell" with a probability P_{dam} .
- (3) The bystander signal is annihilated in the above reaction, and the transformed bystander cell reemits a certain number (k) of bystander signals with a probability P_{re} . In the present model, we assume this probability to follow the Poisson distribution. The probability P_{re} is given by

$$P_{\text{re}}(k) = \frac{\mu^k}{k!} e^{-\mu}. \quad (2)$$

Here, μ is the mean value of the signal number. Then, the total reemission probability, P_{reT} , is deduced by the summation of $P_{\text{re}}(k)$ over $k = 1$ to infinity (the case $k = 0$ is excluded because this brings about no emission).

- (4) All signals have a certain life time (60 hr) and disappear at that time.

The basic idea in this model is that the signal transmission between cells is made by mobile entities such as molecules (but the identity of them remains to be seen). The simulation is performed with a Monte Carlo technique, where 259200 steps are tracked for demonstrating 3 days in real experimental time. This procedure is repeated to achieve statistically satisfactory iterations for a variety of initial random seeds. The program code is written in FORTRAN90, and the Mersenne Twister is used as the random number generator. The cell damage probability $P_{\text{dam}} = 0.01$ is chosen in consideration of the fact that cytokine-specific receptors cover 1% of the cell surface [27]. Although Xia et al. presumed the life time of all signals to be 36 hours [22], we assumed the life time to be 60 hours since Mothersill and Seymour showed that bystander signals are still active at 60 hours after irradiation [6]. Furthermore, the number of original signals generated at the irradiated cell was set to be 10, 15, 20, 25, or 30. For each original signal number, the mean value of the reemitting signal number, μ , was varied from 0.5 to 5.0 for estimating the optimal number of the reemission signals.

3. Results and Discussion

Investigations using the microbeam technique have pointed out that the RIBE occurs independently of the distance from the irradiated cell, the absorbed dose, and the linear energy transfer (LET) of the ionizing radiation in their experimental conditions [11, 12]. According to Schettino et al., the fraction of damaged cells per annulus is statistically constant over the distance from the irradiated cell for the doses of 0.2 and 2 Gy. The results in the present model were compared with those for the actual fraction of bystander cells as a function of distance from the irradiated cell reported by Schettino et al. In recent studies by Ballarini et al. [20] and Xia et al. [22], normal cells were arrayed at a regular interval between cells in a grid configuration. In such a condition, the distances from the irradiated cell are distributed in a cyclic manner, yielding the signal transmission distance with a periodic pattern. This may lead to incorrect demonstrations for the experimental condition. After the bystander signal tracking in the simulation, the damaged bystander cells were counted, and their X - Y positions were recorded. Figure 1 shows an example of cell distribution in the cell culture under a microbeam irradiation to the center cell represented as a star. The number of original signals is 15, while the mean number of reemission signals (μ) is 2.0. All living cell positions were acquired from the experiment by Schettino et al. Open and filled circles correspond to the healthy cells and the damaged bystander cells, respectively. One-hundred three cells in the experiment were entirely allocated on the

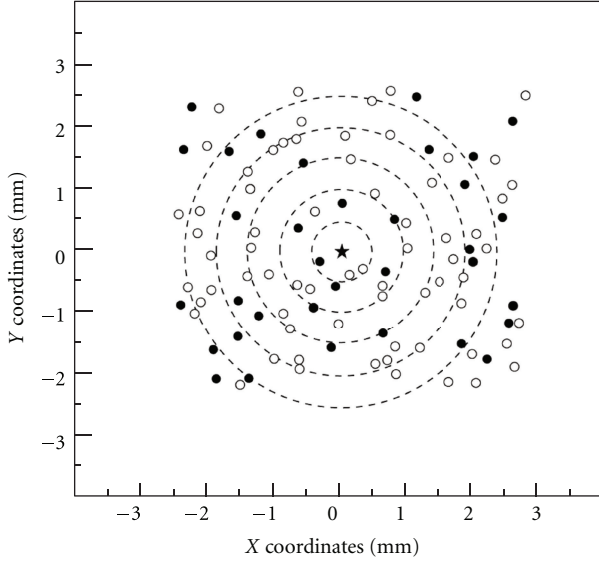


FIGURE 1: An example of the spatial distribution of cells in the simulation. The star is the position of the irradiated cell. Open circles represent the cells that remained to form healthy colonies, while filled circles are cells damaged by bystander responses. Dashed lines are for illustrative purposes only. Here, the number of original signals is 25, while the mean number of reemission signals is 1.5.

dish in the simulation model. The dashed lines mark the virtual circular regions in 3 mm radius about the center of the irradiated cell.

Each region delimited by adjacent dashed lines is defined as an “annulus.” The width of each annulus is set at 0.5 mm. Here, the number of original signals was set to be 25, and the mean number of reemission signals was 1.5. As shown in Figure 1, the damaged bystander cells are sparsely distributed in the cell culture medium, which is consistent with the results reported in previous studies [7, 12, 27].

Figures 2(a) and 2(b) compare the proportion of bystander cells in each annulus in the experimental [25] and simulation results under 0.2 and 2 Gy X-ray irradiation. The simulation results for both cases were obtained with the number of original signals 15 and the mean number of reemission signals 2.0. The agreement between the simulation and experimental results is fairly good, except for the ratio in the fourth annulus from the center in the 2 Gy case. Many simulation trials, within the fluctuation of reemission probability used here, tell us that the ratio of bystander cells does not always decrease monotonically as the distance from the center increases. The uniform spatial distribution of the bystander cells appears presumably as a consequence of the signal transmission process with a reemission probability. As a test of coincidence for the ratios between the experiment and simulation, the root mean square difference (RMSD) was examined for every mean reemission signal number (μ). The formula of RMSD is given by.

$$\text{RMSD (\%)} = \sqrt{\frac{\sum_{i=1}^N [r_{\text{exp}}(i) - r_{\text{sim}}(i)]^2}{N}}. \quad (3)$$

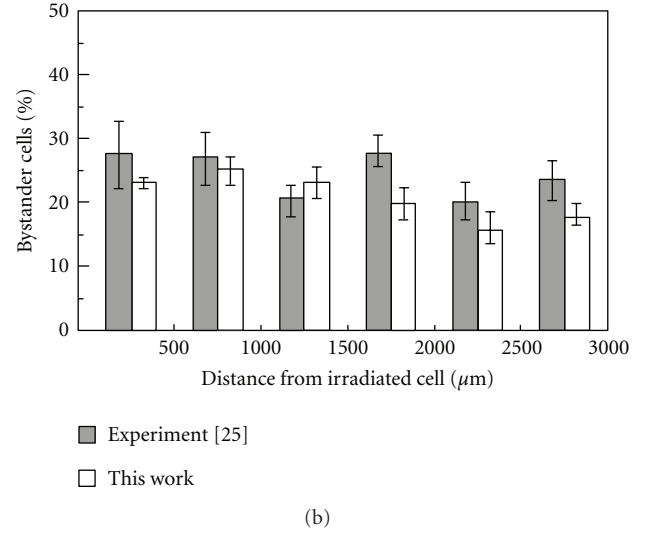
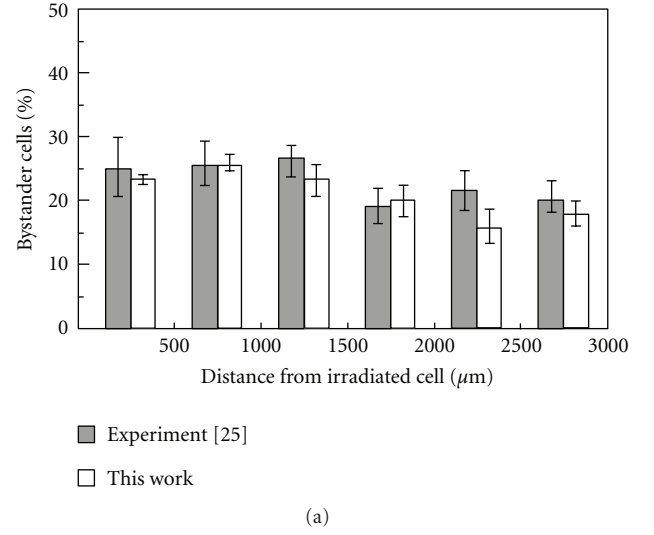


FIGURE 2: Ratio of the bystander cells as a function of distance from the irradiated cell. Gray column represents Experiment [25], white column represents simulation results: (a) for 0.2 Gy, single-cell irradiation, (b) for 2 Gy, single-cell irradiation. Here, the number of original signals is 15, and the mean number of reemission signals is 2.0.

Here, r_{exp} and r_{sim} are the average rates of bystander cells per total cells in each annulus (%) obtained by the experiment and simulation, and i represents an annulus number (up to $N = 6$ in this study). The RMSD versus mean number of reemission signals is shown in Figures 3(a) and 3(b). Each graph illustrates the cases for original signal number of 10, 15, 20, 25, and 30. It should be noted that the RMSD has a minimum in the mean number of reemitted signals ranging from 1.0 to 2.5 in all cases. The result also suggests that the mean number at the minimum of RMSD is inclined to decrease with increasing original signal number.

A salient feature of the present model is that the signals from bystander cells are treated with the reemission probabilities following Poisson statistics. It should be natural that the phenomenon of signal emission is stochastic, and

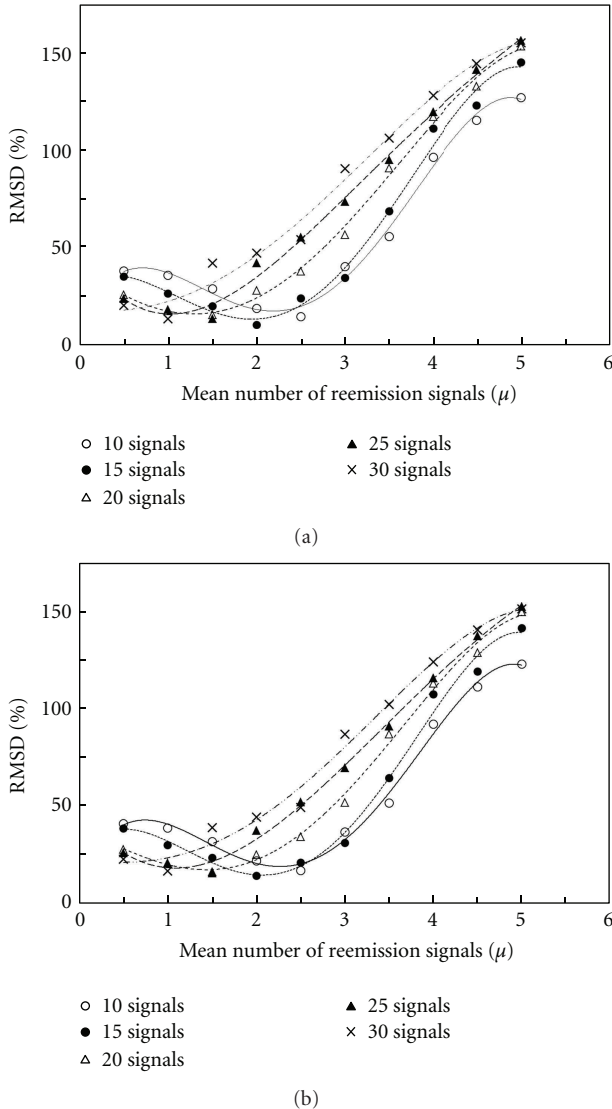


FIGURE 3: The RMSD between simulation and experimental results plotted against the mean number of reemission signals with best-fit curves. Each graph illustrates five cases for original signal number 10, 15, 20, 25, and 30: (a) for 0.2 Gy, (b) for 2 Gy.

thus, the number of released signals from bystander cells obeys Poisson statistics. The advantage of using the Poisson distribution is that the number of parameters for the simulation can be reduced because the distribution is defined by only one parameter (μ). Our simulation results show a fair agreement with the experiment in corresponding conditions, where the optimal probability is deduced through a large number of the simulation runs. As a result, we find that the most probable reemission probability (P_{reT}) fall within 0.63–0.92 for the mean number of signals ranging from 1.0 to 2.5. This procedure to obtain the minimum of RMSD enables us to determine the signal reemission probability without arbitrary adjustments. A natural extension of the simulation would be to compute the time lapse of the signal transmission.

4. Conclusions

In this study, the radiation-induced bystander effect (RIBE) was investigated by using a Monte Carlo simulation technique for a diffusion model of the bystander signals in comparison with the published experimental data. We have estimated the probable number of signals and reemission probability of signals from the bystander cells. The specific points of the model in this study are summarized below.

- (1) The model was constructed by introducing the bystander signal emission following Poisson statistics.
- (2) The simulation was able to reproduce the bystander cell spatial distribution featuring a uniform distribution in accord with the experiment.
- (3) The reemission signal number was deduced by comparing with the experimental result, where the root mean square difference (RMSD) between the simulation and experiment was found to have a minimum as a function of the mean reemission signal number.
- (4) The reemission probability of the signal was deduced in this simulation to range from 0.63 to 0.92, and the mean signal number is between 1.0 and 2.5.

References

- [1] H. Nagasawa and J. B. Little, “Induction of sister chromatid exchanges by extremely low doses of α - particles,” *Cancer Research*, vol. 52, no. 22, pp. 6394–6396, 1992.
- [2] H. Nagasawa and J. B. Little, “Unexpected sensitivity to the induction of mutations by very low doses of alpha-particle radiation: evidence for a bystander effect,” *Radiation Research*, vol. 152, no. 5, pp. 552–557, 1999.
- [3] S. G. Sawant, G. Randers-Pehrson, C. R. Geard, D. J. Brenner, and E. J. Hall, “The bystander effect in radiation oncogenesis: I. Transformation in C3H 10T1/2 cells in vitro can be initiated in the unirradiated neighbors of irradiated cells,” *Radiation Research*, vol. 155, no. 3, pp. 397–401, 2001.
- [4] G. Schettino, M. Folkard, K. M. Prise, B. Vojnovic, A. G. Bowey, and B. D. Michael, “Low-dose hypersensitivity in chinese hamster V79 cells targeted with counted protons using a charged-particle microbeam,” *Radiation Research*, vol. 156, no. 5, pp. 526–534, 2001.
- [5] C. Shao, M. Aoki, and Y. Furusawa, “Medium-mediated bystander effects on HSG cells co-cultivated with cells irradiated by X-rays or a 290 MeV/u carbon beam,” *Journal of Radiation Research*, vol. 42, no. 3, pp. 305–316, 2001.
- [6] C. Mothersill and C. Seymour, “Medium from irradiated human epithelial cells but not human fibroblasts reduces the clonogenic survival of unirradiated cells,” *International Journal of Radiation Biology*, vol. 71, no. 4, pp. 421–427, 1997.
- [7] K. M. Prise, O. V. Belyakov, M. Folkard, and B. D. Michael, “Studies of bystander effects in human fibroblasts using a charged particle microbeam,” *International Journal of Radiation Biology*, vol. 74, no. 6, pp. 793–798, 1998.
- [8] K. M. Prise, G. Schettino, M. Folkard, and K. D. Held, “New insights on cell death from radiation exposure,” *Lancet Oncology*, vol. 6, no. 7, pp. 520–528, 2005.

- [9] O. A. Sedelnikova, A. Nakamura, O. Kovalchuk et al., “DNA double-strand breaks form in bystander cells after microbeam irradiation of three-dimensional human tissue models,” *Cancer Research*, vol. 67, no. 9, pp. 4295–4302, 2007.
- [10] K. M. Prise, G. Schettino, B. Vojnovic, O. Belyakov, and C. Shao, “Microbeam studies of the bystander response,” *Journal of Radiation Research A*, vol. 50, pp. A1–A6, 2009.
- [11] W. F. Morgan, “Non-targeted and delayed effects of exposure to ionizing radiation: I. Radiation-induced genomic instability and bystander effects in vitro,” *Radiation Research*, vol. 159, no. 5, pp. 567–580, 2003.
- [12] K. M. Prise, M. Folkard, and B. D. Michael, “Bystander responses induced by low LET radiation,” *Oncogene*, vol. 22, no. 45, pp. 7043–7049, 2003.
- [13] C. Shao, V. Stewart, M. Folkard, B. D. Michael, and K. M. Prise, “Nitric oxide-mediated signaling in the Bystander response of individually targeted glioma cells,” *Cancer Research*, vol. 63, no. 23, pp. 8437–8442, 2003.
- [14] C. Shao, M. Folkard, and K. M. Prise, “Role of TGF- β and nitric oxide in the bystander response of irradiated glioma cells,” *Oncogene*, vol. 27, no. 4, pp. 434–440, 2008.
- [15] F. Ballarini, M. Biaggi, A. Ottolenghi, and O. Sapora, “Cellular communication and bystander effects: a critical review for modelling low-dose radiation action,” *Mutation Research*, vol. 501, no. 1-2, pp. 1–12, 2002.
- [16] A. Facoetti, L. Mariotti, F. Ballarini et al., “Experimental and theoretical analysis of cytokine release for the study of radiation-induced bystander effect,” *International Journal of Radiation Biology*, vol. 85, no. 8, pp. 690–699, 2009.
- [17] D. J. Brenner, J. B. Little, and R. K. Sachs, “The bystander effect in radiation oncogenesis: II. A quantitative model,” *Radiation Research*, vol. 155, no. 3, pp. 402–408, 2001.
- [18] I. K. Khvostunov and H. Nikjoo, “Computer modelling of radiation-induced bystander effect,” *Journal of Radiological Protection A*, vol. 22, no. 3, pp. A33–A37, 2002.
- [19] H. Nikjoo and I. K. Khvostunov, “Biophysical model of the radiation-induced bystander effect,” *International Journal of Radiation Biology*, vol. 79, no. 1, pp. 43–52, 2003.
- [20] F. Ballarini, D. Alloni, A. Facoetti, A. Mairani, R. Nano, and A. Ottolenghi, “Modelling radiation-induced bystander effect and cellular communication,” *Radiation Protection Dosimetry*, vol. 122, no. 1–4, pp. 244–251, 2006.
- [21] I. Shuryak, R. K. Sachs, and D. J. Brenner, “Biophysical models of radiation bystander effects: 1. Spatial effects in three-dimensional tissues,” *Radiation Research*, vol. 168, no. 6, pp. 741–749, 2007.
- [22] J. Xia, L. Liu, J. Xue, Y. Wang, and L. Wu, “Modeling of radiation-induced bystander effect using Monte Carlo methods,” *Nuclear Instruments and Methods in Physics Research B*, vol. 267, no. 6, pp. 1015–1018, 2009.
- [23] M. Richard, R. P. Webb, K. J. Kirkby, and N. F. Kirkby, “A computer model of the Bystander effect: effects of individual behaviours on the population response,” *Applied Radiation and Isotopes*, vol. 67, no. 3, pp. 440–442, 2009.
- [24] M. A. Ebert, N. Suchowerska, M. A. Jackson, and D. R. McKenzie, “A mathematical framework for separating the direct and bystander components of cellular radiation response,” *Acta Oncologica*, vol. 49, no. 8, pp. 1334–1343, 2010.
- [25] G. Schettino, M. Folkard, K. M. Prise, B. Vojnovic, K. D. Held, and B. D. Michael, “Low-dose studies of Bystander cell killing with targeted soft X rays,” *Radiation Research*, vol. 160, no. 5, pp. 505–511, 2003.
- [26] K. Jacobson and J. Wojcieszyn, “The translational mobility of substances within the cytoplasmic matrix,” *Proceedings of the National Academy of Sciences of the United States of America*, vol. 81, no. 21, pp. 6747–6751, 1984.
- [27] H. R. Petty, *Molecular Biology of Membranes*, Springer, New York, NY, USA, 1st edition, 1993.

Research Article

(Radio)Biological Optimization of External-Beam Radiotherapy

Alan E. Nahum and Julien Uzan

Physics Department, Clatterbridge Cancer Centre, Bebington CH63 4JY, UK

Correspondence should be addressed to Alan E. Nahum, alan.nahum@clatterbridgecc.nhs.uk

Received 19 July 2012; Accepted 31 August 2012

Academic Editor: Eva Bezak

Copyright © 2012 A. E. Nahum and J. Uzan. This is an open access article distributed under the Creative Commons Attribution License, which permits unrestricted use, distribution, and reproduction in any medium, provided the original work is properly cited.

“Biological optimization” (BIOP) means planning treatments using (radio)biological criteria and models, that is, tumour control probability and normal-tissue complication probability. Four different levels of BIOP are identified: Level I is “isotoxic” individualization of prescription dose D_{presc} at fixed fraction number. D_{presc} is varied to keep the NTCP of the organ at risk constant. Significant improvements in local control are expected for non-small-cell lung tumours. Level II involves the determination of an individualized isotoxic combination of D_{presc} and fractionation scheme. This approach is appropriate for “parallel” OARs (lung, parotids). Examples are given using our BioSuite software. Hypofractionated SABR for early-stage NSCLC is effectively Level-II BIOP. Level-III BIOP uses radiobiological functions as part of the inverse planning of IMRT, for example, *maximizing TCP whilst not exceeding a given NTCP*. This results in non-uniform target doses. The NTCP model parameters (reflecting tissue “architecture”) drive the optimizer to emphasize different regions of the DVH, for example, penalising high doses for quasi-serial OARs such as rectum. Level-IV BIOP adds functional imaging information, for example, hypoxia or clonogen location, to Level III; examples are given of our prostate “dose painting” protocol, *BioProp*. The limitations of and uncertainties inherent in the radiobiological models are emphasized.

1. Introduction

1.1. Advances in Radiotherapy Technology and Practice from the 1960s to the Present. The practice of external-beam radiation therapy is heavily influenced by the technology available in any one era. In the 1960s linear accelerators began to replace Cobalt machines [1]. Thus higher (bremsstrahlung) photon energies with improved tissue penetration became available. The next major advance was computerized treatment planning systems (TPSs) and shortly thereafter computer tomography (CT) provided 3-D images of the patient anatomy which were imported into the TPS [2]. Through advances in dose computation “algorithms” for megavoltage photon beams, the first planning systems worthy of the adjective “3-D” were developed and began to be available commercially [3]. These early 3-D TPSs made vastly improved targeting of the tumour volume possible but also revealed just how much normal tissue was irradiated using the crude collimation techniques of the time. Beam’s eye view (BEV) computer graphics then led to much improved beam shaping, firstly through custom casting of

shielding blocks (which became standard practice in N. America in the 1980s) and subsequently via the computer-controlled multileaf collimator [4]. Already at this stage the improved sparing of normal tissues encouraged efforts at “dose escalation” [5]. However, the really major advance was intensity modulation (IMRT) with its associated “inverse planning” which took normal-tissue sparing or “sculpting” to a whole new level [6–8]. One could now ask the TPS to create a treatment plan which significantly reduced the volume of high dose to even “concave” organs at risk (OAR) situated tightly adjacent to the target volume (in practice the PTV), for example, rectum to the prostate gland. More generally, a vastly increased number of degrees of freedom in the inverse planning process were now available. And the onward march of technology shows no signs of abating. Tomotherapy Hi-Art (Accuray) and more recently RapidArc (VARIAN) and VMAT (Elekta) have provided practical solutions for converting multifield IMRT into continuously rotating intensity modulation, originally known as IMAT [9], making IMRT easier and faster to deliver. In parallel with these advances in beam delivery and treatment planning,

on-couch patient imaging was being steadily developed, from the early EPIDS [10] through to kV cone-beam CT [11] which is driving “image guidance” or IGRT. In addition to all this increasing sophistication of megavoltage-*photon* techniques, gantry-based, high-energy, scanned-beam proton therapy is now becoming available in the more affluent parts of the world, principally the USA, Japan, and Europe, thereby achieving even higher degrees of “conformality” and hence greater normal tissue sparing than is possible with any photon-beam technique [12–15].

1.2. How Tumour Dose Is Prescribed. The advances in technology described above have been translated into increases in dose to the tumour, but this has largely been by a “one-size-fits-all” strategy, that is, *escalate the (prescription) dose D_{presc} to the same value for every patient (e.g., due to the adoption of IMRT, protons, etc.) or change the number of fractions in the same way for each patient (e.g., prostate or breast hypofractionation due to low tumour α/β).*

Despite the vastly increased normal-tissue-sparing and tumour-targeting ability at our disposal, the way in which the dose to the tumour is “prescribed” has hardly changed at all. With very few exceptions, strict protocols are followed. These specify for a given tumour type the precise radiation dose that shall be delivered, within tightly defined uniformity limits (e.g., the PTV shall be encompassed by the 95% isodose), in a fixed number of fractions (delivered daily between Monday and Friday). This rigid predetermination of the very quantities, the total and fractional doses to the tumour, D_{presc} and d_{presc} , that determine the probability of local control, removes the single most important weapon for improving treatment outcome—increasing the tumour dose and/or fraction size.

The above dose-escalation strategy has resulted in some modest gains in local control rates, particularly for intermediate- and late-stage prostate tumours [16] for no increase or even decreases in (principally rectal) complication rates. But as will be demonstrated in what follows, a rigid predefined dose prescription will lead to underdosage in some patients and to adverse effects from overdosage in others [17]. With reference to the different levels of biological optimization described in what follows, we label the above approach “level-zero optimization.”

2. Materials and Methods

2.1. Radiobiological Models for TCP and NTCP. Models for estimating the probability of tumour (local) control (TCP) and of normal-tissue complication (NTCP) were first proposed in the second half of the 1980s and the first half of the 1990s (see [18] for a useful summary of the various models and associated references). In the intervening period of 20 years or so the active use of these models has largely been confined to *evaluating* treatment plans, despite a very considerable literature on the analysis of clinical outcome data for determining “best fit” parameter values, recently summarized by the QUANTEC project on normal tissue complications [19]. By definition these best-fit parameters

make the models reproduce the clinical data points they were fitted to, but the associated confidence intervals are usually fairly wide. The source of this sometimes large uncertainty may reside in the functional form of the model but also in the nature of the data and the way they are reported. However, it should be borne in mind that uncertainty is intrinsic to radiotherapy treatments; for example, meeting normal tissue dose criteria is not a guarantee against the occurrence of a complication. To some extent, biological models are also subject to this uncertainty. All the radiobiological evaluations given in this paper should be understood as estimates based on the best-fit parameters available today.

It is emphasized that the current TCP, NTCP models are hybrid in nature; they apply to the *individual* patient’s dose distribution, expressed in terms of dose-volume histograms (DVHs), but to the *population-averaged* patient biology. Because in general we do not know the radiosensitivity of the tumour clonogens of the patient in question [20], the “Marsden” TCP model [21, 22] uses a mean α and an assumed standard deviation σ_α over the population; how these parameters are obtained for a given tumour type is briefly described in the next section. The currently used NTCP models also involve population-averaged biology though this is generally implicit rather than explicit in their mathematical form.

Certain radiobiological models are wholly or partly mechanistic (e.g., Marsden TCP, Relative Seriality [18]) while others are purely phenomenological (Lyman [23] and Kutcher et al. [24]). In all cases, some assumptions are explicitly or implicitly made so as to render the problem of predicting the outcome of radiotherapy mathematically manageable. For example, the LKB model considers all volume elements of a particular organ to have the same importance for the function of this organ. Furthermore the 3-D dose distribution in the organ/tissue is represented by a dose-volume histogram, which is inherently 2-D and does not include any spatial information. The Marsden TCP model assumes firstly that a tumour is only “controlled” (i.e., eliminated) when every single clonogen has been “killed” (i.e., rendered incapable of further division), and further, at least as applied in the examples given here, that all the clonogens have the same radiosensitivity and that this remains constant from fraction to fraction. It is important to keep in mind these assumptions.

In the present paper our focus is firmly on using NTCP and TCP models to change or *optimize* the way that (external-beam) treatment planning is done. The *power* of this approach is illustrated by Figure 1. However, in cases where metrics such as EUD for tumours [25, 26], gEUD for normal tissues [27], and mean lung dose (MLD) [28] are closely correlated with either TCP or NTCP then optimization based on these surrogate quantities can also be classed as *radiobiological optimization*.

2.2. The Different “Levels” of Radiobiological Optimization. Radiobiological models can be used to optimize treatment plans in a variety of ways. We have found it convenient

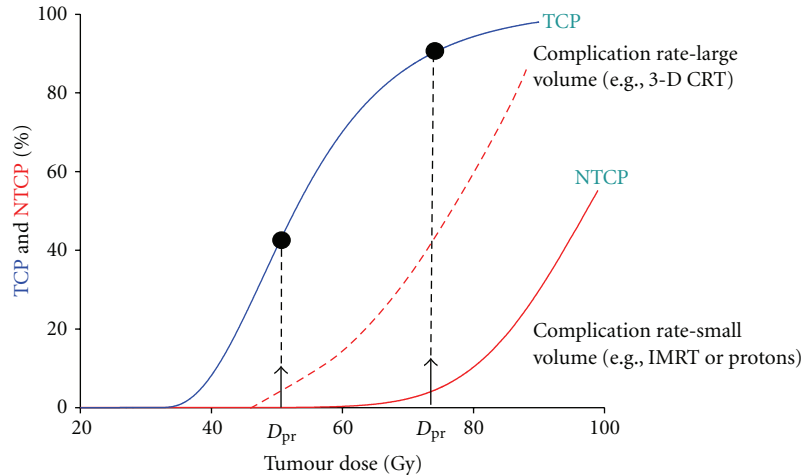


FIGURE 1: Illustration of the potential of TCP/NTCP-based optimization; the two arrows on the “Tumour Dose” axis indicate two different “isotoxic” prescription doses, D_{pr} , associated with the full and dashed NTCP curves which correspond to “large volume” and “small volume” dose coverage of the OAR. The improvement in TCP, from $\approx 45\%$ to $\approx 90\%$, that would result from such a change in dose to the tumour, is also shown.

to define five different “levels,” in approximate order of increasing sophistication:

Level I. Individualisation of D_{presc} on an *isotoxic* (i.e., iso-NTCP) basis.

Level II. Individualisation of not only D_{presc} but also the *number of fractions* on an *isotoxic* basis.

Level III. The use of radiobiological functions (EUD and/or NTCP and TCP) in the *inverse planning* algorithm.

Level IV. Additionally, patient-specific information from functional imaging is added to radiobiological inverse planning dose-painting.

Level V. Individual patient biology, for example from genomics, is added to any of the above.

Levels I to IV will be discussed in turn and illustrated by examples generated using software created at our centre.

3. Results and Discussion

3.1. Isotoxic Prescription Dose Customization: Level I. Shortly after the appearance of the first NTCP models [23, 24, 29] it was suggested that these models could be used to choose an optimum dose to the tumour [30, 31]; this was followed by more detailed studies such as [32]. However, it is only relatively recently that “isotoxic” clinical protocols have been put into practice [33].

The basic idea is illustrated in Figures 2 and 3. The standard Clatterbridge protocol for the radical radiotherapeutic treatment of non-small-cell lung tumours was, until around 2009, to treat to a total dose of 55 Gy in 20 fractions over 4 weeks [34]. A relatively straightforward 3-beam 6 MV technique was employed. Figure 2 shows the NTCP values

(grade 2 radiation pneumonitis) for a series of 24 patients treated around 2005-6; the NTCPs were computed from the DVHs of the paired lung minus the GTV using the Lyman-Kutcher-Burman (LKB) NTCP model [23, 24] with parameters from [35]; naturally correction was made for the varying fraction sizes in the DVHs, using $\alpha/\beta = 3$ [18]. The wide spread in these values is immediately evident, from as low as $\approx 2\%$ to as high as $\approx 22\%$, corresponding to the large differences in normal lung coverage by the beams, caused by patient-to-patient differences in tumour size and location. In no sense could it be said that all these patients were “treated to tolerance.” Local control rates were estimated to be in the region of 35% [36].

For the same cohort, the prescription doses were recomputed so that the NTCP for each case was 10%. For a small number of the treatment plans, D_{presc} was reduced below its “isotoxic” value due to the oesophageal constraint (set at $D_{max} = 63$ Gy for 20 fractions). An additional constraint we imposed was not to allow the TCP to exceed 99.0%; this restricted the highest value of D_{presc} to around 85 Gy. In all cases the number of fractions remained at 20. The “spectrum” of prescription doses is shown in Figure 3(a). In only two cases did this remain at ≈ 55 Gy. Figure 3(b) shows the TCP values “before” (pale blue) and “after” (maroon) dose customization, estimated using the “Marsden” TCP model [21, 22] with parameters from [37] (see below). The spread in TCP at the constant D_{presc} of 55 Gy is due to the variation in GTVs, which is translated into initial clonogen number N_0 via the clonogen density ρ_{clon} . The TCPs for the “isotoxic” prescription doses range from $\approx 5\%$ to $\approx 100\%$ (to be precise, 99%). The really important number is the average TCP which has increased from $\approx 44\%$ to $\approx 60\%$. This has been achieved for absolutely no increase in the average NTCP, which is $\approx 10\%$ in both cases. In clinical practice the resulting increase in the average local control rate may be even greater, as the *reduction* in D_{presc} for a number of patients in this modelling exercise would probably not be applied clinically.

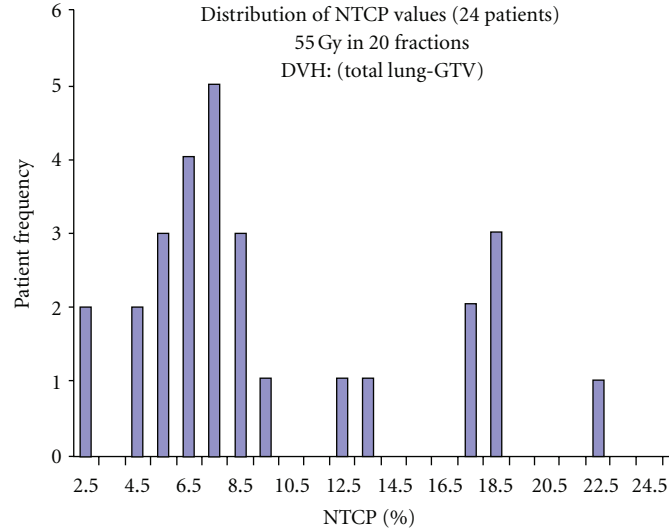


FIGURE 2: The distribution of NTCP values (grade 2 pneumonitis) estimated for a series of Clatterbridge NSCLC patients all with a D_{presc} of 55 Gy in 20 fractions; LKB model used with parameters $\alpha/\beta = 3$; $TD_{50} = 24.5$ Gy; $m = 0.37$, $n = 1$ [35]. The extremely wide variation in NTCP is simply a reflection of the wide variation in tumour sizes, tumour position, and hence volume of lung in the radiation fields. Note that the average NTCP was 9.5% [36] (adapted from [38]).

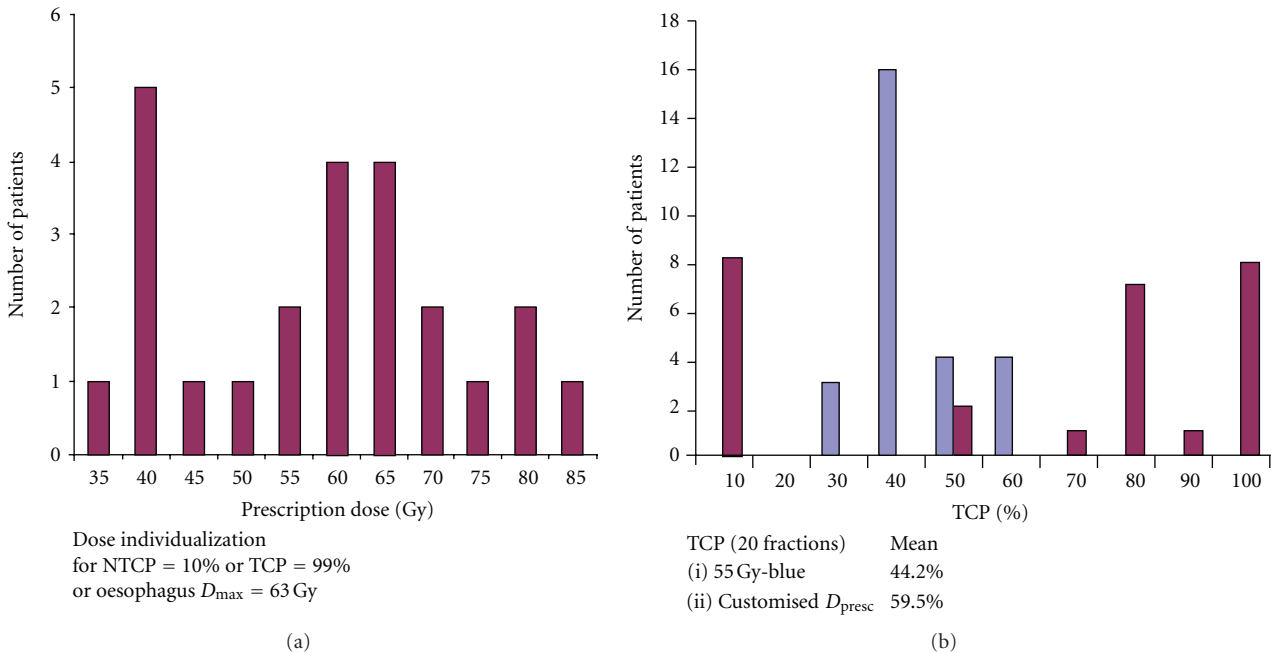


FIGURE 3: (a) The spectrum of D_{presc} resulting from “isotoxic” NTCP = 10% (grade 2 radiation pneumonitis) or TCP = 99% or D_{max} (oesophagus) = 63 Gy (whichever is the lowest) for the 24 patients of Figure 2. (b) TCP values for the constant 55 Gy prescription dose (blue) and the individualized D_{presc} shown in Figure 3(a). The increase in the mean TCP over the patient sample is obtained for no change in mean NTCP (adapted from Malik et al. (2007) with the TCP values recalculated using the parameters in [37]).

The parameters used in the TCP estimation were $N_0 = 10^7$ clons cm^{-3} ; $\bar{\alpha} = 0.307$ Gy^{-1} , $\sigma_{\alpha} = 0.037$ Gy^{-1} , $\alpha/\beta = 10$ Gy; $T_{\text{dbl}} = 3.7$ days; $T_{\text{delay}} = 20.9$ days. These were derived by fitting the predictions of the TCP model to published clinical outcomes [37] for a wide range of fraction sizes, total doses, and overall treatment times [36, 39, 40]; the fit was excellent.

3.2. *Treatment Protocols Based on Level-I Optimization.* In the UK two current phase I/II trials for radical radiotherapy of NSC lung tumours have been developed based on “isotoxic” dose individualization. The IDEAL-CRT trial [34, 43] involves 30 daily fractions over 6 weeks, with the prescription dose D_{presc} adjusted until NTD_{mean} (mean normalized total dose) for the non-involved lung is equal to

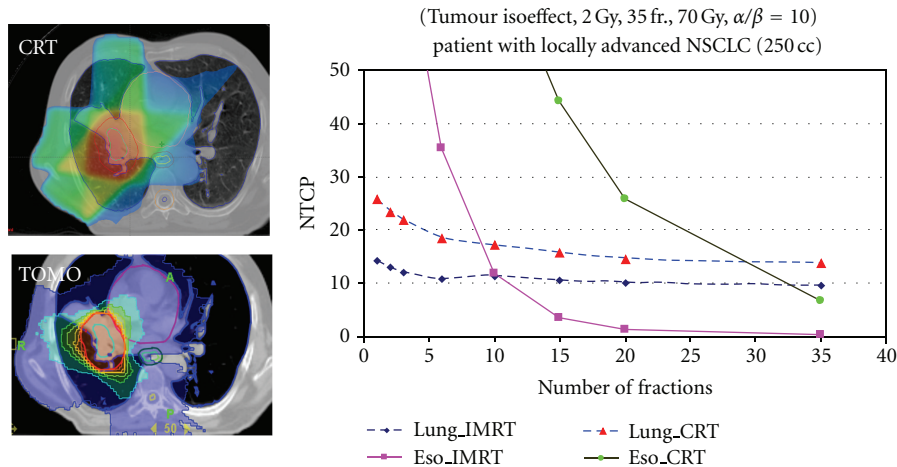


FIGURE 4: The variation of NTCP for radiation pneumonitis and oesophagitis, respectively, as a function of the number of fractions for a NSCLC lung radiotherapy case planned using tomotherapy (IMRT) and 3-D conformal techniques. The total dose is adjusted for tumour isoeffect using $\alpha/\beta = 10$. The increase in oesophageal NTCP is consistent with the conventional application of the Withers formula [41], but the near constancy of lung NTCP is definitely not. Note also that the NTCP values are consistently lower for the more conformal tomotherapy plan (from [42]).

18.2 Gy; this corresponds to a 20% rate of grade 2, or greater, pneumonitis. D_{presc} is then reduced by 10% to compensate for the possible effect of the concurrent chemotherapy. additionally, D_{presc} is restricted to a window of 63–73 Gy.

The I-START (ISoToxic Accelerated RadioTherapy) protocol [44] is a 20-fraction, 4-week treatment, radiation alone, and stages II to IIIb NSCLC patients are eligible. D_{presc} is chosen such that $\text{NTD}_{\text{mean}} = 17.0$ Gy and is restricted to the range 58–65 Gy, unless further limited due to cardiac, spinal cord or oesophageal constraints. This can be compared to the standard Clattebridge protocol of 55 Gy in 20 fractions for this patient group. It should be noted that both protocols are for fixed numbers of fractions; consequently increasing D_{presc} means that the dose per fraction is also increased.

Van Baardwijk et al. [33] described an individualized dose prescription study of 166 Stage-III NSCLC patients. Patients were treated to the maximally tolerable dose (MTD) by *increasing the number of fractions* (of 1.8 Gy twice daily) until normal-tissue constraints for the noninvolved lung and spinal cord were met. They reported favourable 1- and 2-year overall survival with acceptable toxicity.

One of the clear advantages of this type of optimization is that improvements in the degree of conformality of treatment plans for any given tumour type, due, for example, to moving from 3-D conformal to intensity modulation, from fixed, few-field IMRT to rotational IMRT (Tomotherapy, RapidArc, VMAT, etc.), or even from megavoltage photons to protons, are automatically translated into increases in the target dose, and therefore into probable improvements in clinical outcome.

3.3. Level-II Optimization: Customization of the Prescription Dose and Fraction Number under “Isotoxicity”. Fractionation is possibly the most “radiobiological” of all the variables in external-beam radiotherapy [45, 46]. The classic textbook recipe is that as small a fraction size as is practicable should

be used to maximize the “therapeutic ratio” (see Figure 1), which follows logically if α/β is low for late-reacting normal tissues and high for tumour clonogens [46–48]. However, two issues complicate this oversimplified picture. Firstly, increasing the number of fractions may well take the overall treatment time beyond 3 weeks, and therefore, in the case of lung and head and neck tumours, into the clonogen proliferation time zone [40], leading to a loss of local control for a given tumour BED [49]. Secondly, the LQ-based “Withers” formula for computing *normal-tissue* isoeffect as a function of α/β , dose per fraction and total dose [41, 50] is frequently used in an illogical manner. If instead of setting the dose in the Withers’ expression equal to the (tumour) prescription dose—that is, the “textbook” procedure—it is chosen to be representative of the “behaviour” of the normal tissue to which it is intended to apply (e.g., close to the mean organ dose for the case of “parallel” lung), then it can be shown that much larger fraction sizes can be safely used, especially for highly conformal treatment plans [42, 51]. Figure 4 illustrates this for the case of a lung tumour surrounded by “parallel” lung tissue; similar curves can be found in Vogelius et al. [52].

The BioSuite software [53] enables the impact of changing the number of fractions over a wide range to be explored. Figures 5 and 6 have been generated using BioSuite’s “isotoxic optimization” option, with the choice of 10% NTCP for radiation pneumonitis (RP), for two contrasting treatment plans for NSCLC lung tumour radiotherapy. For the case of Figure 5, for the (standard) prescription of 55 Gy in 20 fractions, the TCP was 48.0% and the NTCP (RP) 6.6%. When the (total) dose is increased to make $\text{NTCP}(\text{RP}) = 10\%$, we see how the TCP goes through a maximum at around 15 fractions and then decreases, due to clonogen proliferation ($T_{\text{delay}} = 21$ days, $T_{\text{dbl}} = 3$ days assumed). The optimum number of fractions is thus 15, that is, a 3-week treatment. This figure represents the “classical radiobiology”

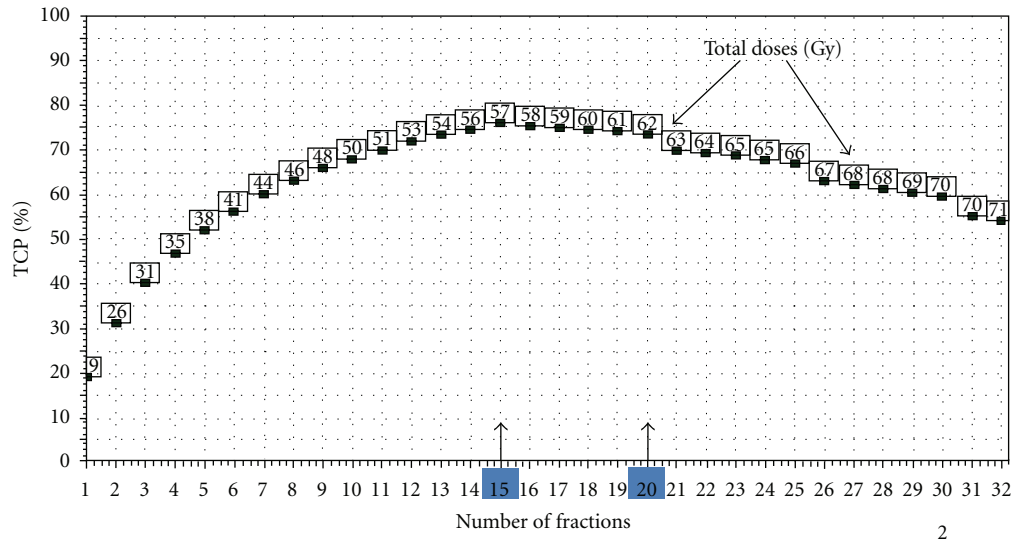


FIGURE 5: The variation of TCP with number of fractions, where the total dose (the numbers in the little squares) is adjusted to keep maintain isotoxicity, in this case 10% NTCP for the endpoint of grade 2 radiation pneumonitis (for parameters see Figure 2). The plot was generated by the BioSuite software [53]. In this case the standard prescription of 55 Gy in 20 fractions yielded TCP = 48%, NTCP = 6.6% (BioSuite is available from julien.uzan@clatterbridgecc.nhs.uk).

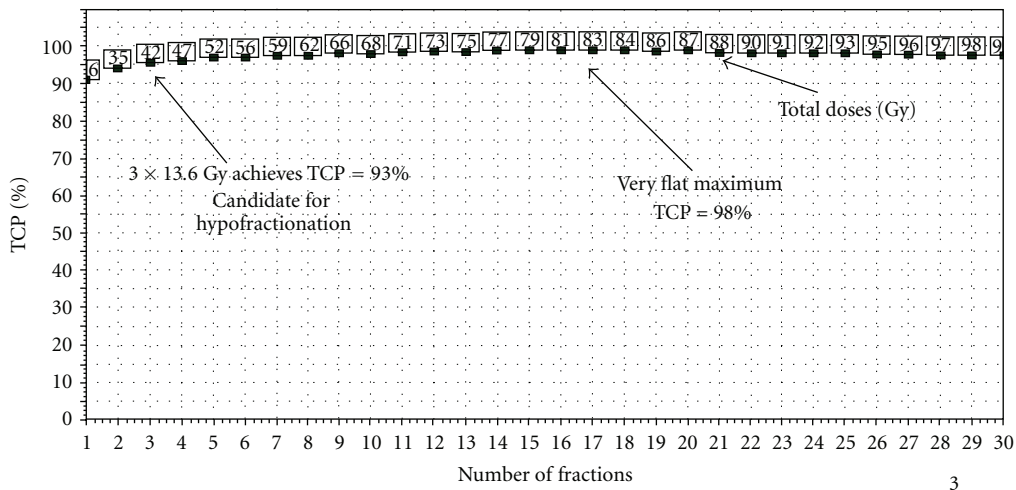


FIGURE 6: The variation of TCP with number of fractions, where the total dose (the numbers in the little squares) is adjusted to keep maintaining isotoxicity, in this case 10% NTCP for the endpoint of grade 2 radiation pneumonitis (for LKB parameters see Figure 2). The plot was generated by the BioSuite software [53]. In this case the standard prescription of 55 Gy in 20 fractions yielded TCP = 50.4%, NTCP = 4.3% (BioSuite is available from julien.uzan@clatterbridgecc.nhs.uk).

behaviour of the therapeutic ratio for a proliferating tumour (e.g., [49, 54]).

The treatment plan analysed in Figure 6 is also for a NSC lung tumour, but here the tumour is much smaller and more favourably located. The coverage of the non-involved lung is much less and this results in a very different dependence of TCP on the fraction number. This is a clear case of the effective dose in the normal lung being very much lower than the tumour dose, thus completely invalidating the conventional use of Withers' isoeffect formula (see the discussion at the beginning of this section).

The examples in the above two figures illustrate very clearly how different one patient can be from another in terms of the dependence of TCP on the number of fractions

under lung isotoxicity. This strongly suggests that when the principal organ at risk behaves in a "parallel" fashion (as does the lung [55]), and there is evidence for tumour clonogen proliferation [40], biologically optimized radiotherapy will result in customizing the fractionation scheme based on the patient's treatment plan. The extreme hypofractionation employed in so-called stereoblastic radiotherapy (SABR, formerly known as SBRT) for early stage NSC lung tumours [56] is effectively an example of this, though the dose is not generally individualized. However, for many of the reported series of SABR treatments local control rates are so high for acceptably low complication rates that it could be argued that there is no need for isotoxic dose customization [57, 58].

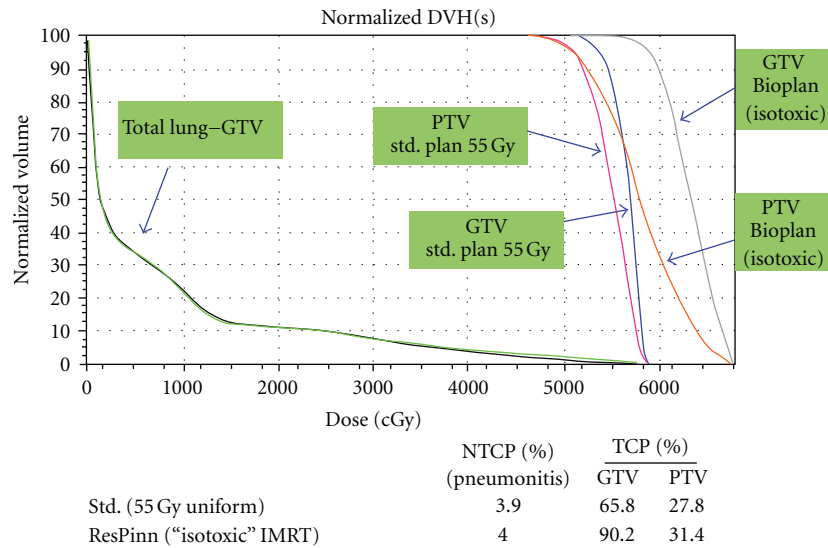


FIGURE 7: Dose-volume histograms for a radiobiologically guided inverse plan (3-field IMRT) aiming to maximize TCP for the same NTCP (labelled as “Bio-Plan (isotoxic)”) compare to a standard (3-field) treatment plan delivering 55 Gy (in 20 daily fractions) to a NSC lung tumour. The target volume (PTV, GTV) doses are more heterogeneous in the radiobiological plan. The increases in TCP values for the standard and radiobiologically optimized plans are also shown; the TCP parameters are from Nahum et al. [37]—see the subsection on “Level I” BIOP.

Hoffmann et al. [17] conducted an *in silico* trial, not dissimilar to the one described in the previous section (Figures 2 and 3). They individualized the dose prescription taking into account dose constraints not only for lung but also for spinal cord, oesophagus, brachial plexus, and heart. The number of fractions was set at 15, 20, and 33. They found that dose escalation was possible in 79% of the cases. They emphasized that to take the tumour dose to even higher levels it was essential to employ techniques which maximally spare the oesophagus.

3.4. Level-III BIOP: Radiobiologically Guided Inverse Planning. No modification of the treatment plan, that is, of the relative dose distributions, is involved in Level I or Level II optimization. Level III moves beyond this and, in the context of intensity modulation, exploits the mathematical properties of the TCP and NTCP functions in creating the “inverse” plan. This approach has one obvious advantage over dose-volume-based approaches to inverse planning: the number of degrees of freedom available to the optimizer is significantly increased. The intensity of each beamlet comprising the plan becomes a variable which can be adjusted to produce the best possible plan, from a radiobiological point of view. Thus the optimizer is now free to find solutions such as a reduction in the target dose adjacent to a critical normal tissue coupled with a boost to other parts of the target volume [59]. Obviously the target volume dose will no longer be uniform, but the TCP function will automatically take care of the effect of “hot” and “cold” spots.

There are however a couple of hurdles to overcome before this method can be applied. Firstly, all TPS inverse optimization engines work by minimizing a global cost function which is a measure of how well a plan meets clinical requirements (e.g., [8, 60]). For dose-based planning, these

requirements are formulated in terms of dose/volume limits (e.g., maximum dose of 50 Gy in OAR1, minimum dose of 64 Gy in target volume 2, etc.). In the case of radiobiological planning, however, the objective function to be minimized should contain TCP- and NTCP-based criteria, possibly in addition to dose/volume-based ones. One possibility is to define the objective function so that the optimizer will try to maximize TCP while keeping NTCP equal to or below some user-defined threshold. Another possibility is to let the optimizer find the dose distribution yielding the highest “uncomplicated tumour local control probability” also called $P+$ [61, 62]. The mathematical form of the objective function has a critical influence on the resulting dose distribution.

Secondly, inverse planning engines rely on some form of *gradient descent* algorithm to minimize the objective function (e.g., [60]). These algorithms can be trapped in local minima [8], corresponding to suboptimal plans, when the objective function possesses specific mathematical properties such as nonconvexity. While the functions for TCP and NTCP in the most widely used models are intrinsically nonconvex, mathematical transformations can help to make these functions amenable to gradient descent minimization (with limitations, see reference [63]). In practice, very few commercial TPS include this kind of optimization. When they do, radiobiological models are simplified to improve the reliability of the inverse optimization process [64] at the expense of the radiobiological therapeutic ratio.

We give below an example of radiobiological optimization, for the case of a non-small cell lung tumour. This was created by ourselves by coding an objective function involving the Marsden TCP and LKB NTCP models inside the Pinnacle Research Interface (PHILIPS Oncology Systems) [65]. The parameters used were the same as in the “Level-II” example described earlier. The resulting (cumulative) DVHs are shown in Figure 7.

In searching for the highest TCP for a fixed NTCP the optimiser creates beams with a higher intensity in the centre (not shown explicitly here) resulting in nonuniform distributions in the PTV and the GTV; the corresponding DVHs are labelled as “Bio-Plan (isotoxic)” in the figure. There is a significant TCP increase while the DVHs for the “paired” lung minus the GTV (“uninvolved” lung) for the standard and radiobiologically optimized plans are virtually identical, thus demonstrating that the optimizer was able to keep the NTCP virtually constant. The much lower TCP calculated for the PTV, which is a somewhat artificial result, is a result of two factors: firstly and obviously the PTV volume is considerably larger than that for the GTV thus automatically reducing the TCP, but secondly the dose inhomogeneity in the PTV is very much greater. This serves to emphasize that if this strategy is to be implemented clinically then it will be very important to minimize tumour motion, due principally to respiration. Witte et al. [66] describe a sophisticated implementation of level-III BIOP involving not only TCP and NTCP but also the effect of random and systematic errors; their software platform was also the Pinnacle Research Interface.

Engelsman et al. [67] showed that departing from a uniform dose to lung tumours could result in an increase in the therapeutic ratio. Their approach was much less sophisticated than radiobiological inverse planning; they explored the effect of reducing the field sizes, and thus PTV-CTV margin, thereby causing the dose in the tumour to be inhomogeneous. Simultaneously they increased the beam monitor units for all the beams in order to keep the NTCP constant. The tumour EUD, which is closely correlated with the TCP, went through a maximum at a margin size far below the one generally recommended. Similar results were obtained by Baker et al. [68] and by Popescu et al. [69]. In the latter case 4DCT images, reconstructed over the respiration cycle, were used as input to the Pinnacle research TPS, which accumulated the doses in each voxel as the images were deformed by respiration. It was found that the margin width yielding the *highest* TCP for *constant* NTCP for the uninvolved lung (all the doses were rescaled for each case) was around 5 mm, compared to the standard clinical choice of 15 mm. The above three approaches could be classed as “forward-planned radiobiological optimization,” though they belong to “Level III” as they involve modifications to the treatment plan in order to increase the TCP.

A fixed number of fractions has been assumed in these examples of level-III radiobiological optimization. This need not be the case, though it is difficult to see how the number of fractions, n_{frac} , can be added as an independent variable in the inverse planning procedure, as the values of TCP and NTCP for a given dose depend on n_{frac} . This means that the inverse optimization would need to be performed several times, varying n_{frac} each time. One possible strategy to reduce the number of iterations could be to choose a standard number of fractions, say 20, perform the radiobiological optimization, and export the DVHs to *BioSuite*. Then a TCP versus n_{frac} curve (similar to those of Figures 5 and 6) could suggest an optimum value of n_{frac} which could be fed back

to the TPS and the inverse radiobiological optimizer then re-run with this modified numbers of fractions.

3.5. Level IV BIOP—Adding Patient-Specific Information from Functional Imaging. Currently a great deal of attention is being devoted to how information on individual tumour “biology” revealed by function imaging can be used for modifying the dose to the specific regions of the target (e.g., [69–73]). If the particular tumour property being imaged is related to clonogen density then it makes obvious sense to boost the dose to the identified subvolumes. Similarly if the images can be translated into the degree of hypoxia then the radiosensitivity in the TCP model can be suitably modified. The descriptive term “dose painting” has entered the radiotherapy lexicon to describe the various approaches being tried.

We describe below our own work with intermediate- and high-risk prostate tumours. The dominant interprostatic lesions (DILs) are identified using a combination of diffusion-weighted MR, choline PET and template biopsies. Our BIOPROP protocol makes use of our PRI-based radiobiological inverse planning (see previous section on Level III BIOP). The objective function attempts to maximise the TCP in the DILs (see Figure 8) while keeping the NTCP for the rectum below 7%, for each of two distinct endpoints, bleeding and faecal incontinence. Additionally there are physical dose constraints of 74 Gy minimum dose outside the DILs but inside the PTV and a maximum urethral dose of 74 Gy. To date we have delivered a small number of pilot treatments in 37 fractions.

The Pinnacle Research Interface (PRI) cannot be used clinically. Prostate tumours are currently treated at Clatterbridge using *RapidArc* (VARIAN) which is a form of rotational IMRT [9] planned on the Eclipse (VARIAN) TPS [74]. Consequently we wanted to deliver our inverse radiobiologically optimised dose painting plans using *RapidArc*. Our solution was to transfer the PRI-derived DVHs to the Eclipse TPS and use these to drive the *RapidArc* optimizer. An example of the resulting DVHs is shown in Figure 8.

It can be noted that the DIL DVH for the *RapidArc* plan corresponds to a more homogeneous dose (between 80 and 83 Gy) than that for the Pinnacle plan, which was created using 11 fixed IM fields. This is because it was not possible to ask the *RapidArc* optimizer to “maximize the TCP”. However, the effect is only to reduce the TCP by 1.5%. Our analysis of the first 5 BioProp treatments indicates an average TCP = 84.7% corresponding to maximum doses in the DILs from 82.4 to 87.4 Gy, compared to TCP = 70–71% for the standard 74 Gy treatment (parameters assumed in the TCP model: $\bar{\alpha} = 0.262 \text{ Gy}^{-1}$, $\sigma_{\alpha} = 0.045 \text{ Gy}^{-1}$, $\alpha/\beta = 10$, $\rho_{\text{clon}} = 10^7 \text{ cm}^{-3}$; these were obtained from a fit to the clinical outcomes reported by Dearnaley et al. [75]).

3.6. Level V BIOP—Adding Individual Patient Biology to any of the above Levels. As far as we are aware there are no specific examples in the literature of either *in silico* or clinical studies of this further refinement of radiobiological optimization strategies. As discussed earlier, the currently

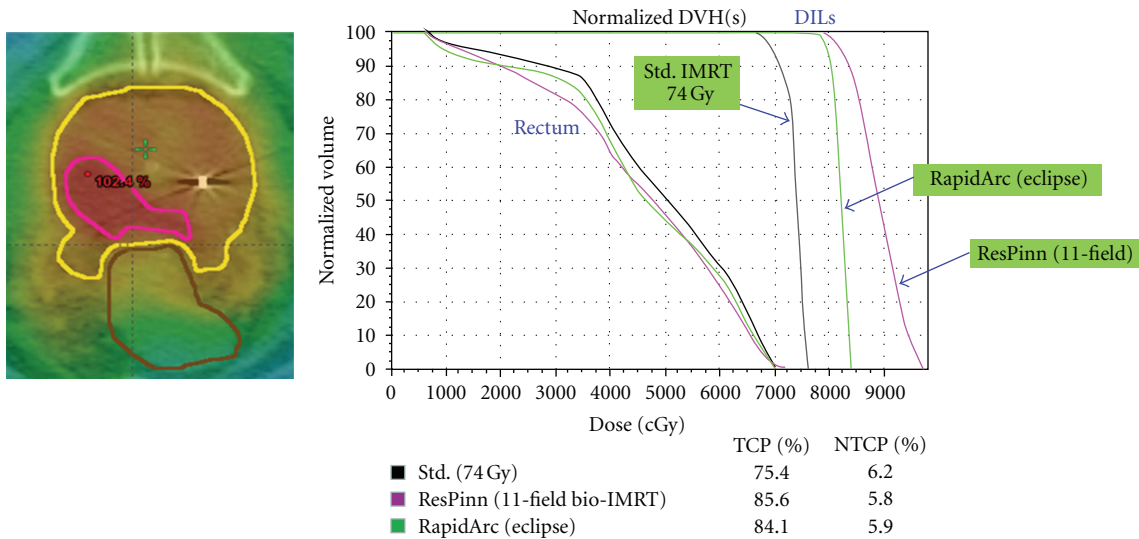


FIGURE 8: An example of a treatment under the Clatterbridge BIOPROP radiobiologically optimized prostate dose-painting protocol. The DIL is shown in pink on the left. The DVHs for the standard and dose painting plans are shown on the right. The TCP values are computed assuming that all the clonogens are contained in the DIL (or that any clonogens outside are 100% controlled). The NTCP values shown in the table correspond to rectal bleeding.

used TCP and NTCP models are hybrids in the sense that whilst they make predictions for a specific treatment plan (to be precise for the DVHs computed from the plan) they effectively do so for a population of patients with that specific treatment plan. Thus what $TCP = 65\%$ means is that 65 out of 100 patients will have a tumour of that size controlled by the dose distribution in question. If, however, we knew the radiosensitivity of the tumour clonogens for the patient undergoing treatment [20], then this prediction would be overwhelmingly converted into either one or zero that is, controlled/not controlled, with the TCP increasingly rapidly from zero to unity over a very narrow range of doses [18, 21, 22]. This information would then enable us to choose the lowest prescription dose still achieving say $TCP > 99\%$. Equally well, a prediction of a complication rate of say 6.0% means that for that specific dose distribution in the normal tissue in question, 6 out of 100 patients will experience the complication. Were we to possess information on the individual biology of the patient this prediction would in principle be narrowed down to either a very low (possibly zero) probability or a very high one. These issues have been explored by, amongst others, Lambin et al. [76] and Rutkowska [77].

Tucker et al. [78] showed that single nucleotide polymorphisms (SNPs) can significantly improve the ability of the Lyman MLD model to predict the incidence of radiation pneumonitis. In a study on clinical risk factors the same group showed that the generalized Lyman model with patient smoking status taken into account produced NTCP estimates up to 27 percentage points different from the model based on dose-volume factors alone [79]. Valdagni et al. [80] attempted to understand why, despite “excellent” rectal dose-volume histograms (DVHs), certain patients treated for prostate cancer exhibited late rectal bleeding (LRB) whereas

others with “poor” DVHs did not. Thirty-five genes involved in DNA repair/radiation response were analyzed. It was found that nine genes were significantly down-regulated in the low-risk bleeder group versus the high-risk bleeder and high-risk non-bleeder groups; four genes were significantly upregulated in the high-risk non-bleeder group compared to the other groups. It is to be hoped that studies such as these will result in the NTCP models capable of making different predictions for “biologically different” patients having very similar DVHs, and ultimately in the incorporation of such improved models into the various levels of radiobiological optimization discussed here [81, 82].

4. Summary and Conclusions

The recent AAPM task group report on the use and QA of biologically related models for treatment planning [83] stated in the Introduction:

Until recently, the quality of a RT plan has been judged by physical quantities, that is, dose and dose-volume (DV) parameters, thought to correlate with biological response rather than by estimates of the biological outcome itself. It is widely recognized that the DV criteria, which are merely surrogate measures of biological responses, should be replaced by biological indices in order for the treatment process to more closely reflect clinical goals of RT. Developments in our understanding of advantages and limitations of existing dose-response models begin to allow the incorporation of biological concepts into a routine treatment planning process.

This paper has proposed several ways (or levels) in which the “biological indices” TCP and NTCP can be incorporated directly into the treatment planning process, not merely in order to evaluate and compare rival plans (e.g., Iori et al. [84]), but to *optimize* treatment plans in terms of the prescription dose and number of fractions, thereby improving clinical outcomes. As a result of much careful research, summarized in the QUANTEC (QUAntitative Analysis of Normal Tissue Effects in the Clinic) series of papers [85], the predictions of especially the widely applied and researched Lyman-Kutcher-Burman NTCP model [23, 24] are now sufficiently reliable for certain important organs/tissues and endpoints (rectal bleeding [86], pneumonitis [55], radiation-induced liver disease, xerostomia in the parotid glands, possibly also cardiac complications [87]) that treatment protocols involving “isotoxic” tumour dose individualization can be developed and applied [17, 33, 34, 44]. Software such as *BioSuite* [53] makes this straightforward as long as only prescription dose *rescaling* and/or fraction number customization is involved. In order to plan and deliver radiobiologically based IMRT, however, treatment planning systems must incorporate TCP and NTCP into the objective functions; at the time of writing full-blown radiobiological inverse planning is possible in at most two of the commercial systems [64, 83], though planning based on gEUD [27] is more widely available.

By taking full advantage of the steadily improving degree of conformality achievable with modern techniques, the individualization of fractionation (towards fewer fractions) has huge radiobiological potential. Furthermore, hypofractionation also delivers increased patient convenience and a reduction in cost per treatment course, which could be especially important for proton therapy [13]. Two notes of caution are in order however. Firstly the methods and models employed to generate much of the data in this paper (e.g., Figures 4, 5 and 6) are either directly, in the case of the Marsden TCP model [18, 21, 22, 31], or indirectly, in the case of Lyman-Kutcher-Burman NTCP model [18, 23, 24], based on the linear-quadratic expression linking (cell) surviving fraction and absorbed dose [41, 45–50, 88]. At doses per fraction above ≈ 10 Gy, however, the so-called *generalized* linear quadratic model proposed by Wang et al. [89] and by Carlone et al. [90] may be more correct, though this is by no means universally accepted [91]. Whatever the “truth” eventually turns out to be, if the LQ model does overpredict cell killing at very large fraction sizes then at such doses per fraction LQ-based radiobiological models will result in an *overprediction* of NTCP but an *underprediction* of TCP. Consequently the resulting hypofractionation schemes are highly unlikely to cause excessive complication rates [58]. Secondly, regarding proton-beam radiotherapy there is an added complication that is (thankfully!) not present when considering low-LET modalities (which include the bremsstrahlung photon beams produced in linear accelerators): the biological effect of a given number of Grays of absorbed dose is not the same everywhere in the patient (or in a phantom); it depends on the proton energy spectrum [92–94]. Though this dependence of proton RBE on energy and hence on depth, and therefore position in the patient,

probably never exceeds $\approx 10\%$, Dale et al. [93] have pointed out that a 10% uncertainty in RBE is precisely equivalent to a 10% uncertainty in dose in photon treatment plans, which would not be tolerated. Therefore more research is required on proton RBE variation [92, 93].

In conclusion, if today’s sophisticated imaging, treatment planning and radiation-delivery techniques, and tomorrow’s genome-based patient biology are to be translated into maximum clinical benefit then the stipulation of a fixed dose to the target volume in today’s treatment protocols must be replaced by *individualized doses*, and, in certain situations, *individualized fractionation*. In the right hands biomathematical models of radiation effect are powerful tools [95, 96]; to paraphrase Chapman and Gillespie [97], let’s use them!

Acknowledgments

Among the many colleagues who have contributed significantly to the ideas and the work described in this paper the authors would especially like to mention Beatriz Sanchez-Nieto, Giovanna Gagliardi, Mauro Iori, Aswin Hoffmann, Zafar Malik, Chinnamani Eswar, Jason Lester, Isabel Syndikus, Diana Tait, Colin Baker, John Fenwick, Eva Rutkowska, Vanessa Panettieri, Philip Mayles, Don Chapman, Gordon Steel, Roger Dale, Charlie Deehan, Jack Fowler, Marco Carlone, Pavel Stavrev, Marnix Witte, Joe Deasy, Ruggero Ruggieri, Marco Schwarz, Claudio Fiorino, Stefano Gianolini, and Riccardo Valdagni. They also wish to thank Kjell Eriksson of RaySearch AB for the use of ORBIT and Philips Oncology Systems for the use of the Pinnacle Research Interface.

References

- [1] L. Loverock, “Linear accelerators, ch. 36,” in *Handbook of Radiotherapy Physics. Theory and Practice*, P. Mayles, A. Nahum, and J. C. Rosenwald, Eds., pp. 197–239, Taylor & Francis, London, UK, 2007.
- [2] A. Neal, “Patient data acquisition, ch. 30,” in *Handbook of Radiotherapy Physics. Theory and Practice*, P. Mayles, A. Nahum, and J. C. Rosenwald, Eds., pp. 647–655, Taylor & Francis, London, UK, 2007.
- [3] M. Bidmead and J. C. Rosenwald, “Dose evaluation of treatment plans, ch. 35,” in *Handbook of Radiotherapy Physics. Theory and Practice*, P. Mayles, A. Nahum, and J. C. Rosenwald, Eds., pp. 719–729, Taylor & Francis, London, UK, 2007.
- [4] P. Mayle and P. Williams, “Megavoltage photon beams, ch. 22,” in *Handbook of Radiotherapy Physics. Theory and Practice*, P. Mayles, A. Nahum, and J. C. Rosenwald, Eds., pp. 451–481, Taylor & Francis, London, UK, 2007.
- [5] D. M. Tait, A. E. Nahum, L. C. Meyer et al., “Acute toxicity in pelvic radiotherapy; a randomised trial of conformal versus conventional treatment,” *Radiotherapy and Oncology*, vol. 42, no. 2, pp. 121–136, 1997.
- [6] I. Lax and A. Brahme, “Rotation therapy using a novel high-gradient filter,” *Radiology*, vol. 145, no. 2, pp. 473–478, 1982.
- [7] A. Brahme, J. E. Roos, and I. Lax, “Solution of an integral equation encountered in rotation therapy,” *Physics in Medicine and Biology*, vol. 27, no. 10, pp. 1221–1229, 1982.

- [8] “Conformal and intensity-modulated radiotherapy,” in *Handbook of Radiotherapy Physics Theory and Practice*, S. Webb, Ed. P. Mayles, A. Nahum, and J. C. Rosenwald, Eds., pp. 943–985, Taylor & Francis, London, UK, 2007.
- [9] M. Iori, M. Paiusco, E. Cagni et al., “The intensity modulated multiple arc (imma) technique: forward & inverse planned procedures to deliver hypofractionated imat treatments,” *Current Radiopharmaceuticals*, vol. 2, no. 3, pp. 149–159, 2009.
- [10] C. Mubata, “Portal imaging devices, ch. 14,” in *Handbook Of Radiotherapy Physics. Theory And Practice*, P. Mayles, A. Nahum, and J. C. Rosenwald, Eds., pp. 261–269, Taylor & Francis, London, UK, 2007.
- [11] D. A. Jaffray, J. H. Siewerdsen, J. W. Wong, and A. A. Martinez, “Flat-panel cone-beam computed tomography for image-guided radiation therapy,” *International Journal of Radiation, Oncology, Biology, Physics*, vol. 53, no. 5, pp. 1337–1349, 2002.
- [12] A. J. Lomax, T. Böhringer, A. Bolsi et al., “Treatment planning and verification of proton therapy using spot scanning: initial experiences,” *Medical Physics*, vol. 31, no. 11, pp. 3150–3157, 2004.
- [13] H. Nyström, “The role of protons in modern and biologically-guided radiotherapy,” *Acta Oncologica*, vol. 49, no. 7, pp. 1124–1131, 2010.
- [14] J. M. Schippers and A. J. Lomax, “Emerging technologies in proton therapy,” *Acta Oncologica*, vol. 50, no. 6, pp. 838–850, 2011.
- [15] E. Roelofs, M. Engelsman, and C. Rasch, “Results of a multicentric in silico clinical trial (ROCOCO): comparing radiotherapy with photons and protons for non-small cell lung cancer,” *Journal of Thoracic Oncology*, vol. 7, pp. 165–176, 2012.
- [16] G. A. Viani, E. J. Stefano, and S. L. Afonso, “Higher-than-conventional radiation doses in localized prostate cancer treatment: a meta-analysis of randomized, controlled trials,” *International Journal of Radiation, Oncology, Biology, Physics*, vol. 74, no. 5, pp. 1405–1418, 2009.
- [17] A. L. Hoffmann, E. G. C. Troost, H. Huizenka, J. H. A. M. Kaanders, and J. Bussink, “Individualized dose prescription for hypofractionation in advanced non-small-cell lung cancer radiotherapy: an *in silico* trial,” *International Journal of Radiation Oncology, Biology, Physics*, vol. 83, pp. 1596–1602, 2012.
- [18] A. Nahum and G. Kutcher, “Biological evaluation of treatment plans, ch. 36,” in *Handbook of Radiotherapy Physics Theory and Practice*, P. Mayles, A. Nahum, and J. C. Rosenwald, Eds., pp. 731–771, Taylor & Francis, London, UK, 2007.
- [19] A. Jackson, L. B. Marks, S. M. Bentzen et al., “The Lessons of QUANTEC: recommendations for reporting and gathering data on dose-volume dependencies of treatment outcome,” *International Journal of Radiation Oncology, Biology, Physics*, vol. 76, no. 3, pp. S155–S160, 2010.
- [20] C. M. L. West, “Intrinsic radiosensitivity as a predictor of patient response to radiotherapy,” *British Journal of Radiology*, vol. 68, no. 812, pp. 827–837, 1995.
- [21] S. Webb and A. E. Nahum, “A model for calculating tumour control probability in radiotherapy including the effects of inhomogeneous distributions of dose and clonogenic cell density,” *Physics in Medicine and Biology*, vol. 38, no. 6, pp. 653–666, 1993.
- [22] A. E. Nahum and B. Sanchez-Nieto, “Tumour control probability modelling: basic principles and applications in treatment planning,” *Physica Medica*, vol. 17, no. 2, pp. 13–23, 2001.
- [23] J. T. Lyman, “Complication probability as assessed from dose-volume histograms,” *Radiation Research*, vol. 104, no. 2, pp. S13–S19, 1985.
- [24] G. J. Kutcher, C. Burman, L. Brewster, M. Goitein, and R. Mohan, “Histogram reduction method for calculating complication probabilities for three-dimensional treatment planning evaluations,” *International Journal of Radiation Oncology, Biology, Physics*, vol. 21, no. 1, pp. 137–146, 1991.
- [25] A. Niemierko, “Reporting and analyzing dose distributions: a concept of equivalent uniform dose,” *Medical Physics*, vol. 24, no. 1, pp. 103–110, 1997.
- [26] M. A. Ebert, “Viability of the EUD and TCP concepts as reliable dose indicators,” *Physics in Medicine and Biology*, vol. 45, no. 2, pp. 441–457, 2000.
- [27] A. Niemierko, “A generalized concept of equivalent uniform dose (EUD),” *Medical Physics*, vol. 26, p. 1101, 1999.
- [28] S. L. S. Kwa, J. V. Lebesque, J. C. M. Theuvs et al., “Radiation pneumonitis as a function of mean lung dose: an analysis of pooled data of 540 patients,” *International Journal of Radiation Oncology, Biology, Physics*, vol. 42, no. 1, pp. 1–9, 1998.
- [29] P. Källman, A. Agren, and A. Brahme, “Tumour and normal tissue responses to fractionated non-uniform dose delivery,” *International Journal of Radiation Biology*, vol. 62, no. 2, pp. 249–262, 1992.
- [30] T. S. Lawrence, R. J. Tesser, and R. K. Ten Haken, “An application of dose volume histograms to the treatment of intrahepatic malignancies with radiation therapy,” *International Journal of Radiation Oncology, Biology, Physics*, vol. 19, no. 4, pp. 1041–1047, 1990.
- [31] A. E. Nahum and D. M. Tait, “Maximising local control by customised dose prescription for pelvic tumours,” in *Advanced Radiation Therapy: Tumour Response Monitoring and Treatment Planning*, A. Breit, Ed., pp. 425–431, Springer, Heidelberg, Germany, 1992.
- [32] B. Sanchez-Nieto, A. E. Nahum, and D. P. Dearnaley, “Individualization of dose prescription based on normal-tissue dose-volume and radiosensitivity data,” *International Journal of Radiation Oncology, Biology, Physics*, vol. 49, no. 2, pp. 487–499, 2001.
- [33] A. Van Baardwijk, S. Wanders, L. Boersma et al., “Mature results of an individualized radiation dose prescription study based on normal tissue constraints in stages I to III non-small-cell lung cancer,” *Journal of Clinical Oncology*, vol. 28, no. 8, pp. 1380–1386, 2010.
- [34] J. D. Fenwick, A. E. Nahum, Z. I. Malik et al., “Escalation and intensification of radiotherapy for stage III non-small cell lung cancer: opportunities for treatment improvement,” *Clinical Oncology*, vol. 21, no. 4, pp. 343–360, 2009.
- [35] K. De Jaeger, M. S. Hoogeman, M. Engelsman et al., “Incorporating an improved dose-calculation algorithm in conformal radiotherapy of lung cancer: re-evaluation of dose in normal lung tissue,” *Radiotherapy and Oncology*, vol. 69, no. 1, pp. 1–10, 2003.
- [36] Z. Malik and C. Eswar, “Clinical audit of NSCLC radiotherapy outcomes at Clatterbridge Centre for Oncology,” unpublished.
- [37] A. E. Nahum, J. Uzan, P. Jain, Z. I. Malik, J. D. Fenwick, and C. Baker, “Quantitative tumour control predictions for the radiotherapy of non-small-cell lung tumours,” *Medical Physics*, vol. 38, 1, article 3641 pages, 2011.
- [38] Z. Malik, C. Eswar, J. Dobson, J. Fenwick, and A. E. Nahum, “Dose-individualisation for lung cancer radiotherapy—are we ready?” *Lung Cancer*, vol. 57, no. 1, supplement, pp. S8–S9, 2007.

- [39] M. K. Martel, R. K. Ten Haken, M. B. Hazuka et al., "Estimation of tumor control probability model parameters from 3-D dose distributions of non-small cell lung cancer patients," *Lung Cancer*, vol. 24, no. 1, pp. 31–37, 1999.
- [40] M. Saunders, S. Dische, A. Barrett, A. Harvey, G. Griffiths, and M. Parmar, "Continuous, hyperfractionated, accelerated radiotherapy (CHART) versus conventional radiotherapy in non-small cell lung cancer: mature data from the randomised multicentre trial," *Radiotherapy and Oncology*, vol. 52, no. 2, pp. 137–148, 1999.
- [41] H. R. Withers, H. D. Thames, and L. J. Peters, "A new isoeffect curve for change in dose per fraction," *Radiotherapy and Oncology*, vol. 1, no. 2, pp. 187–191, 1983.
- [42] R. Calandrino, S. Broggi, G. M. Cattaneo, C. Fiorino, A. E. Nahum, and F. Fazio, "Some radiobiological considerations on the potential of IMRT in non-standard fractionation," *Radiotherapy & Oncology*, vol. 76, p. S23, 2005.
- [43] V. Panettieri, Z. I. Malik, C. V. Eswar et al., "Influence of dose calculation algorithms on isotoxic dose-escalation of non-small cell lung cancer radiotherapy," *Radiotherapy and Oncology*, vol. 97, no. 3, pp. 418–424, 2010.
- [44] J. Lester, L. Nixon, P. Mayles et al., "The I-START Trial: ISoToxic accelerated radiotherapy in locally advanced non-small cell lung cancer, 2012 The I-START Trial: ISoToxic accelerated radiotherapy in locally advanced non-small cell lung cancer," *Lung Cancer*, vol. 75, no. 1, supplement, p. S51, 2012.
- [45] H. D. Thames and J. H. Hendry, *Fractionation in Radiotherapy*, Taylor & Francis, London, UK, 1987.
- [46] G. Steel, "Dose fractionation in radiotherapy, ch. 9," in *Handbook of Radiotherapy Physics Theory and Practice*, P. Mayles, A. Nahum, and J. C. Rosenwald, Eds., pp. 163–182, Taylor & Francis, London, UK, 2007.
- [47] M. C. Joiner and S. M. Bentzen, "Fractionation: the linear quadratic approach," in *Basic Clinical Radiobiology*, M. Joiner and A. van der Kogel, Eds., pp. 102–119, Hodder Arnold, 4th edition, 2009.
- [48] R. G. Dale, "The application of the linear-quadratic dose-effect equation to fractionated and protracted radiotherapy," *British Journal of Radiology*, vol. 58, no. 690, pp. 515–528, 1985.
- [49] J. F. Fowler, "21 Years of biologically effective dose," *British Journal of Radiology*, vol. 83, no. 991, pp. 554–568, 2010.
- [50] S. M. Bentzen and M. C. Joiner, "The linear quadratic approach in clinical practice," in *Basic Clinical Radiobiology*, M. Joiner and A. van der Kogel, Eds., pp. 120–134, Hodder Arnold, 4th edition, 2009.
- [51] A. E. Nahum and J. D. Chapman, "The interaction between tissue radiobiological properties ("architecture"), dose distribution and optimal fraction size—profound implications for conformal and heavy-particle radiation therapy," *International Journal of Radiation Oncology, Biology, Physics*, vol. 55, p. 446, 2003.
- [52] I. S. Vogelius, D. C. Westerly, G. M. Cannon, and S. M. Bentzen, "Hypofractionation does not increase radiation pneumonitis risk with modern conformal radiation delivery techniques," *Acta Oncologica*, vol. 49, no. 7, pp. 1052–1057, 2010.
- [53] J. Uzan and A. E. Nahum, "Radiobiologically guided optimisation of the prescription dose and fractionation scheme using BioSuite," *British Journal of Radiology*, vol. 85, pp. 1279–1286, 2012.
- [54] J. F. Fowler, W. A. Tomé, J. D. Fenwick, and M. P. Mehta, "A challenge to traditional radiation oncology," *International Journal of Radiation Oncology, Biology, Physics*, vol. 60, no. 4, pp. 1241–1256, 2004.
- [55] L. B. Marks, S. M. Bentzen, J. O. Deasy et al., "Radiation dose-volume effects in the lung," *International Journal of Radiation Oncology, Biology, Physics*, vol. 76, no. 3, pp. S70–S76, 2010.
- [56] I. Lax, H. Blomgren, I. Naslund, and R. Svanstrom, "Stereotactic radiotherapy of malignancies in the abdomen. Methodological aspects," *Acta Oncologica*, vol. 33, no. 6, pp. 677–683, 1994.
- [57] P. Baumann, J. Nyman, M. Hoyer et al., "Outcome in a prospective phase II trial of medically inoperable stage I non-small-cell lung cancer patients treated with stereotactic body radiotherapy," *Journal of Clinical Oncology*, vol. 27, no. 20, pp. 3290–3296, 2009.
- [58] B. M. Wennberg, P. Baumann, G. Gagliardi et al., "NTCP modelling of lung toxicity after SBRT comparing the universal survival curve and the linear quadratic model for fractionation correction," *Acta Oncologica*, vol. 50, no. 4, pp. 518–527, 2011.
- [59] M. Schwarz, M. Alber, J. V. Lebesque, B. J. Mijnheer, and E. M. F. Damen, "Dose heterogeneity in the target volume and intensity-modulated radiotherapy to escalate the dose in the treatment of non-small-cell lung cancer," *International Journal of Radiation Oncology, Biology, Physics*, vol. 62, no. 2, pp. 561–570, 2005.
- [60] M. Iori, "Methods for physical and radiobiological optimisation in radiotherapy with intensity modulation," *Physica Medica*, vol. 17, no. 2, pp. 55–73, 2001.
- [61] A. Brahme, "Individualizing cancer treatment: biological optimisation models in treatment and planning," *International Journal of Radiation Oncology, Biology, Physics*, vol. 49, pp. 327–337, 2001.
- [62] J. A. Peñagaricano, N. Papanikolaou, C. Wu, and Y. Yan, "An assessment of Biologically-based Optimization (BORT) in the IMRT era," *Medical Dosimetry*, vol. 30, no. 1, pp. 12–19, 2005.
- [63] A. L. Hoffmann, D. Den Hertog, A. Y. D. Siem, J. H. A. M. Kaanders, and H. Huizenga, "Convex reformulation of biologically-based multi-criteria intensity-modulated radiation therapy optimization including fractionation effects," *Physics in Medicine and Biology*, vol. 53, no. 22, pp. 6345–6362, 2008.
- [64] V. A. Semenenko, B. Reitz, E. Day, X. S. Qi, M. Miften, and X. A. Li, "Evaluation of a commercial biologically based IMRT treatment planning system," *Medical Physics*, vol. 35, no. 12, pp. 5851–5860, 2008.
- [65] J. Uzan, A. E. Nahum, P. Mayles, and I. Syndikus, "Radiobiologically-based inverse optimisation of IMRT plans for prostate cancer," *Radiotherapy & Oncology*, vol. 96, no. 1, supplement, p. S178, 2010.
- [66] M. G. Witte, J. Van Der Geer, C. Schneider, J. V. Lebesque, M. Alber, and M. Van Herk, "IMRT optimization including random and systematic geometric errors based on the expectation of TCP and NTCP," *Medical Physics*, vol. 34, no. 9, pp. 3544–3555, 2007.
- [67] M. Engelsman, P. Remeijer, M. Van Herk, J. V. Lebesque, B. J. Mijnheer, and E. M. F. Damen, "Field size reduction enables Iso-NTCP escalation of tumor control probability for irradiation of lung tumors," *International Journal of Radiation Oncology, Biology, Physics*, vol. 51, no. 5, pp. 1290–1298, 2001.
- [68] M. Baker, M. Nielsen, O. Hansen, J. W. Jahn, S. Korreman, and C. Brink, "Isotoxic dose escalation in the treatment of lung cancer by means of heterogeneous dose distributions in the presence of respiratory motion," *International Journal of Radiation Oncology, Biology, Physics*, vol. 81, pp. 849–555, 2011.

- [69] I. A. Popescu, M. Chadrasekaran, J. Uzan et al., “Radiobiological optimisation of 4D NSCL plans: small margins yield highest TCP for moving tumours,” *Radiotherapy & Oncology*, vol. 96, no. 1, supplement, p. S178, 2010.
- [70] Y. Kim and W. A. Tomé, “Dose-painting IMRT optimization using biological parameters,” *Acta Oncologica*, vol. 49, no. 8, pp. 1374–1384, 2010.
- [71] S. M. Bentzen and V. Gregoire, “Molecular imaging-based dose painting: a novel paradigm for radiation therapy prescription,” *Seminars in Radiation Oncology*, vol. 21, no. 2, pp. 101–110, 2011.
- [72] Å. Søvik, E. Malinen, Ø. S. Bruland, S. M. Bentzen, and D. R. Olsen, “Optimization of tumour control probability in hypoxic tumours by radiation dose redistribution: a modelling study,” *Physics in Medicine and Biology*, vol. 52, no. 2, pp. 499–513, 2007.
- [73] M. Iori, A. Botti, M. Paiusco et al., “18F-fluorocholine (F-CHO) PET-guided dose painting of prostate tumours using either TCP or EUD optimized to account for spatial clonogen redistribution,” *Radiotherapy & Oncology*, vol. 96, no. 1, supplement, p. S125, 2010.
- [74] K. Otto, “Volumetric modulated arc therapy: IMRT in a single gantry arc,” *Medical Physics*, vol. 35, no. 1, pp. 310–317, 2008.
- [75] D. P. Dearnaley, M. R. Sydes, J. D. Graham et al., “Escalated-dose versus standard-dose conformal radiotherapy in prostate cancer: first results from the MRC RT01 randomised controlled trial,” *Lancet Oncology*, vol. 8, no. 6, pp. 475–487, 2007.
- [76] P. Lambin, S. F. Petit, H. J. W. L. Aerts et al., “The ESTRO Breur lecture 2009. from population to voxel-based radiotherapy: exploiting intra-tumour and intra-organ heterogeneity for advanced treatment of non-small cell lung cancer,” *Radiotherapy and Oncology*, vol. 96, no. 2, pp. 145–152, 2010.
- [77] E. Rutkowska, *Mechanistic Simulation of Normal-Tissue Damage during Radiotherapy [Ph.D. thesis]*, University of Liverpool, 2010.
- [78] S. L. Tucker, M. Li, T. Xu et al., “Incorporating single-nucleotide polymorphisms into the Lyman model to improve prediction of radiation pneumonitis,” *International Journal of Radiation Oncology, Biology, Physics*. In press.
- [79] S. L. Tucker, H. H. Liu, Z. Liao et al., “Analysis of radiation pneumonitis risk using a generalized Lyman model,” *International Journal of Radiation Oncology, Biology, Physics*, vol. 72, no. 2, pp. 568–574, 2008.
- [80] R. Valdagni, T. Rancati, M. Ghilotti et al., “To bleed or not to bleed. A prediction based on individual gene profiling combined with dose-volume histogram shapes in prostate cancer patients undergoing three-dimensional conformal radiation therapy,” *International Journal of Radiation Oncology, Biology, Physics*, vol. 74, no. 5, pp. 1431–1440, 2009.
- [81] T. Rancati, C. Fiorino, G. Fellin et al., “Inclusion of clinical risk factors into NTCP modelling of late rectal toxicity after high dose radiotherapy for prostate cancer,” *Radiotherapy and Oncology*, vol. 100, pp. 124–130, 2011.
- [82] C. M. L. West, R. M. Elliott, and N. G. Burnet, “The genomics revolution and radiotherapy,” *Clinical Oncology*, vol. 19, no. 6, pp. 470–480, 2007.
- [83] X. Allen Li, M. Alber, and J. O. Deasy, “The use and QA of biologically related models for treatment planning: short report of the TG-166 of the therapy physics committee of the AAPM,” *Medical Physics*, vol. 39, pp. 1386–1409, 2012.
- [84] M. Iori, G. M. Cattaneo, E. Cagni et al., “Dose-volume and biological-model based comparison between helical tomotherapy and (inverse-planned) IMAT for prostate tumours,” *Radiotherapy and Oncology*, vol. 88, no. 1, pp. 34–45, 2008.
- [85] QUANTEC, *International Journal of Radiation Oncology, Biology, Physics*, vol. 76, no. 3, supplement, 2010.
- [86] C. Fiorino, R. Valdagni, T. Rancati, and G. Sanguineti, “Dose-volume effects for normal tissues in external radiotherapy: pelvis,” *Radiotherapy and Oncology*, vol. 93, no. 2, pp. 153–167, 2009.
- [87] G. Gagliardi, L. S. Constine, V. Moiseenko et al., “Radiation dose-volume effects in the heart,” *International Journal of Radiation Oncology, Biology, Physics*, vol. 76, no. 3, pp. S77–S85, 2010.
- [88] J. D. Chapman, “Single-hit mechanism of tumour cell killing by radiation,” *International Journal of Radiation Biology*, vol. 79, no. 2, pp. 71–81, 2003.
- [89] J. Z. Wang, Z. Huang, S. S. Lo, W. T. C. Yuh, and N. A. Mayr, “A generalized linear-quadratic model for radio-surgery, stereotactic body radiation therapy, and high-dose rate brachytherapy,” *Science Translational Medicine*, vol. 2, no. 39, p. 39ra48, 2010.
- [90] M. Carlone, D. Wilkins, P. Raaphorst, M. Guerrero, and X. A. Li, “The modified linear-quadratic model of Guerrero and Li can be derived from a mechanistic basis and exhibits linear-quadratic-linear behaviour,” *Physics in Medicine and Biology*, vol. 50, no. 10, pp. L9–L15, 2005.
- [91] J. P. Kirkpatrick, D. J. Brenner, and C. G. Orton, “The linear-quadratic model is inappropriate to model high dose per fraction effects in radiosurgery,” *Medical Physics*, vol. 36, no. 8, pp. 3381–3384, 2009.
- [92] N. Tilly, *Radiobiological investigations of proton and light ion therapy [Ph.D. thesis]*, University of Stockholm, 2002.
- [93] R. G. Dale, B. Jones, and A. Cárabe-Fernández, “Why more needs to be known about RBE effects in modern radiotherapy,” *Applied Radiation and Isotopes*, vol. 67, no. 3, pp. 387–392, 2009.
- [94] A. Nahum, G. Gagliardi, and A. Kacperek, “How should we apply biological models to heavy charged-particle treatment plans?” *Radiotherapy & Oncology*, vol. 96, no. 1, supplement, p. S537, 2010.
- [95] D. R. Wigg, *Applied Radiobiology and Bioeffect Planning*, Medical Physics Publishing, Madison, Wis, USA, 2001.
- [96] R. Dale and D. Jones, *Radiobiological Modelling in Radiation Oncology*, British Institute of Radiology, London, UK, 2007.
- [97] J. D. Chapman and C. J. Gillespie, “The power of radiation biophysics—let’s use it,” *International Journal of Radiation Oncology, Biology, Physics*, vol. 84, pp. 309–311, 2012.

Research Article

Microdosimetry for Targeted Alpha Therapy of Cancer

Chen-Yu Huang,¹ Susanna Guatelli,² Bradley M. Oborn,^{2,3} and Barry J. Allen⁴

¹ Centre for Experimental Radiation Oncology, St. George Clinical School, University of New South Wales, Kogarah, NSW 2217, Australia

² Illawarra Cancer Care Centre, Wollongong, NSW 2522, Australia

³ Centre for Medical Radiation Physics, University of Wollongong, NSW 2522, Australia

⁴ Ingham Institute of Applied Medical Research, Faculty of Medicine, University of Western Sydney, Liverpool, NSW 2170, Australia

Correspondence should be addressed to Chen-Yu Huang, cyhuangsysu@gmail.com

Received 3 July 2012; Accepted 25 July 2012

Academic Editor: Eva Bezak

Copyright © 2012 Chen-Yu Huang et al. This is an open access article distributed under the Creative Commons Attribution License, which permits unrestricted use, distribution, and reproduction in any medium, provided the original work is properly cited.

Targeted alpha therapy (TAT) has the advantage of delivering therapeutic doses to individual cancer cells while reducing the dose to normal tissues. TAT applications relate to hematologic malignancies and now extend to solid tumors. Results from several clinical trials have shown efficacy with limited toxicity. However, the dosimetry for the labeled alpha particle is challenging because of the heterogeneous antigen expression among cancer cells and the nature of short-range, high-LET alpha radiation. This paper demonstrates that it is inappropriate to investigate the therapeutic efficacy of TAT by macrodosimetry. The objective of this work is to review the microdosimetry of TAT as a function of the cell geometry, source-target configuration, cell sensitivity, and biological factors. A detailed knowledge of each of these parameters is required for accurate microdosimetric calculations.

1. Introduction

Targeted alpha therapy (TAT) can provide selective systemic radiotherapy to primary and metastatic tumors (even at a low dose rate and hypoxia region) [1]. It permits sensitive discrimination between target and normal tissue, resulting in fewer toxic side effects than most conventional chemotherapeutic drugs. Monoclonal antibodies (MAbs) that recognize tumor-associated antigens are conjugated to potent alpha emitting radionuclides to form the alpha-immunoconjugate (AIC) (Figure 1). The AIC can be administered by intralesional, orthotopic, or systemic injection. Targeted cancer cells are killed by the short-range alpha radiation, while sparing distant normal tissue cells, giving the minimal toxicity to normal tissue [2].

An alpha particle with energy of 4 to 9 MeV can deposit about 100 keV/ μm within a few cell diameters (40–90 μm), causing direct DNA double-strand breaks, which lead to cancer cell apoptosis [3]. Cell survival is relatively insensitive to the cell cycle or oxygen status for alpha radiation [4]. TAT is potent enough to eradicate disseminated cancer cells or cancer stem cells that are minimally susceptible to chemo- or

radio-resistance. The relative biological effect (RBE) of alpha particles is from 3 to 7 [5], which means that for the same absorbed dose, the acute biological effects of alpha particles are 3 to 7 times greater than the damage caused by external beam photons or beta radiation.

TAT is ideally suited to liquid cancers or micrometastases [6]. However the regression of metastatic melanoma lesions after systemic TAT in a phase I clinical trial for metastatic melanoma has broadened the application to solid tumors [7]. The observed tumor regression could not be ascribed to killing of all cancer cells in the tumors by TAT and led to the hypothesis that tumors could be regressed by a mechanism called tumor antivascular alpha therapy (TAVAT) [8]. Therapeutic efficacy relates to the extravasation of the AIC through porous tumor vascular walls and widened endothelial junctions into the perivascular space in the solid tumor. The AICs bind to antigenic sites on the membranes of pericytes and contiguous cancer cells around the capillary. The alpha-particle emitters are localized close to the vascular endothelial cells (ECs), which are irradiated by alpha particles and killed. Subsequent tumor capillary closure, causing

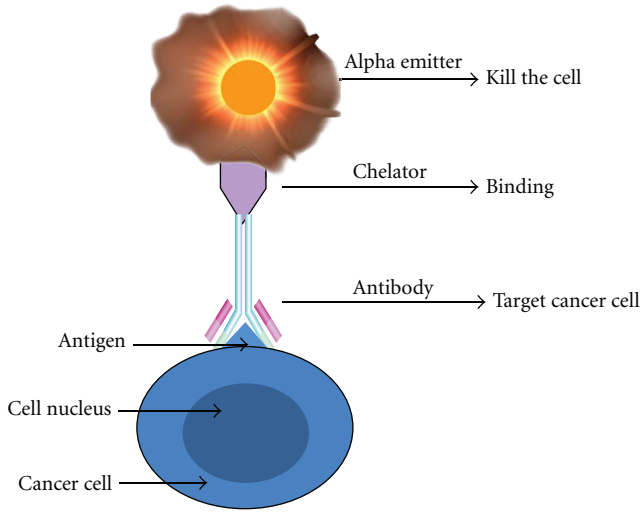


FIGURE 1: Schematic diagram of an AIC targeting a cell.

depletion of oxygen and nutrition, is the likely cause of cancer cell death and tumor regression [8, 9].

2. Microdosimetry

2.1. Microdosimetry Concept. Radiation dosimetry is the study of the physical properties of radiation energy deposition in tissue. It can be used to optimize treatments and allow comparison of different therapeutic approaches, as well as to study the basic methods of irradiation of biological matter [10]. Radiation dose in conventional external radiotherapy is a macroscopic concept. Upon the properties of the short path length alpha emissions and the spatial distribution of the radionuclide relative to the small target volumes, microdosimetry is indispensable for TAT to investigate the physical properties of radiation energy deposition in biological cells [11].

The dosimetry of TAT is distinguished from that of beta immunotherapy [12] or external beam radiotherapy in three different ways.

- (1) *Short path length of alpha particles.* The high energy of alpha particles is deposited in a short range [13]. Some cell nuclei receive multiple alpha particle hits, while others receive no hits. The amounts of energy deposited vary greatly from target to target, leading to a wide frequency distribution [14].
- (2) *Small target volume.* The alpha track length is comparable to cellular/subcellular sizes causing high LET within the small target volume. It is important to understand the differing biological effects on individual cells [15]. Given the energy delivered along an alpha-particle track and its potential cytotoxicity, the dosimetry for estimating mean absorbed dose may not always yield physically or biologically meaningful information of radiation energy deposition in biological cells. Instead, stochastic or microdosimetric methodologies may be required [16].

- (3) *Nonuniform distribution of radioisotopes.* The heterogeneous antigen expression and tumor uptake leads to variable spatial microdosimetric distributions of the AIC [17]. Spatial and temporal changes of the source activity in the target can also occur [4]. When the distribution of radio-labeled antibody is nonuniform, techniques of dose averaging over volumes greater in size than the individual target volumes can become inadequate predictors of the biological effect [18].

The specific energy is the most important quantity for microdosimetry as it can be used to calculate the cancer cell survival rate. Specific energy (z Gy) is the ratio of the energy deposited (ϵ Joule) to the mass of the target (m kg) (1) and has the same units as absorbed dose [19]. The mean specific energy equals the absorbed dose [15]. Although microdosimetry is concerned with the same concept of energy deposition per unit mass as dosimetry, the difference in the length of alpha particle and small size of the target volume introduces stochastic effects which are negligible in conventional dosimetry [20].

$$z = \frac{\epsilon}{m} \text{ Gy.} \quad (1)$$

The stochastic quantity of specific energy z can be used to investigate biological effects [21]. The cell survival fraction (SF) is given by

$$\text{SF} = e^{-z/z_0}, \quad (2)$$

where z_0 is the absorbed dose required to reduce cell survival to 37% [22].

Many microdosimetric models have been developed since Roesch's initial work [23]. Two different microdosimetric methods can be used. Experimental measurement with high-resolution solid-state microdosimeters is one way. The high spatial resolution and the tissue-equivalence correction detectors have been applied for hadron therapy and Boron neutron capture therapy [24–26]. On the other hand, dose distributions can be calculated with analytical calculations [15] or Monte Carlo techniques based on fundamental physical principles [27]. The latter method is more practical and much less expensive [19].

2.2. Microdosimetry Case Study. It is inappropriate to evaluate the background dose for radioimmunotherapy, especially for TAT by conventional dosimetry. For example, in the phase I clinical trial for metastatic melanoma, patients received up to 25 mCi of ^{213}Bi [7]. Assuming that all the activity injected in patient remains in the blood, 25 mCi corresponds to 3.65×10^{12} ^{213}Bi atoms in the macrodosimetry point of view. Taking the average energy of 8.32 MeV, the total energy lost would be 4.8 Joules. The absorbed dose (z) received by blood (5 L) would be calculated by

$$z = \frac{\epsilon}{m} = \frac{4.8 \text{ J}}{5 \text{ kg}} \approx 1 \text{ Gy.} \quad (3)$$

The above dosimetry would indicate that the blood system would receive an absorbed dose of ~ 1 Gy from alpha particle

TABLE 1: Experimental values of z_0 for *in vitro* exposure to alpha radiation.

Cell line	AIC	z_0 (Gy)	Reference
MCF7	^{225}Ac -Herceptin	0.27	[47]
BT	^{225}Ac -Herceptin	0.37	[47]
MDA	^{225}Ac -Herceptin	0.53	[47]
Line 1	^{213}Bi -13A	1.4	[36]
EMT-6	^{213}Bi -13A	1.7	[36]

irradiation. The risk for unwanted radiation exposures of normal tissues would be too high.

However, by using Geant4 Monte Carlo microdosimetry calculation, the actual dose to endothelial cells is ~ 2 cGy and to lymphocyte is ~ 10 cGy [28], being 2% and 10% of the macroscopic absorbed dose, respectively, and is too low to post any serious damage. In other words, unless alphas actually hit their target, their energy is lost to the medium and has no effect on normal tissue.

Memorial Sloan Kettering found that the maximum tolerance dose was in excess of 1 mCi/kg for bone marrow toxicity [29]. In the melanoma clinical trial [4], 25 mCi converts to ~ 0.3 mCi/kg and is well below that value. Thus, the clinical trial result is consistent with the Monte Carlo calculations. The entirely different result from two dosimetry methods shows it is essential to use microdosimetry method for TAT.

3. Factors Affecting TAT Microdosimetry Result

3.1. The Choice of the Target. Microdosimetry depends on the choice of target, for example, the entire cell, cell nucleus, or DNA. This is because the size of the target will affect both the energy deposition and the mass which determines the specific energy.

As has been substantiated by *in vitro* and *in vivo* experiments, the radiosensitive sites are associated with DNA in the cell nucleus. Microdosimetry research target has fluctuated between DNA and cell nucleus. For alpha particles with a range of a few cell diameters, the cell nucleus is an appropriate choice for the target considering the genome is assumed to be randomly distributed throughout the cell nucleus, and its specific location is not well known [20]. However, under the circumstances that if the particle (e.g., Auger electrons) range is a few μm and the source decays within 1 or 2 nm of the DNA molecule, radiation dose to the cell nucleus may be inadequate to predict radiation toxicity, and determination of the energy deposition to the DNA molecule may be necessary [30].

3.2. Target and Source Configuration. The TAT microdosimetry dose is highly sensitive to experimental factors such as the nucleus size and source distribution, kinetics of the AIC, and subcellular distribution of the radionuclide.

Because of the short range of alpha particles, even small changes in the thickness or diameter of the cell nucleus can influence the dose distribution. Simplified spheroid models

with different cell and nucleus radii are used to model cells [4, 15, 31]. Recently some more realistic models with geometric parameters taken from monolayer or suspended cells measurement were built [32–35].

The position of the source relative to the target cell nucleus is another major factor in determining the hit probability, specific energy, and ultimately the efficacy of TAT [36]. For a spherical single-cell model, the specific energy from activity internalized in the cell nucleus, in the cytoplasm, on the cell membrane, or in the medium can differ as much as 150 times [37]. Rapidly internalized antibodies or radioisotopes are superior because of markedly greater intracellular retention and higher probability of hit. However, caution is needed as some animal studies indicate that the retention of ^{111}In and ^{90}Y is prolonged in normal organs such as bone, liver, and kidney as well [38].

3.3. Cell Sensitivity. The z_0 value is highly sensitive to experimental factors such as the distribution of DNA within the nucleus (i.e., the phase of the cell cycle) and the number and spatial distribution of the alpha particle sources relative to the target cell nucleus [39]. It is also expected that the *in vitro* cell sensitivity will vary between different cells within a given tumor. Table 1 shows a survey of TAT *in vitro* experiments, which illustrated that z_0 values for cancer cell lines exposed to alpha radiation can vary as much as 6 times, indicating that for a given specific energy, the biological responses can also vary 6 times or more (SF in (2)).

3.4. Radioisotopes. The clinical application of TAT is focused on alpha particle emitters of ^{211}At , ^{213}Bi , ^{223}Ra , and ^{225}Ac [40–42]. The physical properties of these radionuclides, including half-life, mean particle energy, maximum particle energy, and average range in tissue, affect the therapeutic result and are listed in Table 2 [43, 44].

For an AIC with a long residence time in a tumor, a radionuclide with a long half-life will deliver more decays than one with a short half-life ($t_{1/2}$) for the same initial radioactivity [44]. The number of radionuclides (N) to produce activity (A) is

$$N = \frac{A}{\lambda} = \frac{A}{(0.693/t_{1/2})}. \quad (4)$$

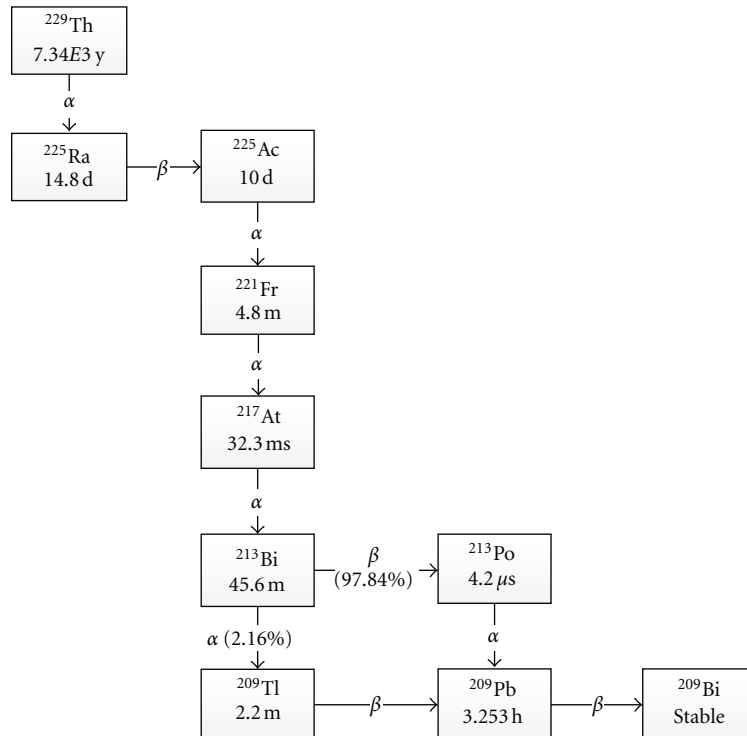
For TAT aimed at destroying all cancer cells in the tumor, deep penetration and uniform distribution of the AIC would be crucial. Thus, the longer half-life radioisotope would be a better choice. However, if the aim is to destroy tumor capillaries, poor AIC diffusion away from the capillaries and shorter half-life would be an advantage [19].

The longer half-life of ^{225}Ac and the 4 alpha particle emissions (Figure 2) gives greater toxicity and can prolong survival in the mouse xenograft models for several cancers [45]. However, the drawback is that the binding energy of the chelation is not strong enough to withstand the alpha particle recoil energy of the Actinium ion (between 100 and 200 keV). Daughters of ^{225}Ac will lose tumor selectivity and could diffuse away, causing cell damage in normal tissue [16, 46].

TABLE 2: Physical properties of alpha-particle emitters.

Radionuclide	Z	Half-life	Mean particle energy* (MeV)	Maximum energy (MeV)	Average range (μm)	<LET> ($\text{keV}/\mu\text{m}$)
^{211}At	85	7.2 h	6.79	7.45	60	71
^{213}Bi	83	45.6 min	8.32	8.38	84	61
^{223}Ra	88	11.43 d	5.64	7.59	45	81
^{225}Ac	89	10.0 d	6.83	8.38	61	71

*weighted average of emissions.

FIGURE 2: The decay chain of ^{225}Ac and ^{213}Bi .

3.5. Biological Factors. There are great complexities of the mammalian cell, the nucleus and its internal structures and pathways, types of DNA damage, and cellular repair. For cancer-cell cluster or solid-tumor modeling, a precise kinetic description of AICs diffusing through cells and saturating antigenic sites is needed for microdosimetry. The number of AICs in the solid tumor depends critically on the capillary permeability and the number of antigens expressed on cells that can vary 10-fold and more. As such, the calculations rest on realistic assumptions but results, in spite of the quantitative nature of the Monte Carlo calculation, are qualitative only.

4. Conclusion

Targeted Alpha Therapy uses radio-isotopes that emit alpha radiation to kill targeted cancer cells. It is most effective in the elimination of single-cancer cells and micrometastases before the tumors grow to become clinically evident. The application has been extended to the treatment of solid tumors by tumor antivascular alpha therapy. Because the short range of alpha particles is comparable to the size of the biological

target and the variable distribution of alpha emitters, stochastic processes apply, and Monte Carlo calculations of microdosimetry are indispensable in the investigation of biological response mechanisms.

Acknowledgment

The authors wish to thank Professor Anatoly Rozenfeld for his support.

References

- [1] M. R. Zalutsky and O. R. Pozzi, "Radioimmunotherapy with α -particle emitting radionuclides," *Quarterly Journal of Nuclear Medicine and Molecular Imaging*, vol. 48, no. 4, pp. 289–296, 2004.
- [2] V. Rajkumar, J. L. Dearling, A. Packard, and R. B. Pedley, "Research Spotlight—radioimmunotherapy: optimizing delivery to solid tumors," *Therapeutic Delivery*, vol. 2, no. 5, pp. 567–572, 2011.
- [3] G. Sgouros, "Alpha-particles for targeted therapy," *Advanced Drug Delivery Reviews*, vol. 60, no. 12, pp. 1402–1406, 2008.

- [4] J. C. Roeske and T. G. Stinchcomb, "Dosimetric framework for therapeutic alpha-particle emitters," *Journal of Nuclear Medicine*, vol. 38, no. 12, pp. 1923–1929, 1997.
- [5] M. R. McDevitt, G. Sgouros, R. D. Finn et al., "Radioimmunotherapy with alpha-emitting nuclides," *European Journal of Nuclear Medicine*, vol. 25, no. 9, pp. 1341–1351, 1998.
- [6] J. G. Jurcic, S. M. Larson, G. Sgouros, M. R. McDevitt, R. D. Finn, and C. R. Divgi, "Targeted α particle immunotherapy for myeloid leukemia," *Blood*, vol. 100, no. 4, pp. 1233–1239, 2002.
- [7] C. Raja, P. Graham, S. M. Abbas Rizvi et al., "Interim analysis of toxicity and response in phase I trial of systemic targeted alpha therapy for metastatic melanoma," *Cancer Biology and Therapy*, vol. 6, no. 6, pp. 846–852, 2007.
- [8] B. J. Allen, C. Raja, S. Rizvi, E. Y. Song, and P. Graham, "Tumour anti-vascular alpha therapy: a mechanism for the regression of solid tumours in metastatic cancer," *Physics in Medicine and Biology*, vol. 52, no. 13, pp. L15–L19, 2007.
- [9] B. J. Allen, "Can α -radioimmunotherapy increase efficacy for the systemic control of cancer?" *Immunotherapy*, vol. 3, no. 4, pp. 455–458, 2011.
- [10] M. Bardies and P. Pihet, "Dosimetry and microdosimetry of targeted radiotherapy," *Current Pharmaceutical Design*, vol. 6, no. 14, pp. 1469–1502, 2000.
- [11] R. F. Hobbs, S. Baechler, D. X. Fu et al., "A model of cellular dosimetry for macroscopic tumors in radiopharmaceutical therapy," *Medical Physics*, vol. 38, no. 6, pp. 2892–2903, 2011.
- [12] T. C. Karagiannis, "Comparison of different classes of radionuclides for potential use in radioimmunotherapy," *Hellenic Journal of Nuclear Medicine*, vol. 10, no. 2, pp. 82–88, 2007.
- [13] R. M. Macklis, B. M. Kinsey, A. I. Kassis et al., "Radioimmunotherapy with alpha-particle-emitting immunoconjugates," *Science*, vol. 240, no. 4855, pp. 1024–1026, 1988.
- [14] H. Zaidi and G. Sgouros, Eds., *Therapeutic Applications of Monte Carlo Calculations in Nuclear Medicine*, vol. 9, vol. 30, Institute of physics, London, UK, 2003.
- [15] T. G. Stinchcomb and J. C. Roeske, "Analytic microdosimetry for radioimmunotherapeutic alpha emitters," *Medical Physics*, vol. 19, no. 6, pp. 1385–1394, 1992.
- [16] M. R. McDevitt, G. Sgouros, R. D. Finn et al., "Radioimmunotherapy with alpha-emitting nuclides," *European Journal of Nuclear Medicine*, vol. 25, no. 9, pp. 1341–1351, 1998.
- [17] S. Sofou, "Radionuclide carriers for targeting of cancer," *International Journal of Nanomedicine*, vol. 3, no. 2, pp. 181–199, 2008.
- [18] D. T. Goodhead, "Panel discussion: do non-targeted effects impact the relation between microdosimetry and risk?" *Radiation Protection Dosimetry*, vol. 143, no. 2–4, pp. 554–556, 2011.
- [19] C. Y. Huang, B. M. Oborn, S. Guatelli, and B. J. Allen, "Monte Carlo calculation of the maximum therapeutic gain of tumor antivasculature alpha therapy," *Medical Physics*, vol. 39, no. 3, pp. 1282–1288, 2012.
- [20] J. L. Humm, J. C. Roeske, D. R. Fisher, and G. T. Y. Chen, "Microdosimetric concepts in radioimmunotherapy," *Medical Physics*, vol. 20, no. 2, pp. 535–542, 1993.
- [21] D. T. Goodhead, "Energy deposition stochastics and track structure: what about the target?" *Radiation Protection Dosimetry*, vol. 122, no. 1–4, pp. 3–15, 2006.
- [22] D. E. Charlton, A. I. Kassis, and S. J. Adelstein, "A comparison of experimental and calculated survival curves for V79 cells grown as monolayers or in suspension exposed to alpha irradiation from ^{212}Bi distributed in the growth medium," *Radiation Protection Dosimetry*, vol. 52, no. 1–4, pp. 311–315, 1994.
- [23] W. C. Roesch, "Microdosimetry of internal sources," *Radiation Research*, vol. 70, no. 3, pp. 494–510, 1977.
- [24] A. B. Rosenfeld, G. I. Kaplan, M. G. Carolan et al., "Simultaneous macro and micro dosimetry with MOSFETs," *IEEE Transactions on Nuclear Science*, vol. 43, no. 6, pp. 2693–2700, 1996.
- [25] P. D. Bradley and A. B. Rosenfeld, "Tissue equivalence correction for silicon microdosimetry detectors in boron neutron capture therapy," *Medical Physics*, vol. 25, no. 11, pp. 2220–2225, 1998.
- [26] P. D. Bradley, A. B. Rosenfeld, B. Allen, J. Coderre, and J. Capala, "Performance of silicon microdosimetry detectors in boron neutron capture therapy," *Radiation Research*, vol. 151, no. 3, pp. 235–243, 1999.
- [27] S. Incerti, N. Gault, C. Habchi et al., "A comparison of cellular irradiation techniques with alpha particles using the Geant4 Monte Carlo simulation toolkit," *Radiation Protection Dosimetry*, vol. 122, no. 1–4, pp. 327–329, 2006.
- [28] C. Y. Huang, S. Guatelli, B. M. Oborn, and B. J. Allen, "Background dose for systemic targeted Alpha therapy," *Progress in Nuclear Science and Technology*, vol. 2, pp. 187–190, 2011.
- [29] T. L. Rosenblat, M. R. McDevitt, D. A. Mulford et al., "Sequential cytarabine and α -particle immunotherapy with bismuth-213-lintuzumab (HuM195) for acute myeloid leukemia," *Clinical Cancer Research*, vol. 16, no. 21, pp. 5303–5311, 2010.
- [30] H. Nikjoo, S. Uehara, D. Emfietzoglou, and L. Pinsky, "A database of frequency distributions of energy depositions in small-size targets by electrons and ions," *Radiation Protection Dosimetry*, vol. 143, no. 2–4, pp. 145–151, 2011.
- [31] J. L. Humm and L. M. Chin, "A model of cell inactivation by alpha-particle internal emitters," *Radiation Research*, vol. 134, no. 2, pp. 143–150, 1993.
- [32] S. J. Kennel, R. Boll, M. Stabin, H. M. Schuller, and S. Mirzadeh, "Radioimmunotherapy of micrometastases in lung with vascular targeted ^{213}Bi ," *British Journal of Cancer*, vol. 80, no. 1–2, pp. 175–184, 1999.
- [33] D. E. Charlton, "The survival of monolayers of cells growing in clusters irradiated by ^{211}At appended to the cell surfaces," *Radiation Research*, vol. 151, no. 6, pp. 750–753, 1999.
- [34] Y. Kvinnsland, T. Stokke, and E. Aurlien, "Radioimmunotherapy with alpha-particle emitters: microdosimetry of cell with a heterogeneous antigen expression and with various diameters of cells and nuclei," *Radiation Research*, vol. 155, no. 2, pp. 288–296, 2001.
- [35] S. Incerti, H. Seznec, M. Simon, P. Barberet, C. Habchi, and P. Moretto, "Monte Carlo dosimetry for targeted irradiation of individual cells using a microbeam facility," *Radiation Protection Dosimetry*, vol. 133, no. 1, pp. 2–11, 2009.
- [36] S. J. Kennel, M. Stabin, J. C. Roeske et al., "Radiotoxicity of bismuth-213 bound to membranes of monolayer and spheroid cultures of tumor cells," *Radiation Research*, vol. 151, no. 3, pp. 244–256, 1999.
- [37] N. Chouin, K. Bernardeau, F. Davodeau et al., "Evidence of extranuclear cell sensitivity to alpha-particle radiation using a microdosimetric model—I. Presentation and validation of a microdosimetric model," *Radiation Research*, vol. 171, no. 6, pp. 657–663, 2009.
- [38] Z. Yao, K. Garmestani, K. J. Wong et al., "Comparative cellular catabolism and retention of astatine-, bismuth-, and lead-radiolabeled internalizing monoclonal antibody," *Journal of Nuclear Medicine*, vol. 42, no. 10, pp. 1538–1544, 2001.
- [39] G. Sgouros, J. C. Roeske, M. R. McDevitt et al., "MIRD pamphlet No. 22 (Abridged): Radiobiology and dosimetry of

- α -particle emitters for targeted radionuclide therapy,” *Journal of Nuclear Medicine*, vol. 51, no. 2, pp. 311–328, 2010.
- [40] B. Pohlman, J. Sweetenham, and R. M. Macklis, “Review of clinical radioimmunotherapy,” *Expert Review of Anticancer Therapy*, vol. 6, no. 3, pp. 445–461, 2006.
- [41] S. Nilsson, R. H. Larsen, S. D. Fosså et al., “First clinical experience with α -emitting radium-223 in the treatment of skeletal metastases,” *Clinical Cancer Research*, vol. 11, no. 12, pp. 4451–4459, 2005.
- [42] B. J. Allen, “Clinical trials of targeted alpha therapy for cancer,” *Reviews on Recent Clinical Trials*, vol. 3, no. 3, pp. 185–191, 2008.
- [43] X. Zhu, M. R. Palmer, G. M. Makrigiorgos, and A. I. Kassis, “Solid-tumor radionuclide therapy dosimetry: new paradigms in view of tumor microenvironment and angiogenesis,” *Medical Physics*, vol. 37, no. 6, pp. 2974–2984, 2010.
- [44] A. I. Kassis, “Therapeutic radionuclides: biophysical and radiobiologic principles,” *Seminars in Nuclear Medicine*, vol. 38, no. 5, pp. 358–366, 2008.
- [45] M. R. McDevitt, D. Ma, L. T. Lai et al., “Tumor therapy with targeted atomic nanogenerators,” *Science*, vol. 294, no. 5546, pp. 1537–1540, 2001.
- [46] J. Schwartz, J. S. Jaggi, J. A. O’donoghue et al., “Renal uptake of bismuth-213 and its contribution to kidney radiation dose following administration of actinium-225-labeled antibody,” *Physics in Medicine and Biology*, vol. 56, no. 3, pp. 721–733, 2011.
- [47] Å. M. Ballangrud, W. H. Yang, S. Palm et al., “Alpha-particle emitting atomic generator (actinium-225)-labeled trastuzumab (Herceptin) targeting of breast cancer spheroids: efficacy versus HER2/neu expression,” *Clinical Cancer Research*, vol. 10, no. 13, pp. 4489–4497, 2004.

Research Article

Study of Tumor Growth under Hyperthermia Condition

Qing Zhu,¹ Aili Zhang,¹ Ping Liu,^{1,2} and Lisa X. Xu^{1,2}

¹ School of Biomedical Engineering, Shanghai Jiao Tong University, Shanghai 200240, China

² Med-X Research Institute, Shanghai Jiao Tong University, Shanghai 200240, China

Correspondence should be addressed to Aili Zhang, zhangaili@sjtu.edu.cn and Lisa X. Xu, lisaxu@sjtu.edu.cn

Received 2 May 2012; Revised 22 July 2012; Accepted 23 July 2012

Academic Editor: Scott Penfold

Copyright © 2012 Qing Zhu et al. This is an open access article distributed under the Creative Commons Attribution License, which permits unrestricted use, distribution, and reproduction in any medium, provided the original work is properly cited.

The new concept of keeping primary tumor under control *in situ* to suppress distant foci sheds light on the treatment of metastatic tumor. Hyperthermia is considered as one of the means for controlling tumor growth. To simulate the tumor growth, a continuum mathematical model has been introduced. The newest understanding of the Warburg effect on the cellular metabolism and diffusion of the nutrients in the tissue has been taken into consideration. The numerical results are compared with the *in vivo* experimental data by fitting the tumor cell doubling time/tumor cell growth rate under different thermal conditions. Both the tumor growth curve and corresponding average glucose concentration have been predicted. The numerical results have quantitatively illustrated the controlling effect on tumor growth under hyperthermia condition in the initial stage.

1. Introduction

Cancer is the second major cause of human death in the world, and its mortality rate is growing every year [1]. Treatments include surgery, radiotherapy, chemotherapy, and gene therapy. Thermal therapy has also been intended to locally destroy tumor cells or enhance the body defense against tumor cells. However, recurrent rate of malignant tumor is still high [2], and the efficacy of the existing therapeutic means is yet to be improved. A new concept has been proposed recently that the primary tumor suppresses distal foci [3, 4]. This sheds new light on tumor treatment. Keeping the primary tumor *in situ* but restricting its size might enable the host to impede the development of distal foci and progression of metastasis.

For tumor growth, there are three distinct stages: avascular, vascular, and metastatic/invasive stage. Mathematical models have been developed to perform parametric studies on factors influencing tumor growth or to evaluate the outcome of tumor treatment modalities [5, 6]. Model-based numerical studies would enable one to extrapolate more spatial and temporal information from the experimental findings and to make predictions [7]. Laird [8] first found that the tumor growth data-fitted Gompertz function could be used to simulate the entire growth curve, which was

defined as an empirical model. Hu and Ruan [9] studied the suppression effect of immunity system on tumor growth by merging the Gompertz function into a cellular automaton model. Other mathematical models based on certain biological assumptions have also been attempted to predict tumor growth curve using fundamental physics, such as mass/energy conservation. Greenspan [10] introduced surface tension into the diffusion model developed by Burton [11]. Tumor growth/inhibition factors [12, 13], cell adhesions [14, 15], angiogenesis [16, 17] and invasion [18, 19] were further considered to describe tumor growth at different stages.

Models focusing on the avascular stage [20–27] have been well studied and could be easily applied to *in vitro* experiment. Ward and King [23, 24] and Casciari et al. [28] proposed a continuum mathematical model focusing on how nutrients' concentration affects tumor growth. These models typically consist of reaction-diffusion equations. Forbes [29] further incorporated energy metabolism (ATP production rate) into the growth model. However, most of these models have not taken the Warburg effect into consideration, which fundamentally differentiates the tumor cell metabolism from that of the normal cells.

In 1930, Warburg (1930) proposed that tumor cells preferentially underwent glycolysis when consuming glucose

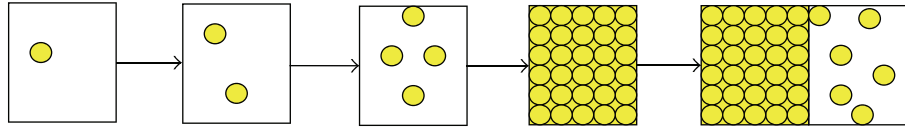


FIGURE 1: Schematic of tumor growth. The tumor starts with one single cell (represented by the yellow circle), and the cells differentiate continuously. When the infinitesimal unit of the space volume is filled up with the tumor cells, they grow into the next volume unit.

even under aerobic conditions. Unregulated glucose uptake and lactic acid production have been found in tumor cells as compared to normal cells [30, 31]. It indicates that tumor cells obtain energy to maintain their viability primarily relying on anaerobic metabolism. This phenomenon was termed as “the Warburg effect.” Anaerobic glycolysis consumes one molecule of glucose to produce 2 molecules of ATP as compared with oxidative phosphorylation which can produce 38 molecules of ATP [31–40]. Although the latter is much more efficient in glucose utilization, the rate of anaerobic glycolysis is much faster than aerobic metabolism. Therefore, the inefficient metabolism pathway might still supply enough energy for tumor cells to maintain their activities and differentiate at the cost of unreasonable consumption of glucose. The mechanisms causing the Warburg effect have been explained by gene mutation [38], signaling pathway alternations, possible defects in mitochondria [36, 41], and microenvironment deterioration (hypoxia or fluctuation of oxygen) [34, 37, 42]. Heiden et al. [32] have reported that biomass synthesis in tumor cells plays a role in the Warburg effect. Furthermore, he has determined nutrition utilizations in tumor cells: 85% of glucose converting to lactate in cytoplasm, 5% reacting in mitochondria, and 10% synthesizing biomass. As the metabolic activities greatly influence the growth of tumor, it is necessary to include this unique metabolic mode of tumor in mathematical models.

Although thermal treatment has been applied in clinical applications for many years, most of them were used as short-term treatments. There are three classes of the treatment strategies [43–45]: with a mild temperature at 40~41°C for 6~72 hours until the thermal dose is equivalent to 5 minutes at 43°C; a moderate temperature at 42~45°C for 15~60 minutes; and high temperature >50°C for 4~6 minutes. Both mild and moderate temperature treatments (40~45°C) termed as hyperthermia treatment impair mammalian cells by protein denaturation and membrane damage and could cause cell death *in situ* [46].

In the present study, a mathematical model of tumor growth has been built by combining ATP production rate and the mechanism of the Warburg effect. It is validated by the tumor growth measurements *in situ* and further applied to study the hyperthermia effect on tumor metabolism over a period of time.

2. Theory

2.1. Experimental Study of Tumor Growth. Animal study of tumor metabolisms under long-term hyperthermia has been studied [47]. In the study, tumor cells were injected into the back of Balb/c mice around 6~8 weeks. Mice were grouped

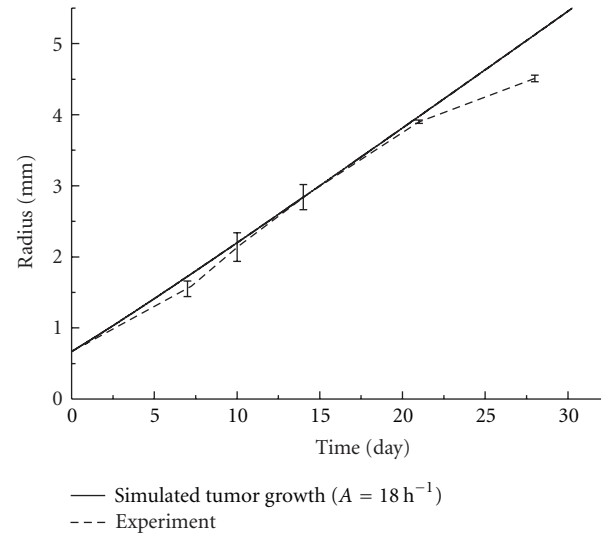


FIGURE 2: Tumor growth curve of the experimental measurements versus the numerical simulation of the control group.

randomly into the control and treatment groups with 6 in each group. In the treatment group, the tumor region of the mice was heated via a 15 mm-diameter circular heating pad for 28 days. On each day, it was heated for 12 hours with an interval of 12 hours. The supplying power of the heating pad was controlled to maintain the tumor surface tissue temperature at 39°C. Tumor sizes of both the control and treatment groups were measured and recorded at 3, 7, 10, 14, 21, 28 days, respectively. The experimental results are shown in Figures 2–5 with the permission of the authors.

2.2. Model Development. At the avascular stage of a solid tumor, tumor cells proliferate and tumor grows like a spheroid without restriction. In our model, the tumor is assumed to start from one single tumor cell (as illustrated in Figure 1), and to grow into a homogenous spheroid over a period of time. This is an assumption used by many models [7, 10, 14, 16, 23, 24, 29] and acceptable when the diameter of tumor is less than 2~4 mm prior to microvascular development. In addition, only living tumor cells are supposed to take the space of the spheroid. The proliferation of tumor cells is related to local concentration of nutrients. In this model, nutrients are simplified to the main source of energy (glucose) only. Glucose diffuses passively into tumor tissue from the outer rim of the tumor, where its concentration remains at a constant over the initial tumor growth period.

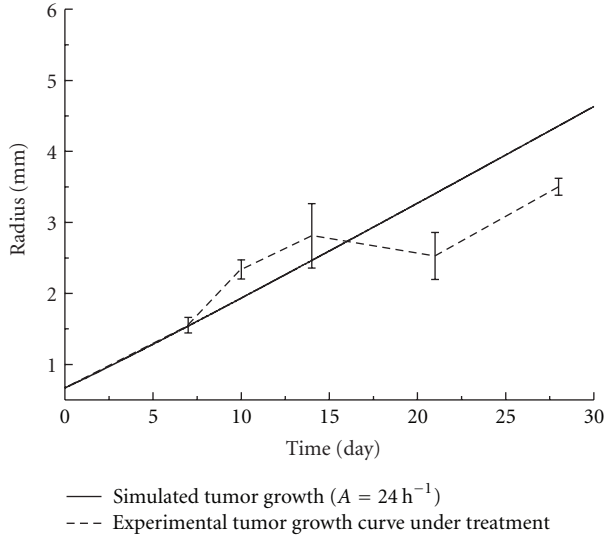


FIGURE 3: Tumor growth curve of the experimental measurements versus the numerical simulation of the treatment group (39°C) ($n = 6$).

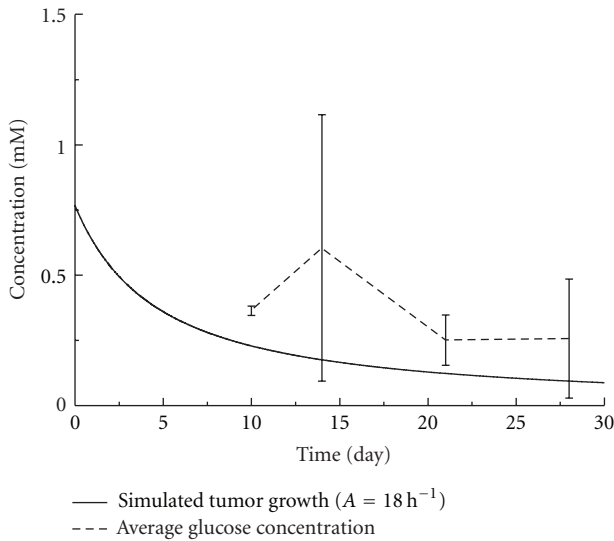


FIGURE 4: Average glucose concentration of the experimental measurements versus the numerical simulation of the control group.

Usually, the glucose is metabolized through two different pathways: aerobic and anaerobic, depending on the cell status and physiological conditions. According to the recent understanding of the Warburg effect [32, 38], in tumor metabolism, about 5% of glucose undergoes aerobic pathway, and 85% takes the anaerobic pathway to produce ATP. The rest of 10% glucose is utilized for biomass synthesis necessary for cell divisions.

Through anaerobic pathway, glucose first degrades into pyruvate, and pyruvate converts into lactate by lactate dehydrogenase in the cytoplasm. While in the aerobic metabolism, pyruvate will further react with oxygen, and produce water and carbon dioxide inside mitochondria. It is clear that

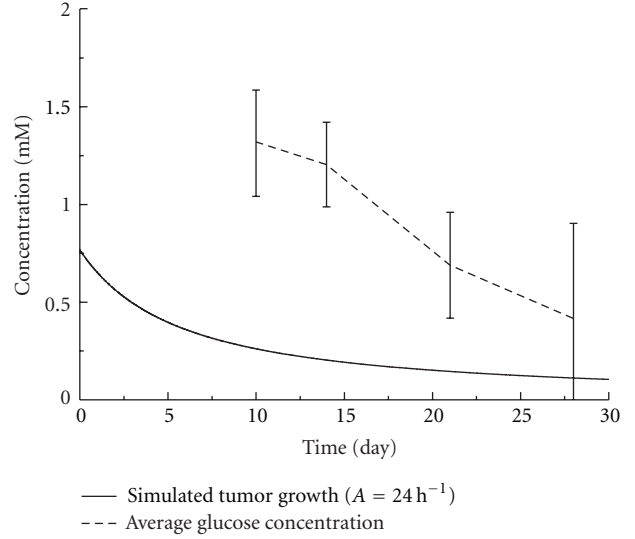
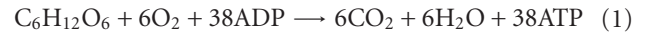


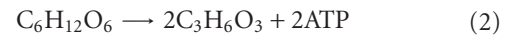
FIGURE 5: Average glucose concentration of the experimental measurement versus the numerical simulation of the treatment group.

not only the metabolic site and end products are different, but also the amount of energy produced differs. Through aerobic metabolism, one mole of glucose consumes 6 moles of oxygen and produces 38 moles of ATP, while in anaerobic metabolism only 2 moles of ATP per mole glucose could be produced without oxygen. These reactions are simplified and presented by the following formulae

Aerobic respiration:



Anaerobic respiration:



The proliferation rate of tumor cells is supposed to rely on the ATP production rate, which is determined by the metabolic reactions:

$$Q_{\text{ATP}} = 38Q_{g,\text{AR}} + Q_{\text{lac}}, \quad (3)$$

where $Q_{g,\text{AR}}$ is the glucose assumption rate due to aerobic respiration, Q_{lac} is the lactate production rate.

Following the hypothesis of Heiden [32], the glucose consumption rate due to aerobic metabolism and the lactate production rate could be derived from the uptake rate of glucose by tumor cells:

$$Q_{g,\text{AR}} = 5\%Q_g, \quad (4)$$

$$Q_{\text{lac}} = 85\% \times 2 \times Q_g,$$

where Q_g is the cellular glucose uptake rate.

Then the ATP production rate Q_{ATP} could be calculated:

$$Q_{\text{ATP}} = 5\% \times 38 \times Q_g + 85\% \times 2 \times Q_g. \quad (5)$$

The cellular uptake rate of glucose depends on both the extracellular level of glucose concentration and the ability of cell uptake. The reaction is assumed to be enzyme reaction and followed Michaelis-Menten kinetics' equation [10, 25]:

$$Q_g = Q_{g\max} \frac{c_g}{c_g + K_g}, \quad (6)$$

where $Q_{g\max}$ is the maximum glucose uptake rate per tumor cell, c_g is the glucose concentration in tumor tissue, and K_g is saturate concentration.

The concentrations of nutrients (both glucose and lactate) are assumed to be functions of tumor spheroid radius that are changing with the rate of cell proliferation [7]:

$$\frac{dc_g}{dt} = D_g \nabla^2 c_g - Q_g l, \quad (7)$$

where D_g is the diffusion coefficient of glucose and reported to be $1.05 * 10^{-6}$ cm²/s for EMT6/R0 spheroid, and l is the number of living cell per unit volume.

The concentration of glucose at the boundary is decided by the average value of glucose concentration in blood—5 mM, and the tumor is assumed symmetric, thus the boundary conditions for (5) are as follows

Boundary condition:

$$\left. \frac{\partial c_g}{\partial t} \right|_{r=0} = 0, \quad c_g \Big|_{r=R} = 5 \text{ mM}, \quad (8)$$

where R is the radius of solid tumor.

The distribution of lactate in tumor is determined by

$$\frac{dc_{\text{lac}}}{dt} = D_{\text{lac}} \nabla^2 c_{\text{lac}} - Q_{\text{lac}} l, \quad (9)$$

where c_{lac} is the concentration of lactate in tumor tissue, and D_{lac} is the effective diffusion coefficient of glucose and lactate. The boundary conditions are:

$$\left. \frac{\partial c_{\text{lac}}}{\partial t} \right|_{r=0} = 0, \quad c_{\text{lac}} \Big|_{r=R} = 0 \text{ mM}. \quad (10)$$

The diffusion coefficient of lactate could be determined from the glucose diffusivity [25]:

$$D_{\text{lac}} = D_g \left(\frac{MW_g}{MW_{\text{lac}}} \right)^{3/4}, \quad (11)$$

where MW_g and MW_{lac} are molecular weights of glucose and lactate, respectively.

Assuming that all viable space in tumor tissue is filled with living and tightly packed tumor cells (see Figure 1), the number of living cells per unit tumor tissue volume is

$$l = \frac{1}{V_L}, \quad (12)$$

where V_L is the volume of a living tumor cell. It is obtained through *in vitro* measurement. Diameters of more than 150

suspended 4T1 tumor cells are measured and averaged to get the volume of a single cell. Its average radius is 13.41 μm with a standard deviation of 2.21 μm . With this radius, the tumor cell volume was calculated and the result is listed in Table 1.

By solving the above listed equations together, the ATP production rate and concentrations of glucose and lactate inside the tumor tissue could be obtained. The relationship between ATP production rate and cell growth rate is proposed and well parameterized by Forbes et al. [29]:

$$k_l = A \frac{Q_{\text{ATP}}}{Q_{\text{ATP}} + K_{\text{ATP}}}, \quad (13)$$

where k_l is cell growth rate of tumor cells, A is the maximum cell growth rate, and K_{ATP} is saturation ATP production rate.

In this model, tumor growth is considered as tumor cells moving outward while all space occupied. In other words, tumor growth is mainly due to living tumor cells' proliferation, then the moving velocity of the tumor spheroid rim is given as

$$v(t, R(t)) = \frac{\int_0^{R(t)} k_l l V_L r^2 dr}{R(t)^2}, \quad (14)$$

where r is radial distant from center of tumor spheroid, and $R(t)$ is the radius of tumor spheroid at time t . The radius of tumor spheroid at time $t + dt$ is

$$R(t+dt) = \int_t^{t+dt} v(t, R(t)) dt + R(t). \quad (15)$$

The average concentration of the metabolites is calculated from the integration of the substances' distribution throughout tumor tissue divided by the tumor tissue volume as

$$\bar{c}(t) = \frac{\int_0^{R(t)} (c(r) \cdot 4\pi r^2) dr}{(4/3)\pi R(t)^3}. \quad (16)$$

By substituting the dimensionless quantities and parameters as defined below into the above equations, the dimensionless equations could be obtained.

The dimensionless variables are defined as

$$c_g^* = \frac{c_g}{c_{g,0}}, \quad c_{\text{lac}}^* = \frac{c_{\text{lac}}}{c_{g,0}}, \quad r^* = \frac{r}{R(t)}, \quad t^* = \frac{t}{1/A}, \quad (17)$$

where $c_{g,0} = 5 \text{ mM}$.

TABLE 1: List of variables used in modeling.

Variable	Description	Unit
c_g	Glucose concentration	mM
c_{lac}	Lactate concentration	mM
Q_g	Glucose uptake rate	mol/cell/sec
Q_{lac}	Lactate production rate	mol/cell/sec
Q_{ATP}	ATP production rate	mol/cell/sec
k_l	Cell proliferation time	1/h
L	Number of living cells in certain unit volume	cells/cm ³
R	Radius of tumor spheroid	cm
V	Tumor growth velocity	cm/h
T	Growth time	h

Thus, the dimensionless equations are

$$\begin{aligned}
Q_{ATP}^* &= 85\% * 2 * Q_g^* + 5\% * 38 * Q_g^* \\
Q_g^* &= \frac{Q_g}{Q_{g \max}} = \frac{c_g^*}{c_g^* + K_g/c_{g,0}} \\
Q_{lac}^* &= \frac{Q_{lac}}{Q_{g \max}} = \frac{c_{lac}^*}{c_{lac}^* + K_{lac}/c_{g,0}} \\
\frac{dc_g^*}{dt^*} &= \frac{1}{A} \left(\nabla^2 c_g^* - \frac{R(t)^2 Q_{g \max}}{DV_L c_{g,0}} Q_g^* \right) \\
c_g^* \Big|_{r^*=1} &= 1 \quad \frac{dc_g^*}{dt^*} \Big|_{r^*=0} = 0 \\
\frac{dc_{lac}^*}{dt^*} &= \frac{1}{A} \left(\nabla^2 c_{lac}^* - \frac{R(t)^2 Q_{g \max}}{DV_L c_{g,0}} Q_{lac}^* \right) \\
c_{lac}^* \Big|_{r^*=1} &= 0 \quad \frac{dc_{lac}^*}{dt^*} \Big|_{r^*=0} = 0 \\
k_l^* &= \frac{k_l}{A} = \frac{Q_{ATP}^*}{Q_{ATP}^* + K_{ATP}/Q_{g \max}} \\
R(t) &= \int_0^t (v^* R(t) A) d\left(\frac{t^*}{1/A}\right) + R_0.
\end{aligned} \tag{18}$$

Tumor growth *in vivo* is actually a complex process, which involves many influencing factors such as gene mutation, immune system, tumor cell mechanism effect, tumor angiogenesis, metabolic waste, and tumor microenvironment. It is difficult to include all these factors into one single model. The present model is built based on energy production only and all other influencing factors are lumped into the maximum cell growth rate parameter A . The behavior of tumor growth is determined by the maximum cell growth rate A and it is determined by fitting to the animal experiment data. The other parameters used are all listed in Tables 1 and 2. The constants (D_g , $Q_{g \max}$) listed in Table 2 are taken from EMT6/Ro tumor, whose biophysical constants have been well studied. EMT6 is a mouse breast cancer cell line that grows in the Balb/C strain. 4T1 cells are assumed to be similar to EMT6 biophysically in the present modeling.

To solve the equations listed above, discrete algorithm is built. The one-dimensional tumor space is divided into 1000 intervals evenly. The time increment Δt is set to be small enough to guarantee the solver stability. The diffusion-reaction equations are then differentiated using the finite difference method. The tumor radius at certain time t is used as an input into the differentiated equation, and the forward elimination and backward substitution method is used to solve these differentiated equations to obtain the glucose concentration distribution, the corresponding ATP production rate, tumor growth rate, the velocity of the moving boundary of tumor, and the new tumor radius at a given time t . The updated tumor radius is then used as an input into the equations iteratively, until the difference between two iterations is small enough. For the next time step ($t + \Delta t$), the radius of tumor is derived from the original radius at time t and radius increment during Δt . This process is repeated until the final convergence reached in simulation.

The maximum cell growth rate parameter A is fitted from the animal experimental data. The reciprocal of A ranged from 0~50 h, with an interval of 0.2 h. Each A is then substituted to the mathematical model to obtain a simulated curve, which is compared with the animal experimental data using the coefficient of determination (R2) as a criteria. The optimal A is chosen in correspondance to the maximum achieved R2 value.

3. Results and Discussion

By fitting the numerical model with the experimentally measured tumor growth data, the parameter A for tumor growth with and without treatment was obtained. The fitted curve and the experimental results were shown in Figures 2 and 3, respectively.

For the control group, the tumor growth curve during the first 28 days was well captured by the energy-based model developed in this study (Figure 2). The fitted maximum cell growth rate parameter A was (18 h)⁻¹. However, after 28 days, the tumor growth slowed down and became nonlinear, which could no longer be described by the current mathematical model. It implied that alternations in tumor metabolism and some impedimental mechanisms might appear which led to cell death when tumor radius

TABLE 2: List of constants used in modeling (cell type—EMT6/Ro).

Variable	Description	Value	Authors
D_g	Glucose diffusion coefficient	$1.05 \times 10^{-6} \text{ cm}^2/\text{s}$	Casciari et al., 1988 [28]
$Q_{g \max}$	Maximum glucose uptake rate	$1.33 \times 10^{-16} \text{ mol}/(\text{cell sec})$	Casciari et al., 1992 [25]
K_g	Glucose saturation constant	$4.0 \times 10^{-2} \text{ mM}$	Casciari et al., 1992 [25]
V_L	Living cell volume	$1.26 \times 10^{-9} \text{ cm}^3$	Experiment
$c_{g,0}$	Glucose concentration at tumor rim	5.5 mM or less	Freyer and Sutherland, 1986 [55]
K_{ATP}	Cell growth saturation constant	$3.75 \times 10^{-19} \text{ mol}/\text{cells}$	Venkatasubramanian et al., 2006 [29]

reached about 4~5 mm in diameter. These factors were not considered in the present model.

Tumor growth in mice under long-term mild hyperthermia treatment was also fitted and shown in Figure 3. It was obvious that the growth rate of tumor was much slower and the fitted maximum cell growth rate A was $(24 \text{ h})^{-1}$. The model predicted the general trend of tumor growth well in the first 15 days. The oscillation occurred in the growth curve that was not observed in the control group could be attributed to the thermal interference, although the causing mechanism is yet to be further explored. Moreover, it was clear that the model overestimated the tumor growth under the hyperthermia condition after 15 days. This indicates that more complex effects on the system might be triggered by hyperthermia after a period of time. It could be related to tumor angiogenesis, the activities of enzymes in different pathways associated with tumor cell metabolism and proliferation and so forth, which cannot be simply modeled based on energy consumption.

With the fitted parameter A , the distribution of glucose in tumor has also been obtained. The average concentration of glucose in the tumor was calculated and compared to the experimental results. Seen from Figures 4 and 5, the average concentrations of glucose tended to decrease which agreed well with the experimental results. There existed significant differences between experimental and numerical results, especially for the group under the long-term mild hyperthermia treatment. This was likely because in the present model only glucose consumption for cell proliferation was considered. There could be excessive supply of glucose from the conceivable blood vessels inside tumor and the decreased cellular uptake of glucose due to heat. A more sophisticated model taking these factors into consideration should be developed to accurately predict the glucose distribution in tumor tissue.

As there are no publications on the nutrition diffusion and cell uptake rate of 4T1 tumor cells, the data for EMT6/Ro tumor has been used. Although EMT6/Ro tumor cells are expected to possess similar properties, the dependence of these parameters on tumor species might also introduce some errors in the simulations. Therefore, parametric studies were performed and the influences on the glucose uptake rate and the diffusion coefficient were studied as shown in Figures 6 and 7. It was clear that the variation of tumor growth caused by 10% changes of either two factors was less than 5%.

In the present model, besides the Warburg effect, the influence of all other factors such as blood perfusion,

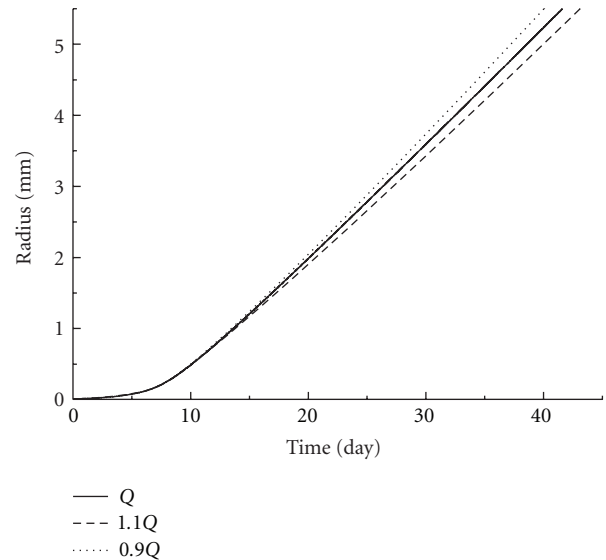


FIGURE 6: Parametric study of the tumor growth rate under different glucose uptake rates in tumor cells. Solid line stands for glucose uptake rate from reference [29]. Dot and dash lines represent 10% increase and decrease, respectively.

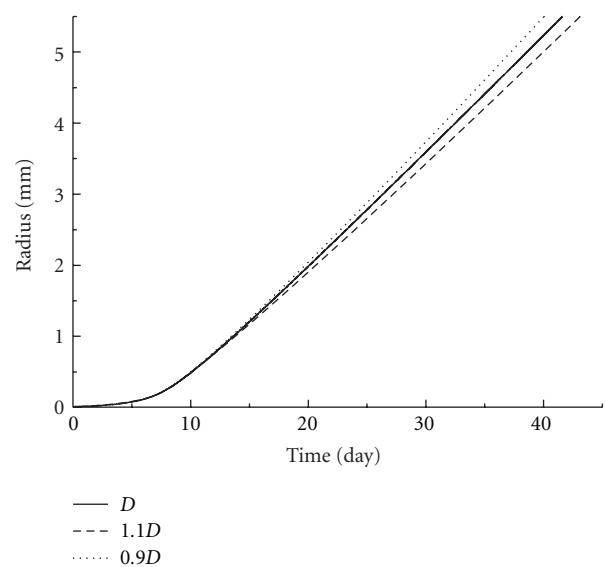


FIGURE 7: Parametric study of the tumor growth rate under different glucose diffusion coefficients in tumor tissue. Solid line stands for glucose diffusion value from reference [29]. Dot and dash lines represent 10% increase and decrease, respectively.

immunity, and other growth or necrosis factors, has been lumped into a simple parameter A . Using tumor growth data from the experimental studies, the maximum tumor cell growth rate *in vivo* under the normal condition was fitted to be $(18\text{ h})^{-1}$, and the linear tumor growth at the early stage was successfully modeled without consideration of cell death. The growth was found to be excessively inhibited by the long-term mild hyperthermia treatment. In fact, during the treatment, both the temperature gradient and inhomogeneity existed, and the higher temperature could impair tumor cells by denaturation or destruction of cellular membrane, cellular skeleton, and nucleus [48]. The long-term mild hyperthermia treatment might also affect the activities of enzymes in different pathways associated with tumor cell metabolism and proliferation, stimulate the immunology factors such as hsp70, which could arouse body system defense and eliminate tumor cells specifically [49]. Besides, Song's study [50] revealed that under mild hyperthermia ($41\sim 42^\circ\text{C}$, 30 min) blood perfusion in tumor tissue could increase 1.5~2 folds as compared to that prior to the treatment. Tumor vasculature is very sensitive to heat, as it is loosely organized and usually lacks of smooth muscles [51–54]. Tumor cells would suffer from starvation due to the damage of the angiogenesis. All these influences on tumor growth are not linear and could not be accurately represented by a single parameter. This warrants further investigation into more detailed modeling of the long-term hyperthermia effect on tumor growth in the near future.

4. Conclusion

An energy-based model linking tumor growth with cell proliferation rate has been developed in this study to investigate the hyperthermia treatment effect. In the model, the new understanding of the Warburg Effect was for the first time taken into account for tumor cellular metabolism regardless of the concentration of oxygen. The maximum cell growth rate was used as an integrated variable responding to changes under different environments. Trends of initial tumor growth and changes of the average glucose concentration in tumor were successfully modeled. The comparison of the maximum tumor cell growth rate has revealed a slowdown of tumor growth under the long-term mild hyperthermia condition. To accurately predict the tissue glucose level and the corresponding metabolites, especially under the long-term hyperthermia, the model needs to be further developed.

Acknowledgments

This work has been supported by the National Natural Science Foundation of China (NSFC51076095, NSFC50725622) and Shanghai Municipal Science and Technology Commission (10QA1403900).

References

- [1] A. Jemal, R. Siegel, E. Ward, Y. Hao, J. Xu, and M. J. Thun, "Cancer statistics, 2009," *CA Cancer Journal for Clinicians*, vol. 59, no. 4, pp. 225–249, 2009.

- [2] O. Abe, R. Abe, K. Enomoto et al., "Effects of radiotherapy and of differences in the extent of surgery for early breast cancer on local recurrence and 15-year survival: an overview of the randomised trials," *Lancet*, vol. 366, no. 9503, pp. 2087–2106, 2005.
- [3] B. Fisher, N. Gunduz, and E. A. Saffer, "Influence of the interval between primary tumor removal and chemotherapy on kinetics and growth of metastases," *Cancer Research*, vol. 43, no. 4, pp. 1488–1492, 1983.
- [4] K. Camphausen, M. A. Moses, W. D. Beecken, M. K. Khan, J. Folkman, and M. S. O'Reilly, "Radiation therapy to a primary tumor accelerates metastatic growth in mice," *Cancer Research*, vol. 61, no. 5, pp. 2207–2211, 2001.
- [5] N. L. Komarova, "Mathematical modeling of tumorigenesis: mission possible," *Current Opinion in Oncology*, vol. 17, no. 1, pp. 39–43, 2005.
- [6] T. W. Secomb, D. A. Beard, J. C. Frisbee, N. P. Smith, and A. R. Pries, "The role of theoretical modeling in microcirculation research," *Microcirculation*, vol. 15, no. 8, pp. 693–698, 2008.
- [7] T. Roose, S. J. Chapman, and P. K. Maini, "Mathematical models of avascular tumor growth," *SIAM Review*, vol. 49, no. 2, pp. 179–208, 2007.
- [8] A. K. Laird, "Dynamics of tumor growth," *British journal of cancer*, vol. 13, pp. 490–502, 1964.
- [9] R. C. Hu and X. G. Ruan, "A simple cellular automaton model for tumor-immunity system," in *Proceedings of the IEEE International Conference on Robotics, Intelligent Systems and Signal Processing*, vol. 1-2, pp. 1031–1035, 2003.
- [10] H. P. Greenspan, "Models for growth of a solid tumor by diffusion," *Applied Mathematics*, vol. 51, no. 4, pp. 317–340, 1972.
- [11] A. C. Burton, "Rate of growth of solid tumours as a problem of diffusion," *Growth, Development and Aging*, vol. 30, no. 2, pp. 157–176, 1966.
- [12] Y. Kim and A. Friedman, "Interaction of tumor with its micro-environment: a mathematical model," *Bulletin of Mathematical Biology*, vol. 72, no. 5, pp. 1029–1068, 2010.
- [13] H. M. Byrne and M. A. Chaplain, "Growth of nonnecrotic tumors in the presence and absence of inhibitors," *Mathematical Biosciences*, vol. 130, no. 2, pp. 151–181, 1995.
- [14] A. R. A. Anderson, "A hybrid mathematical model of solid tumour invasion: the importance of cell adhesion," *Mathematical Medicine and Biology*, vol. 22, no. 2, pp. 163–186, 2005.
- [15] L. Preziosi and A. Tosin, "Multiphase modelling of tumour growth and extracellular matrix interaction: mathematical tools and applications," *Journal of Mathematical Biology*, vol. 58, no. 4-5, pp. 625–656, 2009.
- [16] A. R. A. Anderson and M. A. J. Chaplain, "Continuous and discrete mathematical models of tumor-induced angiogenesis," *Bulletin of Mathematical Biology*, vol. 60, no. 5, pp. 857–899, 1998.
- [17] P. Macklin, S. McDougall, A. R. A. Anderson, M. A. J. Chaplain, V. Cristini, and J. Lowengrub, "Multiscale modelling and nonlinear simulation of vascular tumour growth," *Journal of Mathematical Biology*, vol. 58, no. 4-5, pp. 765–798, 2009.
- [18] J. A. Adam, "Mathematical models of prevascular spheroid development and catastrophe-theoretic description of rapid metastatic growth/tumor remission," *Invasion and Metastasis*, vol. 16, no. 4-5, pp. 247–267, 1996.
- [19] A. M. Stein, T. Demuth, D. Mobley, M. Berens, and L. M. Sander, "A mathematical model of glioblastoma tumor spheroid invasion in a three-dimensional in vitro experiment," *Biophysical Journal*, vol. 92, no. 1, pp. 356–365, 2007.

- [20] D. Grecu, A. S. Carstea, A. T. Grecu et al., “Mathematical modelling of tumor growth,” *Romanian Reports in Physics*, vol. 59, no. 2, pp. 447–455, 2007.
- [21] Y. Jiang, J. Pjesivac-Grbovic, C. Cantrell, and J. P. Freyer, “A multiscale model for avascular tumor growth,” *Biophysical Journal*, vol. 89, no. 6, pp. 3884–3894, 2005.
- [22] J. A. Sherratt and M. A. J. Chaplain, “A new mathematical model for avascular tumour growth,” *Journal of Mathematical Biology*, vol. 43, no. 4, pp. 291–312, 2001.
- [23] J. P. Ward and J. R. King, “Mathematical modelling of avascular-tumour growth,” *IMA Journal of Mathematics Applied in Medicine and Biology*, vol. 14, no. 1, pp. 39–69, 1997.
- [24] J. P. Ward and J. R. King, “Mathematical modelling of avascular-tumour growth II: modelling growth saturation,” *IMA Journal of Mathematics Applied in Medicine and Biology*, vol. 16, no. 2, pp. 171–211, 1999.
- [25] J. J. Casciari, S. V. Sotirchos, and R. M. Sutherland, “Mathematical modelling of microenvironment and growth in EMT6/Ro multicellular tumour spheroids,” *Cell Proliferation*, vol. 25, no. 1, pp. 1–22, 1992.
- [26] M. A. J. Chaplain and B. D. Sleeman, “A mathematical model for the growth and classification of a solid tumor: a new approach via nonlinear elasticity theory using strain-energy functions,” *Mathematical Biosciences*, vol. 111, no. 2, pp. 169–215, 1992.
- [27] M. A. J. Chaplain, “Avascular growth, angiogenesis and vascular growth in solid tumours: the mathematical modelling of the stages of tumour development,” *Mathematical and Computer Modelling*, vol. 23, no. 6, pp. 47–87, 1996.
- [28] J. J. Casciari, S. V. Sotirchos, and R. M. Sutherland, “Glucose diffusivity in multicellular tumor spheroids,” *Cancer Research*, vol. 48, no. 14, pp. 3905–3909, 1988.
- [29] R. Venkatasubramanian, M. A. Henson, and N. S. Forbes, “Incorporating energy metabolism into a growth model of multicellular tumor spheroids,” *Journal of Theoretical Biology*, vol. 242, no. 2, pp. 440–453, 2006.
- [30] O. Warburg, “On the origin of cancer cells,” *Science*, vol. 123, pp. 309–314, 1956.
- [31] O. Warburg, *The Prime Cause and Prevention of Cancer*, Konrad Triltsch, Würzburg, Germany, 1969.
- [32] M. G. V. Heiden, L. C. Cantley, and C. B. Thompson, “Understanding the warburg effect: the metabolic requirements of cell proliferation,” *Science*, vol. 324, no. 5930, pp. 1029–1033, 2009.
- [33] C. V. Dang and G. L. Semenza, “Oncogenic alterations of metabolism,” *Trends in Biochemical Sciences*, vol. 24, no. 2, pp. 68–72, 1999.
- [34] L. M. Postovit, M. A. Adams, G. E. Lash, J. P. Heaton, and C. H. Graham, “Oxygen-mediated regulation of tumor cell invasiveness—involvement of a nitric oxide signaling pathway,” *Journal of Biological Chemistry*, vol. 277, no. 38, pp. 35730–35737, 2002.
- [35] J. Bussink, J. H. A. M. Kaanders, and A. J. Van Der Kogel, “Tumor hypoxia at the micro-regional level: clinical relevance and predictive value of exogenous and endogenous hypoxic cell markers,” *Radiotherapy and Oncology*, vol. 67, no. 1, pp. 3–15, 2003.
- [36] R. A. Gatenby and R. J. Gillies, “Why do cancers have high aerobic glycolysis?” *Nature Reviews Cancer*, vol. 4, no. 11, pp. 891–899, 2004.
- [37] M. C. Brahim-Horn and J. Pouyssegur, “Oxygen, a source of life and stress,” *FEBS Letters*, vol. 581, no. 19, pp. 3582–3591, 2007.
- [38] P. P. Hsu and D. M. Sabatini, “Cancer cell metabolism: warburg and beyond,” *Cell*, vol. 134, no. 5, pp. 703–707, 2008.
- [39] B. S. Peskin and M. J. Carter, “Chronic cellular hypoxia as the prime cause of cancer: what is the de-oxygenating role of adulterated and improper ratios of polyunsaturated fatty acids when incorporated into cell membranes?” *Medical Hypotheses*, vol. 70, no. 2, pp. 298–304, 2008.
- [40] R. Moreno-Sánchez, S. Rodríguez-Enríquez, A. Marín-Hernández, and E. Saavedra, “Energy metabolism in tumor cells,” *FEBS Journal*, vol. 274, no. 6, pp. 1393–1418, 2007.
- [41] R. J. DeBerardinis, J. J. Lum, G. Hatzivassiliou, and C. B. Thompson, “The biology of cancer: metabolic reprogramming fuels cell growth and proliferation,” *Cell Metabolism*, vol. 7, no. 1, pp. 11–20, 2008.
- [42] Y. Chen, R. Cairns, I. Papandreou, A. Koong, and N. C. Denko, “Oxygen consumption can regulate the growth of tumors, a new perspective on the Warburg effect,” *PLoS One*, vol. 4, no. 9, Article ID e7033, 2009.
- [43] P. R. Stauffer and S. N. Goldberg, “Introduction: thermal ablation therapy,” *International Journal of Hyperthermia*, vol. 20, no. 7, pp. 671–677, 2004.
- [44] A. Chicheł, J. Skowronek, M. Kubaszewska, and M. Kanikowski, “Hyperthermia-Description of a method and a review of clinical applications,” *Reports of Practical Oncology and Radiotherapy*, vol. 12, no. 5, pp. 267–275, 2007.
- [45] J. R. Oleson, M. W. Dewhirst, J. M. Harrelson, K. A. Leopold, T. V. Samulski, and C. Y. Tso, “Tumor temperature distributions predict hyperthermia effect,” *International Journal of Radiation Oncology Biology Physics*, vol. 16, no. 3, pp. 559–570, 1989.
- [46] J. R. Lepock, “Cellular effects of hyperthermia: relevance to the minimum dose for thermal damage,” *International Journal of Hyperthermia*, vol. 19, no. 3, pp. 252–266, 2003.
- [47] M. Na, C. Chao, Z. Ai-li et al., “Thermal environmental effect on breast tumor growth,” *Journal of Shanghai Jiaotong University*, vol. 27, no. 5, pp. 501–505, 2009.
- [48] J. L. R. Roti, H. H. Kampinga, R. S. Malyapa et al., “Nuclear matrix as a target for hyperthermic killing of cancer cells,” *Cell Stress and Chaperones*, vol. 3, no. 4, pp. 245–255, 1998.
- [49] J. Dong, P. Liu, and L. X. Xu, “Immunologic response induced by synergistic effect of alternating cooling and heating of breast cancer,” *International Journal of Hyperthermia*, vol. 25, no. 1, pp. 25–33, 2009.
- [50] C. W. Song, “Effect of local hyperthermia on blood flow and microenvironment: a review,” *Cancer Research*, vol. 44, no. 10, supplement, pp. S4721–S4730, 1984.
- [51] C. W. Song, A. Lokshina, and J. G. Rhee, “Implication of blood flow in hyperthermic treatment of tumors,” *IEEE Transactions on Biomedical Engineering*, vol. 31, no. 1, pp. 9–16, 1984.
- [52] H. Maeda, J. Wu, T. Sawa, Y. Matsumura, and K. Hori, “Tumor vascular permeability and the EPR effect in macromolecular therapeutics: a review,” *Journal of Controlled Release*, vol. 65, no. 1–2, pp. 271–284, 2000.
- [53] D. T. Connolly, D. M. Heuvelman, R. Nelson et al., “Tumor vascular permeability factor stimulates endothelial cell growth and angiogenesis,” *Journal of Clinical Investigation*, vol. 84, no. 5, pp. 1470–1478, 1989.
- [54] Y. Shen, A. Zhang, and L. X. Xu, “Mechanical study on tumor microvessel damage induced by alternate cooling and heating treatment,” in *Proceedings of the 11th ASME Summer Bioengineering Conference (SBC’09)*, part A and B, pp. 593–594, June 2009.

- [55] J. P. Freyer and R. M. Sutherland, "Regulation of growth saturation and development of necrosis in EMT6/Ro multicellular spheroids by the glucose and oxygen supply," *Cancer Research*, vol. 46, no. 7, pp. 3504–3512, 1986.

Research Article

Atomic Radiations in the Decay of Medical Radioisotopes: A Physics Perspective

B. Q. Lee, T. Kibédi, A. E. Stuchbery, and K. A. Robertson

Department of Nuclear Physics, Research School of Physics and Engineering, The Australian National University, Canberra, ACT 0200, Australia

Correspondence should be addressed to T. Kibédi, tibor.kibedi@anu.edu.au

Received 21 March 2012; Revised 17 May 2012; Accepted 17 May 2012

Academic Editor: Eva Bezak

Copyright © 2012 B. Q. Lee et al. This is an open access article distributed under the Creative Commons Attribution License, which permits unrestricted use, distribution, and reproduction in any medium, provided the original work is properly cited.

Auger electrons emitted in nuclear decay offer a unique tool to treat cancer cells at the scale of a DNA molecule. Over the last forty years many aspects of this promising research goal have been explored, however it is still not in the phase of serious clinical trials. In this paper, we review the physical processes of Auger emission in nuclear decay and present a new model being developed to evaluate the energy spectrum of Auger electrons, and hence overcome the limitations of existing computations.

1. Introduction

Unstable atomic nuclei release excess energy through various radioactive decay processes by emitting radiation in the form of particles (neutrons, alpha, and beta particles) or electromagnetic radiation (gamma-ray photons). Most of the applications using nuclear isotopes are based on the fact that the interaction of the radiations passing through material will depend on their type (photons, neutral, or charged particles) and the transferred energy. Most radioisotopes used in clinical therapy emit β particles, which are ionizing radiations. The biological effect is often characterized by the so-called *linear energy transfer*, LET, expressed in units of $\text{keV}/\mu\text{m}$, which is a measure of the energy deposited along the particle track. A new class of radionuclides [1], including Tb^{149} , Bi^{213} , Po^{211} , At^{211} , Ra^{223} , Ac^{225} , Ac^{227} , Th^{226} , and U^{230} , which emit α particles (made up of two protons and two neutrons) have been considered for therapy. The LET for most therapeutic α emitters ranges from 25 to $230 \text{ keV}/\mu\text{m}$. On the other hand, electrons and positrons emitted in nuclear β decay, and in the internal conversion processes, referred to here as β particles, have kinetic energies ranging from tens of keV to several MeV and their LET is much lower, typically $\sim 0.2 \text{ keV}/\mu\text{m}$.

A third type of ionizing radiation is Auger electrons [2], named after the French physicist Pierre Victor Auger. When an inner-shell electron is removed from an atom,

the vacancy will be filled by an electron from the outer shells and the excess energy will be released as an X-ray photon, or by the emission of an Auger electron. Referred to as atomic radiations, X-ray and Auger electron emission are competing processes. The atomic transition rates, and whether X-ray or Auger emission is dominant, depend on the atomic number, the electron shells involved, and the electron configuration of the atom. The full relaxation of the inner-shell vacancy is a multistep process, resulting in a cascade of atomic radiations. The energy of emitted X-rays and/or Auger electrons depends on the atomic number, the electron shells and electron configuration involved, and is typically in the range from a few eV to 100 keV. Due to their short range (nm to μm), Auger electrons with relatively low energies can have a much higher LET. For example, for electron energies below 1 keV the LET peaks at around $26 \text{ keV}/\mu\text{m}$ [3]. In comparison to α or β particles, Auger electrons have a much shorter range in material, which makes them ideal tools for targeted radiation therapy [4]. Figure 1 shows a pictorial comparison of the interaction sites for these three types of ionizing radiation.

Since the early 70s, when the use of Auger electrons for cancer therapy was first suggested (see the review by Howell [5]), considerable advances have been made in the understanding of the radiobiological effect of low-energy electrons. The use of Auger emitters for radiation therapy is often cited in the literature as a viable option, however the

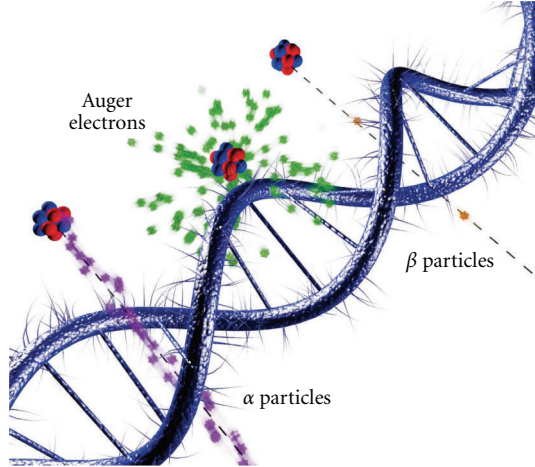


FIGURE 1: Interactions of ionizing radiations on the scale of DNA. (Courtesy of Thomas Tunningley, ANU).

clinical research is still yet to come. According to the recent review of Buchegger et al. [4], the three main requirements of this type of targeted therapy are: (i) suitable tumor selective agent to bind the radioactive material to the tumor cells, (ii) consecutive internal irradiation cycles, and (iii) reduction of unwanted radiation damage outside the living cancer tissue. To address all these aspects would require a complex approach, however in this paper we will only focus on the physical processes required to evaluate the Auger emission in nuclear decay. We start our discussion with an overview of the current knowledge; then we propose a new approach to overcome the limitations of the current computations used for low-energy Auger emission from medical isotopes.

2. Radioactive Decay Processes

When a vacancy is created in an inner electron shell, the residual atom is left in an excited state. Such a vacancy can be created by photoionization, ion-atom collisions, electron bombardment, electron capture (EC), or internal conversion electron (CE) processes. EC and CE are the only processes which involve nuclear decays and changes in nuclear structure. Typical atomic events involving the K -shell are shown in Figure 2.

In electron capture the nucleus decays by absorbing an atomic electron and emitting a neutrino



The condition for electron capture decay is

$$E_\nu = Q^+ - E_i - E_X > 0, \quad (2)$$

where Q^+ is the energy difference in atomic masses between parent and daughter ground states, E_i is the energy of the final nuclear state in the daughter nucleus, and E_X is the binding energy of the captured electron, X . The released energy, E_ν , will be shared by the emitted neutrino and, if applicable, the Bremsstrahlung photon or shaking

electron. For allowed transitions nearly all vacancies occur on the s shells (K , L_1 , M_1 , etc.) with the inner-most shells dominating. Comprehensive compilations of the relevant electron capture probability ratios for the K , L , M , N , and O shells were presented by Schönfeld [6]. Leaving aside the effect of β^+ decay, which may compete with electron capture, the basic relation between the subshell capture ratios (P_X) is

$$P_K + P_L + P_M + P_N + P_O = 1. \quad (3)$$

The individual terms can be calculated from their ratios. For example, for P_K we get

$$P_K = \left\{ 1 + \frac{P_L}{P_K} \left[1 + \frac{P_M}{P_L} \left(1 + \frac{P_N}{P_M} \left(1 + \frac{P_O}{P_N} \right) \right) \right] \right\}^{-1}, \quad (4)$$

and one can obtain the P_L/P_K ratio as

$$\frac{P_L}{P_K} = k_{LK} \times \left(\frac{\Delta E - E_{L1}}{\Delta E - E_K} \right)^2, \quad (5)$$

where the k_{LK} factors are tabulated in [6], and ΔE is the energy difference between the parent and daughter states. For allowed and nonunique first forbidden transitions, the dominant contribution is from the K , L_1 , M_1 , and N_1 shells, however, the contributions of the L_2 , M_2 , and N_2 shells should not be neglected. The L_1/L_2 ratios can be calculated from amplitudes of the bound electron radial wave functions [7].

Nuclei undergoing electromagnetic decays will emit γ -rays, internal conversion electrons, or if the transition energy is higher than twice the electron rest mass, electron-positron pairs. In the internal conversion process an atomic electron is ejected from one of the atomic shells. The electron conversion coefficient is defined as the ratio of the probabilities of the emission of atomic electrons from shell X (P_X) to the emission of γ -rays (P_γ):

$$\alpha_X = \frac{P_X}{P_\gamma}. \quad (6)$$

The kinetic energy of the electron, $E_{CE,X}$, can be deduced from the transition energy, E_{tr} , and the binding energy of the atomic shell, $E_{BE,X}$, as follows:

$$E_{CE,X} = E_{tr} - E_{BE,X} - E_{recoil}, \quad (7)$$

where E_{recoil} is the recoil energy of the emitting atom, which in most cases is very small. Transitions involving conversion electrons are only possible if $E_{CE,X} > 0$. For example, the 2.1726 keV transition from the decay of Tc^{99m} can only proceed with internal conversion from the M_1 and higher shells. Theoretical internal conversion electron emission rates can be obtained from [8].

3. X-Rays and Auger Electrons

It is customary to assume that the radioactive atom initially is in the neutral, ground state electronic configuration. Immediately after an electron capture or internal conversion event,

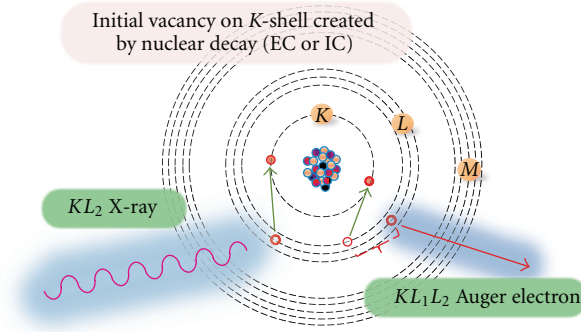


FIGURE 2: Relaxation of a vacancy in the K shell by X-ray and Auger emission.

the atom will be excited. In 1923, Rosseland [9] postulated that the atom relaxes via both radiative and nonradiative processes. Radiative processes will involve the emission of X-rays with characteristic energies as the atomic electrons are reorganized to fill the vacancy. In X-ray emission, an electron in an outer shell, Y , makes a transition to a vacancy in the inner shell, X , and the emitted energy of the X-ray is

$$E_{XY} = E_{BE,X} - E_{BE,Y}, \quad (8)$$

where $E_{BE,X}$ and $E_{BE,Y}$ are the binding energies of the atomic shells involved. The fluorescence yield, ω_X , is defined as the number of radiative (X-ray) transitions per vacancy in any shell or subshell X . Considering all possible shells, subshells, Y , involved in filling the vacancy on the K shell (X is equal to K -shell), the X-ray yield, Y_{KY} can be expressed as

$$Y_{KY} = f_K \omega_K N_{KY}, \quad (9)$$

where f_K is the number of primary vacancies on the K -shell, and N_{KY} is the relative intensity of various X-ray transitions with $\sum N_{KY} = 1$.

Pierre Auger made the first confirmed experimental observation of the nonradiative process in 1925 [2]. Nonradiative processes (also called “*radiationless processes*” or the “*Auger effect*”) similarly involve the redistribution of atomic electrons but result in the emission of an atomic electron (Auger electron). The Auger electron process XYZ involves three electron (sub-)shells. An electron in an outer shell, Y , makes a transition to the vacancy in an inner shell, X , and an electron in outer shell Z is ejected. The energy of the Auger electron can be expressed as:

$$E_{XYZ} = E_{BE,X} - E_{BE,Y} - E_Z^Y, \quad (10)$$

where $E_{BE,X}$ and $E_{BE,Y}$ are the neutral atom binding energies for shell X and Y . E_Z^Y is the binding energy of an electron on the Z -shell when the atom is already ionized with a single vacancy on the atomic shell Y . This process will result in vacancies in both the Y and Z shells from a single initial vacancy in the X shell. For example, if X is the K -shell, Y the L_1 subshell, and Z the L_2 subshell the electron is called a KL_1L_2 Auger electron. In Coster-Kronig (CK) transitions one of the final vacancies is in the same principal shell (Y)

as the initial vacancy (X). Similarly to (9) the Auger electron yield can be expressed as

$$Y_{KYZ} = f_K(1 - \omega_K)N_{KYZ}, \quad (11)$$

where N_{KYZ} is the relative intensity of various Auger transitions with $\sum \sum N_{KYZ} = 1$. The sums are over all energetically possible Y and all possible Z with binding energies $E_{BE,Y} \geq E_{BE,Z}$.

4. Vacancy Propagation

The rearrangement of the atomic structure will continue until all primary, secondary, and subsequent vacancies are filled by the emission of X-rays and Auger electrons, or until no more transitions are energetically possible. In the latter case, the vacancy has reached the valence shell. This is the region where solid state, or chemical effects might be dominant. The correct treatment of such effects is beyond the scope of the present paper.

The full relaxation of the initial vacancy created in the nuclear event (Section 2) is a multistep process. While the fundamental physical picture of the individual atomic transitions remains similar to the one described above, the atomic structure will continuously change. This change will affect both the atomic-binding energies and transition rates.

Considering the number of possible atomic configurations, the procedure of evaluating the atomic radiation spectrum becomes very complex. Table 1 compares the various calculated Auger electron yields of radioisotopes of medical importance. These include Tc^{99m} , In^{111} , $I^{123,125}$, and Tl^{201} . The table contains six calculations, which follow two fundamentally different approaches. The key features of the relevant physical data and assumptions are also listed and will be discussed below.

In the so-called “*deterministic approach*” (DET and DET++), the contributions from filling each vacancy are computed using closed formulae, similar to (9) and (11). Provided that all relevant transition rates are known, this approach has very small computational requirements and it was used by the Radiation Dose Assessment Resource (RADAR) [10, 11], the Decay Data Evaluation Project (DDEP) [12], and Eckerman and Endo [13]. This approach

TABLE 1: Calculated Auger electron yields for selected medical radioisotopes.

	RADAR [10, 11]	DDEP [12]	Eckerman and Endo [13]	Howell [14]	Stepanek [15]	Pomplun [16]	Present study
Nuclear decay data ^(a)	ENSDF	DDEP	ENSDF	ENSDF	ENSDF	ICRP38	ENSDF
Conversion coefficients	[17]	[8, 18]	[18, 19]	[18]	[15]	[17, 20, 21]	[8]
Electron capture ratios	[22]	[23]	[24]	[22, 25]	[22, 25]	[22]	[23]
Atomic shells	K, L	K, L	K–O	K–O	K–N	K–N	K–R
Atomic transition rates ^(b)	[7, 26]	[27–29]	[30, 31]	[32–35] (A)	[30]	[32–34] (A)	[30]
	RADLST	EMISSION	EDISTR04	[27, 36] (X)		[37, 38] (X)	
Atomic transition energies ^(c)	NAB [39]	SE [40]	NAB [30]	Z/Z + 1(A) NAB (X)	DF	DF [41]	DF [42]
Vacancy propagation ^(d)	DET	DET	DET++	MC	MC	MC	MC
Charge neutralization	No	No	No	Yes	No	No	No
Auger electron yield per nuclear decay							
^{99m} Tc (6.007 h)	0.122	0.13	4.363	4.0		2.5	3.37
¹¹¹ In (2.805 d)	1.136	1.16	7.215	14.7	6.05		5.75
¹²³ I (13.22 h)	1.064	1.08	13.71	14.9		6.4	
¹²⁵ I (59.4 d)	1.77	1.78	23.0	24.9	15.3		
²⁰¹ Tl (3.04 d)	0.773	0.614	20.9	36.9			

^(a)ENSDF: evaluated nuclear structure file [43]; DDEP: decay data evaluation project [12]; ICRP38: international commission on radiological protection [44].

^(b)Computer codes: RADLST by Burrows [26], EMISSION by Schönfeld and Janßen [45], and EDISTR04 by Endo et al. [46]; (A): Auger electrons, (X): X-rays.

^(c)Transition energies deduced from: NAB: neutral atom binding energies; SE: semiempirical Auger energies $Z/Z + 1$ approximated from neutral atom binding energies [47]; DF: relativistic Dirac-Fock calculations.

^(d)Approach to treat vacancy cascades: DET: deterministic, using closed formulae; DET++: deterministic, using up to 3000 possible transitions; MC: Monte Carlo approach.

is quite reasonable and simple for transitions involving vacancies on the K and L shells. However a more realistic description must include the outer shells and hence requires that a very large number of transitions be considered. A set of approximating formulae were presented in the pioneering work of Dillman [48] to evaluate the L - and M -series atomic radiations. Dillman used a rather coarse approach, which assumed that these radiations carry a low total energy and may be treated as a “single group” [48]. This work led to the development of the EDISTR code [48] to evaluate the complete spectrum of atomic radiations. Recently, Endo et al. [46] have further improved the EDISTR code. In general, the accuracy of these “deterministic predictions” largely depends on the inclusion of outer shells.

An alternative approach is to base the calculations on “Monte Carlo” (MC) techniques, which prove to be better suited to the inclusion of all possible paths in the relaxation process. Such simulations begin with the selection of the nuclear decay process and the consequent creation of the initial vacancy. During the propagation of the initial vacancy, the next transition is randomly selected from all available atomic transitions, using the transition rates as weighting factors. Table 1 includes results from Howell [14], Stepanek [15], and a very recent calculation by Pomplun [16]. As indicated in the table, the Monte Carlo approach allows the incorporation of all atomic shells with the potential to produce low-energy Auger electrons with high radiotoxicity.

Common in both approaches is the necessity to know all relevant transition energies and transition rates. All 6 calculations listed in Table 1 use transition rates from existing tabulations based on a combination of experimental data, systematics (obtained by interpolation and extrapolation), as well as theoretical calculations, which often used different assumptions, wave functions, and so forth. The two most often cited works are from Bambynek et al. [7] and the Evaluated Atomic Data Library, EADL, by Perkins et al. [30]. Most of the data presented in these compilations are for cases when there is a single vacancy on one of the atomic shells. In an effort to compensate for this limitation, the calculations presented in Table 1 have employed various corrections. One of these is the so-called Krause-Carlson correction [49], which takes into account the effect of multiple vacancies on a shell accumulated in the course of the relaxation process. Most of these calculations neglect the shakeup and shakeoff effects, which might be significant for transition rates when a vacancy is created on the outermost shells [50].

The transition energies are usually derived from atomic binding energies. As for the transition rates, the atomic binding energies are also affected by changes in the atomic configuration occurring during the relaxation process. Some of the calculations listed in Table 1 simply use neutral atom-binding energies (NAB) or semiempirical values (SE) from Larkins [40]. Others use the $Z/Z + 1$ rule [47] to estimate the Auger electron energies. Only the two most recent

Monte Carlo approaches (Stepanek [15] and Pomplun [16]) use theoretical values obtained from relativistic Dirac-Fock calculations.

In summary, existing computations of Auger electron spectra are far from complete. Most of them are based on transition rates and transition energies obtained for single vacancies. It is also evident that the correct treatment of the relevant transition energies and rates requires a much more sophisticated computational approach than was available twenty or more years ago, when the EADL data base was developed.

5. New Ab Initio Calculations of Auger Transition Rates

The starting point to fully explore the potential of the targeted Auger-electron-based therapy is an accurate description of the relevant atomic radiation spectrum from the decaying radioisotopes. Recognizing the lack of a consistent theoretical model, the August 2011 IAEA special meeting on Intermediate-term Nuclear Data Needs for Medical Applications [51] concluded that: “A comprehensive calculational route also needs to be developed to determine the energies and emission probabilities of the low-energy X-rays and Auger electrons to a higher degree of detail and consistency than is available at present.” The document identifies a number of radioisotopes as potential candidates for targeted microdosimetry at the cellular level: Ga⁶⁷, Ge⁷¹, Br⁷⁷, Tc^{99m}, Pd¹⁰³, In¹¹¹, I¹²⁵, Nd¹⁴⁰, Ta¹⁷⁸, Pt^{193m}, Pt^{195m}, and Hg¹⁹⁷. The document also concludes that for many of these isotopes further experimental studies and rigorous assessments of the existing nuclear structure information are also required.

To improve the understanding of the atomic radiation spectra in nuclear decay a new approach is required, which should use new theoretical transition energies and rates. In addressing this need we propose to adopt the following protocol for a new Monte Carlo approach.

- (a) *Nuclear structure data* will be extracted from the Evaluated Nuclear Structure File (ENSDF) [43]. ENSDF is maintained regularly and this will ensure the use of the most up-to-date information to evaluate the nuclear event.
- (b) *Electron capture rates* will be taken from the Schönfeld compilation [6] and subshell electron capture ratios will be calculated from (4) and (5).
- (c) *Internal conversion coefficients* (ICC) will be taken from *BrIcc* [8]. The ICC values in that tabulation were calculated using relativistic Dirac-Fock wave functions. It is important to note that most of the previous ICC calculations assumed that the atomic vacancy created in the conversion process is filled instantly. Therefore, the conversion coefficients were calculated for the neutral atom. High-precision experimental conversion coefficients [52] indicate that the effect of the atomic vacancy should be taken into account. It is particularly important for cases when the transition energies are close to one

of the shell binding energies, where the conversion coefficient is larger, and therefore the yield of atomic radiations is larger too. *BrIcc* uses the so called “Frozen Orbital” approximation [42] to take into account the effect of the atomic vacancy. The *BrIcc* data tables cover all atomic shells and transition energies starting from 1 keV above the shell-binding energies and continuing up to 6000 keV.

- (d) *Auger and X-ray transition energies and rates* will be calculated using the most recent version of the General Purpose Relativistic Atomic Structure program, GRASP2K [53] and the Relativistic Atomic Transition and Ionization Properties, RATIP [54] codes. The RATIP program package was developed in the late 90s for the calculation of atomic transition and ionization properties for atoms with arbitrary charge/vacancy distributions [55], similar to those expected during the vacancy propagation process. Calculations will be carried out at every propagation step for the actual atomic configuration of the ionized atom. The calculated rates and energies together with the atomic configuration will be stored, so CPU intensive calculations need not be repeated.
- (e) The vacancy creation and the atomic relaxation processes from *EC decay* and from *internal conversion* will be treated independently. In all practical cases IC takes place *after* the daughter atom is fully relaxed following an EC event, so internal conversion takes place in a neutral atom. This assumption is not valid in rare cases wherein the nuclear level half-life of the daughter nucleus is much shorter than the time needed for the atom to fully relax. For example, a shift of 20 ± 7 eV of the *K* conversion electron line of the 963 keV transition in the electron capture decay of Eu^{152m} [56] is one of the few experimental observations of this rare scenario. Depending on the level scheme, the radioactive decay may produce multiple electromagnetic transitions, which depending on the conversion coefficient may proceed with the emission of multiple conversion electrons. There is a finite, usually very small probability, that a second conversion electron is emitted before the vacancy created in the first conversion process could fully relax. Based on the average nuclear and atomic half-lives, it is a very unlikely event, and it will not be considered in our model.
- (f) The *ab initio treatment of the propagation process* including the random sampling of the available decay channels will ensure the realistic evaluation of the atomic spectra. A key element of the proposed model is the use of transition energies and transition rates calculated for the given atomic configuration (see (d) above). While in terms of computing requirements this is an expensive approach, it should improve the accuracy of the model.
- (g) The *atom is assumed to be free*, and any influence from the chemical environment or solid-state effects

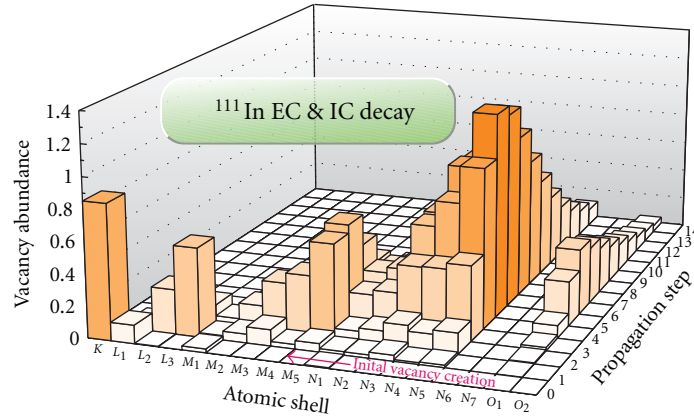


FIGURE 3: Vacancies created during the relaxation process in In^{111} .

is neglected. In our model the propagation of a particular vacancy will be terminated if there is no higher state energetically available, or if it has reached the valence shell. However the propagation of the event is not complete while there are any inner vacancies still left; the propagation of these vacancies will continue until all have reached the valence shell. In contrast, Howell [14] has assumed that once a vacancy reaches the valence shell, it will be immediately neutralized by absorbing electrons from the neighboring environment. There is strong evidence that this assumption is not correct. Specifically, the Auger cascade takes about 10^{-16} to 10^{-14} s to complete, and as pointed out recently by Robertson [57] and Pomplun [16], the proposed neutralization process is too slow to have an effect on the much faster propagation process. In the proposed model it will therefore be assumed that the vacancies on the valence shell(s) will remain unfilled throughout the entire atomic relaxation process. The atomic processes involved in neutralization of the ionized atom at the end of the above vacancy propagation would go beyond the scope of the present study.

It also should be noted that in many medical applications, the radioactive nuclide is attached to a molecule, which will affect the atomic transition energies and rates, particularly for the outermost shells. None of the previous calculations listed in Table 1 consider this effect. The relativistic multiconfiguration Dirac-Fock method we propose to use has the potential to incorporate the chemical environment, however, at least initially, this option will not be considered in our model.

6. Pilot Study

To explore the implications of this new approach, a *pilot model* was developed. This model follows the proposed approach, except that fixed atomic transition rates were taken from the EADL [30] data base. EADL contains X-ray, Auger electron (including Coster-Kronig and super Coster-Kronig) transition probabilities and energies for an atom with

a single vacancy. These were calculated with a Dirac-Hartree-Slater method using j - j coupling. These calculations use semiempirical corrections to improve the accuracy for low-energy Coster-Kronig transitions. Since the EADL contains the most complete atomic data available to date, and since it describes the total transition rates correctly, it was adopted for the pilot model. However, the transition energies from EADL have been replaced with values deduced from binding energies calculated at each propagation step using the RAINE Dirac-Fock code [42]. The RAINE code tends to slightly overestimate the binding energies of the inner shells and this results in some of the K Auger lines appearing above their experimental values [57, 58]. Transitions with negative energies, that is, energetically not allowed, were excluded. This approach, at least on the superficial level, takes into account the effect of the presence of multiple vacancies and should improve the accuracy of the transition energies.

Using the pilot model, detailed calculations have been carried out for two of the isotopes listed in Table 1: $\text{Tc}^{99\text{m}}$ and In^{111} . Figure 3 shows the abundance of atomic vacancies for each atomic shell during the atomic vacancy cascade. Vacancy creation from the nuclear decay occurs at step "0," and events with up to 14 propagation steps are indicated. The plot was generated by evaluating 1,000,000 EC decays of In^{111} , one of the commonly used radioisotopes for nuclear imaging. More than 97.5% of the initial vacancies are from electron capture on the K - and L_1 -shells. Closer examination of the graph reveals how the vacancies "*migrate*" towards the outer shells. For most of the events, the created vacancies take 7 or 8 propagation steps to reach the outer shells. Beyond that number of propagation steps, the vacancy abundance in Figure 3 shows a decrease because events with more steps become increasingly unlikely. Some key features of the propagation process include: the highest abundances of the vacancies are on the last subshell of each principal shell: L_3 , M_5 , and N_5 . (N_6 and N_7 are not occupied.) As the vacancies approach the outer shells (M and N) they are retained longer; that is, they are more likely to survive for several propagation steps.

In Tables 2 and 3, the nuclear and atomic transition energies and yields obtained for $\text{Tc}^{99\text{m}}$ and In^{111} are compared

TABLE 2: Average radiation yields and energies of ^{99m}Tc . For every entry the first line contains the energies in keV, and the second line (in italics) contains the emission probabilities.

	RADAR [10, 11]	DDEP [12]	Eckerman and Endo [13]	Howell [14]	Pomplun [16]	Present study (pilot model)
Nuclear radiations						
γ_1		2.1726(4)			2.1	2.1726(4)
		<i>7.4(2)E - 9</i>			<i>1.05E - 2</i>	<i>7.3(2)E - 9</i>
CE - M	1.6	[1.628 : 1.919]	1.748	1.82	1.779 ^(a)	1.781
	<i>7.46E - 1</i>	<i>8.80(24)E - 1</i>	<i>8.62E - 1</i>	<i>9.91E - 1</i>	<i>9.14E - 1</i>	<i>8.75E - 1</i>
CE - N		[2.104 : 2.170]	2.173		2.060 ^(a)	2.139
		<i>1.17(3)E - 1</i>	<i>1.30E - 1</i>		<i>7.53E - 2</i>	<i>1.15E - 1</i>
CE - O						2.166
						<i>2.50E - 6</i>
γ_2	140.5	140.511(1)	140.5	141	140.5	140.511(1)
	<i>8.906E - 1</i>	<i>8.85(2)E - 1</i>	<i>8.91E - 1</i>	<i>8.89E - 1</i>	<i>9.012E - 1</i>	<i>8.906E - 1</i>
CE - K	119.5	119.467(1)	119.5	119	119.4	119.467
	<i>8.80E - 2</i>	<i>9.20(27)E - 2</i>	<i>8.92E - 2</i>	<i>8.43E - 2</i>	<i>8.440E - 2</i>	<i>8.79E - 2</i>
CE - L	137.5	[137.468 : 137.834]	137.5 ^(a)	137	137.4 ^(a)	137.494
	<i>1.07E - 2</i>	<i>1.142(35)E - 2</i>	<i>1.087E - 2</i>	<i>1.36E - 2</i>	<i>1.14E - 2</i>	<i>1.07E - 2</i>
CE - M	140.0	[139.967 : 140.258]	140.1	140	140.1 ^(a)	139.977
	<i>1.9E - 3</i>	<i>2.09(6)E - 3</i>	<i>1.99E - 3</i>	<i>3.70E - 3</i> ^(b)	<i>2.70E - 3</i>	<i>1.94E - 3</i>
CE - N				140.5	140.4	140.4
				<i>3.80E - 4</i>	<i>3.00E - 4</i>	<i>3.13E - 4</i>
CE - O						140.5
						<i>2.13E - 5</i>
γ_3	142.6	142.683(1)				142.683(1)
	<i>2E - 4</i>	<i>2.3(2)E - 4</i>				<i>2.5(2)E - 4</i>
CE - K	121.6	121.631(25)	121.6	122		121.586
	<i>5.5E - 3</i>	<i>6.7(6)E - 3</i>	<i>5.50E - 3</i>	<i>5.90E - 3</i>		<i>6.51E - 3</i>
CE - L	139.6	[139.632 : 139.998]	139.8 ^(a)	140		139.741
	<i>1.7E - 3</i>	<i>2.15(20)E - 3</i>	<i>1.75E - 3</i>	<i>2.50E - 3</i>		<i>2.05E - 3</i>
CE - M	142.1		142.2			142.140
	<i>3E - 4</i>		<i>3.48E - 4</i>			<i>4.00E - 4</i>
CE - N						142.57
						<i>6.12E - 5</i>
CE - O						142.62
						<i>1.50E - 6</i>
X-rays						
$K\alpha_1$	18.4	18.3672	18.33	18.4	18.36	18.421
	<i>4.02E - 2</i>	<i>4.21(12)E - 2</i>	<i>4.06E - 2</i>	<i>3.89E - 2</i>	<i>3.65E - 2</i>	<i>4.05E - 2</i>
$K\alpha_2$	18.3	18.251	18.21	18.3	18.24	18.302
	<i>2.10E - 2</i>	<i>2.22(7)E - 2</i>	<i>2.14E - 2</i>	<i>2.17E - 2</i>	<i>1.96E - 2</i>	<i>2.13E - 2</i>
$K\beta$	20.6	20.677 ^(a)	20.59	20.7 ^(a)	20.7 ^(a)	20.729
	<i>1.20E - 2</i>	<i>1.30(4)E - 2</i>	<i>6.53E - 3</i> ^(c)	<i>1.18E - 2</i>	<i>9.10E - 3</i>	<i>1.18E - 2</i>
L	2.4	[2.134 : 3.002]		2.45	2.499	2.466
	<i>4.8E - 3</i>	<i>4.82(12)E - 3</i>		<i>4.90E - 3</i>	<i>4.2E - 3</i>	<i>4.72E - 3</i>
M				0.236		0.263
				<i>1.20E - 3</i>		<i>7.83E - 4</i>
N						0.047
						<i>8.73E - 1</i>

TABLE 2: Continued.

	RADAR [10, 11]	DDEP [12]	Eckerman and Endo [13]	Howell [14]	Pomplun [16]	Present study (pilot model)
Auger electrons						
KLL		[14.86 : 15.58] $1.49(6)E - 2$	15.42 $1.48E - 2$	15.3 $1.26E - 2$	15.3 $1.42E - 2$	15.37 $1.48E - 2$
KLX		[17.43 : 18.33] $2.79(10)E - 3$	17.82 $5.59E - 3$	17.8 $4.70E - 3$	17.83 $4.60E - 3$	17.85 $5.58E - 3$
KXY		[19.93 : 21.00] $2.8(1)E - 4$			20.32 $4.0E - 4$	20.27 $5.07E - 4$
K total	15.5 $2.07E - 2$	$2.15(8)E - 2$	$2.04E - 2$	$1.73E - 2$	$1.92E - 2$	16.15 ^(a) $2.08E - 2$
CK LLM						0.054 $9.20E - 3$
CK LLX				0.0429 $1.93E - 2$	0.1721 $1.13E - 2$	0.144 $9.48E - 3$
LMM			2.054 $9.03E - 2$	2.05 $8.68E - 2$	2.032 $8.47E - 2$	2.016 $9.02E - 2$
LMX			2.333 $1.41E - 2$	2.32 $1.37E - 2$	2.326 $1.10E - 2$	2.328 $1.41E - 2$
LXY				2.66 $1.20E - 3$	2.631 $6.00E - 4$	2.654 $6.07E - 4$
L total	2.2 $1.02E - 1$ ^(d)	[1.6 : 2.9] $1.089(9)E - 1$ ^(d)	2.09 ^(a) $1.04E - 1$	1.77 ^(a) $1.21E - 1$	1.86 ^(a) $1.08E - 1$	1.765 $1.24E - 1$
CK MMX			0.1142 $7.09E - 1$	0.116 $7.47E - 1$	0.09578 $3.49E - 1$	0.104 $7.10E - 1$
MXY			0.2061 $1.08E + 0$	0.226 $1.10E + 0$	0.1818 $1.116E + 0$	0.170 $1.10E + 0$
Super CK NNN						0.014 $5.36E - 1$
CK NNX			0.02961 $2.47E + 0$	0.0334 $1.98E + 0$	0.01291 $8.723E - 1$	0.012 $8.45E - 1$
Total energy release per nuclear decay (keV)						
γ -rays				124.997		125.133
CE electrons				15.383		15.232
X-rays				1.367		1.433
Auger electrons				0.899		0.833

^(a) Evaluated from subshell data.^(b) M-, N-shell summed contribution.^(c) $K\beta_1$ only.^(d) Auger electrons only, does not include Coster-Kronig transitions.

with literature values from RADAR [10, 11], DDEP [12], Eckerman & Endo [13], Howell [14] and Stepanek [15, 59]. Our values are given in the last column of the tables, which are based on 10 million (^{99m}Tc) and 1 million (^{111}In) Monte Carlo events. Each entry of these tables consists of two rows. Transition energies (in keV) are given in the first row and transition probabilities (in units of emission per nuclear decay) are in the second row. The contribution of internal conversion for each atomic subshell is evaluated, however the summary tables presented here only give values averaged for

the principal shells. The electron capture decay of In^{111} will also produce atomic vacancies. The electron capture events are not listed explicitly in Table 3, but the associated atomic radiations are fully accounted for in Table 3.

The main part of Tables 2 and 3 is concerned with the atomic radiations. One of the benefits of the Monte Carlo approach is the ability to consider all possible transitions, providing that they are energetically allowed and the corresponding transition rates are known. In the present computation for each transition, the type (Auger electron

TABLE 3: Average radiation yields and energies of ^{111}In . For every entry the first line contains the energies in keV, and the second line (in italic) contains the emission probabilities.

	RADAR [10, 11]	DDEP [12]	Eckerman and Endo [13]	Howell [14]	Stepanek [15, 59]	Present study (pilot model)
Nuclear radiations						
γ_1		150.81(3) <i>1.5(15)E - 5</i>				150.81(3) <i>~3E - 5</i>
γ_2	171.3 <i>9.02E - 1</i>	171.28(3) <i>9.061(20)E - 1</i>	171.3 <i>9.06E - 1</i>	171 <i>9.06E - 1</i>		171.28(3) <i>9.065(25)E - 1</i>
CE - K	144.6 <i>7.80E - 2</i>	144.57(3) <i>8.13(20)E - 2</i>	144.6 <i>8.51E - 2</i>	145 <i>8.24E - 2</i>		144.57 <i>8.39E - 2</i>
CE - L	167.3 <i>1.06E - 2</i>	[167.3 : 167.7] <i>1.02(3)E - 2</i>	167.3 ^(a) <i>1.08E - 2</i>	167 <i>1.00E - 2</i>		167.29 <i>1.05E - 2</i>
CE - M	170.5 <i>2.0E - 3</i>	[170.51 : 170.88] <i>1.97(5)E - 3</i>	170.7 <i>2.09E - 3</i>	171 <i>1.40E - 3^(b)</i>		170.52 <i>2.01E - 3</i>
CE - N+	171.2 <i>4E - 4</i>		171.3 <i>4.35E - 4</i>			171.18 <i>3.92E - 4</i>
CE - N						171.18 <i>3.70E - 4</i>
CE - O						171.27 <i>2.40E - 5</i>
γ_3	245.4 <i>9.40E - 1</i>	245.35(4) <i>9.412(6)E - 1</i>	245.4 <i>9.41E - 1</i>	245 <i>9.37E - 1</i>		245.35(4) <i>9.409(18)E - 1</i>
CE - K	218.7 <i>4.93E - 2</i>	218.64(4) <i>4.93(10)E - 2</i>	218.7 <i>5.04E - 2</i>	219 <i>5.21E - 2</i>		218.64 <i>5.03E - 2</i>
CE - L	241.4 <i>7.9E - 3</i>	[241.33 : 241.81] <i>7.70(15)E - 3</i>	241.5 ^(a) <i>7.96E - 3</i>	241 <i>9.10E - 3</i>		241.46 <i>7.89E - 3</i>
CE - M	244.6 <i>1.5E - 3</i>	[244.58 : 244.95] <i>1.50(3)E - 3</i>	244.7 <i>1.56E - 3</i>	245 <i>1.90E - 3^(b)</i>		244.63 <i>1.51E - 3</i>
CE - N+	245.3 <i>3E - 4</i>		245.4 <i>3.09E - 4</i>			245.26 <i>2.70E - 4</i>
CE - N						245.26 <i>2.58E - 4</i>
CE - O						245.34 <i>1.20E - 5</i>
X-rays						
$K\alpha_1$	23.2 <i>4.433E - 1</i>	23.1739 <i>4.447(26)E - 1</i>	23.15 <i>4.50E - 1</i>	23.2 <i>4.63E - 1</i>	23.3 <i>4.58E - 1</i>	23.25 <i>4.51E - 1</i>
$K\alpha_2$	23.0 <i>2.350E - 1</i>	22.9843 <i>2.365(18)E - 1</i>	22.96 <i>2.40E - 1</i>	23.0 <i>2.40E - 1</i>	23.1 <i>2.37E - 1</i>	23.06 <i>2.39E - 1</i>
$K\beta$	26.1 <i>1.450E - 1</i>	26.19 ^(a) <i>1.466(16)E - 1</i>	26.25 ^(a) <i>7.87E - 2</i>	26.2 ^(a) <i>1.37E - 1</i>	26.3 ^(a) <i>1.48E - 1</i>	26.26 <i>1.42E - 1</i>
L	3.1 <i>6.90E - 2</i>	[2.77: 3.95] <i>6.78(14)E - 2</i>		3.23 <i>4.99E - 2</i>	3.25 <i>7.83E - 2</i>	3.23 <i>6.90E - 2</i>
M				0.356 <i>3.00E - 3</i>	0.431 <i>2.50E - 3</i>	0.424 <i>2.54E - 1</i>
N+					0.0521 <i>7.75E - 1</i>	0.068 <i>1.03E + 0</i>

TABLE 3: Continued.

	RADAR [10, 11]	DDEP [12]	Eckerman and Endo [13]	Howell [14]	Stepanek [15, 59]	Present study (pilot model)
Auger electrons						
KLL		[18.675; 19.636] $1.05(3)E - 1$	19.28 $1.06E - 1$	19.1 $1.03E - 1$	19.3 $9.84E - 2$	19.23 $1.07E - 1$
KLX		[21.923; 23.172] $4.5(2)E - 2$	22.42 $4.37E - 2$	22.3 $3.94E - 2$	22.5 $4.35E - 2$	22.46 $4.39E - 2$
KXY		[25.171; 26.028] $5(1)E - 3$	25.58 $4.33E - 3$	25.5 $3.60E - 3$	25.7 $4.10E - 3$	25.64 $4.29E - 3$
K total	19.3 $1.56E - 1$					20.3 $1.55E - 1$
CK LLM						0.032 $4.82E - 2$
CK LLX				0.183 $1.51E - 1$	0.247 $1.52E - 2$	0.234 $1.32E - 1$
LMM			2.611 $8.16E - 1$	2.59 $8.35E - 1$	2.60 $8.03E - 1$	2.58 $8.16E - 1$
LMX			3.054 $1.88E - 1$	3.06 $1.90E - 1$	3.06 $1.81E - 1$	3.06 $1.88E - 1$
LXY			3.515 $1.14E - 2$	3.53 $1.09E - 2$	3.54 $1.05E - 2$	3.54 $1.13E - 2$
L total	2.7 $9.80E - 1^{(c)}$	[3.404; 3.804] $1.005(8)E + 0^{(c)}$				2.31 $1.20E + 0$
CK MMX			0.1280 $8.86E - 1$	0.125 $9.15E - 1$	0.0103 $8.57E - 1$	0.098 $8.59E - 1$
MXY			0.3454 $2.12E + 0$	0.350 $2.09E + 0$	0.328 $2.05E + 0$	0.308 $2.12E + 0$
Super CK NNN						0.020 $5.38E - 1$
CK NNX			0.03677 $3.04E + 0$	0.0388 $2.54E + 0$	0.0268 $1.49E + 0$	0.017 $6.81E - 1$
NXY				0.00847 $7.82E + 0$	0.0518 $3.63E - 1$	0.054 $2.06E - 1$
Total energy release per nuclear decay (keV)						
γ -rays				366.532 ^(d)		386.154
CE electrons				25.957		27.657
X-rays				19.966		19.994
Auger electrons				6.750		6.678

^(a) Evaluated from subshell data.

^(b) M-, N-shell summed contribution.

^(c) Auger electrons only, does not include Coster-Kronig transitions.

^(d) Possible misprint in the original paper, should read 386.532 keV.

or X-ray), the emitted energy, and the corresponding full atomic configuration is stored on disk. A separate program is used to extract the average energy and yield for any transition type of interest. The grouping of the atomic transitions follows the convention established in previous studies. While

for the transitions involving vacancies on the *K* and *L* shells there is a general agreement between our values and most of the other calculations, for the other shells it is evident that either no data is given in previous studies, or their energies and/or rates are different.

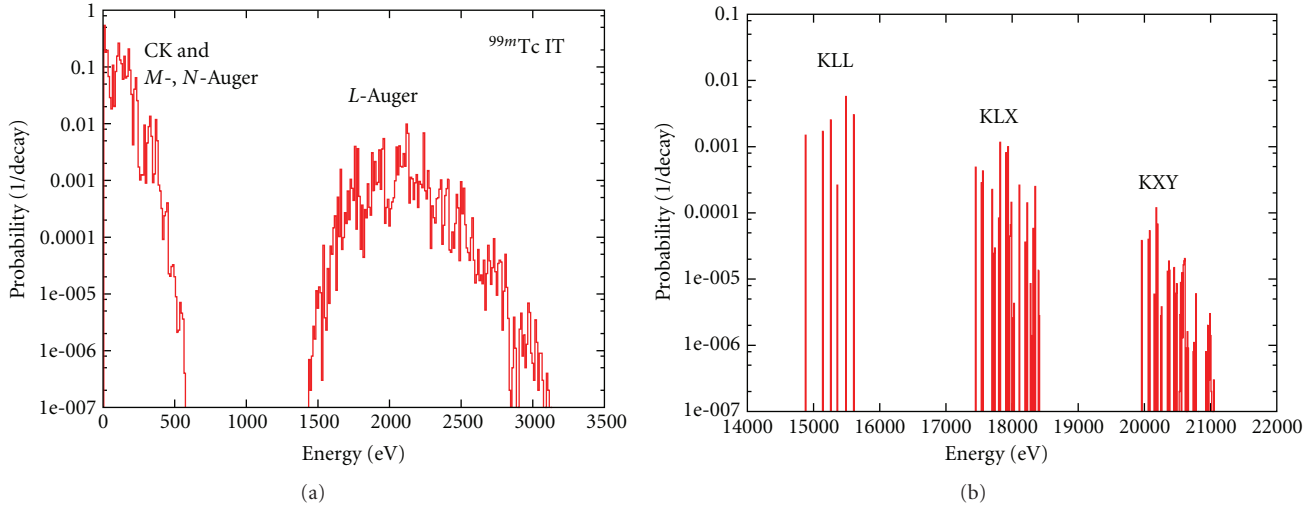


FIGURE 4: Calculated energy spectrum of Auger electrons in the decay of Tc^{99m} . The vertical axis is the probability per nuclear decay for a 10 eV energy bin. (a) is the low-energy (0–3500 eV), and (b) shows the K -shell Auger lines.

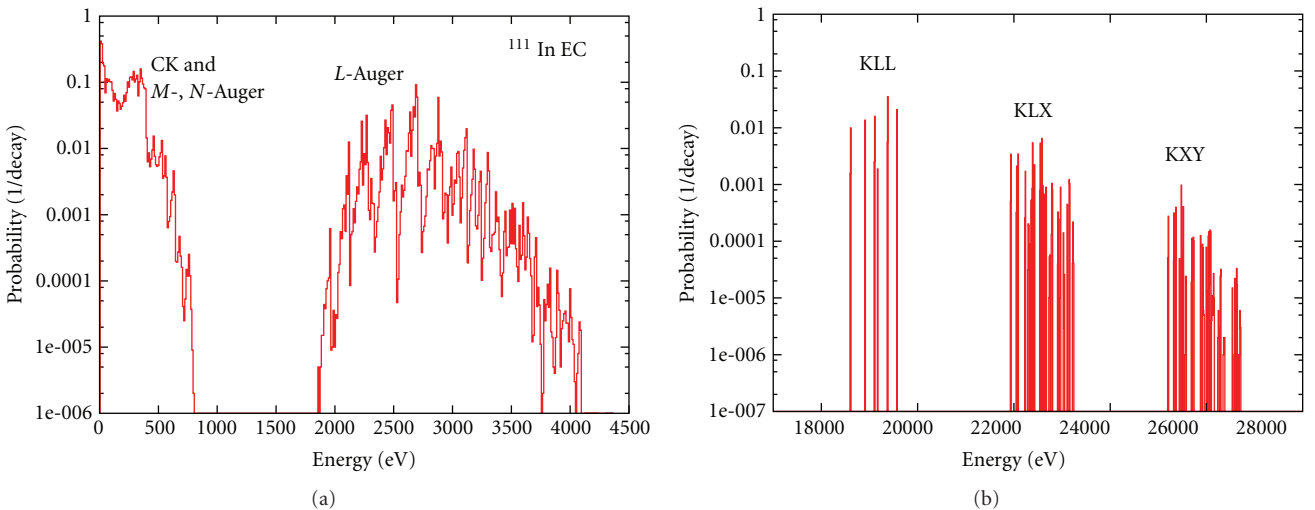


FIGURE 5: Calculated energy spectrum of Auger electrons in the decay of In^{111} . The vertical axis is the probability per nuclear decay for a 10 eV energy bin. (a) is the low-energy (0–4500 eV) and (b) shows the K -shell Auger lines.

The most notable difference is for the NXY Auger electrons in the EC decay of In^{111} between our pilot model and Stepanek [15, 59] and Howell [14]. The later one can be attributed to the so-called “fast neutralization” approach resulting in significantly larger numbers of Auger electrons. By filling the valence vacancies instantly, fast neutralization creates significantly more opportunities for other vacancies to be filled by Auger processes, especially in large atoms. The slower neutralization approach in the present study, coupled with consideration of the charge distribution at each stage of the cascade, recognises that many of the NXY Auger and NNX Coster-Kronig transitions become energetically impossible once the atom has lost a few electrons. Some X-ray transitions are available to take their place. Further studies are required to explore both

experimentally and theoretically the full extent of the atomic relaxation process leading to the full neutralization of the atom.

The calculated Auger electron energy spectra for Tc^{99m} and In^{111} are shown in Figures 4 and 5. In the case of Tc^{99m} more than 450 transition types (10) have been computed. Most transition types have multiple satellite lines at a range of energies corresponding to different atomic configurations. For the Tc^{99m} our computations resulted in a spectrum with more than 87000 Auger lines. For clarity, a 10 eV energy bin was used in these plots and the frequency of the transitions was converted to *yields per nuclear decay*. Apart from the work of Eckerman and Endo [13], energy spectra have never been calculated for radioisotopes listed in Table 1. Only a few experimental investigations exist on the detailed

energy spectrum of these Auger electron emitters. The only known Auger-electron spectra measured for $\text{Tc}^{99\text{m}}$ [60] and In^{111} [61] cover a relatively high-energy range: 1.50–2.32 keV ($^{99\text{m}}\text{Tc}$) and 1–6 and 15–35 keV (^{111}In). While for some energy regions (1.5–4 keV for In^{111}) the experimental spectra are in agreement with our calculations, detailed experimental spectra are required to benchmark our calculations. This is particularly important for low Auger energies ($E < 1$ keV), which have the largest potential for targeted Auger therapy [4].

An important result of the pilot model is the calculated total yield of Auger electrons: $\text{Tc}^{99\text{m}}$: 3.37 and In^{111} : 5.75 electrons per radioactive decay of the parent atom. In accord with our assumption that valence-shell vacancies persist, these results are consistent with those of Pomplun [16]. We have therefore demonstrated that our calculations using the *pilot model* can reproduce the previous Monte Carlo calculations for these isotopes.

7. Conclusions

There is continuing interest in medical applications of Auger electrons which accompany nuclear decay, particularly for the targeted treatment of cancer cells at the DNA scale. In most cases these applications are based on theoretical predictions of the emitted Auger and X-ray spectra. As it is evident from Table 1, there is a significant difference in the Auger yields reported in the literature over the last 20 years. Most of this difference can be attributed to the lack of detailed knowledge of the relevant atomic transition rates, most prominently in the outer (M , N , etc.) shells. Simplistic assumptions regarding the atomic configurations during the intermediate steps of vacancy propagation and the incomplete treatment of the effect of multiple vacancies also limit the validity of earlier calculations.

We are developing a new model using *ab initio* calculations based on the relativistic Dirac-Fock approach and Monte Carlo techniques, which has the potential to overcome these limitations. Pilot calculations for the isotopes $\text{Tc}^{99\text{m}}$ and In^{111} , based on fixed transition rates from the EADL database [30], are in satisfactory agreement with previous computations.

References

- [1] G. Sgouros, "Alpha-particles for targeted therapy," *Advanced Drug Delivery Reviews*, vol. 60, no. 12, pp. 1402–1406, 2008.
- [2] P. Auger, "Sur l'effet photoélectrique composé," *Journal de Physique et le Radium*, vol. 6, no. 6, p. 205, 1925.
- [3] A. I. Kassis, "The amazing world of Auger electrons," *International Journal of Radiation Biology*, vol. 80, no. 11–12, pp. 789–803, 2004.
- [4] F. Buchegger, F. Perillo-Adamer, Y. M. Dupertuis, and A. B. Delaloye, "Auger radiation targeted into DNA: a therapy perspective," *European Journal of Nuclear Medicine and Molecular Imaging*, vol. 33, no. 11, pp. 1352–1363, 2006.
- [5] R. W. Howell, "Auger processes in the 21st century," *International Journal of Radiation Biology*, vol. 84, no. 12, pp. 959–975, 2008.
- [6] E. Schönfeld, "Calculation of fractional electron capture probabilities," *Applied Radiation and Isotopes*, vol. 49, p. 1353, 1998.
- [7] W. Bambynek, B. Crasemann, R. W. Fink et al., "X-ray fluorescence yields, Auger, and Coster-Kronig transition probabilities," *Reviews of Modern Physics*, vol. 44, no. 4, pp. 716–813, 1972.
- [8] T. Kibédi, T. W. Burrows, M. B. Trzhaskovskaya, P. M. Davidson, and C. W. Nestor, "Evaluation of theoretical conversion coefficients using BrIcc," *Nuclear Instruments and Methods in Physics Research A*, vol. 589, no. 2, pp. 202–229, 2008.
- [9] S. Rosseland, "Zur Quantentheorie der radioaktiven Zerfallsvorgänge," *Zeitschrift für Physik A*, vol. 14, no. 1, pp. 173–181, 1923.
- [10] RADIATION DOSE ASSESSMENT RESOURCE (RADAR), <http://www.doseinfo-radar.com/RADARHome.html>.
- [11] M. G. Stabin and L. C. Q. P. da Luz, "Decay data for internal and external dose assessment," *Health Physics*, vol. 83, no. 4, pp. 471–475, 2002.
- [12] Decay Data Evaluation Project, $^{99\text{m}}\text{Tc}$: C. Morillon, M. M. Bé, V. P. Chechev, A. Egorov (2012); ^{111}In : V. P. Chechev (2006); ^{123}I : V. Chisté, M. M. Bé (2004); ^{125}I : V. Chisté, M. M. Bé (2010); ^{201}Tl : E. Schönfeld, R. Dersch (2005), <http://www.nucleide.org/DDEP-WG/DDEPdata.htm>.
- [13] K. F. Eckerman and A. Endo, *MIRD: Radionuclide Data and Decay Schemes*, Society of Nuclear Medicine, Reston, Va, USA, 2007.
- [14] R. W. Howell, "Radiation spectra for Auger-electron emitting radionuclides: report No. 2 of AAPM Nuclear Medicine Task Group No. 6," *Medical Physics*, vol. 19, no. 6, pp. 1371–1384, 1992.
- [15] J. Stepanek, "Methods to determine the fluorescence and Auger spectra due to decay of radionuclides or due to a single atomic-subshell ionization and comparisons with experiments," *Medical Physics*, vol. 27, no. 7, pp. 1544–1554, 2000.
- [16] E. Pomplun, "Monte Carlo-simulated Auger electron spectra for nuclides of radiobiological and medical interest—a validation with noble gas ionization data," *International Journal of Radiation Biology*, vol. 88, no. 1–2, pp. 108–114, 2012.
- [17] R. S. Hager and E. C. Seltzer, "Internal conversion tables part I: K -, L -, M -shell conversion coefficients for $Z = 30$ to $Z = 103$," *Nuclear Data Sheets A*, vol. 4, no. 1–2, pp. 1–11, 1968.
- [18] F. R. Rösel, H. M. Friess, K. Alder, and H. C. Pauli, "Internal conversion coefficients for all atomic shells ICC values for $Z = 30 - 67$," *Atomic Data and Nuclear Data Tables*, vol. 21, no. 2–3, pp. 91–289, 1978, *ibid* vol. 21, p. 291, 1978.
- [19] I. M. Band, M. B. Trzhaskovskaya, and M. A. Listengarten, "Internal conversion coefficients for $E5$ and $M5$ nuclear transitions, $30 \leq Z \leq 104$," *Atomic Data and Nuclear Data Tables*, vol. 21, no. 1, pp. 1–47, 1978.
- [20] O. Dragoun, Z. Plajner, and F. Schmutzler, "Contribution of outer atomic shells to total internal conversion coefficients," *Atomic Data and Nuclear Data Tables*, vol. 9, no. 2, pp. 119–135, 1971.
- [21] I. M. Band, M. B. Trzhaskovskaya, and M. A. Listengarten, "Internal conversion coefficients for atomic numbers $Z \leq 30$," *Atomic Data and Nuclear Data Tables*, vol. 18, no. 5, pp. 433–457, 1976.
- [22] N. B. Gove and M. J. Martin, "Log-f tables for beta decay," *Atomic Data and Nuclear Data Tables*, vol. 10, no. 3, pp. 205–219, 1971.
- [23] E. Schönfeld, "Tables for the calculation of electron capture probabilities," Tech. Rep. PTB-6.33-95-2, 1995.

- [24] W. Bambynek, H. Behrens, M. H. Chen et al., "Orbital electron capture by the nucleus," *Reviews of Modern Physics*, vol. 49, no. 1, pp. 77–221, 1977.
- [25] M. J. Martin and P. H. Blichert-toft, "Radioactive atoms: Auger-electron, α -, β -, γ -, and X-ray data," *Atomic Data and Nuclear Data Tables*, vol. 8, no. 1-2, p. 1, 1970.
- [26] T. W. Burrows, *The Program RADLST*, National Nuclear Data Center, Brookhaven National Laboratory, 1988.
- [27] J. H. Scofield, "Relativistic Hartree Slater values for K and L X-ray emission rates," *Atomic Data and Nuclear Data Tables*, vol. 14, no. 2, pp. 121–137, 1974.
- [28] E. Schönfeld and H. Janßen, *Untersuchungen zu verknüpfungen von konstanten der atomhülle*, vol. 37, PTB, Braunschweig, Germany, 1995.
- [29] M. M. Bé, V. Chisté, and C. Duijieu, "Detailed calculation of K- and L-Auger electron emission intensities following radioactive disintegration," *Applied Radiation and Isotopes*, vol. 64, no. 10-11, pp. 1435–1439, 2006.
- [30] S. T. Perkins, D. E. Cullen, H. H. Chen, J. H. Hubbell, J. Rathkopf, and J. Scofield, "Tables and graphs of atomic subshell and relaxation data derived from the LLNL evaluated atomic data library (EADL), $Z = 1-100$," Tech. Rep. UCRL-50400, Lawrence Livermore National Laboratory, 1991.
- [31] D. E. Cullen, "Program RELAX: a code designed to calculate atomic relaxation spectra of X-rays and electrons," Tech. Rep. number UCRLID-II0438, Lawrence Livermore National Laboratory, 1992.
- [32] M. H. Chen, B. Crasemann, and H. Mark, "Relativistic radiationless transition probabilities for atomic K- and L-shells," *Atomic Data and Nuclear Data Tables*, vol. 24, no. 1, pp. 13–37, 1979.
- [33] E. J. McGuire, "M-shell Auger, Coster-Kronig, and radiative matrix elements, and Auger and Coster-Kronig transition rates in j-j coupling," Research Report SC-RR-710835, Sandia Laboratories, 1972.
- [34] E. J. McGuire, "N-shell Auger, Coster-Kronig, and radiative matrix elements, and Auger and Coster-Kronig transition rates in j-j coupling," Research Report SAND-75-0443, Sandia Laboratories, 1975.
- [35] A. I. Kassis, S. J. Adelstein, C. Haydock, and K. S. R. Sastry, "Thallium-201: an experimental and a theoretical radiobiological approach to dosimetry," *Journal of Nuclear Medicine*, vol. 24, no. 12, pp. 1164–1175, 1983.
- [36] S. T. Manson and D. J. Kennedy, "X-ray emission rates in the Hartree Slater approximation," *Atomic Data and Nuclear Data Tables*, vol. 14, no. 2, pp. 111–120, 1974.
- [37] L. Storm and H. I. Israel, "Photon cross sections from 1 keV to 100 MeV for elements $Z = 1$ to $Z = 100$," *Atomic Data and Nuclear Data Tables*, vol. 7, no. 6, pp. 565–681, 1970.
- [38] M. O. Krause, "Atomic radiative and radiationless yields for K and L shells," *Journal of Physical and Chemical Reference Data*, vol. 8, no. 2, p. 307, 1979.
- [39] J. A. Bearden and A. F. Burr, "Reevaluation of X-ray atomic energy levels," *Reviews of Modern Physics*, vol. 39, no. 1, pp. 125–142, 1967.
- [40] F. P. Larkins, "Semiempirical Auger-electron energies for elements $10 \leq Z \leq 100$," *Atomic Data and Nuclear Data Tables*, vol. 20, no. 4, pp. 311–387, 1977.
- [41] J. P. Desclaux, "A multiconfiguration relativistic DIRAC-FOCK program," *Computer Physics Communications*, vol. 9, no. 1, pp. 31–45, 1975.
- [42] I. M. Band, M. B. Trzhaskovskaya, C. W. Nestor Jr., P. O. Tikkanen, and S. Raman, "Dirac-Fock internal conversion coefficients," *Atomic Data and Nuclear Data Tables*, vol. 81, no. 1-2, pp. 1–334, 2002.
- [43] Evaluated Nuclear Structure Data File (ENSDF), NNDC, BNL, <http://www.nndc.bnl.gov/ensdf/index.jsp>.
- [44] International Commission on Radiological Protection (ICRP), *Radionuclide Transformations*, vol. 38 of ICRP publication, Pergamon Press, Oxford, UK, 1983.
- [45] E. Schönfeld and H. Janßen, "Calculation of emission probabilities of X-rays and Auger electrons emitted in radioactive disintegration processes," *Applied Radiation and Isotopes*, vol. 52, no. 3, pp. 595–600, 2000.
- [46] A. Endo, Y. Yamagichi, and K. F. Eckerman, "Nuclear decay data for dosimetry calculation: revised data of ICRP publication 38," Tech. Rep. JAERI 1347, Japan Atomic Energy Research Institute, 2005.
- [47] M. F. Chung and L. H. Jenkins, "Auger electron energies of the outer shell electrons," *Surface Science*, vol. 22, no. 2, pp. 479–485, 1970.
- [48] L.T. Dillman, "EDISTR—a computer program to obtain a nuclear decay data base for radiation dosimetry," Tech. Rep. ORNL/TM-6689, Department of Energy, Oak Ridge National Laboratory, 1980.
- [49] M. O. Krause and T. A. Carlson, "Vacancy cascade in the reorganization of Krypton ionized in an inner shell," *Physical Review*, vol. 158, no. 1, pp. 18–24, 1967.
- [50] T. A. Carlson and C. W. Nestor Jr., "Calculation of electron shake-off probabilities as the result of X-ray photoionization of the rare gases," *Physical Review A*, vol. 8, no. 6, pp. 2887–2894, 1973.
- [51] A. L. Nichols, S. M. Qaim, and R. C. Noy, Eds., "Technical meeting on intermediate-term nuclear data needs for medical applications: cross sections and decay data," Summary Report INDC(NDS)-0596, INDC International Nuclear Data Committee, 2011.
- [52] T. Kibédi, T. W. Burrows, M. B. Trzhaskovskaya, and C. W. Nestor Jr., "Internal conversion coefficients—how good are they now?" in *Proceedings of the International Conference on Nuclear Data for Science and Technology*, O. Bersillon, F. Gunsing, E. Bauge, R. Jacqmin, and S. Leray, Eds., p. 57, EDP Sciences, Nice, France, April 2007.
- [53] P. Jönsson, X. He, C. Froese Fischer, and I. P. Grant, "The grasp2K relativistic atomic structure package," *Computer Physics Communications*, vol. 177, no. 7, pp. 597–622, 2007.
- [54] S. Fritzsche, "The RATIP program for relativistic calculations of atomic transition, ionization and recombination properties," *Computer Physics Communications*, vol. 183, no. 7, pp. 1525–1559, 2012.
- [55] M. Patanen, S. Urpelainen, T. Kantia, S. Heinämäki, S. Aksela, and H. Aksela, "4f photoionization and subsequent Auger decay in atomic Pb: relativistic effects," *Physical Review A*, vol. 83, no. 5, Article ID 053408, 5 pages, 2011.
- [56] V. V. Bulgakov, V. I. Kirishchuk, V. T. Kupryashkin et al., "Detection of shift effects in the 936 keV K-line internal conversion transition due to atom ionization after electron capture of ^{152m}Eu ," *Bulletin of the Academy of Sciences of the USSR*, vol. 51, no. 11, p. 1, 1987.
- [57] K. A. Robertson, *Atomic radiations in nuclear decay [Honours thesis]*, Australian National University, 2010.
- [58] T. Kibédi, M. B. Trzhaskovskaya, M. Gupta, and A. E. Stuchbery, "Conversion coefficients for superheavy elements," *Atomic Data and Nuclear Data Tables*, vol. 98, no. 2, pp. 313–355, 2012.
- [59] J. Stepanek, S. A. Ilvonen, A. A. Kuronen, J. S. Lampinen, S. E. Savolainen, and P. J. Välimäki, "Radiation spectra of ^{111}In ,

- ^{113}mIn and ^{114}mIn ,” *Acta Oncologica*, vol. 39, no. 6, pp. 667–671, 2000.
- [60] V. N. Gerasimov, A. G. Zelenkov, V. M. Kulakov et al., “Study of spectrum of conversion electron from the 2.1726-keV transition in $^{99\text{m}}\text{Tc}$ placed into the metallic Tc matrix,” *Yadernaya Fizika*, vol. 34, p. 3, 1981.
- [61] E. A. Yakushev, A. Kovalík, D. V. Filosofov et al., “An experimental comparison of the K- and L-Auger electron spectra generated in the decays of ^{140}Nd and ^{111}In ,” *Applied Radiation and Isotopes*, vol. 62, no. 3, pp. 451–456, 2005.

Review Article

***In Silico* Modelling of Treatment-Induced Tumour Cell Kill: Developments and Advances**

Loredana G. Marcu^{1,2,3} and Wendy M. Harriss-Phillips^{1,2}

¹ Department of Medical Physics, Royal Adelaide Hospital, North Terrace, Adelaide, SA 5000, Australia

² School of Chemistry and Physics, University of Adelaide, Adelaide, SA 5000, Australia

³ Faculty of Science, University of Oradea, 410087 Oradea, Romania

Correspondence should be addressed to Loredana G. Marcu, loredana.marcu@health.sa.gov.au

Received 14 February 2012; Revised 10 May 2012; Accepted 14 May 2012

Academic Editor: Scott Penfold

Copyright © 2012 L. G. Marcu and W. M. Harriss-Phillips. This is an open access article distributed under the Creative Commons Attribution License, which permits unrestricted use, distribution, and reproduction in any medium, provided the original work is properly cited.

Mathematical and stochastic computer (*in silico*) models of tumour growth and treatment response of the past and current eras are presented, outlining the aims of the models, model methodology, the key parameters used to describe the tumour system, and treatment modality applied, as well as reported outcomes from simulations. Fractionated radiotherapy, chemotherapy, and combined therapies are reviewed, providing a comprehensive overview of the modelling literature for current modellers and radiobiologists to ignite the interest of other computational scientists and health professionals of the ever evolving and clinically relevant field of tumour modelling.

1. The Need for *In Silico* Modelling

Modern treatment delivery methods for external beam radiotherapy employ techniques such as intensity modulated radiation therapy (IMRT) and image guided radiation therapy (IGRT) to deliver high radiation doses to the tumour planning target volume (PTV) or multiple PTV's with ever increasing accuracy and precision. However, to further improve outcomes for individual patients it will be necessary to explore in more detail the radiobiological processes that occur in human tumours and to predict optimal treatment plans for the individual patient. There is an increasing need to incorporate cellular behaviour and characteristics into individualised treatment planning and delivery. Undoubtedly, the future of cancer research rests on a multidisciplinary approach.

The pursuit of an enhanced treatment regimen is conventionally performed through well-designed, randomised clinical trials. Clinical trials are indispensable prerequisites to establish novel therapeutic principles. Nevertheless, trials are lengthy processes which involve several influential factors for a decisive outcome: trial design, patient selection and

followup, complex data analysis, and interpretation. Furthermore, trials cannot explore the sensitivity of the outcome to input parameters and covariates.

Models are an efficient way to complement the results of clinical trials. Beside animal models and cell lines, which are often used for preclinical studies, there are computer models (*in silico* models) encompassing mathematical, physical, and engineering concepts representing the biological world.

Models in cancer treatment are simplified tools to reproduce the biological system, thus they do not accurately reflect the fine details of the real scenario. To compensate for some of its deficiencies, the approach of computer modelling has several advantages:

- (i) input parameters can be easily changed and results rapidly obtained;
- (ii) various mechanisms can be studied in isolation, determining their impact on specific processes;
- (iii) extreme values for different parameters may be considered, and limiting factors determined for biologically valid results;

- (iv) treatment outcome can be predicted with quantitative end points or “iso-effects”;
- (v) models can answer the complex question of “*what if?*”

Computer models can be used to simulate tumour cell kinetics and dynamics, drug pharmacokinetics, therapies and give similar results to those in experimental tumours. Models are needed to open further research avenues and to suggest relationships between radiobiological parameters.

The *in silico-in vitro-in vivo* chain (Figure 1) is gaining worldwide recognition among scientists and their mutual role in cancer research is illustrated through the great advances of the last decades. *In silico* models are valuable data input sources for both *in vitro* and *in vivo* models (solid arrow). Mutually, the latter offer feedback to *in silico* models in support of further developments and optimisation (dashed arrow).

When modelling the processes involved in the damage and elimination of tumour cells on the microscopic level, development of an algorithm to propagate a virtual tumour mass is first required. One approach has been to generate a full-sized macroscopic tumour mass with a predefined volume, cell type distribution, and so forth, based on average tumour statistics or a particular tumour of clinical interest; however, other modellers have used a *first principles* approach and have “grown” the virtual tumour starting from a single cell (or small group of cells). The tumour growth process is in itself a large area of research, allowing for investigations into the cell kinetics of malignant tissue. This line of study also provides modellers with ideas about how to simulate cell propagation *during treatment*, which is crucial because many treatments are delivered over multiple weeks or even months. As many of the models discussed are of the latter variety (modelling tumour growth as well as treatment), the proceeding section of this paper provides an overview of the key analytical and stochastic tumour growth models in the literature.

2. Tumour Growth Models

2.1. Introduction. The goals of tumour modelling vary among researchers and may focus on one key biological/radiobiological mechanism or explore mechanisms and ranges of parameter values. Many models aim to identify mechanisms and parameter values at the cellular level which are responsible for macroscopic tumour outcomes, for example, the cell kinetic properties affecting the tumour growth or shrinkage rates. Modelling can add to the understanding of cellular proliferative hierarchy and the differentiation processes, evolution of genetic mutations, tumour morphology, tumour pressure gradients, angiogenesis and oxygen distributions, diffusion of nutrients, and so forth.

The modelling methodology employed to simulate a biological system may be analytical or stochastic in nature. Analytical (mathematical) methodology is more traditional, utilising deterministic equation-based methods, often in the form of a set of equations incorporating multiple parameters. Stochastic methods use random number generation and

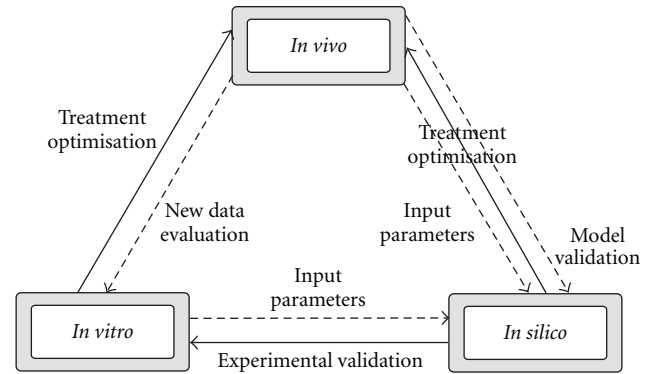


FIGURE 1: The *in silico-in vitro-in vivo* chain. The solid arrows illustrate data input whereas the dashed arrows represent the feedback data used for model validation in support of further optimisation.

probability distribution functions to simulate cell propagation and evolution of the tumour, for example, Monte Carlo (MC) methodology. Monte Carlo methodology enables a system to be modelled from first principles. It is a form of computation using random sampling and iteration to simulate the evolution of a physical or biological system and involves the use of probability distribution functions for decision making, for example, for the allocation of parameter values from a range of possible values. This technique is useful for modelling systems with a large number of coupled degrees of freedom, which are difficult to solve using equation-based methods.

Tumours are complex entities, diverse and heterogeneous, yet all share the ability to proliferate beyond the constraints limiting the growth in normal tissue. The growth of tumours is best represented by an exponential increase of cell number in time. Exponential growth is the simplest mode of growth assuming no cell loss or infertility. By growing exponentially, the tumour volume increases by a constant fraction in equal time intervals. Many human tumours during their growth show exponential behavior; however, there are tumours going through irregular or decelerating growth [31]. A more accurate description for the irregular tumour growth is given by the Gompertzian growth curves (Figure 2). During Gompertzian growth, the doubling time increases steadily as the tumour grows larger. The progressive slowing of Gompertzian growth may be more the result of decreased cell production rather than increased cell loss [31].

It is generally accepted that human cancers grow in an exponential or Gompertzian manner. This assumption is based on analysis of the growth of transplantable animal tumours and on averages of tumour growth in human populations. Although not valid for all individual tumours, exponential growth may accurately describe averages of human tumour growth [32]. However, there is data showing inconsistencies with exponential or Gompertzian kinetics, explainable by irregular growth kinetics.

Model parameterisation greatly depends on the available pool of biological, biochemical, or biophysical quantities used within the equations or model algorithm. When it

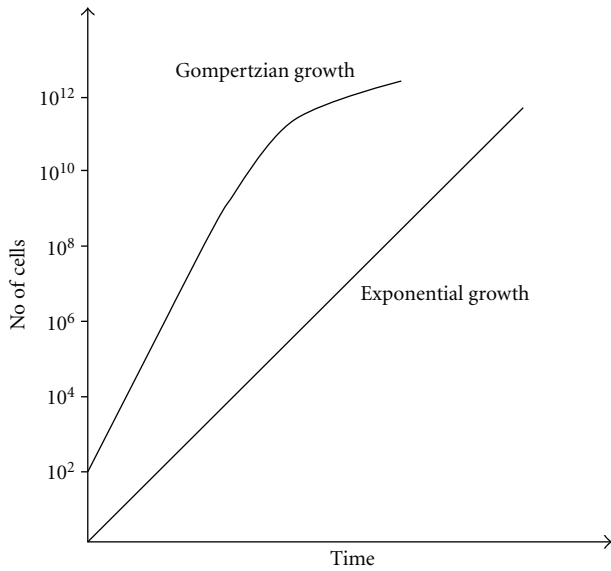


FIGURE 2: Tumour growth curves.

comes to tumour growth, modelling of both kinetic and dynamic properties are envisaged. Cellular composition, volume doubling time, growth factor, cell loss factor, labelling index, cell cycle phase-related properties (length, radiosensitivity), and oxygenation status are some of the most commonly implemented modelling parameters. Also depending on the objective of the model, treatment-related factors are often found among input parameters.

2.2. Avascular Tumour Growth Models. One of the earliest models of tumour growth and cell cycle simulation using the Monte Carlo approach is CELLSIM [1]. CELLSIM operates with a large initial number of cells, placed in different phases of the cell cycle whereby cells are modelled in groups rather than being followed individually. Therefore each group enters and exits a state together. When the number of groups reaches a certain limit, a reassignment algorithm will combine them making larger groups, where the new parameters are calculated using the weighted average of the previous ones. CELLSIM simulates cell cycle and distribution of cells along the cycle with and without cytotoxic treatment and it does not focus on tumour growth curves. However, the description of the model implies exponential growth behaviour.

Cellular automata models, also known as tessellation automata or cellular structure models, are one of the first types of cellular growth models developed *in silico*. These models consist of a regular grid of cells, each cell having assigned a certain state. New generations of cells are created based on predefined rules determining the state of each cell. For tumour growth simulations, cellular automata models became popular due to their ease of use. Qi et al. [33] developed such model describing the surveillance of the immune system against cancer by taking into account as main parameters the microscopic mechanisms of malignant growth (cell proliferation), the cytotoxic behaviours of the

immune system as well as the mechanical pressure inside the tumour. The influence of these parameters on the Gompertzian growth of tumours is modelled.

Several early tumour growth models have also considered the Gompertzian distribution to describe the shape of the tumour growth curve. Gyllenberg and Webb [34] explained the Gompertzian growth curve by expressing the rates of cells transitioning reversibly between the proliferative and resting states as a function of tumour size, therefore incorporating variable growth fractions. Their mathematical model employs quiescence as a mechanism to explain characteristic Gompertz-type growth curves. The model distinguishes between two types of cells within the tumour, proliferating and quiescent. The theory behind the tumour growth model is based on empirical data suggesting that the larger the tumour, the more likely it is that a proliferating cell becomes quiescent and the more unlikely it is that a quiescent cell reenters the proliferating cycle, therefore diminishing the growth fraction. The same group [35] has later incorporated into the model a new parameter defining the size of individual cells and modelled the dependence of tumour growth on this parameter, in addition to cell transition between compartments.

A stochastic model of tumour growth and invasion looking into the relationship between the histological pattern of tumours and their functional properties was developed by Smolle and Stettner [36]. The model showed that cell division, migration, and death are influenced by both autocrine and paracrine growth factors, inducing therefore changes in tumour pattern. These findings support the observation whereby the functional properties of tumours together with the tumour microenvironment dictate the histological pattern of tumours.

The implementation of growth regulation and control mechanisms into three-dimensional models (spatio-temporal) of epithelial cell populations was the focus of an individual cell-based model aiming to simulate the growth pattern and behaviour of a number of different epithelial cell populations from undifferentiated stem cells up to tumour cells [37]. The mechanisms implemented in the model are: cell-cell adhesion, which plays a role in the inhibition of epithelial growth at high cellular density, and cell-substrate interaction, with role in cell cycle progress. The interplay between cell parameter variation and selective knockouts of regulations and control mechanisms shows that the cell-substrate anchorage has the largest impact on the population morphology. Furthermore, the balance between the strength of cell-substrate anchorage and the trigger for contact inhibition determines the way the intrinsic cell growth time affects the population growth. The authors have underlined the advantages of individual cell-based models which are parameterized by measurable cell properties in describing the complex process of cell population growth.

2.3. Vascular Tumour Growth Models. When modelling clinical-sized tumours comprising up to 10^8 to 10^{10} cells, simulating tumour oxygenation is generally considered a requirement for most tumour types in order for model growth curves to match well with *in vivo* data. Lack of oxygen

in tissue, hypoxia, is commonly defined by a pO_2 (partial pressure of oxygen) threshold of 10 mm Hg, although clinical trials may use 2.5 or 5.0 mm Hg thresholds when reporting experimental results such as the Hypoxic Fraction (HF) of cells in the tumour. It is now commonly known that low tumour oxygenation results in radioresistance and is a major contributor to treatment failure due to tumour recurrence [38]. Consequently tumour growth model research often involves the consideration of tumour cell oxygen levels and the mechanisms by which the cells receive the oxygen from blood vessels, for example, radial diffusion from cylindrical vessel to the surrounding tumour tissue. In models, the vessels may be simulated three-dimensionally within a lattice, or more simply, the final oxygen distribution to the cells may be modelled without specifically modelling the vessels themselves.

Since the initial experimental and subsequent mathematical modelling of tissue hypoxia by Gray et al. [39] based on diffusion theory [40], interest in modelling tumour hypoxia has been relatively constant, although segmented in its aims. After initial interest in the late 1950s and into the 1970s [41–45] during which more basic mathematical diffusion based models and animal experimental work were carried out regarding tumour hypoxia and growth, the 1980s to the early 21st century saw the emergence of models that aimed to simulate vascularised tumour treatment and/or growth in the literature [2, 7, 46–51]. The modelled mechanisms of oxygen delivery and responses of the tumour in these models range from considerations of simple oxygen diffusion to considerations of oxygen consumption rates, vessel size/density/location, slowing of the cell cycle, induced cell death via necrosis and application of oxygen enhancement ratios relating to ionising radiation sensitivity.

The 1980s saw the first real-time stochastic applications of tumour computer models, which paved the path for the complex Monte Carlo simulations of the current era. The tumour models reported on during the last decade tend to involve more detailed cell line specific kinetics and also include one or more treatment modalities with the option of individual patient data input, for example, spatial PET imaging hypoxia information, the review of which will be encompassed in the proceeding sections of this paper. However, a group concentrating on tumour growth based on the work of Anderson et al. [52, 53] provides a good example of new modelling research not only on the process of angiogenesis but also the distribution of chemical factors including VEGF, ECM, DMA, and molecular oxygen [54]. Consequently distributions of blood vessel pressure and fluid velocity related spatial distributions within a tumour could be produced and their impact on tumour growth studied. This group provides a thorough review of angiogenetic modelling in their publications. Stochastic tumour growth models from the 1980s to the present often simulate not only tumour growth dynamics but also treatment of a virtual tumour, for example, the work of Duchting et al. [7, 8], Borkenstein et al. [20, 21], Stamatakos et al. [14, 15], Harriss-Phillips et al. [29] and Marcu and Bezak [55].

3. *In Silico* Cancer Treatment Models

3.1. Modelling of Radiotherapy-Induced Cell Kill. Predicting the outcomes of fractionated radiotherapy using models was initially developed utilising theories such as the Power Law equation of the Nominal Standard Dose theory of fractionated cell kill [56] and various extensions to the theory, as well as multitarget and multihit cell kill models of the 1960's and 1970's, for example, Cohen's target-cell model [57]. However from the early 1980s onwards, the Linear Quadratic (LQ) model of radiation induced cell kill has dominated the literature for its use in predicting the relationship between fractionated radiation dose and cell kill for doses per fraction near 2 Gy. LQ theory was based on the pioneering work of Lea and Catcheside [58] and on the hypothesis of single strand and double strand DNA aberrations as the source of radiation induced cell damage.

Use of the standard LQ equation became extremely popular in the mid 1980s and was soon extended by many authors by the addition of various modification factors for modelling effects such as the "time-factor" [59] for rapidly responding tumours and the oxygenation enhancement ratio (OER) [60] for tumours experiencing radioresistance due to hypoxia. Other equation-based models such as the binary misrepair model and models of repair capacity saturation were also devised and later compared to the LQ model [61], which yielded similar results under specific conditions, for example, 2 Gy per fraction. Dale and Jones have provided a thorough review of the history of mathematical fractionated radiotherapy models [62], which is recommended as a key text for all tumour model researchers, as are review articles by Fowler [63, 64] and Bentzen [65].

Alongside the development and widespread clinical implementation of the LQ model, other models were emerging in the last two decades of the 20th century. These models were initially mathematical based; however, a subset of modellers soon branched out into the utilisation of stochastic modelling techniques to describe the action and impact of ionising radiation on living tissue. As the models became more sophisticated, so too did the requirement not only to describe the effects of radiation more accurately, but also to model on smaller and smaller scales. Imaging modalities were beginning to collect data on the "mm" to cellular scales depending on the modality used, creating huge data sets when modelling tumours of macroscopic volumes.

Macroscopic tumour modelling is most relevant for comparisons to human data and eventual translation into clinical use, consequently the modelling of the tumour vascular system became of interest. Inclusion of oxygenation parameters in models was driven by the increasing realisation of the importance of tumour hypoxia as reported from large clinical trials for certain tumour sites, for example, head and neck [66–68]. Consequently, use of techniques and theories such as diffusion theory for the transport of oxygen through tissue [40] were employed by modellers. This particular theory was not a new one; however, theories such as this were now becoming increasingly utilised and incorporated into new sophisticated mathematical and hybrid mathematical-stochastic (automaton) models [6, 45].

Due to the advances and increasing usability of personal digital computers in the 1980s, the field of tumour and treatment modelling was boosted, particularly in the US and in European countries such as Germany and Norway. One of the first stochastic tumour growth and/or radiotherapy models of avascular tumours was called *CELLSIM* and later the 2D *CELLGROW* [1, 2], as previously mentioned in this paper. The treatment component of this model involves randomised “cell groups” (representing groups of cells) death based on LQ surviving fractions (SF) and focuses on cell cycle kinetics the impact of cell grouping on the statistical outcomes of phase blocking and cytotoxic drugs.

In the following decade, a mathematical model describing the changes in tumour growth during development and LQ-based cell kill emerged [3], simulating exponential cell proliferation at small sizes and Gompertzian-shaped growth at larger sizes. Deterministic equations are used to plot tumour mass curves as a function of time. Radiotherapy is modelled, with varying regimes, and the surviving cell fraction determined as a function of time. In the 1980s and well into the 1990s, groups led by Duchting and Kocher were each developing stochastic models of tumour growth and radiotherapy. Duchting et al.’s work was the first to explore cell by cell modelling of a tumour cell population in a growth medium (tumour spheroids), with the inclusion of cellular oxygenation parameters as well as many cellular kinetic and radiation schedule parameters (six schedules reported on) available for modification by the user [7–10]. Kocher et al.’s work [11, 12] also considered cellular oxygenation by modelling a regular array of vessels in 3D within a tumour mass, with 3 different schedules simulated. Both groups modelled slow versus rapid growth kinetic and studied the impact on treatment response, and either manipulated with the LQ equation by means of single OER values or unique α and β parameter values for hypoxic tissue.

Another mathematical model was reported in the late 1990s from Wouters and group [13, 69], which was also concerned with modelling tumour oxygenation and also the process of reoxygenation, considering two levels of oxidic status versus a full range of pO_2 values. In the next few years a stochastic model of tumour growth was developed, simulating cells with ranges of proliferative capacity (epithelial hierarchy), and investigating the kinetics of accelerated repopulation and treatments including radiotherapy and chemotherapy [4, 5, 70]. The model showed that while cellular recruitment from the quiescent phase into the cell cycle does not constitute a key mechanism in tumour repopulation after radiotherapy, loss of asymmetry in stem cell division, even for a small percent of stem cells, could be the key process in tumour regrowth.

In 2002, two mathematical tumour treatment models incorporating stochastic parameter distribution were reported on, one aiming to model and clinically verify accurate microvascular density and heterogeneity in a 2D tumour cross section with cylindrical vessels [18, 19] and the other simulating the delivering altered doses to different cells based on oxygen status. In the later model, chronic (permanent) as well as acute (temporal) hypoxia was investigated, and overall a 20% to 50% boost in dose to the hypoxic cell population

(up to 20% chronic hypoxic volume) required the same dose to control the tumour as for an oxidic tumour.

Søvik and colleagues [27] have developed a model aiming to “dose-paint” radioresistant tumour subvolumes with higher than normal doses, using clinically relevant oxygenation distributions in a mathematical spatial automaton model. Reoxygenation was also considered. The group concluded that prescribing varying doses to different parts of the tumour can significantly increase tumour control probability although the rate of reoxygenation was found to be the crucial parameter. Tumours with no reoxygenation had the most benefit of dose redistribution. The level of chronic hypoxia influenced outcome more than the level of acute hypoxia.

The modelling work of Daşu et al. [23, 71, 72] explored not only the measurement process of key parameters in tumour models and the effects of hypofractionation, but also the effects of chronic and acute hypoxia on tumour control in a mathematical probabilistic model [24, 25]. Results justified the need for a full description of tumour oxygenation to predict treatment outcomes and showed that temporal oxygenation changes between treatment fractions are less important than the presence of chronic hypoxia.

Finally, there have been a number of stochastic vascularised tumour growth and/or radiotherapy treatment models produced in the past decade. Of those reviewed herein, one is a purely temporal model, while the others are spatial-temporal. In general, most modern models simulate cell growth on an individual cell basis; however, there is a trend in some models to average cellular properties and model “tumour voxels” or “geometrical” cells. This is often performed because of the large tumour volumes being applied and owing to the direct input of imaging (anatomy and/or functional) data into the models. This direct input is used in some model as an alternative to simulating the tumour growth process, and rather the tumour is created at full size based on clinical data, ready for treatment simulation. There are advantages and disadvantages to this technique, including the lack of understanding/research into microscopic aspects of the tumour, that is, cellular kinetics and how kinetic parameters change with tumour volume, but also the benefits of individualising the model for a particular patient and therefore providing more direct outcomes to compare with clinical data.

The Greek modelling group led by Stamatakos have published many papers regarding their models of growth and radiotherapy for lung and brain tumours. Initial work began with a 3D discrete time step model [16] (extending upon pioneering work by Duchting in the 1980s) with spatial visualisation and modelling *in vitro* tumour spheroids for small lung cell carcinoma. Since 2004, the group has published models of *in vivo* tumour systems [14, 15, 17, 73–75], concentrating on glioblastoma multiform and the incorporation of experimental and clinical data into the model. The model now uses the concept of a “geometrical cell” (GC) to average cellular properties obtained from imaging data and uses a grid size of up to 120^3 . A comparison between six radiotherapy fractionation schedules has been performed by varying parameters such as the cell loss factor,

OER, OER_{β} , cell cycle time and mutated versus wild type p53 status. Results show that accelerated schedules are superior to conventionally fractionated ones and that wild type tumours (higher α/β) respond well compared to mutated tumours.

Borkenstein et al. [20] considered angiogenesis in their work and used an individual cell approach to spatially model tumour growth and radiotherapy treatment. Capillaries are placed at intervals in a 3D lattice, with cellular oxygenation based on the distance to the nearest capillary cell. Cells in a hypoxic state secrete an angiogenesis factor in proportion to the number of hypoxic cells in the tumour. Radiotherapy is based on LQ theory, with reoxygenation and accelerated repopulation also modelled. Various radiotherapy schedules have been compared, using OER values of 3.0 and 2.5. Results show that total doses of 86 Gy versus 78 Gy are required to achieve tumour control for conventional and accelerated schedules, respectively. Harting has extended the work by modelling a hypoxia-induced angiogenesis factor excreted radially from hypoxic cells [21, 22].

HYP-RT is a temporal stochastic model [29, 30], simulating individual tumour cell division and the effects of fractionated radiotherapy, with assumed randomised spatial cell placement in the tumour. The model is based on the proliferative hierarchy of epithelial cells, simulating head and neck squamous cell carcinoma growth and radiotherapy, with hypoxia modelled using realistic oxygen distributions and a dose per fraction dependent OER curve. The model is capable of simulating the effects of reoxygenation of hypoxic tumours as well as accelerated repopulation. Results show that accelerated repopulation and the percentage of stem cells are the two most important parameters controlling growth rate and radiotherapy outcome. An average simulated hypoxic tumour requires an extra 16 Gy in total dose to achieve tumour control using conventional fractionation. Accelerated repopulation had the effects of requiring an increase in dose per fraction of 0.5 to 1.0 Gy to control the extra cell growth. Hyperfractionated schedules using 2×1.1 Gy per day were found to be most effective, justified by efficient cell kill and relatively low early and late normal tissue toxicities, as predicted by biological effective dose.

A stochastic tumour simulation model [28] using cell line specific parameters and functional pretreatment PET/CT data was developed to investigate the effects of oxygenation on the radiation therapy outcome for HNSCC. Rather than using a three-dimensional lattice, this group uses a one-dimensional list of “cell groups” to store temporal cellular data, in order to minimise the number of stochastic calculations and processes. Patient data is imported (oxygenation and proliferation information) based on image voxels from PET scans, with one voxel representing approximately 10^6 cells. LQ cell kill is applied to simulate radiotherapy, with OER values for voxels taken into account. Chronic hypoxia and reoxygenation is considered, as were individual cell cycle phases and radiosensitivities. The results show that tumour responses vary as tumour oxygenation levels decrease and that oxygenation varied in time throughout treatment in a similar manner to human tumours. Tissue

growth curves followed *in vitro* cell line data for un-irradiated and irradiated cell lines (*HNSCC-1*), with an accurate time delay of tumour shrinkage predicted.

As mentioned in a number of the preceding model outlines, the majority of modern models use the standard LQ theory as a basis for stochastic cell kill; however, some models attempt to readdress cell survival theory by means of new equation sets. Such an example of this is the model by Hanin and Zaider [76] who have aimed to develop a cell survival model accounting for micro-dosimetric effects of radiation damage. Poisson based theory of DNA damage is no longer followed, instead normal shaped distributions are utilised making the model potentially suited to low, intermediate and high dose per fraction regimens.

In-silico tumour growth and/or treatment models have various degrees of complexity, with numerous assumptions applied, as is inherent in all modelling applications. Commonly, the goal of the modeller is to determine the optimal treatment strategy, for example, dose fraction sizes and timing, to achieve tumour control or total cell kill for a specific tumour type. The goal should also be to achieve optimised tumour cell kill within minimal normal tissue toxicity levels, ideally on an individual patient basis. This goal, however, is very challenging for reasons including: data gathering from reliable *in vivo* experiments, the large and varied patient sets in clinical trials and the extremely complex biological and chemical processes involved in carcinogenesis and tumour evolution. Tumour radiotherapy modelling requires not only accurate radiation damage models but also the implementation of how the tumour cells respond to sublethal or lethal damage, which may change with dose received, tumour volume, oxygenation levels and numerous other cell line specific and individual tumour-based factors. Nevertheless, the development of models has and will continue to assist radiobiologists and clinicians in predicting tumour behaviour and understanding microscopic mechanisms and impact upon macroscopic and measurable tumour parameters, and as such the research should continue and be encouraged.

A selection of key tumour models from the literature are tabulated below regarding avascular tumour radiotherapy models (Table 1) and vascular tumours (Table 2). Readers should note that many hundreds if not thousands of articles have been published in peer-reviewed scientific journals on expansions and clinical data fitting to the models mentioned in this paper and many other models in the literature (for example, the use of mathematical distributions of values for radiosensitivity parameters or oxygenation parameters, as well as splitting up the equations into those tailored specifically for late and early responding tissues [77–81]). However, it is beyond the scope of the current review to explore the use and/or interpretation of clinical data by means of *in silico* radiotherapy models.

While the vast majority of tumour growth and treatment response models (such as the ones presented above) are simulated on a cellular level, models on a smaller scale are a hot topic of current investigation. Monte Carlo models targeting the cell nucleus and cytoplasm have been developed using the ever-expanding GEANT4 MC simulation toolkit.

TABLE 1: Models that simulate tumour growth and/or radiotherapy, without tumour oxygenation considerations (avascular tumours).

Model details	Objectives	Key parameters	Model outcomes
Stochastic, <i>CELLSIM</i> , and <i>CELLGROW</i> , Donaghey, 1981–1983 [1, 2]	Individual cell/cell group growth model	Phase transition probabilities, proliferation-based commands on up to 90 cell groups, contact inhibition modelled	Monolayer cell growth achieved and RT/drug therapy applied
Mathematical, O'Donoghue, 1997 [3]	Modelling exponential proliferation at small tumour sizes and Gompertzian at larger sizes	3 LQ based parameters, 2 growth related parameters and 1 radiation induced death rate parameter	The effects of RT described in terms of cure (clonogenic cell sterilization) and/or tumour regression/regrowth
Stochastic, Marcu et al., 2002–2006 [4, 5]	Modelling tumour growth and response to radiotherapy	Cell cycle specific surviving fractions (SF_2) based on LQ model. Repopulation mechanisms during RT such as cell recruitment, accelerated stem cell division, and asymmetry loss in stem division	The effect of conventional and altered fractionation radiotherapy on cell survival evaluated. The contribution and likeliness of repopulation mechanisms assessed

Barberet et al. have modelled different cell geometries found in a typical cell population in order to evaluate the absorbed energy from alpha particles and their response to different irradiation protocols [82]. The pictorial results of this sub-cellular model of energy deposition after alpha-particle interaction were in agreement with the experimentally obtained images of DNA double strand breaks signalling proteins. Absorbed dose after cellular irradiation on a nano-scale was the focus of another, technically similar paper, incorporating different alpha-particle sources [83]. While the emphasis of these papers is on the microdosimetric aspects of radiation interaction with tumour cells, this different perspective can bring more insight into the radiobiological processes on a nano-scale, therefore a better understanding of the impact of radiation on cell behaviour in its microenvironment.

3.2. Modelling of Chemotherapy-Induced Cell Kill. Chemotherapy agents act via many different pathways and they vastly differ in biochemical structure, molecular mode of action, pharmacology, clearance, and side-effects. Furthermore, in chemotherapy there is no formalism equivalent to the linear quadratic model used in radiotherapy which would describe, in a simplistic yet practical way, cell survival.

While quantitative modelling has great potential, it requires knowledge of the numerical values of multiple parameters in order to characterize the chemotherapy dose regimens. This information is rarely available; therefore, the modelling of combination-chemotherapy regimens (drug cocktails), or of large classes of chemotherapy agents, can induce errors and inaccuracies in the simulation process.

The pool of chemotherapy-induced cell kill models is vast. Similarly to radiotherapy, chemotherapy models are divided between analytical and stochastic and they target various aspects of drug kinetics/dynamics and tumour response. In the paragraphs below, the main chemotherapy model categories are presented by listing the most representative papers from each group. Besides the most common cell kill models that investigate the correlation between tumour

kill and drug concentrations/exposure times (area under the time-concentration curve), there are models studying the effect of various drugs on tumour cell kill along the cell cycle as well as compartment models focusing on drug pharmacokinetics. In addition, there are models which tackle the problem of drug resistance and repopulation during chemotherapy—two major factors which can lead to treatment failure. While models of drug resistance are more commonly reported in the literature, tumour repopulation during chemotherapy is usually a neglected factor when it comes to modelling.

One of the first reviews on chemotherapy modelling was published by Aroesty et al. [84]. The main focus of the paper was on the effects of cell-cycle specific therapy on tumour growth and on the distribution of cells along the cell cycle. Several mathematical models of chemotherapy were developed afterwards considering generalized analytical models for cycle-specific and cycle-non-specific therapies, respectively. The main differences between these two categories lie in the parameters quantifying cycle specificity and variation in growth fraction [85]. Many such models assume that the growth fraction of the tumour cell population responds instantaneously to cell killing by chemotherapy. This is not realistic, as drug pharmacokinetics indicates the existence of a drug “binding time” to achieve cell damage, which does not occur instantaneously. Some chemotherapeutic agents need several hours to form cytotoxic DNA adducts [86]. Moreover, numerous drugs express cytostatic properties, thus arresting the cells into one of the cycle phases before dying. Cell arrest can last for days [87]; therefore, the instantaneous kill is not validated.

Despite the obstacles imposed by chemotherapy modelling, models of drug pharmacokinetics and pharmacodynamics have been developed in the past, using either analytical or probabilistic methods [85]. In fact, the first model to describe pharmacodynamic effects by means of drug-induced tumour growth inhibition *in vitro* was reported by Hill in 1910 [88]. Hill’s model, also called the logistic model,

TABLE 2: Models that simulate tumour growth and/or radiotherapy, incorporating tumour oxygenation (vascularised tumours).

Model details	Objectives	Key parameters	Model outcomes
Mathematical, Tannock, 1972 [6]	To relate oxygen tension, radiosensitivity, and distance from blood vessels	Distance to blood vessel (radial), pO_2 vessel radius, coefficient of diffusion, rate of O_2 consumption, diffusion maximum radius	A full range of oxygen tension values are required to accurately model tissue oxygenation and radiosensitivity with good agreement to clinical data
Stochastic, Duchting et al., 1981–1995 [7–10]	To grow and treat <i>in vitro</i> tumour spheroids (mouse brain and lung) in a nutrient medium as well as the surrounding normal tissue (epidermis)	Rapid versus medium or slow proliferation (CCT adjustment 10 to 30 hours), 120 hour dead cell clearance, LQ radiosensitivity with separate α_{hypoxic} and β_{hypoxic} terms, 30% repair probability of sublethal damage, 10% G_0 phase recruitment, individual cell cycle phase times	Six RT schedules simulated and compared in terms of cell kill to assess TCP and likelihood of epidermal side effects, 3 no./day produced high toxicity and a reduction from 60 to 50 Gy total doses is suggested
Stochastic, Kocher et al., 1997–2000 [11, 12]	Brain tumour growth and RT in a regular 3D lattice	Cell cycle times of 2 or 5 days, regular capillary placement in the lattice, $100 \mu\text{m}$ oxygen diffusion limit to define hypoxia and $140 \mu\text{m}$ to define necrosis, constant OER value of 3.0, 5 day dead cell clearance	Three RT schedules simulated, with accelerated RT more effective on fast growing tumours
Mathematical, Wouters and Brown, 1997 [13]	Equation-based modelling of hypoxic tumour LQ cell kill for tumours with a 2-compartment oxygen level make-up versus intermediate (0.5 to 20 mm Hg) oxygen values	Radial distance of a cell from the tumour boundary to determine oxygenation (2-component model or complete range of pO_2 values considered)	Small impact of full reoxygenation between fractions: hypoxia plays a significant role in determining outcome, 10% hypoxia and 30×2 Gy radiotherapy equates to 10^4 times less cell kill using a full pO_2 range compared to the 2-component oxygenation model
Stochastic, Stamatakis et al., 2001–2010 [14–17]	Simulating lung and brain tumour growth in a 3D lattice to determine optimal individualised RT schedules	Gaussian probability cell cycle times, G_0 phase on 25 hours, reoxygenation during shrinkage, S phase versus non-S phase LQ radiosensitivity values, cellular hypoxia if more than three cells from nutrient source, OER ranging from 1.0 to 3.0 with separation into OER_α and OER_β	OER_β values of 3.0 to 3.5 provide cell kill in agreement with cell culture survival curves, accelerated schedules are beneficial, wild type tumours (higher α/β) respond well compared to mutated tumours
Mathematical, Nilsson et al., 2002 [18]	Simulating realistic oxygenation gradients and cell densities to explore their impact on radiosensitivity at both the microscopic and macroscopic scale	Oxygenation, vessel geometry parameters (density, radius, heterogeneity), oxygen consumption rate, distance from a vessel	Vascular heterogeneity impacts significantly on the hypoxic fraction, local and global dose responses are predicted from LQ theory using the initial clonogenic cell number and the effective radiation distance
Mathematical (stochastic components), Popple et al., 2002 [19]	Predicting tumour control probability after selective boosting hypoxic subvolumes within a tumour mass	Reoxygenation between doses, OER of 2.0 for hypoxic cells, boost and nonboost spatial cell compartments.	A 20% to 50% boost in dose to a subpopulation of hypoxic cells increased tumour control probability equal to that of an oxic tumour, a boost dose to regions of transient hypoxia has little effect
Stochastic, Borkenstein et al., 2004–2010 [20–22]	Simulating hypoxic tumour growth and RT considering hypoxia and angiogenesis	OER = 2.5 and 3.0 (continuous cell oxygenation range in later work), vessels modelled in a regular lattice, angiogenic factors to induce vessel growth and hence pO_2 delivery to cells, distance of a cell from a vessel.	An increase in capillary cell cycle time affects tumour doubling time as does the intercapillary distance, doses of 86 Gy versus 78 Gy are required to control the simulated tumours for conventional and accelerated schedules, respectively
Mathematical (stochastic components), Daşu et al., 1999–2009 [23–26]	Simulating 2D cell distributions to investigate the effects of cell heterogeneity, hypoxia (acute and chronic) on RT outcome	2-compartment oxygenation (2.5 mm Hg hypoxic threshold) versus full oxygenation range, cell heterogeneity	Temporal oxygenation changes between treatment fractions are less important than the presence of chronic hypoxia, and a small degree of hypoxia during every treatment fraction has an effect on tumour response regardless of the changes in spatial hypoxia, a 2-component hypoxia model is not sufficient in describing tumour oxygenation

TABLE 2: Continued.

Model details	Objectives	Key parameters	Model outcomes
Mathematical (stochastic components), Søvik et al., 2007 [27]	Optimising tumour control through redistribution of the delivered dose, “dose painting”	pO ₂ histograms (0 to 102.5 mm Hg), hypoxia defined by 5.0 mm Hg threshold, reoxygenation modelled, heterogeneous cell density, dose delivery based on four pO ₂ thresholds: 2.5, 5.0, 20.0, 102.5 mm Hg, OER _{α,max} and OER _{β,max} of 2.5 and 3.0, OER equation maximum of 3.28	Prescribing varying doses to different parts of the tumour can significantly increase TCP although the rate of reoxygenation is crucial. Tumours with no reoxygenation have the most benefit of dose redistribution. Chronic hypoxia influences outcome more than acute hypoxia
Stochastic, Titz and Jeraj, 2007 [28]	Simulating cell line specific parameters and functional pre-treatment 3D PET/CT data to investigate the effects of oxygenation on RT outcome	5-day cell dead clearance, 36-hour average cell cycle time, OER with <i>K</i> value of 3.0, full pO ₂ range, 1 mm Hg necrotic threshold, individual phase radiosensitivities	Tissue growth curves and reoxygenation data follow <i>in vitro</i> and human clinical data, with an accurate time delay of tumour shrinkage predicted
Stochastic, “HYP-RT,” Harriss-Phillips et al., and Tuckwell et al., 2008–2011 [29, 30]	Simulating hypoxic tumour growth and reoxygenation during RT of HNSCC	LQ-based cell kill with OER consideration, full cellular pO ₂ distribution (1 to 100 mm Hg), OER curve changing with dose per fraction, reoxygenation as well as accelerated repopulation between dose fractions	Hyperfractionation using 2 × 1.1 Gy per day is optimal for HNSCC, hypoxic tumours require 16 Gy extra dose during conventional radiotherapy compared to oxyc tumours, and the maximum value and shape of the oxygen enhancement ratio curve that may be dependent on dose per fraction are crucial for prediction of TCP

is still commonly used to illustrate the concentration-effect relationship for various drugs based on statistical fits to a sigmoidal curve. However, when cell cycle specificity comes into play, the model has its own limitations.

There are several models studying the effect of various drug concentrations and exposure times on tumour control. Gardner [89] proposed an exponential kill model to predict the shape of dose-response curves based on several parameters: cycle phase specificity of the drug, cycle time, drug concentration, and exposure time. The analytical equations presented are able to predict the inhibitory concentration to achieve a certain percentage of cell kill.

Numerous studies have used the “area under the time-concentration curve” (AUC) as an approach to model chemotherapy. The area under the curve is a commonly used measure of total drug exposure and is obtained by plotting the concentration of the agent as a function of time and obtaining AUC by integration. While for some drugs (like alkylating agents) the effect is proportional to the AUC [90], for others, the duration of exposure may be more important than concentration; therefore, the relationship between AUC and tumour response is weaker. For certain drugs, such as Cisplatin, studies show that AUC is a good predictor of response [91–93]. Moreover, since the magnitude of exposure to Cisplatin is, through the DNA-adducts formation, the major determinant of the response rate, the AUA (area under the DNA adduct-time curve), also offers a reliable prediction in tumour response [93].

The AUC models are usually based on *in vitro* data regarding time dependency of drug potency, slope of the concentration-effect curves, and relative degree of drug

resistance. Levasseur et al. [92] have created a pharmacodynamic model to facilitate the quantitative assessment of the growth-inhibitory effect of anticancer agents as a function of concentration and exposure time. Empirical mathematical expressions were built into a global concentration-time-effect model which showed that it was possible to modulate drug effect, response heterogeneity, and drug resistance by altering the time of exposure to the agents.

Compartment Models. There are convenient ways to describe drug pharmacokinetics inside the body, that is, the way plasma concentration of a drug changes over time. Depending on their properties (distribution, metabolism, clearance) drugs follow multicompartmental behaviour (usually two or three-compartment models) (Figure 3). The common aim of these models is to find optimal tumour control in cancer chemotherapy via cell cycle specificity. One-compartment models are very simplistic as they consider the whole body as a single unit (compartment) in which the drug concentration is assumed to be uniform. This assumption is not valid for tumours, as the uptake of chemotherapeutic agents varies as a function of cellular proliferation (cytotoxic agents preponderantly target cells with high mitotic index). In two compartment models drug disposition is biexponential, whereby the drug is distributed into a second compartment but is eliminated from the first. Three compartment models are more complex as they have two peripheral compartments where drugs are distributed before elimination from the central compartment. Compartment models are commonly used in PET studies to evaluate the pharmacokinetics of specific radioisotopes.

On a cellular level, compartment models are designed for investigations into cell-cycle kinetics. In these models,

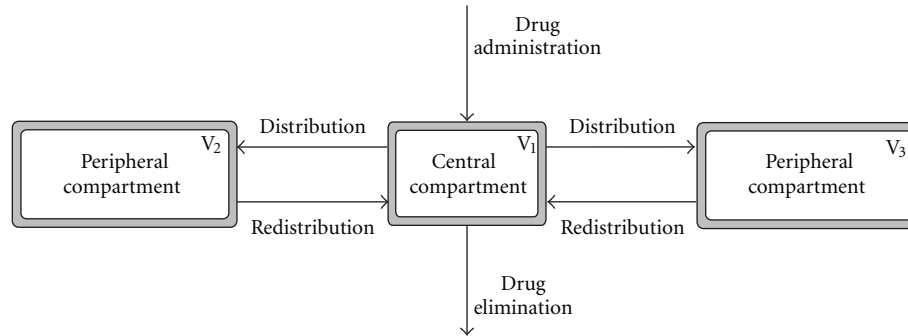


FIGURE 3: Schematic representation of a three-compartment model.

the compartments are represented by the phases of the cell cycle, starting with the growth phase G_1 which leads into the DNA synthesis phase S , followed by another growth phase G_2 which then leads to mitosis, M . The options are to divide the cell cycle into two (usually $G_1 + S$ and $G_2 + M$) or three compartments (usually G_1 , S and $G_2 + M$). This division into compartments facilitates the modelling of cell cycle-specific drugs, that is, different classes of chemotherapeutic agents (such as cytotoxic agents, cytostatic agents or recruiting agents—when the G_0 resting phase is also taken into account). This type of cell cycle kinetics modelling was introduced by Swierniak et al. in the 1980s [94] and later extended into more complex simulations [95, 96].

Chemo-related factors such as drug diffusion, uptake/binding, clearance and their effect on cell cycle progression are individually incorporated in various spatio-temporal models [97–99]. A more complex mathematical simulation has accounted for all the above parameters with the intention of modelling the interaction between drugs and the heterogeneous tumour microenvironment [100]. In this work, a multicompartiment pharmacokinetic analysis of two drugs (paclitaxel and 5-fluorouracil) with different transport characteristics is modelled with emphasis on drug diffusion, clearance, and cytotoxicity, leading to a cell distribution along the cycle similar to experimentally obtained data. A major finding of the simulation was the observation that cell-cycle specific drugs might not offer unique advantages over cell-cycle nonspecific drugs. An added result of the model is the chemoresponsiveness to paclitaxel of slowly growing tumours which was shown to be higher than of fast growing ones due to high repopulation in between cycles of chemotherapy in the latter tumour group (which could not be compensated by the drug's cytotoxic effect).

Another multi-compartment model to predict cellular response of different cell lines to mitotic arrest when exposed to paclitaxel was developed by Basse et al. [101] with statistical results validated against flow cytometry analyses.

On similar principles of compartment modelling, the pharmacodynamics of Cisplatin have been simulated [91] by considering transport reaction processes between extracellular and intracellular compartments, with drug species classified into extracellular concentration, intracellular concentration, concentration bound to DNA and concentration

released from DNA as a result of DNA repair. The model is based on the assumption that cell kill depends on the peak level of DNA-bound intracellular platinum and for short exposure times it yields predictions similar to those resulting from AUC-type models. The major problems with compartment models, as with any other chemotherapy simulations, are the identification of cell cycle parameters which can influence drug kinetics, thus short- and long-term effects.

One of the major challenges of chemotherapy is associated with drug resistance caused by mutations in cancer cells. *Models of drug resistance* started to be developed in the late 1970s, with the Goldie Coldman [102] model on the theory of evolution of drug resistance by clonal selection. Their model was based on biological assumptions stating that drug resistance results from clonal selection of randomly occurring mutants which are completely impervious to the drug. The analytical model followed the development of the mutant cell population as well as the sensitive tumour cells, considering that the same growth kinetics applies to both groups of cells. Clinically, such an assumption is not realistic, as sensitive cells are killed more easily than mutant resistant ones. Another oversimplification of their model was to consider drug resistance as all-or-none (mutants, deemed to be more resistant, were completely unresponsive to the drug). Therefore, progressively higher levels of resistance can be expected to emerge with continued treatment.

Birkhead et al. [103] have designed a model that brings the principles of the Goldie-Coldman model closer to the actual clinical practice. The modelled tumour includes three cell categories: cells presenting with intrinsic resistance, the second group characterized by acquired resistance, and the third group being a sensitive population, responsive to the drug. Various drug concentrations are administered to study tumour response in time. The model relates to chemotherapy treatment in general, therefore, in order to simulate treatment strategies, specific values have to be used for cell-kill and resistance. This requirement is a limitation to the model, due to the lack of biological data and the uncertainties in the existing values for larger groups of patients.

Mathematical models of gene amplification were developed by Kimmel and Axelrod [104] to study cellular drug resistance. Their models are based on the principle whereby,

at each cell generation, there is a probability of increasing/decreasing the gene copies per cell. The consequence of this probabilistic mechanism is reflected in the increased number of genes (gene amplification) found in tumour cells which confer resistance to chemotherapeutic agents. The novelty of the model lies in the description of the probabilities of the changes in numbers of gene copies in each cell, that is, the rates of gene amplification and deamplification. The model investigates the mechanisms and conditions responsible for a stable distribution of the number of gene copies as supported by experimental data.

Ample modeling of drug resistance was undertaken by Komarova [105] and Komarova and Wodarz [106]. Using a stochastic approach involving a discrete state space Markov process, their model allocates each cell type resistance properties. Cells can acquire resistance to drugs by means of mutations (where resistance to one drug does not imply resistance to another drug). In order to develop resistance to a number of n drugs, a cell must accumulate n mutations. Drug-induced cell death is regulated by the extent of drug resistance, whereby cells resistant to all drugs are not killed by the drug while cells susceptible to certain drugs are labelled with a drug-induced death rate dependent on treatment intensity. The model concluded that the success of the treatment is independent on turnover rate (the ratio of the natural death rate and replication rate) for one-drug treatments but dependent on turnover rate for multiple-drug treatments. A more specific Monte Carlo model, looking into tumour resistance to Cisplatin was developed by Marcu et al. [107] by modelling two classes of drug-resistance mechanisms: one leading to low drug uptake and the other responsible for the decreased susceptibility to the induction of apoptosis. To quantify the extent of drug resistance, the Cisplatin resistance factor (CRF) was defined. Drug resistance was shown to be a cumulative process: for low drug uptake, resistance seemed to cumulate linearly or even supralinearly for very low uptake. When decreased susceptibility to the induction of apoptosis was modelled, resistance increased over a sigmoid pattern.

Modelling of crossresistance in cyclic chemotherapy treatment was tackled by Katouli and Komarova [108] showing that the general rule in cyclic treatment in order to avoid cross-resistance would be “best-drug-first, worst-drug-longer,” meaning that the optimal strategy is to start the chemocycle with the more powerful drug but use longer cycles for the weaker drug.

While repopulation during radiotherapy is an extensively studied aspect associated with treatment failure, *tumour repopulation during chemotherapy* is usually a neglected factor. As shown by Davis and Tannock [109] the impact of repopulation between cycles of chemotherapy on treatment response may be comparable to that of intrinsic or acquired chemoresistance. These findings have been confirmed by a stochastic model of tumour growth and response to chemotherapy [110]. Cellular recruitment was modelled by releasing various percentages of quiescent cells into the mitotic cycle after each drug-caused cell kill. The onset of repopulation was also simulated, with both immediate onset and late onset of cell recruitment. Repopulation during chemotherapy was shown to be a highly potent

phenomenon; similar to drug resistance, therefore it should not be neglected during treatment.

Models are useful tools to simulate novel treatment schedules designed to improve treatment outcome by means of higher therapeutic ratio. Such a novel regimen for Cisplatin was suggested by Marcu and Bezak [55] in a neoadjuvant setting, based on previously grown tumour model using probabilistic methods of tumour development and response to therapy. The proposed model suggests that Cisplatin be delivered every three days leads to similar tumour control as the daily regimen, but with better organ sparing and higher therapeutic ratio than the weekly drug schedule.

Mechanistic mathematical models developed to improve the design of chemotherapy regimen were summarised by Gardner [111] and Gardner and Fernandes [112]. Mechanistic models are tools which incorporate patient-specific cell kinetic parameters and allow for prediction of heterogeneous outcome across patients. Such models, based on drug pharmacokinetics and dynamics incorporating subpopulation drug resistance, cell division, and apoptotic rates were designed by Gardner [113] to kinetically tailor treatment (KITT model) to individual patients. An impressive number of 26896 tumours were modelled to build a decision tree for prognosis and the simulated predictions were in good accord with clinical trial results. These models are needed to explain multiple-drug interactions, the evolution of drug resistance inside tumour cells, cellular kinetics and the choice of chemotherapeutical agents.

The literature on chemomodelling shows that optimum treatment strategies are hard to derive mainly because of lack of quantitative knowledge of the biological parameters of cancer chemotherapy. While quantitative data for a specific drug can be obtained from specific *in vitro* experiments, the number of unknown parameters originating from multidrug interaction turns modelling into an exigent task.

3.3. Modelling of Tumour Response to Combined Treatment.

The literature is scarce on combined chemoradiotherapy models, a possible reason being the lack of quantitative experimental data on radiation-drug interactions. Studies which model combined treatment techniques aim their focus towards factors such as (1) timing between agents, (2) optimal combined schedules, (3) the extent of agent interaction (additive, antagonistic, or synergistic), (4) dose-effect and (5) acquired resistance to treatment, to name just a few.

Goldie and coworkers [114] simulated alternating chemotherapy and radiation on a hepatoma, based on experimental data. The model was built on a previously developed tumour growth model with three discrete compartments: stem cells, differentiating cells, and end cells. The main focus of the model was on stem cells, which have been classified into various resistant groups: cells resistant to chemotherapy but radiation sensitive, cells resistant to radiation but chemo sensitive, cells sensitive to both treatments, with the final group of cells resistant to both therapies. The aim of the combined model was to alternate radiotherapy with chemotherapy (cyclophosphamide) in various protocols in

TABLE 3: Difficulties in tumour growth and treatment response modelling relating to suitable input biological data.

Parameters/information that are difficult to obtain (quantitatively)	Reason for the difficulty	Overcoming the difficulty
Aggressiveness and time of onset of accelerated repopulation	Intertumour variability that is unknown cannot measure/estimate for individual patients without cell biopsy sample used in <i>in vitro</i> tests which may alter results	Grouping patients into tumours that are likely to have slow or fast repopulation by some means of genetic/pathologic testing—however methods currently unknown
The extent of various mechanisms responsible for tumour repopulation during treatment	The interplay between recruitment, accelerated stem division, abortive division and loss of asymmetrical division, in stem cells makes it difficult to evaluate their individual effect	Research stem cell properties for rapidly proliferating tumours. Sensitivity study on each individual and combined parameter when modelling
Input of individualised tumour data, for example, intrinsic radiosensitivity, differences in stem/transit or quiescent cell radiosensitivity	Currently no pretreatment testing due to logistics and time of testing	Research cell type/proliferative capacity-dependent radiosensitivities for different tumour cell lines, individualised radiosensitivity pre-treatment testing (requires staff/money/time)
Tumour oxygenation/reoxygenation	Different in every tumour, changes in time, access to equipment, for example, daily/weekly PET, invasive nature of <i>in vivo</i> quantitative data gathering, for example, Eppendorf/Oxy Lab probe	Access and research into the feasibility and drug development for daily/weekly PET scans, with tracers that can image hypoxic regions with various thresholds, for example, 2.5, 5.0, 10 mm Hg
Drug pharmacokinetics	Lack of quantitative <i>in vivo</i> assays	Using <i>in vitro</i> data if existent, parameter estimation and sensitivity study. Molecular pharmacological modelling is required
Cell survival data for chemotherapy	Lack of mathematical formalism equivalent to the LQ model used in radiotherapy	Using <i>in vitro</i> data if existent for that particular agent

order to achieve an optimal tumour control. They have concluded that combined regimen is more effective in eliminating the stem cells than any of the two modality regimens alone.

Cisplatin and radiotherapy for advanced head and neck cancers was stochastically modelled by Marcu et al. [70] looking at cell survival (tumour control) after various combined schedules. The treatment modules were applied on a previously developed virtual tumour consisting of kinetic parameters characteristic to squamous cell carcinomas of the head and neck. The model showed that while weekly Cisplatin, which is the current standard of care, has improved radiotherapy by only 6%, daily administration of Cisplatin led to a 35% improvement in tumour control as compared to radiation alone. Furthermore, optimal treatment outcome was obtained when Cisplatin was administered very closely to radiotherapy (immediately before or after irradiation) due to Cisplatin pharmacokinetics.

Besides radiotherapy and chemotherapy, immunotherapy has become an important aspect of today's cancer management. Based on logistic tumour growth law, the combination of chemotherapy with immunotherapy was recently simulated by Hu and colleagues [115] to address the antagonistic, additive and/or synergistic effect of the combined treatment *in silico*, in order to select an optimal chemotherapeutic protocol. The theoretical model simulates the dynamic evolution of tumour population density under dual coupling periodic interventions (treatment). The model outcome is in fine agreement with Loewe's additivity model, a universal reference model for drug interaction, showing that the curative effect of the combined treatment

is strongly dependent on the intensity, nature (sub/supra-additive) and the timing of the individual treatments. This study could serve as a useful preclinical pharmacokinetic assessment of drug-drug or drug-immunotherapy interaction.

4. Conclusions

To further increase the power of complex tumour modelling into the future, greater depth of knowledge of tumour biology on an individual tumour basis will be required. This data is likely to be at micro(cellular) level as well as genetic and chemical level within the tumour. The data required for model input, necessitating the need for *in vivo* tumour measurement and/or imaging (before and at regular intervals during treatment), may include levels of specific protein synthesis and activity, a full description of tumour oxygenation from 0 to approximately 40 mm Hg, intrinsic radiosensitivity levels and cell kinetic behaviour of all cell types involved including all primary tumour cell types, vessel (endothelial cells), surrounding normal cell information, patient condition variable such as immune system responses in the form of DNA damage repair efficiency.

Specific difficulties of data gathering for tumours models are listed in Table 3 and generally include the following:

- (i) variations between patients;
- (ii) the dynamic nature of the parameters desired;
- (iii) time/expense due to complexity of testing procedures, for example, protein analysis;

- (iv) understanding the mechanisms of microscopic processes within the tumour which are often interrelated.

While overcoming the difficulties imposed by these parameters can be a complicated task due to clinical confines in obtaining quantifiable data, there is always an option to undertake computational sensitivity studies of specific parameters within biologically plausible limits.

The future of *in silico* tumour modelling is challenging, but wide open for expansion through the dedication of radiobiology, medical physics, and computational science researchers. Assumptions, estimations, idealisations, and trial-end-error situations will constantly be part of the modelling process. Nevertheless, despite its limitations, mathematical and computational modelling is already playing an integral role in several aspects of cancer management and it is expected to gain more ground in the near future by complementing other preclinical studies.

References

- [1] C. E. Donaghey, "CELLSIM: cell cycle simulation made easy," *International Review of Cytology*, vol. 66, pp. 171–210, 1980.
- [2] C. E. Donaghey, "CELLSIM and CELLGROW: tools for cell kinetic modeling," *ISA Transactions*, vol. 22, no. 4, pp. 21–24, 1983.
- [3] J. A. O'Donoghue, "The response of tumours with Gompertzian growth characteristics to fractionated radiotherapy," *International Journal of Radiation Biology*, vol. 72, no. 3, pp. 325–339, 1997.
- [4] L. Marcu, T. van Doorn, and I. Olver, "Modelling of post-irradiation accelerated repopulation in squamous cell carcinomas," *Physics in Medicine and Biology*, vol. 49, no. 16, pp. 3767–3779, 2004.
- [5] L. Marcu, T. Van Doorn, S. Zavgorodni, and I. Olver, "Growth of a virtual tumour using probabilistic methods of cell generation," *Australasian Physical and Engineering Sciences in Medicine*, vol. 25, no. 4, pp. 155–161, 2002.
- [6] I. F. Tannock, "Oxygen diffusion and the distribution of cellular radiosensitivity in tumours," *British Journal of Radiology*, vol. 45, no. 535, pp. 515–524, 1972.
- [7] W. Duchting and T. Vogelsaenger, "Recent progress in modelling and simulation of three-dimensional tumor growth and treatment," *BioSystems*, vol. 18, no. 1, pp. 79–91, 1985.
- [8] W. Duchting, T. Ginsberg, and W. Ulmer, "Modeling of radiogenic responses induced by fractionated irradiation in malignant and normal tissue," *Stem Cells*, vol. 13, supplement 1, pp. 301–306, 1995.
- [9] W. Duchting, W. Ulmer, R. Lebrig, T. Ginsberg, and E. Dedeleit, "Computer simulation and modelling of tumor spheroid growth and their relevance for optimization of fractionated radiotherapy," *Strahlentherapie und Onkologie*, vol. 168, no. 6, pp. 354–360, 1992.
- [10] W. Duchting and T. Vogelsaenger, "Three-dimensional pattern generation applied to spheroidal tumor growth in a nutrient medium," *International Journal of Bio-Medical Computing*, vol. 12, no. 5, pp. 377–392, 1981.
- [11] M. Kocher, H. Treuer, and R. P. Müller, "Quantification of tumor reoxygenation during accelerated radiation therapy," *Radiology*, vol. 205, no. 1, pp. 263–268, 1997.
- [12] M. Kocher, H. Treuer, J. Voges, M. Hoevens, V. Sturm, and R. P. Müller, "Computer simulation of cytotoxic and vascular effects of radiosurgery in solid and necrotic brain metastases," *Radiation Therapy and Oncology*, vol. 54, no. 2, pp. 149–156, 2000.
- [13] B. G. Wouters and J. M. Brown, "Cells at intermediate oxygen levels can be more important than the "hypoxic fraction" in determining tumor response to fractionated radiotherapy," *Radiation Research*, vol. 147, no. 5, pp. 541–550, 1997.
- [14] G. S. Stamatakos, E. A. Kolokotroni, D. D. Dionysiou, E. C. Georgiadi, and C. Desmedt, "An advanced discrete state-discrete event multiscale simulation model of the response of a solid tumor to chemotherapy: mimicking a clinical study," *Journal of Theoretical Biology*, vol. 266, no. 1, pp. 124–139, 2010.
- [15] G. S. Stamatakos, V. P. Antipas, N. K. Uzunoglu, and R. G. Dale, "A four-dimensional computer simulation model of the in vivo response to radiotherapy of glioblastoma multiforme: studies on the effect of clonogenic cell density," *British Journal of Radiology*, vol. 79, no. 941, pp. 389–400, 2006.
- [16] G. S. Stamatakos, E. I. Zacharaki, M. I. Makropoulou et al., "Modeling tumor growth and irradiation response in vitro—a combination of high-performance computing and web-based technologies including VRML visualization," *IEEE Transactions on Information Technology in Biomedicine*, vol. 5, no. 4, pp. 279–289, 2001.
- [17] D. D. Dionysiou, G. S. Stamatakos, D. Gintides, N. Uzunoglu, and K. Kyriaki, "Critical parameters determining standard radiotherapy treatment outcome for glioblastoma multiforme: a computer simulation," *The Open Biomedical Engineering Journal*, vol. 2, pp. 43–51, 2008.
- [18] J. Nilsson, B. K. Lind, and A. Brahme, "Radiation response of hypoxic and generally heterogeneous tissues," *International Journal of Radiation Biology*, vol. 78, no. 5, pp. 389–405, 2002.
- [19] R. A. Popple, R. Ove, and S. Shen, "Tumor control probability for selective boosting of hypoxic subvolumes, including the effect of reoxygenation," *International Journal of Radiation Oncology Biology Physics*, vol. 54, no. 3, pp. 921–927, 2002.
- [20] K. Borkenstein, S. Levegrün, and P. Peschke, "Modeling and computer simulations of tumor growth and tumor response to radiotherapy," *Radiation Research*, vol. 162, no. 1, pp. 71–83, 2004.
- [21] C. Harting, P. Peschke, K. Borkenstein, and C. P. Karger, "Single-cell-based computer simulation of the oxygen-dependent tumour response to irradiation," *Physics in Medicine and Biology*, vol. 52, no. 16, pp. 4775–4789, 2007.
- [22] C. Harting, P. Peschke, and C. P. Karger, "Computer simulation of tumour control probabilities after irradiation for varying intrinsic radio-sensitivity using a single cell based model," *Acta Oncologica*, vol. 49, no. 8, pp. 1354–1362, 2010.
- [23] A. Dasu and J. Denekamp, "Superfractionation as a potential hypoxic cell radiosensitizer: prediction of an optimum dose per fraction," *International Journal of Radiation Oncology Biology Physics*, vol. 43, no. 5, pp. 1083–1094, 1999.
- [24] A. Daşu, I. Toma-Daşu, and M. Karlsson, "Theoretical simulation of tumour oxygenation and results from acute and chronic hypoxia," *Physics in Medicine and Biology*, vol. 48, no. 17, pp. 2829–2842, 2003.
- [25] A. Daşu, I. Toma-Daşu, and M. Karlsson, "The effects of hypoxia on the theoretical modelling of tumour control probability," *Acta Oncologica*, vol. 44, no. 6, pp. 563–571, 2005.
- [26] I. Toma-Daşu, A. Daşu, and A. Brahme, "Dose prescription and optimisation based on tumour hypoxia," *Acta Oncologica*, vol. 48, no. 8, pp. 1181–1192, 2009.

- [27] Å. Søvik, E. Malinen, Ø. S. Bruland, S. M. Bentzen, and D. R. Olsen, "Optimization of tumour control probability in hypoxic tumours by radiation dose redistribution: a modelling study," *Physics in Medicine and Biology*, vol. 52, no. 2, pp. 499–513, 2007.
- [28] B. Titz and R. Jeraj, "An imaging-based tumour growth and treatment response model: investigating the effect of tumour oxygenation on radiation therapy response," *Physics in Medicine and Biology*, vol. 53, no. 17, pp. 4471–4488, 2008.
- [29] W. M. Harriss-Phillips, E. Bezak, and E. K. Yeoh, "Monte Carlo radiotherapy simulations of accelerated repopulation and reoxygenation for hypoxic head and neck cancer," *British Journal of Radiology*, vol. 84, no. 1006, pp. 903–918, 2011.
- [30] W. Tuckwell, E. Bezak, E. Yeoh, and L. Marcu, "Efficient Monte Carlo modelling of individual tumour cell propagation for hypoxic head and neck cancer," *Physics in Medicine and Biology*, vol. 53, no. 17, pp. 4489–4507, 2008.
- [31] G. G. Steel, Ed., *The Growth Kinetics of Tumours*, Oxford University Press, Oxford, UK, 1977.
- [32] M. W. Restsky, D. E. Swartzendruber, R. H. Wardwell, and P. D. Bame, "Is Gompertzian or exponential kinetics a valid description of individual human cancer growth?" *Medical Hypotheses*, vol. 33, no. 2, pp. 95–106, 1990.
- [33] A. S. Qi, X. Zheng, C. Y. Du, and B. S. An, "A cellular automaton model of cancerous growth," *Journal of Theoretical Biology*, vol. 161, no. 1, pp. 1–12, 1993.
- [34] M. Gyllenberg and G. F. Webb, "Quiescence as an explanation of Gompertzian tumor growth," *Growth, Development and Aging*, vol. 53, no. 1-2, pp. 25–33, 1989.
- [35] M. Gyllenberg and G. F. Webb, "A nonlinear structured population model of tumor growth with quiescence," *Journal of Mathematical Biology*, vol. 28, no. 6, pp. 671–694, 1990.
- [36] J. Smolle and H. Stettner, "Computer simulation of tumour cell invasion by a stochastic growth model," *Journal of Theoretical Biology*, vol. 160, no. 1, pp. 63–72, 1993.
- [37] J. Galle, M. Loeffler, and D. Drasdo, "Modeling the effect of deregulated proliferation and apoptosis on the growth dynamics of epithelial cell populations in vitro," *Biophysical Journal*, vol. 88, no. 1, pp. 62–75, 2005.
- [38] M. Nordmark, S. M. Bentzen, V. Rudat et al., "Prognostic value of tumor oxygenation in 397 head and neck tumors after primary radiation therapy. An international multicenter study," *Radiotherapy and Oncology*, vol. 77, no. 1, pp. 18–24, 2005.
- [39] L. H. Gray, A. D. Conger, M. Ebert, S. Hornsey, and O. C. Scott, "The concentration of oxygen dissolved in tissues at the time of irradiation as a factor in radiotherapy," *British Journal of Radiology*, vol. 26, no. 312, pp. 638–648, 1953.
- [40] S. E. Hill, "A simple visual method for demonstrating the diffusion of oxygen through rubber and various other substances," *Science*, vol. 67, no. 1736, pp. 374–376, 1928.
- [41] E. A. Wright and P. Howard-Flanders, "The influence of oxygen on the radiosensitivity of mammalian tissues," *Acta Radiologica*, vol. 4, no. 1, pp. 26–32, 1957.
- [42] M. M. Elkind, R. W. Swain, T. Alescio, H. Sutton, and W. B. Moses, "Oxygen, nitrogen, recovery and radiation therapy," in *University of Texas, M.D. Anderson Hospital and Tumor Institute of Cellular Radiation Biology: A Symposium Considering Radiation Effects in the Cell and Possible Implications for Cancer Therapy, a Collection of Papers*, pp. 442–461, Williams & Wilkins, Baltimore, Md, USA, 1965.
- [43] I. F. Tannock and G. G. Steel, "Tumor growth and cell kinetics in chronically hypoxic animals," *Journal of the National Cancer Institute*, vol. 45, no. 1, pp. 123–133, 1970.
- [44] J. M. Brown, "Evidence for acutely hypoxic cells in mouse tumours, and a possible mechanism of reoxygenation," *British Journal of Radiology*, vol. 52, no. 620, pp. 650–656, 1979.
- [45] D. L. S. McElwain, R. Callcott, and L. E. Morris, "A model of vascular compression in solid tumours," *Journal of Theoretical Biology*, vol. 78, no. 3, pp. 405–415, 1979.
- [46] D. L. S. McElwain and G. J. Pettet, "Cell migration in multicell spheroids: swimming against the tide," *Bulletin of Mathematical Biology*, vol. 55, no. 3, pp. 655–674, 1993.
- [47] M. A. J. Chaplain and A. R. A. Anderson, "Mathematical modelling, simulation and prediction of tumour-induced angiogenesis," *Invasion and Metastasis*, vol. 16, no. 4-5, pp. 222–234, 1996.
- [48] A. R. Kansal, S. Torquato, G. R. Harsh, E. A. Chiocca, and T. S. Deisboeck, "Simulated brain tumor growth dynamics using a three-dimensional cellular automaton," *Journal of Theoretical Biology*, vol. 203, no. 4, pp. 367–382, 2000.
- [49] K. Måseide and E. K. Rofstad, "Mathematical modeling of chronic hypoxia in tumors considering potential doubling time and hypoxic cell lifetime," *Radiotherapy and Oncology*, vol. 54, no. 2, pp. 171–177, 2000.
- [50] T. S. Deisboeck, M. E. Berens, A. R. Kansal, S. Torquato, A. O. Stemmer-Rachamimov, and E. A. Chiocca, "Pattern of self-organization in tumour systems: complex growth dynamics in a novel brain tumour spheroid model," *Cell Proliferation*, vol. 34, no. 2, pp. 115–134, 2001.
- [51] A. A. Patel, E. T. Gawlinski, S. K. Lemieux, and R. A. Gatenby, "A cellular automaton model of early tumor growth and invasion: the effects of native tissue vascularity and increased anaerobic tumor metabolism," *Journal of Theoretical Biology*, vol. 213, no. 3, pp. 315–331, 2001.
- [52] A. R. A. Anderson, "A hybrid mathematical model of solid tumour invasion: the importance of cell adhesion," *Mathematical Medicine and Biology*, vol. 22, no. 2, pp. 163–186, 2005.
- [53] A. R. A. Anderson, M. A. J. Chaplain, C. García-Reimbert, and C. A. Vargas, "A gradient-driven mathematical model of antiangiogenesis," *Mathematical and Computer Modelling*, vol. 32, no. 10, pp. 1141–1152, 2000.
- [54] Y. Cai, S. Xu, J. Wu, and Q. Long, "Coupled modelling of tumour angiogenesis, tumour growth and blood perfusion," *Journal of Theoretical Biology*, vol. 279, no. 1, pp. 90–101, 2011.
- [55] L.G. Marcu and E. Bezak, "Neoadjuvant cisplatin for head and neck cancer: simulation of a novel schedule for improved therapeutic ratio," *Journal of Theoretical Biology*, vol. 297, pp. 41–47, 2012.
- [56] F. Ellis, "Dose, time and fractionation: a clinical hypothesis," *Clinical Radiology*, vol. 20, no. 1, pp. 1–7, 1969.
- [57] L. Cohen, "A cell population kinetic model for fractionated radiation therapy. I. Normal tissues," *Radiology*, vol. 101, no. 2, pp. 419–427, 1971.
- [58] D. E. Lea and D. G. Catcheside, "The mechanism of the induction by radiation of chromosome aberrations in *Tradescantia*," *Journal of Genetics*, vol. 44, no. 2-3, pp. 216–245, 1942.
- [59] H. R. Whithers, J. M. G. Taylor, and B. Maciejewski, "The hazard of accelerated tumor clonogen repopulation during

- radiotherapy," *Acta Oncologica*, vol. 27, no. 2, pp. 131–146, 1988.
- [60] T. Alper, *Cellular Radiobiology*, Cambridge University Press, Cambridge, UK, 1979.
- [61] D. J. Brenner, L. R. Hlatky, P. J. Hahnfeldt, Y. Huang, and R. K. Sachs, "The linear-quadratic model and most other common radiobiological models result in similar predictions of time-dose relationships," *Radiation Research*, vol. 150, no. 1, pp. 83–91, 1998.
- [62] R. G. Dale and B. Jones, *Radiobiological Modelling in Radiation Oncology*, The British Institute of Radiology, London, UK, 2007.
- [63] J. F. Fowler, "The linear-quadratic formula and progress in fractionated radiotherapy," *British Journal of Radiology*, vol. 62, no. 740, pp. 679–694, 1989.
- [64] J. F. Fowler, "21 years of biologically effective dose," *British Journal of Radiology*, vol. 83, no. 991, pp. 554–568, 2010.
- [65] S. M. Bentzen, "Quantitative clinical radiobiology," *Acta Oncologica*, vol. 32, no. 3, pp. 259–275, 1993.
- [66] J. Dunst, P. Stadler, A. Becker et al., "Tumor volume and tumor hypoxia in head and neck cancers: the amount of the hypoxic volume is important," *Strahlentherapie und Onkologie*, vol. 179, no. 8, pp. 521–526, 2003.
- [67] M. Nordmark and J. Overgaard, "Tumor hypoxia is independent of hemoglobin and prognostic for loco-regional tumor control after primary radiotherapy in advanced head and neck cancer," *Acta Oncologica*, vol. 43, no. 4, pp. 396–403, 2004.
- [68] D. Rischin, R. J. Hicks, R. Fisher et al., "Prognostic significance of [¹⁸F]-misonidazole positron emission tomography-detected tumor hypoxia in patients with advanced head and neck cancer randomly assigned to chemoradiation with or without tirapazamine: a substudy of Trans-Tasman Radiation Oncology Group study 98.02," *Journal of Clinical Oncology*, vol. 24, no. 13, pp. 2098–2104, 2006.
- [69] B. G. Wouters, S. A. Wepler, M. Koritzinsky et al., "Hypoxia as a target for combined modality treatments," *European Journal of Cancer*, vol. 38, no. 2, pp. 240–257, 2002.
- [70] L. Marcu, E. Bezak, and I. Olver, "Scheduling cisplatin and radiotherapy in the treatment of squamous cell carcinomas of the head and neck: a modelling approach," *Physics in Medicine and Biology*, vol. 51, no. 15, pp. 3625–3637, 2006.
- [71] I. Toma-Dașu, A. Dașu, and A. Brahme, "Quantifying tumour hypoxia by PET imaging—a theoretical analysis," *Advances in Experimental Medicine and Biology*, vol. 645, pp. 267–272, 2009.
- [72] I. Toma-Dașu, A. Dasu, and M. Karlsson, "Theoretical simulation of tumour hypoxia measurements," *Advances in Experimental Medicine and Biology*, vol. 578, pp. 369–374, 2006.
- [73] V. P. Antipas, G. S. Stamatakos, N. K. Uzunoglu, D. D. Dionysiou, and R. G. Dale, "A spatio-temporal simulation model of the response of solid tumours to radiotherapy in vivo: parametric validation concerning oxygen enhancement ratio and cell cycle duration," *Physics in Medicine and Biology*, vol. 49, no. 8, pp. 1485–1504, 2004.
- [74] D. D. Dionysiou and G. S. Stamatakos, "Applying a 4D multiscale in vivo tumor growth model to the exploration of radiotherapy scheduling: The effects of weekend treatment gaps and p53 gene status on the response of fast growing solid tumors," *Cancer Informatics*, vol. 2, pp. 113–121, 2006.
- [75] G. S. Stamatakos, E. C. Georgiadi, N. Graf, E. A. Kolokotroni, and D. D. Dionysiou, "Exploiting clinical trial data drastically narrows the window of possible solutions to the problem of clinical adaptation of a multiscale cancer model," *PLoS ONE*, vol. 6, no. 3, Article ID e17594, 2011.
- [76] L. G. Hanin and M. Zaider, "Cell-survival probability at large doses: an alternative to the linear-quadratic model," *Physics in Medicine and Biology*, vol. 55, no. 16, pp. 4687–4702, 2010.
- [77] C. I. Armpilia, R. G. Dale, and B. Jones, "Determination of the optimum dose per fraction in fractionated radiotherapy when there is delayed onset of tumour repopulation during treatment," *British Journal of Radiology*, vol. 77, no. 921, pp. 765–767, 2004.
- [78] M. Carlone, D. Wilkins, B. Nyiri, and P. Raaphorst, "TCP isoeffect analysis using a heterogeneous distribution of radiosensitivity," *Medical Physics*, vol. 31, no. 5, pp. 1176–1182, 2004.
- [79] P. J. Keall and S. Webb, "Optimum parameters in a model for tumour control probability, including interpatient heterogeneity: evaluation of the log-normal distribution," *Physics in Medicine and Biology*, vol. 52, no. 1, pp. 291–302, 2007.
- [80] M. Stuschke and H. D. Thames, "Fractionation sensitivities and dose-control relations of head and neck carcinomas: analysis of the randomized hyperfractionation trials," *Radiation Therapy and Oncology*, vol. 51, no. 2, pp. 113–121, 1999.
- [81] C. J. McGinn, P. M. Harari, J. F. Fowler, C. N. Ford, G. M. Pyle, and T. J. Kinsella, "Dose intensification in curative head and neck cancer radiotherapy-linear quadratic analysis and preliminary assessment of clinical results," *International Journal of Radiation Oncology Biology Physics*, vol. 27, no. 2, pp. 363–369, 1993.
- [82] P. Barberet, F. Vianna, M. Karamitros et al., "Monte-Carlo dosimetry on a realistic cell monolayer geometry exposed to alpha particles," *Physics in Medicine and Biology*, vol. 57, no. 8, pp. 2189–2207, 2012.
- [83] S. Incerti, N. Gault, C. Habchi et al., "A comparison of cellular irradiation techniques with alpha particles using the Geant4 Monte Carlo simulation toolkit," *Radiation Protection Dosimetry*, vol. 122, no. 1–4, pp. 327–329, 2006.
- [84] J. Aroesty, T. Lincoln, N. Shapiro, and G. Boccia, "Tumor growth and chemotherapy: mathematical methods, computer simulations, and experimental foundations," *Mathematical Biosciences*, vol. 17, no. 3–4, pp. 243–300, 1973.
- [85] T. Weldon, *Mathematical Models in Cancer Research*, Institute of Physics, Bristol, UK, 1988.
- [86] M. J. P. Welters, A. M. J. Fichtinger-Schepman, R. A. Baan et al., "Pharmacodynamics of cisplatin in human head and neck cancer: correlation between platinum content, DNA adduct levels and drug sensitivity in vitro and in vivo," *British Journal of Cancer*, vol. 79, no. 1, pp. 82–88, 1999.
- [87] C. M. Sorenson, M. A. Barry, and A. Eastman, "Analysis of events associated with cell cycle arrest at G2 phase and cell death induced by cisplatin," *Journal of the National Cancer Institute*, vol. 82, no. 9, pp. 749–755, 1990.
- [88] A. V. Hill, "The possible effects of the aggregation of the molecules of haemoglobin on its dissociation curves," *The Journal of Physiology*, vol. 40, supplement, pp. 4–7, 1910.
- [89] S. N. Gardner, "A mechanistic, predictive model of dose-response curves for cell cycle phase-specific and—nonspecific drugs," *Cancer Research*, vol. 60, no. 5, pp. 1417–1425, 2000.
- [90] I. F. Tannock and R. P. Hill, *The Basic Science of Oncology*, McGraw-Hill Professional, New York, NY, USA, 1998.

- [91] A. W. El-Kareh and T. W. Secomb, "A mathematical model for cisplatin cellular pharmacodynamics," *Neoplasia*, vol. 5, no. 2, pp. 161–169, 2003.
- [92] L. M. Lévasseur, H. K. Slocum, Y. M. Rustum, and W. R. Greco, "Modeling of the time-dependency of in vitro drug cytotoxicity and resistance," *Cancer Research*, vol. 58, no. 24, pp. 5749–5761, 1998.
- [93] J. H. M. Schellens, J. Ma, A. S. T. Planting et al., "Relationship between the exposure to cisplatin, DNA-adduct formation in leucocytes and tumour response in patients with solid tumours," *British Journal of Cancer*, vol. 73, no. 12, pp. 1569–1575, 1996.
- [94] M. Kimmel and A. Swierniak, "An optimal control problem related to leukaemia chemotherapy," *Scientific Bulletins of the Silesian Technical University*, vol. 65, pp. 120–113, 1983.
- [95] A. Swierniak, A. Polanski, and M. Kimmel, "Optimal control problems arising in cell-cycle-specific cancer chemotherapy," *Cell Proliferation*, vol. 29, no. 3, pp. 117–139, 1996.
- [96] U. Ledzewicz and H. Schättler, "Analysis of a cell-cycle specific model for cancer chemotherapy," *Journal of Biological Systems*, vol. 10, no. 3, pp. 183–206, 2002.
- [97] J. S. Au, S. H. Jang, J. Zheng et al., "Determinants of drug delivery and transport to solid tumors," *Journal of Controlled Release*, vol. 74, no. 1–3, pp. 31–46, 2001.
- [98] T. L. Jackson, "Intracellular accumulation and mechanism of action of doxorubicin in a spatio-temporal tumor model," *Journal of Theoretical Biology*, vol. 220, no. 2, pp. 201–213, 2003.
- [99] A. R. Tzafiriri, E. I. Lerner, M. Flashner-Barak, M. Hinchcliffe, E. Ratner, and H. Parnas, "Mathematical modeling and optimization of drug delivery from intratumorally injected microspheres," *Clinical Cancer Research*, vol. 11, no. 2, part 1, pp. 826–834, 2005.
- [100] R. Venkatasubramanian, M. A. Henson, and N. S. Forbes, "Integrating cell-cycle progression, drug penetration and energy metabolism to identify improved cancer therapeutic strategies," *Journal of Theoretical Biology*, vol. 253, no. 1, pp. 98–117, 2008.
- [101] B. Basse, B. C. Baguley, E. S. Marshall et al., "A mathematical model for analysis of the cell cycle in cell lines derived from human tumors," *Journal of Mathematical Biology*, vol. 47, no. 4, pp. 295–312, 2003.
- [102] J. H. Goldie and A. J. Coldman, "A mathematic model for relating the drug sensitivity of tumors to their spontaneous mutation rate," *Cancer Treatment Reports*, vol. 63, no. 11-12, pp. 1727–1733, 1979.
- [103] B. G. Birkhead, W. M. Gregory, M. L. Slevin, and V. J. Harvey, "Evaluating and designing cancer chemotherapy treatment using mathematical models," *European Journal of Cancer and Clinical Oncology*, vol. 22, no. 1, pp. 3–8, 1986.
- [104] M. Kimmel and D. E. Axelrod, "Mathematical models of gene amplification with applications to cellular drug resistance and tumorigenicity," *Genetics*, vol. 125, no. 3, pp. 633–644, 1990.
- [105] N. Komarova, "Stochastic modeling of drug resistance in cancer," *Journal of Theoretical Biology*, vol. 239, no. 3, pp. 351–366, 2006.
- [106] N. L. Komarova and D. Wodarz, "Stochastic modeling of cellular colonies with quiescence: an application to drug resistance in cancer," *Theoretical Population Biology*, vol. 72, no. 4, pp. 523–538, 2007.
- [107] L. Marcu, E. Bezak, I. Olver, and T. van Doorn, "Tumour resistance to cisplatin: a modelling approach," *Physics in Medicine and Biology*, vol. 50, no. 1, pp. 93–102, 2005.
- [108] A. A. Katouli and N. L. Komarova, "The worst drug rule revisited: mathematical modeling of cyclic cancer treatments," *Bulletin of Mathematical Biology*, vol. 73, no. 3, pp. 549–584, 2011.
- [109] A. J. Davis and I. F. Tannock, "Repopulation of tumour cells between cycles of chemotherapy: a neglected factor," *Lancet Oncology*, vol. 1, no. 2, pp. 86–93, 2000.
- [110] L. Marcu and E. Bezak, "Modelling of tumour repopulation after chemotherapy," *Australasian Physical and Engineering Sciences in Medicine*, vol. 33, no. 3, pp. 265–270, 2010.
- [111] S. N. Gardner, "Cell cycle phase-specific chemotherapy: computational methods for guiding treatment," *Cell Cycle*, vol. 1, no. 6, pp. 369–374, 2002.
- [112] S. N. Gardner and M. Fernandes, "New tools for cancer chemotherapy: computational assistance for tailoring treatments," *Molecular Cancer Therapeutics*, vol. 2, no. 10, pp. 1079–1084, 2003.
- [113] S. N. Gardner, "Modeling multi-drug chemotherapy: tailoring treatment to individuals," *Journal of Theoretical Biology*, vol. 214, no. 2, pp. 181–207, 2002.
- [114] J. H. Goldie, A. J. Coldman, V. Ng, H. A. Hopkins, and W. B. Looney, "A mathematical and computer-based model of alternating chemotherapy and radiation therapy in experimental neoplasms," *Antibiotics and Chemotherapy*, vol. 41, pp. 11–20, 1988.
- [115] W. Y. Hu, W. R. Zhong, F. H. Wang, L. Li, and Y. Z. Shao, "In silico synergism and antagonism of an anti-tumour system intervened by coupling immunotherapy and chemotherapy: a mathematical modelling approach," *Bulletin of Mathematical Biology*, vol. 74, no. 2, pp. 434–452, 2012.

Review Article

***In Silico* Modelling of Tumour Margin Diffusion and Infiltration: Review of Current Status**

Fatemeh Leyla Moghaddasi,^{1,2} Eva Bezak,^{1,2} and Loredana Marcu^{1,2,3}

¹ Department of Medical Physics, Royal Adelaide Hospital, North Terrace, Adelaide, SA 5000, Australia

² School of Chemistry and Physics, The University of Adelaide, North Terrace, Adelaide, SA 5000, Australia

³ Faculty of Sciences, University of Oradea, Oradea, Romania

Correspondence should be addressed to Fatemeh Leyla Moghaddasi, fatemeh.moghaddasi@adelaide.edu.au

Received 13 February 2012; Accepted 11 April 2012

Academic Editor: Scott Penfold

Copyright © 2012 Fatemeh Leyla Moghaddasi et al. This is an open access article distributed under the Creative Commons Attribution License, which permits unrestricted use, distribution, and reproduction in any medium, provided the original work is properly cited.

As a result of advanced treatment techniques, requiring precise target definitions, a need for more accurate delineation of the Clinical Target Volume (CTV) has arisen. Mathematical modelling is found to be a powerful tool to provide fairly accurate predictions for the Microscopic Extension (ME) of a tumour to be incorporated in a CTV. In general terms, biomathematical models based on a sequence of observations or development of a hypothesis assume some links between biological mechanisms involved in cancer development and progression to provide quantitative or qualitative measures of tumour behaviour as well as tumour response to treatment. Generally, two approaches are taken: deterministic and stochastic modelling. In this paper, recent mathematical models, including deterministic and stochastic methods, are reviewed and critically compared. It is concluded that stochastic models are more promising to provide a realistic description of cancer tumour behaviour due to being intrinsically probabilistic as well as discrete, which enables incorporation of patient-specific biomedical data such as tumour heterogeneity and anatomical boundaries.

1. Introduction

Advanced radiotherapy techniques like 3D Conformal Radiotherapy (3D-CRT), Intensity-Modulated Radiation Therapy (IMRT), and Image-guided Radiation Therapy (IGRT) restrict the high dose region to defined target volumes to spare adjacent normal tissue. The margins are generally reduced for modern radiotherapy techniques due to (a) more accurate organ specification with the use of daily image guidance that results in minimization of set up error, and (b) superior conformity of dose distribution to irradiation target volumes. However, a successful implementation of these techniques, that is, achieving an acceptable Tumour Control Probability (TCP) and Normal Tissue Complication Probability (NTCP), requires very accurate target volume delineation. According to ICRU report 50, the “Clinical Target Volume (CTV) is a volume encompassing visible Gross Tumour Volume (GTV) and subclinical malignant disease” [1]. Since subclinical disease cannot be detected by imaging

technologies, in contrast to gross tumour volume, which is the visible extent and location of malignant disease [1], CTV needs to be estimated. To ensure that CTV receives the prescribed dose, the Planning Target Volume (PTV) is drawn to account for several possible uncertainties. These uncertainties are due to both physiologic movements which are not controllable (e.g. patient’s respiration) and to daily set-up variations. PTV is then the volume for which dose calculation is performed and ensures that the whole of CTV will receive the full prescribed radiation dose. Figure 1 schematically illustrates radiotherapy irradiation volumes and their respective uncertainties regarding volume delineation.

Among radiotherapy target volumes, delineation of the Clinical Target Volume (CTV) is the most controversial. To date, there is no consensus regarding the extent of histological disease, thus the question of how far CTV is extended beyond GTV is mostly left to the discretion of radiation oncologists based on their experience, depending on patient’s

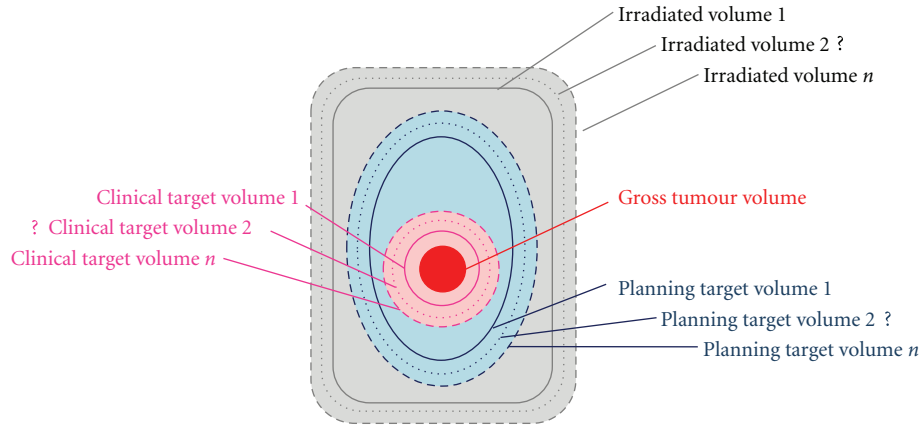


FIGURE 1: Schematic diagram of radiotherapy irradiation volumes.

histopathological data. The uncertainty in CTV represents a limitation on reduction of the irradiated target volume. When the irradiated target volume is reduced due to dose conformity of new treatment modalities, NTCP is improved. On the other hand, the issue of CTV fuzziness becomes a cause of concern because any PTV reduction enhances the risk of missing a part or a few cells of subclinical disease, as illustrated in Figure 2. It is worth mentioning that missing one single cell reduces TCP to 37%. (The Poisson distribution definition for TCP: $TCP = e^{-n(D)}$, where $n(D)$ is the expected number of surviving clonogens.) Therefore, in order to confidently reduce the irradiated target volume, as is the trend with current treatment techniques, the pattern of microscopic extension needs to be known or predicted.

1.1. Biological Background. Normal growth and regeneration of an organ requires cells to undergo cell division and to proliferate. The rate of proliferation, however, is systematically regulated to ensure the balance between cell proliferation and cell loss as well as integrity and functionality of each organ. This regulation occurs at cell cycle check points where progression to a subsequent phase is prevented unless prerequisites are satisfied. DNA lesions are recognized at check points that lead onto repair pathways [4]. Normally, cells with unrepaired DNA cannot continue their cycle and are led to apoptosis (programmed cell death). Any uncontrolled proliferation of cells, ensuing a series of DNA mutations, results in abnormal aggregation of cells called a tumour. An evolving tumour population undergoes two stages, namely, *avascular phase* and *vascular phase* and transition between these two phases requires angiogenesis, a process which involves development and recruitment of blood vessels to supply tumour cells with nutrients [5, 6]. Tumour commences its growth primarily via cell proliferation in an avascular phase. Further in its growth, individual tumour cells secrete a substance called Tumour Angiogenesis Factor (TAF) that initiates angiogenesis [6]. At this stage, that is, the beginning of a vascular phase, tumour acquires the capability to invade locally in the adjacent normal tissue, and later tumour cells can detach themselves from the primary mass and migrate through blood or lymphatic

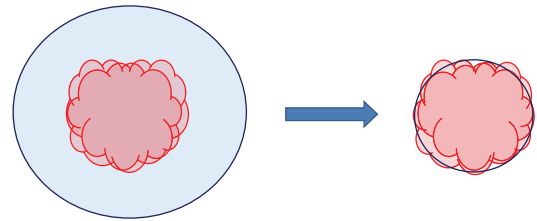


FIGURE 2: Schematic diagram of CTV and PTV correlation for conventional treatment techniques, on the left, as compared to modern treatment techniques, on the right. CTV is indicated by red contour and blue contour defines the PTV. As shown, the reduction of PTV may result in missing a part of microscopic disease that leads to poor treatment efficacy.

system to other sites in the body to produce new colonies (i.e., metastasis) [6–9].

The Extracellular Matrix (ECM) is the external part of tissue on which cells reside. It provides structural support to the cells, regulates intercellular communications and so forth. The ECM also imposes spatial constraint on tumour proliferation. On the other hand, the tumour invasion is known to be facilitated by gradients in the ECM density (i.e., an ECM gradient is a directional rise in ECM density, and its magnitude determines how fast the ECM density rises in that direction). These gradients cause the cells in the outer layer of a tumour to break away from the primary tumour mass and move along the gradient, a phenomenon called *haptotaxis* [9]. It is known that, Matrix Degrading Enzymes (MDEs) produced by cancer cells degrade the surrounding ECM resulting in development of ECM gradients [9].

Apart from proliferation and haptotaxis, other factors like cell-cell adhesion, cell-matrix adhesion, and ECM density also affect cell motility in the course of tumour invasion [6].

In summary, tumour evolution is an interrelated multistage process that starts from a series of cancer-associated gene mutations leading to formation of a colony that could further invade adjacent tissues and finally metastasize in distant organs. Better understanding of biological mechanisms

of cancer development helps to anticipate the behaviour of the tumour that undoubtedly leads to a better treatment efficacy.

1.2. Mathematical Modelling. Mathematical modelling is a suitable tool to generate algorithms to correlate information acquired from imaging techniques to the pattern of growth and tumour invasion. In a typical course of model development, biological phenomena are represented in mathematical equations. The solutions of the equations, in return, provide predictions of tumour evolution, tumour aggressiveness in a given patient, and so forth. The validity of a model is then examined by comparison with available actual data, and iteration is performed until an adequate match is reached and thus a plausible model is obtained. A semirealistic model developed in this manner provides an insight into biological mechanisms of tumour growth and invasion under a variety of circumstances. It also allows for assessment of potential treatment regimens. The model could be useful for clinicians in clinical tumour volume definition.

Oncogenesis can be modelled at three levels: (1) sub-cellular level, (2) cellular and microscopic level that concerns individual cell behaviour while taking into account cell-extracellular matrix (ECM) interactions, and (3) macroscopic level that is related to the evolution of tumour in terms of cell density and mostly is based upon reaction-diffusion equations [10].

In this paper, some of the recent computational and mathematical models developed for tumour growth and invasion are reviewed. Two approaches used for modelling, analytical and stochastic, are discussed individually in the following sections.

2. Deterministic Models

2.1. Analytical Models. Analytical modelling of tumour growth has been typically done based on the reaction-diffusion equations in the literature. Swanson et al. [11] reviewed some recent models developed for glioma of the brain. The problem was initially formulated as a conservation equation by Murray's group [12–14] as: the rate at which tumour cell population changes is equal to diffusion (motility) of tumour cells plus proliferation of tumour cells. For untreated glioma, this can be represented in a mathematical form as [11, 15]

$$\frac{\partial c}{\partial t} = -\nabla \cdot J + \rho c, \quad (1)$$

where $c(x, t)$ denotes the density of tumour at location x and time t , $\nabla \cdot J$ is the diffusion component (i.e., outflow of material out of the system), and ρc is proliferation component (inflow of material in the system), where ρ is the proliferation coefficient. Using the Fick's first law that assumes the diffusive flux flows from high-concentration regions to low-concentration regions, the diffusion component is related to tumour cell density as follows:

$$J = -D \frac{\partial c}{\partial x} \xrightarrow{\text{in 3D}} J = -D \nabla c. \quad (2)$$

Thus (1) takes the form

$$\frac{\partial c}{\partial t} = \nabla \cdot (D \nabla c) + \rho c, \quad (3)$$

where D is diffusion coefficient representing active motility of cancer cells and ∇ denotes spatial gradient operator. The first term, the diffusion component, is related to the periphery of the tumour while the second term, the proliferation component, pertains to active part of tumour core and is described by cellular proliferation laws (e.g., exponential growth) [10]. The assumptions considered in this model were the following.

- (i) Brain tissue is homogeneous thus diffusion coefficient, D , is constant throughout the brain.
- (ii) Tumour growth is generally exponential thus ρc is constant.
- (iii) Boundary condition: $c(x, 0) = f(x)$, where $f(x)$ is initial profile of the tumour and there is no migration beyond brain boundaries.

Thus (3) reduces to

$$\frac{\partial c}{\partial t} = D \nabla^2 c + \rho c. \quad (4)$$

One of the consequences of (4) is that tumour density distribution, c , is a function of the ratio of ρ/D thus two different tumours whose different combinations of ρ and D result in the same ratio of ρ/D , appear the same at a single observation time. Hence, just a single MRI/CT image is not sufficient to estimate CTV correctly without knowing the pattern of tumour cell density distribution.

A more realistic approach was taken by Swanson et al. [2, 17] who introduced the geometry of the brain into the model, thus in the revised form of the model, the following assumptions were considered.

- (i) Complex geometry of brain is introduced, thus diffusion coefficient, D , is not uniform and is a function of location in the brain tissue.
- (ii) Equation (3) is applied to describe the pattern of growth in diffusive models with D being a function of x as follows:

$$D(x) = \begin{cases} D_W, & \text{(diffusion coefficient in} \\ & \text{white matter of the brain),} \\ D_G, & \text{(diffusion coefficient in} \\ & \text{gray matter of the brain),} \end{cases} \quad (5)$$

where $D_W > D_G$.

To determine the model parameters, 12 serial CT scans of a patient, diagnosed with astrocytoma, during his terminal year were examined to derive estimations for velocities of tumour margin advance through grey and white matter, ν_G and ν_W , respectively. Fisher's approximation ($D = \nu^2/4\rho$)

was then applied to correlate velocity, v , of detectable tumour margin with proliferation rate and diffusion coefficients. According to CT scans of the right hemisphere (predominantly grey matter), v_G was identified to be 0.008 cm/day, thus Fisher approximation gives $D_G = 0.0013 \text{ cm}^2/\text{day}$, and D_W being almost five times of D_G becomes $0.0065 \text{ cm}^2/\text{day}$. To assign diffusion coefficients to corresponding brain cells, spatial distribution of white and grey matter was adopted from the brain web database [31]. Applying these determined parameters in the simulation based on (3) describing virtual gliomas growth, two-dimensional plots of tumour cell density on coronal, sagittal and axial planes were generated, as shown in Figure 3. Using these plots, they determined the part of tumour volume that can be visualized using MRI technique. Enhanced MRI technique has a detection threshold of 400 cells/mm². This means that any part of tumour having a concentration below this threshold is not detectable on a MRI image. The comparison between detectable part and simulated profile provides an insight into how far and at what concentration microscopic disease is invaded beyond visible tumour. This model that derived the behaviour of glioma according to two factors (“ D ” and “ ρ ”) demonstrates that the distribution of ME in invasive gliomas does not follow an isotropic pattern that is invariably assumed by clinicians for definition of CTV.

The biomathematical modelling based on (3) in conjunction with serial pre-treatment MRI images of the patient also provides a tool to quantify patient-specific proliferation and diffusion rates. Wang et al. [32] examined two pretreatment MRI images of each of a population of 32 patients diagnosed with Glioblastoma (GBM) to quantify patient-specific kinetic rates of glioma cells (net proliferation and diffusion rates). These parameters are used to predict the course of disease and, more importantly, to assess the efficacy of different treatment plans for each individual patient through a survival analysis. In the survival analysis, the effectiveness of any treatment was measured via the ratio of actual survival time after respective therapy to the calculated survival time (by the model) without therapy.

The evolution of mathematical modelling to gain insight into the mechanism of GBM growth and invasion initiated by Swanson et al. [11, 17] was followed by Stein et al. [20] who developed a continuum model and compared the outcome of the model with 3D *in vitro* experiments on the three dimensional pattern of growth of GBM spheroids. It was concluded that GBM spheroids consist of two classes of cells, namely, proliferating core cells and peripheral migrating cells. This finding was later included in other models like the model of Thalhauser et al. [22] in which three dependent variables, namely, the concentration of migrating cells, proliferating cells and oxygen (mmHg) were correlated in three partial differential equations for tumour development around a central blood microvessel. Analysis of the density distribution profiles of these two classes of cells led to a hypothesis regarding emergence of metastatic phenotype to occur for population of cells containing highly motile cells. This hypothesis is based on the evidence that populations of motile cells grow to lower densities compared to aggressive growers (mobile cells), and hence they are

unlikely to cause vascular network collapse since they cause less compressive pressure on microvessel walls. In a more recent progress, Eikenberry et al. [8] incorporated haptotaxis in GBM models and also extended the model stochastically to form a deterministic-stochastic system for modelling. The mathematical model was developed based on four dependent variables: the concentration of migrating cells, proliferating cells, ECM, and matrix degrading enzyme. The system of partial differential equations was discretized to allow for stochastic estimation of the transition probability between proliferating and migrating class of cells at each grid point. The stochastic nature of the model allows for applying patient-specific geometry of brain and location of tumour inside the brain during simulation. The simulation was performed for an actual clinical case of a GBM patient undergoing a course of treatment including surgical resection, gamma knife, and chemotherapy. The model qualitatively reproduced the actual tumour growth of the patient. However, the model failed to simulate the deformation of surgical cavity.

The spatial-temporal evolution of the brain tumour in the presence of chemotherapy was investigated by Tracqui et al. [2, 12]. Twelve successive CT scans during the terminal year of a patient diagnosed with astrocytoma were studied. The patient received two courses of chemotherapy during 12 months before death, thus (3) can be modified as

$$\frac{\partial c}{\partial t} = \nabla \cdot (D \nabla c) + f(c) - g(c), \quad (6)$$

where $g(c)$ is the cell loss due to chemotherapy and defined as

$$g(c) = [K_1(t) + K_2(t)]c \quad (7)$$

with

$$K_1(t) = \begin{cases} k_1, & \text{during the time the first course} \\ & \text{of drug was delivered,} \\ 0, & \text{during the time the second course} \\ & \text{of drug was delivered,} \end{cases} \quad (8)$$

$$K_2(t) = \begin{cases} 0, & \text{during the time the first course} \\ & \text{of drug was delivered,} \\ k_2, & \text{during the time the second course} \\ & \text{of drug was delivered,} \end{cases}$$

where k_1 and k_2 are positive constants.

The proliferation term, $f(c)$, is typically taken as a linear function of c (exponential proliferation) or a nonlinear function of c (logistic proliferation) when the proliferation is limited, since cell density is close to its maximum:

$$f(c) = \begin{cases} \rho c, & \text{exponential proliferation,} \\ \rho c(1 - c), & \text{logistic proliferation.} \end{cases} \quad (9)$$

The area of tumour was evaluated at each successive CT scan and then the data was compared to the values derived from (6). The comparison between time evolution of

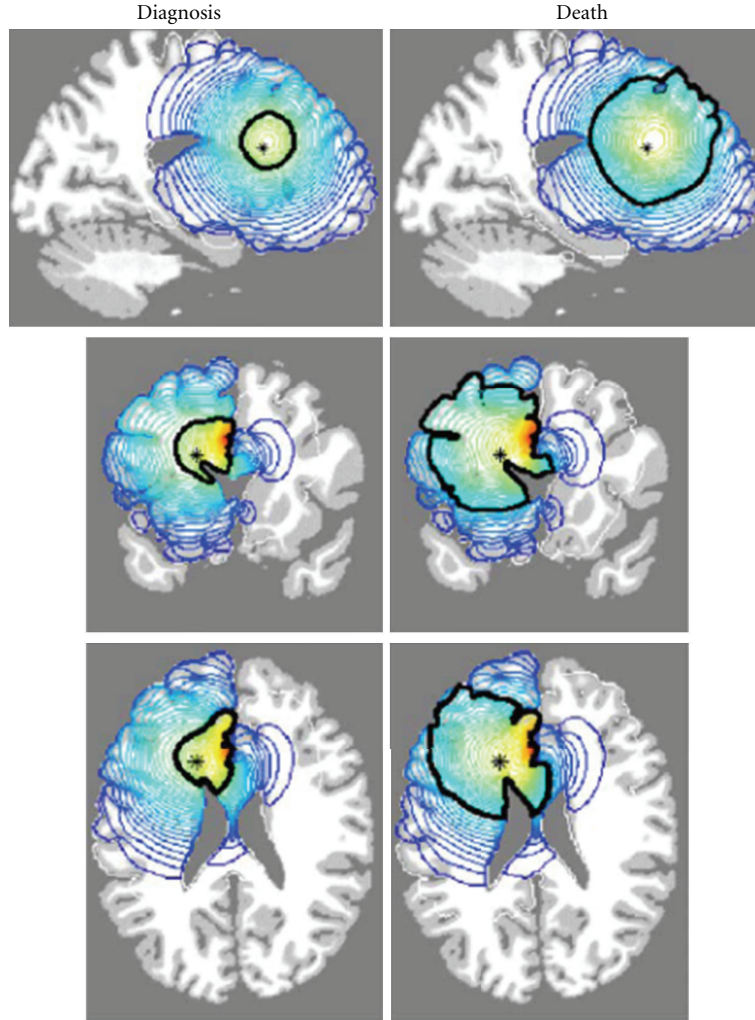


FIGURE 3: The left column corresponds to the tumour at diagnosis and right column corresponds to tumour at death. The dark black contour defines the detectable edge of tumour by (MRI), red contour indicates high density of tumour cells, and blue contour denotes low-density disease. Courtesy of Swanson et al. [2].

simulated tumour area and tumour areas acquired from CT scans showed a distinctive discrepancy, particularly before the end of the first course of chemotherapy. Consequently, the assumptions were revised and it was postulated that there is a second cell density $c_2(x, y, t)$ present which is resistant to the first course of chemotherapy but sensitive to the second course. The insensitivity of the second population was considered to be due to mutations from the radiotherapy administered three years earlier. Given this condition, the system was described mathematically as follows:

$$\begin{aligned} \frac{\partial c_1}{\partial t} &= \nabla \cdot (D \nabla c_1) + \rho_1 c_1 (1 - c) - [K_1(t) + K_2(t)] c_1 \\ \frac{\partial c}{\partial t} &= \nabla \cdot (D \nabla c) + \rho_1 c_1 (1 - c) + \rho_2 c_2 (1 - c) - K_1(t) c_1 \\ &\quad - K_2(t) c, \end{aligned} \quad (10)$$

where ρ_1 and ρ_2 are proliferation rates corresponding to the first and second cell density, respectively, and variable c represents the total density of tumour cells ($c = c_1 + c_2$).

After optimization and identification of unknown parameters, the identified values were found to be in agreement with known biological data (e.g., $D = 1.2 \times 10^{-7} \text{ cm}^2/\text{s}$ which is comparable with estimation of glioma cell migration rate obtained from *in vitro* experiments [33]).

Woodward et al. [15, 34] modified Tracqui's model for the same case study in terms of initial conditions related to distribution of type one and two of cancerous cells. In contrast to Tracqui's model that assumed an approximate initial distribution of 90% of type one and 10% of type two cancerous cells, Woodward included another parameter as the number of type one cells remaining after surgery followed by X-ray therapy 1000 days before the first scan and also assumed that type two cancerous cells are the result of mutations of type one cells three years earlier. This allowed

for prediction of distribution of each type of cells at the time of diagnosis (rather than making a rough estimation) and at any time during the terminal year. Furthermore, the simulated evolution of the tumour was used to retrospectively evaluate different courses of treatments (e.g., different extent of surgical resections instead of chemotherapy) in terms of their respective subclinical recurrence.

Swanson et al. [11, 35] investigated the incorporation of cell loss due to chemotherapy in a more general formulation by defining $g(c)$ to be a periodic function such that for the time periods chemotherapy is on, $g(c)$ is equal to a specific positive constant, k (indicating the rate of cell loss due to chemotherapy), and otherwise is zero. The model was originally formulated assuming homogeneous drug delivery and further developed to take into account heterogeneity in drug delivery, whereby drug delivery is expected to be less in white matter compared to that in gray matter. The experimental observation of shrinkage of gliomas in specific areas together with persistent growth in other areas of the brain following chemotherapy was explained by this model.

Clatz et al. [10] developed a numerical model to simulate the three-dimensional pattern of growth and invasion of Glioblastomas. To account for different diffusion coefficients which are dependent on the brain tissue, the anatomical atlas of the brain in conjunction with Diffusion Tensor Image (DTI) were employed. The algorithm comprised of four steps. First, the patient MRI images were registered on the brain atlas on which gross volumes were delineated by a radiation oncologist. In the second step, the image registered on atlas was used to produce patient's tetrahedral mesh of brain in which diffusion coefficients respective to each voxel were specified using brain atlas and DTI of the patient. Simulation was performed in the third step by applying reaction-diffusion equation on initial tetrahedral mesh of brain. Ultimately, to measure the validity of the model, the simulated profile was compared with brain deformation seen on the patient MRI images in six months later.

Bondiau et al. [36] applied the virtual model of glioma growth developed by Clatz on actual data of a single patient and compared tumour growth pattern derived from the model with current radiotherapy margins. Tumour growth was studied in two scenarios, namely, high diffusion-low proliferation (HD-LP) and high proliferation-low diffusion (HP-LD) tumours. It was observed that, with 2 cm margin, 2.1% and 15.1% of microscopic invasive tumour cells fall outside margin in HP-LD and HD-LP tumours, respectively. Also 53.5% and 55.5% of cells inside margin in HP-LD and HD-LP, respectively, are normal brain cells. Therefore, it was concluded that uniform clinical margins may not be adequate to cover whole tumour neither to spare normal tissue. Although this conclusion is supported by many other studies, the rationale of this comparison is argued on the basis that a model which is based on a single patient clinical data, though sophisticated, cannot be considered as a criterion to assess clinical margins. It first needs to be validated against some actual clinical data (e.g., recurrence rate) in a statistically sufficient number of patients.

The effect of external beam radiation therapy was incorporated in the reaction-diffusion model in the study of

Rockne et al. [23]. Therefore, the conservation of cells (3) can be modified as:

$$\begin{aligned} \frac{\partial c}{\partial t} = & \underbrace{\nabla \cdot (D \nabla c)}_{\text{Diffusion of glioma cells}} + \underbrace{\rho c \left(1 - \frac{c}{k}\right)}_{\text{Logistic proliferation}} \\ & + \underbrace{R(x, t, \text{Dose})c \left(1 - \frac{c}{k}\right)}_{\text{Cell loss due to radiotherapy}}, \\ R(x, t, \text{Dose}) = & \begin{cases} 0, & \text{for } t \notin \text{therapy,} \\ \left(1 - e^{-(\alpha D + \beta D^2)}\right), & \text{for } t \in \text{therapy,} \end{cases} \end{aligned} \quad (11)$$

where D and k denote the dose and tumour carrying capacity, respectively. $R(x, t, \text{Dose})$ is the probability of death of cancer cells (one minus cell survival fraction given by the linear-quadratic model of cell survival ($S = e^{-(\alpha D + \beta D^2)}$)) due to radiotherapy.

In previous models, passive translocation of cells due to ECM-cell interactions and active cell migration were overlooked. Retaining reaction-diffusion formula as the framework, Tracqui [16] introduced the effects of passive translocation of cells due to ECM-cell interactions and active cell migration up to adhesivity gradient. The variables u , ρ , and c were designated for mechanical displacement of cell-ECM composite, density of ECM, and cell density, respectively. The parameter r denotes the proliferation rate of cancer cells. Thus the reaction-diffusion formula (cell conservation equation) takes the following form:

$$\begin{aligned} \frac{\partial c}{\partial t} = & -\nabla \cdot (J_c + J_d + J_h) + rc(1 - c), \\ J_d = & -D \nabla c \text{ (diffusion term),} \\ J_c = & \frac{c \partial u}{\partial t} \text{ (convection term),} \\ J_h = & hc \nabla \rho. \end{aligned} \quad (12)$$

The convection term addresses ECM displacement due to cells convection with velocity $\partial u / \partial t$. Equation (12) indicates that the two new terms inhibit tumour growth. Moreover, the conservation of ECM density reads as

$$\frac{\partial \rho}{\partial t} = \underbrace{-\nabla \cdot \left(\frac{\rho \partial u}{\partial t} \right)}_{\text{convection}} + \underbrace{S(c, p)}_{\text{ECM biosynthesis}} - \underbrace{G(c, p)}_{\text{ECM degradation}}, \quad (13)$$

where $S(c, p)$ and $G(c, p)$ denote the rate of formation and loss of ECM, respectively. For the sake of simplicity, ECM turnover was neglected, that is, $S(c, p) = G(c, p) = 0$. Thus (12) and (13) together with the equation regarding viscoelastic response of ECM to cells' traction force formed a set of differential equations for modelling. Nonhomogeneous and nonsymmetric profile at the tumour surface was obtained by the model. To validate the model, it was suggested to compare growth pattern generated by the model with that

acquired from *in vitro* experiments. To our knowledge, no article addressing such a comparison associated with this model has been found. Synthesis and degradation of ECM which was neglected in primary calculation could be further included.

More recently, the interactions of cell-cell and cell-ECM were considered in a more elaborate way in reaction-diffusion models. Gerisch and Chaplain [6] developed an analytical Partial Differential Equation (PDE) model to simulate tumour growth and invasion both one and two dimensionally. In the study of Gerisch, firstly a local continuum model was formulated based on the system of reaction-diffusion equations proposed by Anderson et al. [21]. It was assumed that the movement of the cells is due to random motility with constant diffusion coefficient D_1 (assuming constant ECM density), and haptotactic response to the ECM gradient. As a matter of fact, cancer cell motility depends on both ECM gradient and density, thus this was a simplifying assumption. The series of differential equations constituting the model are as follows:

$$\begin{aligned}\frac{\partial c}{\partial t} &= \nabla \cdot [D_1 \nabla c - \chi c \nabla v] + \mu_1 c (1 - \vartheta_1 c - \vartheta_2 v), \\ \frac{\partial v}{\partial t} &= -\gamma m v + \mu_2 (1 - \vartheta_1 c - \vartheta_2 v), \\ \frac{\partial m}{\partial t} &= \nabla \cdot [D_3 \nabla m] + \alpha c - \lambda m,\end{aligned}\quad (14)$$

where $c(x, t)$, $v(x, t)$, $m(x, t)$ denote the cancer cell density, the ECM density and the concentration of Matrix Degrading Enzyme (MDE), respectively. The parameters ϑ_1 and ϑ_2 are fractions of unit volume occupied by cancer cells and ECM, respectively. μ_1 , μ_2 , γ , D_3 , α and λ denote proliferation rate of cancer cells, remodelling rate of ECM, degradation rate of ECM, MDE diffusion coefficient, the rate of release, and removal of MDE, respectively. Finally, χ is designated for haptotactic function. Equation (14) differs from that of Anderson in two aspects: Employing logistic proliferation and applying modified haptotactic function to prevent cellular overcrowding at boundaries. There is also a slight difference in definition of Initial Conditions (IC) associated with ECM.

In the second step, Gerisch modified this model (14) to a nonlocal continuum model to include cell-cell and cell-ECM adhesion. To this end, the haptotactic term was substituted with a nonlocal flux term in (14). The nonlocal term represents the velocity of cancer cells due to cellular adhesion (cell-cell adhesion) and to the ECM (cell-ECM adhesion). The growth profile was simulated for both local and nonlocal models and surprisingly the detachment of a cluster of cells that degrades ECM on its way and migrates was obtained.

Within the realm of continuum modelling, the approach that regards a tumour as a continuum medium whose overall dynamic and morphology is dependent on the microenvironment material concentration is reflected in some other works in literature [37–46]. In these models, the concentration of microenvironment materials such as nutrition supply, like oxygen and glucose, and growth inhibitor, which is either

anticancer drugs or chemicals produced by immune system, is assumed to influence individual cells phenotype.

2.2. Hybrid Models. The above-addressed models, both deterministic reaction-diffusion equations whose solutions is in the form of invading travelling waves of cancer cells and mechano-cellular formalism (e.g., Tracqui, 1995 [16]) provide spatio-temporal spread of tumour at macroscopic level. However, the behaviour of tumours at cellular and sub-cellular levels, which becomes important when individual cell effects dominate in the course of tumour growth and invasion, such as the spatio-temporal evolution of tumour cell heterogeneity, cannot be predicted by these modelling approaches [47, 48]. Therefore, the continuum modelling is appropriate for studying systems at a large scale. Discrete modelling can overcome this limitation since it can track individual cells and update their states at each time step. Thus it is an appropriate tool to investigate the interaction between cells and ECM, phenotypic transitions of cells which leads to a nonlinear cancer system to another state that in return affects the overall behaviour and morphology of tumours and so forth. The important drawback of discrete modelling is its increasingly high computational demands as the number of cells being modelled increases. An alternative to these scale-specific models is a multiscale approach that refers to the models that contain more than one spatial and temporal scale to take into account cross-scale mechanisms in the course of tumour growth and evolution [49]. This approach is classified as “hybrid” modelling. A hybrid model comprises of a continuum deterministic part that controls the concentration of ECM and chemicals, and a stochastic discrete part governing cell migration and interactions.

Such a hybrid model of tumour growth and invasion was developed by Anderson [19]. The formalism of hybrid modelling enables to simulate specific cell processes (e.g. proliferation and cell-cell adhesion) and also inclusion of different tumour cell phenotypes at cellular level in a continuum chemical/ECM surrounding. The model parameters consisted of concentration distributions of tumour cell (n), ECM (f), MDE (m), and oxygen (c). The interaction of these parameters was represented in a set of differential equations, as follows:

$$\begin{aligned}\frac{\partial c}{\partial t} &= \overbrace{D_c \nabla^2 c}^{\text{oxygen diffusion}} + \overbrace{\beta f}^{\text{oxygen production}} - \overbrace{\gamma n}^{\text{oxygen uptake}} \\ &\quad - \overbrace{\alpha c}^{\text{oxygen decay}}, \\ \frac{\partial m}{\partial t} &= \overbrace{D_m \nabla^2 m}^{\text{MDE diffusion}} + \overbrace{\mu n}^{\text{MDE production}} - \overbrace{\lambda m}^{\text{MDE decay}}, \\ \frac{\partial f}{\partial t} &= \overbrace{-\delta m f}^{\text{ECM degrading}}, \\ \frac{\partial n}{\partial t} &= \overbrace{D_n \nabla^2 n}^{\text{random motility}} - \overbrace{\chi \nabla \cdot (n \nabla f)}^{\text{haptotaxis}}.\end{aligned}\quad (15)$$

As indicated in the first line of (15), oxygen is diffused into the ECM, consumed by tumour and decayed naturally at rates γ and α , respectively. The hybrid model, that follows the path of each individual cell, requires discretising the system of differential equation based on finite difference method in a given time and space steps [21]. Each point on the grid is correlated to neighbouring grids via coefficients indicating the probability of transition from that grid to another. For example, tumour cell density is expressed as

$$n_{i,j}^{q+1} = n_{i,j}^q P_0 + n_{i+1,j}^q P_1 + n_{i-1,j}^q P_2 + n_{i,j+1}^q P_3 + n_{i,j-1}^q P_4, \quad (16)$$

where indices i and j represent the location and q specifies the time. The coefficients P_0, P_1, \dots, P_4 are probabilities of transition from the grid in question to the respective neighbouring grids. Unlike purely continuum modelling, the hybrid model, being intrinsically multiscale, allows for investigation of the effect of tumour cell heterogeneity on the morphology and phenotypic diversity of invading vascular tumours (e.g., capturing the emergent property of invasive cells) [50]. In the more recent studies of Anderson et al. [51, 52], the hybrid model was used to simulate the shape of a growing tumour under homogeneous and heterogeneous matrix distribution and a phenotypically heterogeneous tumour cell population. Also, the impact of nutrient availability during tumour development on tumour morphology was examined. The models predicted that harsh microenvironment conditions lead to a tumour mass with invasive morphology (fingering margins) dominated with a few aggressive phenotypes. Other studies independently conducted *in vivo* and *in vitro* experiments to examine the role of harsh environment (e.g., hypoxia) in the invasive morphology of tumours [18, 53]. The results of their investigations corresponded to those predicted by the hybrid model. However, neither of them examined phenotypic composition of the resulting tumours, thus these experiments just partially validate the hybrid model.

Malignant tumour invasion, driven by haptotaxis, both in the form of travelling waves (continuum models) [54–56] and hybrid models [57–59], has been also modelled by others. The model developed by Anderson and Chaplain [58] was mathematically analysed by Kubo [60] to investigate asymptotic profiles of solutions. The simulated tumour cell distribution illustrated that a cluster of cells detaches from the original tumour mass and migrates further away from the tumour as the time evolves. The simulated tumour cell distribution shows an explicit detachment of a cluster of cells and qualitatively corresponds to the results of Gerisch's study [6].

The most recent work in the continuum deterministic framework is the study of Swanson [61]. In this study the Proliferation-Invasion (PI) model was developed to produce a Proliferation Invasion Hypoxia Necrosis Angiogenesis (PIHNA) model incorporating the mechanisms related to angiogenesis cascade. Three different cellular types, namely, proliferative, hypoxic, and necrotic were described mathematically in a form of three partial differential equations in which conversions of each type to others due to microenvironmental changes were included. It is known that, while

tumour cells grow and invade according to their respective proliferation and diffusion rates, the microenvironment becomes harsh and leads to the production of Tumour Angiogenic Factor (TAF) by proliferative and hypoxic cells in response to the metabolic demands of tumour. It is worth noting that the rate of production of TAF by hypoxic cells is significantly higher compared to that by proliferative cells. The presence of TAF in tumour microenvironment stimulates vascularisation. These two processes were also represented in two differential equations that formed a system of five equations for modelling. The *in silico* prediction of malignant progression of tumour corresponded well with imaging (MRI) and histologic data of three GBM patients who had approximately similar size of tumour but different hypoxic and necrotic ratios on their MR images. In the context of microscopic extension, this model can predict local invasion. However, it cannot visualize those microscopic clusters of cells detached from main mass of tumour, since it overlooks migration (via haptotaxis).

Table 1 Summarizes the major analytical models of tumour proliferation and diffusion reported in the literature.

Analytical modelling based on conservation of cells has evolved from basic models such as the one proposed by Murray's group [12–14] to very sophisticated models considering many biological mechanisms involved in tumour growth and invasion (e.g., Gerisch and Chaplain [6]). Some significant achievements regarding prediction of tumour behaviour in the course of its progression can also be obtained using this class of modelling. However, in order to obtain a realistic model, other critical characteristics of tumour cell growth are yet to be taken into account. The heterogeneity of diffusion coefficients and multilayer nature of tumours (necrotic, hypoxic, and proliferative layers) brought about by nutrient gradient exemplify the overlooked parameters. Moreover, purely analytical (continuum) modelling seems to be too inflexible to represent the biological phenomena which are intrinsically probabilistic. Therefore, what is actually favoured is not one single precise solution for a given situation provided by analytical models, but rather a probability distribution which better describes the behaviour of such systems.

3. Stochastic Models

Stochastic models are guided by probability distribution. The various techniques used in stochastic modelling are dominated by Monte Carlo and Markov approaches which are generally employed in the simulation of biological systems.

3.1. Markov Model. Markov models are stochastic models which simulate the state of systems with time-dependent random variables possessing Markov property. A stochastic process has Markov property (or memoryless property), if the probability distribution of future states depends only on the present state and not on the preceding sequence of events. This reads mathematically as

$$\begin{aligned} P(X_{n+1} = x \mid X_1 = x_1, X_2 = x_2, \dots, X_n = x_n) \\ = P(X_{n+1} = x \mid X_n = x_n), \end{aligned} \quad (17)$$

TABLE 1: A summary of analytical models of tumour proliferation and diffusion.

Type	Site of modelling	Incorporated mechanisms	Model validation and results	Comments	Reference
Continuum	Glioma	Random motility with uniform diffusion; exponential proliferation	N/A	Prediction of basic behaviour of gliomas (e.g., tumour cell density is a function of ρ/D)	Cruywagen et al. 1995 [14]
Continuum	Astrocytoma	Random motility with uniform diffusion; logistic proliferation; cell loss due to chemotherapy	12 CT images of a patient/agreement between model parameters and experimental data	The model is applicable for a specific course of treatment	Tracqui et al. 1995 [12]
Mechano-chemical	Multisite	Uniform diffusion; logistic proliferation; ECM-cell adhesion; haptotaxis	N/A	While important mechanisms in tumour invasion are considered, the behaviour of tumour at cellular level cannot be predicted Rough prediction of the extent and concentration of local invasion. Applicable for tumours >1 (mm) ³	Tracqui 1995 [16]
Continuum	Glioma	Random motility with nonuniform diffusion; exponential proliferation	Virtual MRI image/obtaining nonisotropic invasion pattern	Migration and departure of cells not taken into account	Swanson et al. 2002, 2000 [2, 17]
Continuum	Glioblastoma	Nonuniform diffusion; exponential proliferation; mass effect	MR images/capable to simulate complex tumour behaviour	Stochastic nature of the model allows to predict avascular invading tumour morphology by following individual cells with different phenotypes at each time and space step	Clatz et al. 2005 [10]
Continuum-Stochastic	Multisite	Random motility with uniform diffusion; haptotaxis; three-population tumour cells; heterogeneous ECM	Model predictions consistent with clinical findings [18]	Assuming two-population tumour cells, proliferative (core) and invasive (periphery), and modelling invasive cells. Applicable for tumours <1 (mm) ³	Anderson 2005 [19]
Continuum	Glioma	Random motility with uniform diffusion; logistic proliferation; radially biased motility; shedding of invasive cell at tumour surface	The model reproduces <i>in vitro</i> experiments data	Simplifying assumptions: uniform diffusion and that haptotaxis is independent of ECM density; the simulation is 2D	Stein et al. 2007 [20]
Continuum	Multisite	Random motility with uniform diffusion; logistic proliferation; ECM-cell adhesion; haptotaxis, Cell-cell adhesion	Comparison to simulation results of Anderson et al. [21]		Gerisch and Chaplain 2008 [6]

TABLE 1: Continued.

Type	Site of modelling	Incorporated mechanisms	Model validation and results	Comments	Reference
Continuum	multisite	Random motility with uniform diffusion; logistic proliferation; two-population tumour cells; oxygen concentration	<i>In vivo</i> tumour growth observation	Assumption: cells could either proliferate or migrate where transition between these two classes is environment-dependent; haptotaxis not considered	Thalhauser et al. 2009 [22]
Continuum-Stochastic	Glioma	Random motility with nonuniform diffusion; logistic proliferation; two-population tumour cells; haptotaxis	The model predicts the tumour growth pattern of a clinical case	Stochastic step of the model allows for introduction of patient-specific parameters (e.g., tumour location)	Eikenberry et al. 2009 [8]
Continuum	Glioma	Random motility with nonuniform diffusion; logistic proliferation; radiotherapy	The biopsies of nine patients/the model reproduces RT response	In contrast with imaging-based RT response, this model incorporates patient-specific tumour growth kinetics to quantify RT outcome	Rockne et al. 2010 [23]

where X_i s are random variables having Markov property. A Markov chain is the simplest Markov model which is a chainlike random process that transforms from one state (i) to another (j) by a transition matrix whose elements are described as

$$p_{ij} = P(X_{n+1} = j \mid X_n = i). \quad (18)$$

Benson et al. [3] produced a theoretical model to predict the microscopic spread of tumour to regional lymph nodes based on anatomical information adopted from the Foundational Model of Anatomy (FMA) in the head and neck cancer. A computational rule-based model was previously proposed in this area, based on clinical data rather than anatomical principles, by Kalet et al. [62]. FMA provides information regarding an almost complete set of drainage pathways or lymph chains which is known to be followed by subclinical spread [63]. The information acquired from FMA was supplemented by clinical data pertaining to lymph chains that span multiple regions. The inputs to the model were primary tumour location and T-stage. In FMA every primary site is associated with its respective lymphatic chains, thus lymphatic chains with subparts corresponding to the primary tumour location were derived from FMA. A sequence of Markov models were developed such that each hidden Markov model was assigned to one position in the pathway where position “0” was labelled for the original tumour. The validity of the model was examined by comparing the model results with two surgical data. Overall, the model overpredicted the metastasis in specific

regions, requiring certain modifications such as revising supplementary data added to FMA. The procedure starting from model inputs to model validation followed by iteration is diagrammatically shown in Figure 4.

3.2. Monte Carlo Model. Monte Carlo (MC) models are widely used in the field of cancer biology and treatment since this method is particularly useful for simulating systems with considerable uncertainty in parameters.

The earliest developed MC models of tumour growth date back to early 80’s, for example the work of Duchting and vogelsaenger [64] for small tumours which took into account nutritional needs of tumours. Aiming to investigate the pattern of *in vivo* cancer development, Qi [65] simulated the distribution of cancer cells in a given biochemical environment as a two dimensional cellular automaton on a square lattice. Qi et al. [66] later advanced the model to take into account proliferation of cancer cells, nutrition supply, mechanical pressure, and the cytotoxic behaviour of immune system and reproduced Gompertz model which is typically used to describe the growth of cancer tumour volume (Gompertz model of cancer tumour volume growth is $V = V_0 \exp(A/B(1 - \exp(1 - Bt)))$, where V is the volume of tumour at time t and V_0 is the initial volume. A and B are parameters). Smolle and Stettner [67] considered a two-dimensional tumour growth model and correlated macroscopic behaviour of tumour (tumour morphology) with the functionality of tumour cells at microscopic level (e.g., interaction of tumour cells with microenvironment).

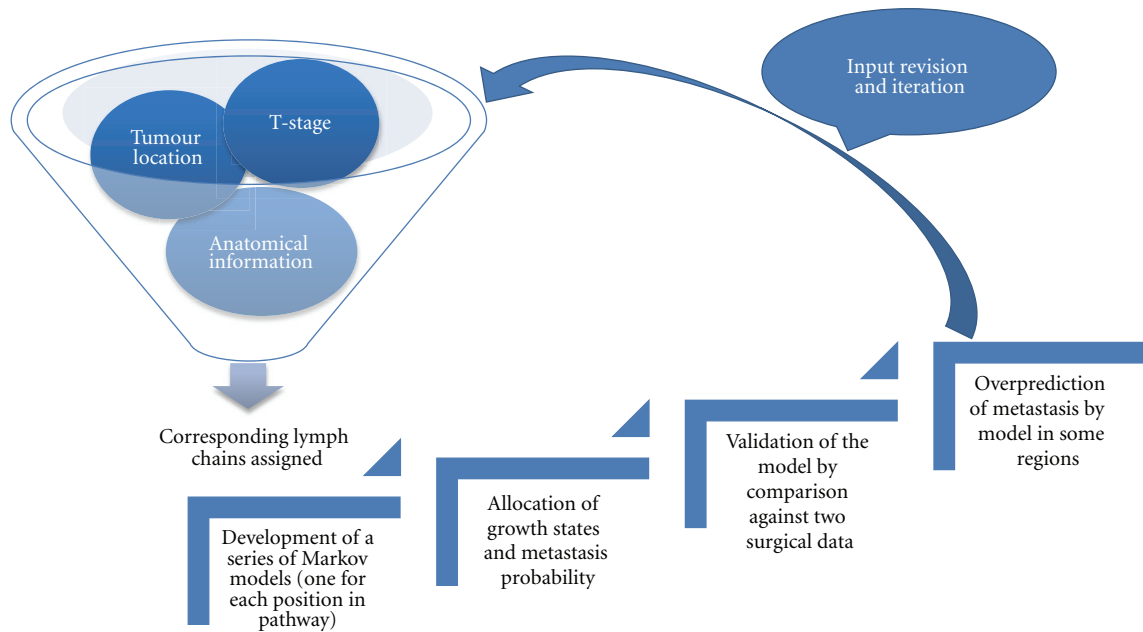


FIGURE 4: Schematic diagram of the Markov model developed by Benson et al. [3].

Later, the invasiveness of tumour in the absence of active motility was studied in a stochastic cellular automata by Smolle et al. [68]. Aimed to provide an algorithm to predict the extent and direction of spread of a brain tumour, another elegant approach was presented in a patient-specific *in vivo* brain tumour growth model which was developed by Wasserman et al. [69]. The model involved a variety of forces associated with microenvironmental (e.g., nutrient and growth inhibitor distributions) and mechanical factors (e.g., cell adhesiveness and resistance of brain parenchyma to expansion) and was implemented via the finite element method. To validate, the model was implemented on a patient MRI data to retrospectively predict the extension of tumour with respect to time. An approximate agreement between simulated tumour extension and MRI image was achieved. It is worth noting that this model explicitly addresses the problem of subclinical boundaries (CTV) in irradiation target definitions.

One of the common approaches in stochastic modelling is the Cellular Automaton (CA) method which employs a grid lattice, with each site in the grid accommodating a finite number of cells in specific states, to grow a tumour from a few cells to macroscopic stages. When the time is incremented by one, the defined biological rules determine the updated states of cells in terms of their current states and microenvironment. A 3D cellular automaton model of untreated brain tumour was developed by Kansal et al. [24, 70]. The site of tumour growth was modelled as a Delaney lattice, made of Voronoi network by connecting those sites whose polyhedra share a common face. Therefore, the density of lattice varied continuously with the radius of tumour, being greater in the centre and reduced towards the surface of the tumour. The tessellation lattice was isotropic, thus it precluded the anisotropies encountered

in the models in which cubic lattice was adopted (e.g., the model presented by Duchting and Vogelsaenger [64]). However, a purely random distribution could result in some regions with either very high or very low cell density corresponding to small and large Voronoi cells, respectively. To preclude biologically unreasonable variations in size of cells, a technique called Random Sequential Addition (RSA) was used. In this technique, during the generation of random points, they are checked for not being within a given distance from neighbouring points. The tumour was proposed to be as a self-organising and ideally spherical biosystem with three different layers (necrotic, nonproliferative, and proliferative) whose thicknesses are governed by nutrition supply gradient diffusing into inner layers. This hypothesis was later supported by an *in vitro* study conducted by Deisboeck et al. [71] and was used in the model developed by Yang and Torquato [72], whereby the effect of microenvironment heterogeneity on morphology of invasive tumours was investigated. Four time-dependent variables investigated in the Kansal's model consist of overall tumour radius, proliferative and nonproliferative thickness, and probability of division. Once the lattice was generated, the initial set up was designated whereupon proliferation algorithm was applied. In the algorithm, the probability of transition of cells between nonproliferative and necrotic was considered to be a function of distance from the edge of tumour (nutrient supply) such that nonproliferative cells located at more than a specific distance from the surface of tumour were turned to necrotic. In addition, the transition between proliferative to non-proliferative occurs when there is no sufficient space for the new cell to be generated by a dividing cell. These transitions were considered stochastic in the 2D cellular automata model presented by Qi [66]. In the same framework, clonal competition (emerging a more

rapidly growing tumour from a more slowly growing parent) was also quantitatively analysed by introducing another set of inputs in the model after a specific time [73].

Aimed to simulate untreated tumour growth and also the response of tumour to different schemes of radiotherapy, a four dimensional, patient-specific, *in vivo* stochastic model was developed by Stamatakos et al. [25, 74, 75]. The model is outlined as a 3D discretising cubic mesh structure in which each mesh accommodates a specific Number of Biological Cells (NBCs) which is called a Geometric Cell (GC). In addition, different phases of tumour cell cycles have been taken into account according to the cytokinetic model proposed by Duchting et al. [76], as illustrated in Figure 5. Three metabolic subregions were considered: proliferating cell regions, resting G_0 cell regions and dead cell regions. The metabolic state of each GC was determined depending on the distribution of its contained cells in different phases. The initial NBC distribution is derived from imaging and histopathological data of each individual patient, whereby the tumour region is apportioned to three metabolic layers: proliferating, resting, and necrotic. Time is discretized and at the end of each time step the GC mesh is updated such that transitions between different metabolic states are estimated and applied (e.g., M cells in a GC for which the mitosis time is over are transited to G_0 or G_1 with the probability depending on the subregion they belong). The time was incremented at the end of each scan and the process iterated. In order to investigate the radiotherapy effect on tumour shrinkage, the Linear Quadratic (LQ) model of surviving fraction ($S = e^{-\alpha D - \beta D^2}$) is employed. Three sets of radio sensitivity parameters (α and β) were assumed corresponding to proliferative, necrotic, and resting states and the tumour regression was simulated for three specific cases: standard fractionation/radiosensitive tumour, standard fractionation/moderately radiosensitive, and hyper fractionation scheme/radiosensitive tumour [77]. The simulations of tumour shrinkage under various therapeutic regimens qualitatively reproduced the clinical observations.

The model was gradually improved to take into account possible parameters involved in tumour growth and response to radiotherapy to achieve a more biologically realistic description of cancer biology and treatment. Antipas et al. [26] studied the effect of hypoxia in radio sensitivity of tumours by introducing Oxygen Enhancement Ratio (OER) parameter and investigated the influence of OER as well as parameters corresponding to cell cycle duration on tumour growth and shrinkage under standard and accelerated fractionation regimens. The model was applied to two GBM cases, a qualitative agreement between simulation results and clinical experience was achieved. In addition, the effect of oxygen on tumour behaviour appeared to conceptually correspond to that derived by Anderson et al. [19, 50, 51]. More recently, Stamatakos et al. [27] introduced the role of neoangiogenesis distribution in a 4D model of *in vivo* tumour growth and response to radiation. In the same framework, Dionysiou et al. [78, 79] conducted parametric studies to investigate the effect of varying parameters on the radiotherapy treatment outcome with emphasis on

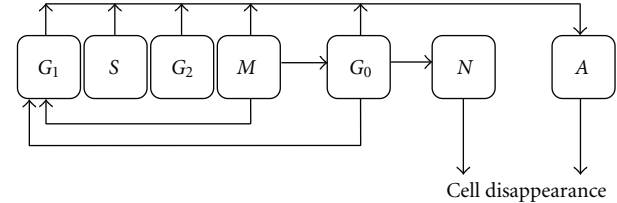


FIGURE 5: The pathway of cells through cell cycle: G_1 phase (gap 1); S phase (DNA synthesis); G_2 phase (gap 2); M phase (mitosis); G_0 phase (if nutrition and oxygen is not sufficient, the cell enters this phase for a limited time); N phase (the cell enters necrotic phase, if it does not receive nutrition until the resting time is expired, otherwise it enters G_1); A phase (apoptotic).

genetic profile of tumour. Though the model includes some simplifying assumptions or may lack some parameters (since biological mechanisms in cancer are not fully understood), the discrete and modulated nature of the model allows for inclusion of further improvements. While this approach, initiated by Stamatakos et al. [25, 74] and refined later by his team [26, 27, 75, 77–79], was aimed to simulate tumour growth and response to radiotherapy, it has the potential to be improved to take into account infiltration of a malignant tumour (e.g., by introducing haptotaxis and cell-cell adhesion). This is enabled due to the discrete and modular character of the model which allows incorporation of further mechanisms without extensive modifications.

Individual-Based Modelling (IBM), which has gained popularity for modelling of biological processes, is another class of stochastic modelling [80]. In IBM approach, the biosystem population is regarded as being composed of individual cells whose sets of traits which determines their interaction with microenvironment vary. The IBM allows for explicit inclusion of variations in specifications of individual cells (heterogeneity). Aiming to investigate cancer invasion and the effect of microenvironment on growing tumour morphology and phenotype a novel IBM model was developed and further extended by Gerlee et al. [9, 30, 81, 82]. The model was constructed on a two-dimensional grid representing ECM, with each point possessing ECM, nutrition and oxygen concentration respective to that point in the ECM. Each point on the grid could either be occupied by a cancer cell or be empty. It was assumed that the cell's behaviour or phenotype is determined based on its interaction with neighbouring cells and microenvironment. Hence, a forward neural network fed with microenvironment variables as inputs to give the response of the cell (phenotype) was established. Three layers were considered for this network: (1) input layer which receives input microenvironment parameters (e.g., number of neighbours, oxygen, glucose consumption and ECM gradient); (2) hidden layer which is connected to the input layer via connection matrix consisting of regulatory genes which control the behaviour of cells via weighting factors (w) of the connection matrix; (3) output layer which is connected to the hidden layer via connection matrix (W) and determines the phenotype (e.g., metabolism, proliferation, quiescence, haptotaxis). The

TABLE 2: Summaries of stochastic models of tumour growth and invasion.

Type	Site of modelling	Incorporated mechanisms	Model validation and results	Comments	Reference
Monte Carlo (cellular automaton model)	Brain	3D tessellation lattice grid, three-population tumour, nutrition gradient, clonal competition, intercellular mechanical stress	N/A	Since active motility is not taken into account, the tumour invasion cannot be investigated	Kansal et al. 2000 [24]
Monte Carlo	multisite	Different phases of cell cycle, three-population tumour cells, shrinkage of tumour due to radiotherapy, cubic grid	Application of the model to small cell lung cancer/qualitative correspondence to <i>in vitro</i> experiments	The microscopic extension cannot be predicted since each grid element is almost 1 mm ³ accommodating 10 ⁶ cells	Stamatakos 2001 [25]
Monte Carlo	Multisite	Different phases of cell cycle, three-population tumour cells, shrinkage of tumour due to radiotherapy, cubic grid, hypoxia	Application of the model to two GBM cases/qualitative correspondence to clinical observations	The possibility to optimize radiotherapy fractionation regimens, unable to depict microscopic spread	Antipas et al. 2004 [26]
Monte Carlo	Multisite	Different phases of cell cycle, three-population tumour cells, shrinkage of tumour due to radiotherapy, cubic grid, hypoxia, neo-angiogenesis	Parametric validation against two different categories of GBM/qualitative correspondence to experiments	Generally, the discrete nature of these models allows for inclusion of other parameters	Stamatakos et al. 2006 [27]
Markov model	Head and Neck	Lymphatic drainage pathway, T-stage, tumour location	Comparison to two surgical data/over prediction of metastasis	Quantitative prediction of microscopic spread was found to be feasible	Benson et al. 2006 [3]
Monte Carlo (individual-based model)	Multisite	Three-population tumour, 2D grid, nutrition and oxygen concentration, different phases of cell cycle	Comparison to the study of Anderson [19] and also experimental results [28, 29]/good agreement	Haptotaxis is not taken into account thus tumour invasion is not depicted	Gerlee and Anderson 2007 [30]
Monte Carlo (individual-based model)	Multisite	Three-population tumour, 2D grid, nutrition and oxygen concentration, different phases of cell cycle, haptotaxis	Comparison to the study of Anderson [19] and also experiment results/good agreement	The influence of evolution of tumour cell phenotype in response to microenvironment on tumour development and progression is an important conclusion to be used in the study of microscopic extension	Gerlee and Anderson 2009 [9]

nutrition concentrations were modelled by reaction diffusion equations according to which concentrations were calculated for each grid at every time step (10^{-1} cell cycle). The emergence of glycolytic phenotype associated with anaerobic metabolism pathway of cells was investigated in subsequent extension of the model [81], and more recently haptotaxis was taken into account [9]. The effect of haptotaxis was included in the model by a differential equation describing degradation of ECM at grid points. Accordingly, cells take the direction with maximum ECM gradient, and when there is no gradient, the existing cells go into proliferation mode until the gradient is sufficient to move. The switch between proliferation and haptotaxis was also depended on

the number of vacant neighbours. The more number of vacancies, the more probable the cell stays in proliferation mode. Finally, it was demonstrated that with the emergence of haptotaxis, tumour growth is altered showing different morphologies (compact or branched) depending on the oxygen and ECM concentration. This outcome was supported by other analyses of the model [82, 83] and conceptually corresponded to the simulation results of the hybrid IBM model of Anderson et al. [19, 51].

To summarize, in clinical situations, physicians propose CTVs based on their experience of the extent of malignant tumours growth. Therefore, the ability to accurately model the tumour extension at microscopic scale is highly desirable.

Within the realm of stochastic modelling, a significant number of research works has been developed to contribute to the understanding of the tumour growth and invasion via a variety of classes of Monte Carlo models. However, irrespective of the class, these studies aim to gain insight into either the biology of cancer growth in general terms or the response of tumour to radiotherapy rather than the microscopic extension of tumour which is to be incorporated in CTV. Hence, there is room for investigation in this respect, in the light of information acquired from these studies. Table 2 summarizes a few major models of tumour growth and invasion which represent various classes of Monte Carlo models.

4. Conclusion

An infiltrating neoplasm undergoes several stages in the course of its growth and progression and understanding of the mechanisms governing the evolution of tumour is required to deliver an appropriate therapy which results in optimal tumour control and reduced normal tissue side effects. Mathematical modelling is recognized as a great tool to facilitate this understanding. Furthermore, mathematical models provide predictions of the probable response of tumour to therapeutic regimens in a variety of circumstances, different in terms of factors such as the tumour microenvironment, and stage. In this paper, we have reviewed the evolution of mathematical modelling of tumour growth and invasion in both analytical and stochastic approaches. Analytical models are capable to describe the behaviour of tumour at macroscopic level for specific conditions; however, they fail to provide predictions at microscopic (cellular and subcellular) level. In addition, the ongoing research to enhance the limited insight into complex and dynamic cancer systems may reveal some further parameters which have to be included in models. However, analytical models are not flexible for these modifications. On the other hand, stochastic models efficiently depict the characteristic and behaviour of tumour as this class of modelling enables introducing new parameters as well as specific anatomical boundaries. Finally, we came to believe that while none of the above-mentioned models address explicitly the microscopic extension of tumour, they have the potential to be used to deduce the extent of subclinical disease which is not detected by imaging techniques. To serve this purpose, however, models have to be further modified, applying the relevant biological parameters, to become site-specific. The tumour sites that have a relatively high histopathological data available, such as prostate and gliomas can be potentially modelled and validated faster than those having little or no clinical data related to their microscopic extension.

References

[1] International Commission of Radiation Units and Measurements, "Prescribing, Recording, and Reporting Photon Beam Therapy," Report 50, ICRU, 1993.

- [2] K. R. Swanson, E. C. Alvord Jr., and J. D. Murray, "Virtual brain tumours (gliomas) enhance the reality of medical imaging and highlight inadequacies of current therapy," *British Journal of Cancer*, vol. 86, no. 1, pp. 14–18, 2002.
- [3] N. Benson, M. Whipple, and I. J. Kalet, "A Markov model approach to predicting regional tumor spread in the lymphatic system of the head and neck," in *Proceedings of the AMIA Annual Symposium*, pp. 31–35, 2006.
- [4] J. K. A. Jameel, V. S. R. Rao, L. Cawkwell, and P. J. Drew, "Radioresistance in carcinoma of the breast," *Breast*, vol. 13, no. 6, pp. 452–460, 2004.
- [5] A. J. F. Griffiths, W. M. Miller, and R. C. Lewontin, *Modern Genetic Analysis*, W. H. Freeman, New York, NY, USA, 1999.
- [6] A. Gerisch and M. A. J. Chaplain, "Mathematical modelling of cancer cell invasion of tissue: local and non-local models and the effect of adhesion," *Journal of Theoretical Biology*, vol. 250, no. 4, pp. 684–704, 2008.
- [7] E. J. Hall and A. J. Giaccia, *Radiobiology for the Radiologist*, Lippincott Williams & Wilkins, 6th edition, 2006.
- [8] S. E. Eikenberry, T. Sankar, M. C. Preul, E. J. Kostelich, C. J. Thalhauser, and Y. Kuang, "Virtual glioblastoma: growth, migration and treatment in a three-dimensional mathematical model," *Cell Proliferation*, vol. 42, no. 4, pp. 511–528, 2009.
- [9] P. Gerlee and A. R. A. Anderson, "Evolution of cell motility in an individual-based model of tumour growth," *Journal of Theoretical Biology*, vol. 259, no. 1, pp. 67–83, 2009.
- [10] O. Clatz, M. Sermesant, P. Y. Bondiau et al., "Realistic simulation of the 3-D growth of brain tumors in MR images coupling diffusion with biomechanical deformation," *IEEE Transactions on Medical Imaging*, vol. 24, no. 10, pp. 1334–1346, 2005.
- [11] K. R. Swanson, C. Bridge, J. D. Murray, and E. C. Alvord, "Virtual and real brain tumors: using mathematical modeling to quantify glioma growth and invasion," *Journal of the Neurological Sciences*, vol. 216, no. 1, pp. 1–10, 2003.
- [12] P. Tracqui, G. C. Cruywagen, D. E. Woodward, G. T. Bartoo, J. D. Murray, and E. C. Alvord, "A mathematical model of glioma growth: the effect of chemotherapy on spatio-temporal growth," *Cell Proliferation*, vol. 28, no. 1, pp. 17–31, 1995.
- [13] J. D. Murray, *Mathematical Biology*, Springer, New York, NY, USA, 3rd edition, 2002.
- [14] G. C. Cruywagen, D. E. Woodward, P. Tracqui, G. T. Bartoo, J. D. Murray, and E. C. Alvord, "The modeling of diffusive tumours," *Journal of Biological Systems*, vol. 3, no. 4, pp. 937–945, 1995.
- [15] H. L. P. Harpold, E. C. Alvord Jr., and K. R. Swanson, "The evolution of mathematical modeling of glioma proliferation and invasion," *Journal of Neuropathology and Experimental Neurology*, vol. 66, no. 1, pp. 1–9, 2007.
- [16] P. Tracqui, "From passive diffusion to active cellular migration in mathematical models of tumour invasion," *Acta Biotheoretica*, vol. 43, no. 4, pp. 443–464, 1995.
- [17] K. R. Swanson, E. C. Alvord Jr., and J. D. Murray, "A quantitative model for differential motility of gliomas in grey and white matter," *Cell Proliferation*, vol. 33, no. 5, pp. 317–329, 2000.
- [18] O. Casanovas, D. J. Hicklin, G. Bergers, and D. Hanahan, "Drug resistance by evasion of antiangiogenic targeting of VEGF signaling in late-stage pancreatic islet tumors," *Cancer Cell*, vol. 8, no. 4, pp. 299–309, 2005.
- [19] A. R. A. Anderson, "A hybrid mathematical model of solid tumour invasion: the importance of cell adhesion," *Mathematical Medicine and Biology*, vol. 22, no. 2, pp. 163–186, 2005.

- [20] A. M. Stein, T. Demuth, D. Mobley, M. Berens, and L. M. Sander, "A mathematical model of glioblastoma tumor spheroid invasion in a three-dimensional in vitro experiment," *Biophysical Journal*, vol. 92, no. 1, pp. 356–365, 2007.
- [21] A. R. Anderson, M. A. J. Chaplain, E. L. Newman, R. J. C. Steele, and A. M. Thompson, "Mathematical modelling of tumour invasion and metastasis," *Computational and Mathematical Methods in Medicine*, vol. 2, no. 2, pp. 129–154, 2000.
- [22] C. J. Thalhauser, T. Sankar, M. C. Preul, and Y. Kuang, "Explicit separation of growth and motility in a new tumor cord model," *Bulletin of Mathematical Biology*, vol. 71, no. 3, pp. 585–601, 2009.
- [23] R. Rockne, J. K. Rockhill, M. Mrugala et al., "Predicting the efficacy of radiotherapy in individual glioblastoma patients in vivo: a mathematical modeling approach," *Physics in Medicine and Biology*, vol. 55, no. 12, pp. 3271–3285, 2010.
- [24] A. R. Kansal, S. Torquato, G. R. Harsh, E. A. Chiocca, and T. S. Deisboeck, "Simulated brain tumor growth dynamics using a three-dimensional cellular automaton," *Journal of Theoretical Biology*, vol. 203, no. 4, pp. 367–382, 2000.
- [25] G. S. Stamatakis, "In vivo tumor growth and response to radiation therapy: a novel algorithmic description," *International Journal of Radiation Oncology, Biology, Physics*, vol. 51, no. 3, p. 240, 2001.
- [26] V. P. Antipas, G. S. Stamatakis, N. K. Uzunoglu, D. D. Dionysiou, and R. G. Dale, "A spatio-temporal simulation model of the response of solid tumours to radiotherapy in vivo: parametric validation concerning oxygen enhancement ratio and cell cycle duration," *Physics in Medicine and Biology*, vol. 49, no. 8, pp. 1485–1504, 2004.
- [27] G. S. Stamatakis, V. P. Antipas, N. K. Uzunoglu, and R. G. Dale, "A four-dimensional computer simulation model of the in vivo response to radiotherapy of glioblastoma multiforme: studies on the effect of clonogenic cell density," *British Journal of Radiology*, vol. 79, no. 941, pp. 389–400, 2006.
- [28] T. G. Graeber, C. Osmanian, T. Jacks et al., "Hypoxia-mediated selection of cells with diminished apoptotic potential in solid tumours," *Nature*, vol. 379, no. 6560, pp. 88–91, 1996.
- [29] C. Y. Kim, M. H. Tsai, C. Osmanian et al., "Selection of human cervical epithelial cells that possess reduced apoptotic potential to low-oxygen conditions," *Cancer Research*, vol. 57, no. 19, pp. 4200–4204, 1997.
- [30] P. Gerlee and A. R. A. Anderson, "An evolutionary hybrid cellular automaton model of solid tumour growth," *Journal of Theoretical Biology*, vol. 246, no. 4, pp. 583–603, 2007.
- [31] D. L. Collins, A. P. Zijdenbos, V. Kollokian et al., "Design and construction of a realistic digital brain phantom," *IEEE Transactions on Medical Imaging*, vol. 17, no. 3, pp. 463–468, 1998.
- [32] C. H. Wang, J. K. Rockhill, M. Mrugala et al., "Prognostic significance of growth kinetics in newly diagnosed glioblastomas revealed by combining serial imaging with a novel biomathematical model," *Cancer Research*, vol. 69, no. 23, pp. 9133–9140, 2009.
- [33] M. R. Chicoine and D. L. Silbergeld, "Assessment of brain tumor cell motility in vivo and in vitro," *Journal of Neurosurgery*, vol. 82, no. 4, pp. 615–622, 1995.
- [34] D. E. Woodward, J. Cook, P. Tracqui, G. C. Cruywagen, J. D. Murray, and E. C. Alvord, "A mathematical model of glioma growth: the effect of extent of surgical resection," *Cell Proliferation*, vol. 29, no. 6, pp. 269–288, 1996.
- [35] K. R. Swanson, E. C. Alvord, and J. D. Murray, "Quantifying efficacy of chemotherapy of brain tumors with homogeneous and heterogeneous drug delivery," *Acta Biotheoretica*, vol. 50, no. 4, pp. 223–237, 2002.
- [36] P. Y. Bondiau, E. Konukoglu, O. Clatz, H. Delingette, M. Frenay, and P. Paquis, "Biocomputing: numerical simulation of glioblastoma growth and comparison with conventional irradiation margins," *Physica Medica*, vol. 27, no. 2, pp. 103–108, 2011.
- [37] H. M. Byrne and M. A. Chaplain, "Growth of nonnecrotic tumors in the presence and absence of inhibitors," *Mathematical Biosciences*, vol. 130, no. 2, pp. 151–181, 1995.
- [38] H. M. Byrne and M. A. J. Chaplain, "Growth of necrotic tumors in the presence and absence of inhibitors," *Mathematical Biosciences*, vol. 135, no. 2, pp. 187–216, 1996.
- [39] H. M. Byrne and M. A. J. Chaplain, "Free boundary value problems associated with the growth and development of multicellular spheroids," *European Journal of Applied Mathematics*, vol. 8, no. 6, pp. 639–658, 1997.
- [40] N. Bellomo and L. Preziosi, "Modelling and mathematical problems related to tumor evolution and its interaction with the immune system," *Mathematical and Computer Modelling*, vol. 32, no. 3–4, pp. 413–452, 2000.
- [41] V. Cristini, J. Lowengrub, and Q. Nie, "Nonlinear simulation of tumor growth," *Journal of Mathematical Biology*, vol. 46, no. 3, pp. 191–224, 2003.
- [42] R. P. Araujo and D. L. S. McElwain, "A history of the study of solid tumour growth: the contribution of mathematical modelling," *Bulletin of Mathematical Biology*, vol. 66, no. 5, pp. 1039–1091, 2004.
- [43] V. Cristini, H. B. Frieboes, R. Gatenby, S. Caserta, M. Ferrari, and J. Sinek, "Morphologic instability and cancer invasion," *Clinical Cancer Research*, vol. 11, no. 19, pp. 6772–6779, 2005.
- [44] P. Macklin and J. Lowengrub, "Evolving interfaces via gradients of geometry-dependent interior Poisson problems: application to tumor growth," *Journal of Computational Physics*, vol. 203, no. 1, pp. 191–220, 2005.
- [45] P. Macklin and J. Lowengrub, "Nonlinear simulation of the effect of microenvironment on tumor growth," *Journal of Theoretical Biology*, vol. 245, no. 4, pp. 677–704, 2007.
- [46] S. Sanga, H. B. Frieboes, X. Zheng, R. Gatenby, E. L. Bearer, and V. Cristini, "Predictive oncology: a review of multidisciplinary, multiscale in silico modeling linking phenotype, morphology and growth," *NeuroImage*, vol. 37, supplement, no. 1, pp. S120–S134, 2007.
- [47] R. A. Gatenby, A. S. Silva, R. J. Gillies, and B. R. Frieden, "Adaptive therapy," *Cancer Research*, vol. 69, no. 11, pp. 4894–4903, 2009.
- [48] T. S. Deisboeck, "Multiscale cancer modeling," *Annual Review of Biomedical Engineering*, vol. 13, pp. 127–155, 2011.
- [49] D. C. Walker and J. Southgate, "The virtual cell—a candidate co-ordinator for 'middle-out' modelling of biological systems," *Briefings in Bioinformatics*, vol. 10, no. 4, pp. 450–461, 2009.
- [50] A. R. A. Anderson and V. Quaranta, "Integrative mathematical oncology," *Nature Reviews Cancer*, vol. 8, no. 3, pp. 227–234, 2008.
- [51] A. R. A. Anderson, A. M. Weaver, P. T. Cummings, and V. Quaranta, "Tumor morphology and phenotypic evolution driven by selective pressure from the microenvironment," *Cell*, vol. 127, no. 5, pp. 905–915, 2006.
- [52] A. R. A. Anderson, K. A. Rejniak, P. Gerlee, and V. Quaranta, "Microenvironment driven invasion: a multiscale multimodel investigation," *Journal of Mathematical Biology*, vol. 58, no. 4–5, pp. 579–624, 2009.

- [53] J. T. Erler, K. L. Bennewith, M. Nicolau et al., “Lysyl oxidase is essential for hypoxia-induced metastasis,” *Nature*, vol. 440, no. 7088, pp. 1222–1226, 2006.
- [54] B. P. Marchant, J. Norbury, and A. J. Perumpanani, “Traveling shock waves arising in a model of malignant invasion,” *SIAM Journal on Applied Mathematics*, vol. 60, no. 2, pp. 463–476, 2000.
- [55] B. P. Marchant, J. Norbury, and J. A. Sherratt, “Travelling wave solutions to a haptotaxis-dominated model of malignant invasion,” *Nonlinearity*, vol. 14, no. 6, pp. 1653–1671, 2001.
- [56] B. P. Marchant, J. Norbury, and H. M. Byrne, “Biphasic behaviour in malignant invasion,” *Mathematical Medicine and Biology*, vol. 23, no. 3, pp. 173–196, 2006.
- [57] A. R. A. Anderson and M. A. J. Chaplain, “A mathematical model for capillary network formation in the absence of endothelial cell proliferation,” *Applied Mathematics Letters*, vol. 11, no. 3, pp. 109–114, 1998.
- [58] A. R. A. Anderson and M. A. J. Chaplain, “Continuous and discrete mathematical models of tumor-induced angiogenesis,” *Bulletin of Mathematical Biology*, vol. 60, no. 5, pp. 857–899, 1998.
- [59] H. B. Frieboes, J. S. Lowengrub, S. Wise et al., “Computer simulation of glioma growth and morphology,” *NeuroImage*, vol. 37, no. 1, supplement, pp. S59–S70, 2007.
- [60] A. Kubo, “Mathematical analysis of a model of tumour invasion and simulations,” *International Journal of Mathematical Models and Methods in Applied Sciences*, vol. 4, no. 3, pp. 187–194, 2010.
- [61] K. R. Swanson, “Quantifying the role of angiogenesis in malignant progression of gliomas: in silico modeling integrates imaging and histology,” *Cancer Research*, vol. 71, no. 24, pp. 7366–7375, 2011.
- [62] I. J. Kalet, M. Whipple, S. Pessah, J. Barker, M. M. Austin-Seymour, and L. G. Shapiro, “A rule-based model for local and regional tumor spread,” in *Proceedings of the AMIA Annual Symposium*, pp. 360–364, 2002.
- [63] C. Rosse, L. G. Shapiro, and J. F. Brinkley, “The digital anatomist foundational model: principles for defining and structuring its concept domain,” in *Proceedings of the AMIA Annual Symposium*, pp. 820–824, 1998.
- [64] W. Duchting and T. Vogelsaenger, “Recent progress in modelling and simulation of three-dimensional tumor growth and treatment,” *BioSystems*, vol. 18, no. 1, pp. 79–91, 1985.
- [65] A. S. Qi, “Multiple solutions of a model describing cancerous growth,” *Bulletin of Mathematical Biology*, vol. 50, no. 1, pp. 1–17, 1988.
- [66] A. S. Qi, “A cellular automaton model of cancerous growth,” *Journal of Theoretical Biology*, vol. 161, no. 1, pp. 1–12, 1993.
- [67] J. Smolle and H. Stettner, “Computer simulation of tumour cell invasion by a stochastic growth model,” *Journal of Theoretical Biology*, vol. 160, no. 1, pp. 63–72, 1993.
- [68] J. Smolle, R. Hofmann-Wellenhof, and R. Fink-Puches, “Cellular invasion without cellular motility in a stochastic growth model,” *Analytical Cellular Pathology*, vol. 10, no. 1, pp. 37–43, 1996.
- [69] R. Wasserman, R. Acharya, C. Sibata, and K. H. Shin, “A patient-specific in vivo tumor model,” *Mathematical Biosciences*, vol. 136, no. 2, pp. 111–140, 1996.
- [70] A. R. Kansal, S. Torquato, G. R. Harsh IV, E. A. Chiocca, and T. S. Deisboeck, “Cellular automaton of idealized brain tumor growth dynamics,” *BioSystems*, vol. 55, no. 1–3, pp. 119–127, 2000.
- [71] T. S. Deisboeck, M. E. Berens, A. R. Kansal, S. Torquato, A. O. Stemmer-Rachamimov, and E. A. Chiocca, “Pattern of self-organization in tumour systems: complex growth dynamics in a novel brain tumour spheroid model,” *Cell Proliferation*, vol. 34, no. 2, pp. 115–134, 2001.
- [72] Y. Jiao and S. Torquato, “Emergent behavior from a cellular automaton model for invasive tumor growth in heterogeneous microenvironments,” *PLoS Computational Biology*, vol. 7, no. 12, 2011.
- [73] A. R. Kansal, S. Torquato, E. A. Chiocca, and T. S. Deisboeck, “Emergence of a subpopulation in a computational model of tumor growth,” *Journal of Theoretical Biology*, vol. 207, no. 3, pp. 431–441, 2000.
- [74] G. S. Stamatakos, E. I. Zacharaki, M. I. Makropoulou et al., “Modeling tumor growth and irradiation response in vitro—a combination of high-performance computing and web-based technologies including VRML visualization,” *IEEE Transactions on Information Technology in Biomedicine*, vol. 5, no. 4, pp. 279–289, 2001.
- [75] G. S. Stamatakos, D. D. Dionysiou, E. I. Zacharaki, N. A. Mquravliansky, K. S. Nikita, and N. K. Uzunoglu, “In silico radiation oncology: combining novel simulation algorithms with current visualization techniques,” *Proceedings of the IEEE*, vol. 90, no. 11, pp. 1764–1777, 2002.
- [76] W. Duchting, T. Ginsberg, and W. Ulmer, “Modeling of radiogenic responses induced by fractionated irradiation in malignant and normal tissue,” *Stem Cells*, vol. 13, no. 1, pp. 301–306, 1995.
- [77] D. D. Dionysiou, G. S. Stamatakos, N. K. Uzunoglu, K. S. Nikita, and A. Marioli, “A four-dimensional simulation model of tumour response to radiotherapy in vivo: parametric validation considering radiosensitivity, genetic profile and fractionation,” *Journal of Theoretical Biology*, vol. 230, no. 1, pp. 1–20, 2004.
- [78] D. D. Dionysiou, G. S. Stamatakos, N. K. Uzunoglu, and K. S. Nikita, “A computer simulation of in vivo tumour growth and response to radiotherapy: new algorithms and parametric results,” *Computers in Biology and Medicine*, vol. 36, no. 5, pp. 448–464, 2006.
- [79] D. D. Dionysiou, “Critical parameters determining standard radiotherapy treatment outcome for glioblastoma multiforme: a computer simulation,” *The Open Biomedical Engineering Journal*, vol. 2, pp. 43–51, 2008.
- [80] A. R. Anderson, M. A. J. Chaplain, and K. A. Rejniak, *Single-Cell-Based Models in Biology and Medicine*, Birkhauser, Basel, Switzerland, 2007.
- [81] P. Gerlee and A. R. A. Anderson, “A hybrid cellular automaton model of clonal evolution in cancer: the emergence of the glycolytic phenotype,” *Journal of Theoretical Biology*, vol. 250, no. 4, pp. 705–722, 2008.
- [82] P. Gerlee and A. R. A. Anderson, “Modelling evolutionary cell behaviour using neural networks: application to tumour growth,” *BioSystems*, vol. 95, no. 2, pp. 166–174, 2009.
- [83] P. Gerlee and A. R. A. Anderson, “Stability analysis of a hybrid cellular automaton model of cell colony growth,” *Physical Review E*, vol. 75, no. 5, Article ID 051911, 2007.

Research Article

Risk-Adaptive Volumetric Modulated Arc Therapy Using Biological Objective Functions for Subvolume Boosting in Radiotherapy

Nicholas Hardcastle^{1,2,3} and Wolfgang A. Tome^{1,3,4}

¹Departments of Human Oncology and Medical Physics, University of Wisconsin-Madison, Madison, WI 53792, USA

²Department of Physical Sciences, Peter MacCallum Cancer Centre, East Melbourne, VIC 3002, Australia

³Centre for Medical Radiation Physics, University of Wollongong, Wollongong, NSW 2522, Australia

⁴Oncophysics Institute, Albert Einstein College of Medicine of Yeshiva University, Jack and Pearl Resnick Campus, 1300 Morris Park Avenue, Bronx, NY 10461, USA

Correspondence should be addressed to Wolfgang A. Tome, tome@humonc.wisc.edu

Received 19 March 2012; Accepted 26 April 2012

Academic Editor: Scott Penfold

Copyright © 2012 N. Hardcastle and W. A. Tome. This is an open access article distributed under the Creative Commons Attribution License, which permits unrestricted use, distribution, and reproduction in any medium, provided the original work is properly cited.

Objectives. Simultaneous integrated boost (SIB) for prostate cancer allows increases in tumor control probability while respecting normal tissue dose constraints. Biological optimization functions that optimize based on treatment outcome can be used to create SIB prostate plans. This study investigates the feasibility of biologically optimized volumetric modulated arc therapy (VMAT) for SIB prostate radiotherapy. **Methods.** Five prostate cancer patients with diffusion-weighted MR images were selected for analysis. A two-step VMAT optimization was performed, which consisted of an initial biological optimization of a static gantry angle delivery followed by conversion of the static delivery to a single arc VMAT plan. A dosimetric analysis was performed on the resulting plans. **Results.** The VMAT plans resulted in a Δ EU_D between the prostate and the boost volume of between 15.1 Gy and 20.3 Gy. Rectal volumes receiving 75.6 Gy ranged from 4.5 to 9.9%. Expected rectal normal tissue complication probabilities were between 8.6% and 21.4%. Maximum bladder doses ranged from 73.6 Gy to 75.8 Gy. Estimated treatment time was 120 s or less. **Conclusions.** The presented biological optimization method resulted in deliverable VMAT plans that achieved sufficient modulation for SIB without violating rectal and bladder dose constraints. **Advances in knowledge.** This study presents a method for creating simultaneous integrated boost VMAT treatments using biological outcome objective functions.

1. Introduction

The benefit of a simultaneous integrated boost (SIB) for prostate cancer is that it allows one to increase the expected tumor control probability (TCP) while at the same time respecting normal tissue dose constraints, compared to the whole prostate dose escalation for plans delivering the same equivalent uniform dose (EUD) to the entire prostate [1, 2]. When delivering an SIB for prostate cancer, biological objective functions for optimization of dose distributions, as opposed to physical dose objective functions can be utilized. That is, direct optimization of biological outcomes can be performed. Using this technique, it has been shown that, for

prostate cancer, SIB can be delivered to a subvolume within the prostate while adhering to normal tissue constraints. [1, 3] SIB techniques allow one to take advantage of advanced imaging techniques to selectively boost the dose to a subvolume of the treatment target that may not be controlled with standard doses and hence require a dose higher than the minimal peripheral prescription dose to be delivered to them to achieve adequate local control.

SIB delivery requires increased modulation of the dose so as to achieve the desired boosting level while maintaining a sufficient dose gradient outside of the target to minimize the dose to surrounding healthy tissues. Kim and Tomé have shown that static gantry angle IMRT can achieve the required

modulation [1, 3–5]. In recent years, volumetric modulated arc therapy (VMAT) has become an attractive method to efficiently deliver modulated dose distributions. VMAT has been shown to result in equivalent dose distributions in prostate cancer in shorter delivery times when compared with static gantry angle intensity modulated radiation therapy (IMRT) [6–8]. Biological optimization of VMAT plans for prostate cancer has also been investigated [6, 9]. The vast majority of these studies have concentrated on prostate only or prostate plus seminal vesicles as the target volume. It can be argued that achievement of sufficient modulation in these cases is more accessible than for more complex treatment geometries. Jolly et al. [10] have provided a robust planning strategy for an SIB technique with VMAT, treating to three dose levels including the prostate and seminal vesicles according to the Conventional or Hypofractionated High-Dose Intensity-Modulated Radiotherapy for Prostate Cancer (CHHiP) protocol [11]. The volume receiving the highest dose under the CHHiP protocol, however, is the full prostate plus a 5 mm margin, so the complexity of these targets is limited. The present study extends the investigation of VMAT for SIB to a more complex geometry, by using a risk-adaptive VMAT optimization method, where the boost volume is a subvolume of the prostate.

2. Methods and Materials

Five patients were selected for analysis. These included two patients using rectal balloons and three patients without rectal balloons. All the patients received a planning kVCT scan as well as a T2 contrast-enhanced magnetic resonance (MR) image. The prostate was contoured as the CTV, which was expanded by 7 mm to obtain the PTV. A biopsy-confirmed subvolume of enhanced contrast uptake on the diffusion weighted imaging (DWI) MR was outlined as the high-risk CTV. The high-risk CTV plus 8 mm was subtracted from the PTV to obtain the residual PTV, PTV-R. A 5 mm expansion was applied to the high-risk CTV to obtain the high-risk PTV, PTV-H. This process resulted in no overlap between PTV-R and PTV-H. The rectal wall was outlined on the patients with rectal balloon, and the full rectum was outlined on the patients with no rectal balloon. The bladder and femoral heads were also outlined. An avoidance structure was outlined, which consisted of a 5 cm wide ring around the PTV plus 2 cm.

All planning was performed with the Pinnacle radiotherapy planning system using the SmartArc VMAT optimization algorithm (v9.100, Philips Radiation Oncology Systems, Fitchburg, WI, USA). A set of research optimization objectives, built into the Pinnacle RTPS as a plugin, that optimize directly on TCP and NTCP were used. The plugin and objective function have been described in detail elsewhere [3]. Briefly, the objective function maximizes the TCP for target volumes while minimizing the NTCP for organs at risk (OARs). The objective function takes the form of

$$\text{UTCP} = \text{TCP}(1 - \text{NTCP}). \quad (1)$$

The TCP and NTCP calculations utilize phenomenological logistic dose response functions that are evaluated

TABLE 1: Biological objective functions and parameters.

ROI	Objective	Dose	m	γ
PTV	NTCP	95	0.11	—
PTV-H	TCP	84.5	—	8
PTV-R	TCP	64.5	—	8
Rectum	NTCP	76.9	0.13	—
Rectum	NTCP	55.9	0.15	—
Normal	NTCP	55	0.13	—

on a voxel-by-voxel basis. That is, the TCP and NTCP are calculated for each voxel, where each voxel has its own value of D_{50} and γ_{50} (for TCP) and D_{50} and m (for NTCP) based on the physiological makeup of the tumor. D_{50} is the dose that yields a tumor control probability or normal tissue complication probability of 50% for TCP and NTCP respectively, and γ_{50} and m are parameters describing the slope of the dose response curve at the 50% probability point for TCP and NTCP, respectively. TCP and NTCP are calculated on a voxel-by-voxel basis so as to be able to account for subtumor variations in the dose response curves for tumor control and normal tissue complication. In this study, the tumor is divided into two subvolumes requiring separate parameters to describe their dose response curve, and normal structures are approximated as one subvolume. The reader is referred to Kim and Tomé for details and derivation of the TCP and NTCP functions. [3]

A two-step process was used for optimization. In the first step, a set of 15 beams were distributed every 24° around the patient. These were selected to mimic the positions of the initial fluence maps used in the SmartArc optimization process. Intensity modulation of the ideal fluence was then performed using the biological optimization function described above. The optimization objectives for each organ and target are given in Table 1. TCP objectives were used on the PTV-H and the PTV-R. In addition to these TCP objectives on the target, an NTCP objective was used on the original PTV to limit the PTV dose to less than 100 Gy. Two NTCP objectives were used on the rectum. The first used the values of D_{50} and m representing grade 2 or higher rectal bleeding from the QUANTEC study [12]. Since the QUANTEC values are related to grade 2 or higher rectal bleeding these tended to penalize only the high dose region of the rectum. Therefore, a second NTCP objective function was used to reduce the mid-low doses, the values of which were taken from the NTCP parameter fitting by Tucker et al. [13]. We note that although these values were derived also for grade 2 or higher rectal bleeding, the parameter values penalize mid-low doses thus were used as a surrogate for rectal toxicities related to mid-low doses.

The optimization was run until the objective value was reduced below a given value, typically 5–10 iterations. The second step of the optimization involved creating a single arc VMAT plan using the SmartArc optimization tool and an Elekta Infinity linear accelerator with the X MLC for delivery (Elekta North America, Atlanta, GA, USA). A 360° arc was selected, with a collimator angle of 30° and dose

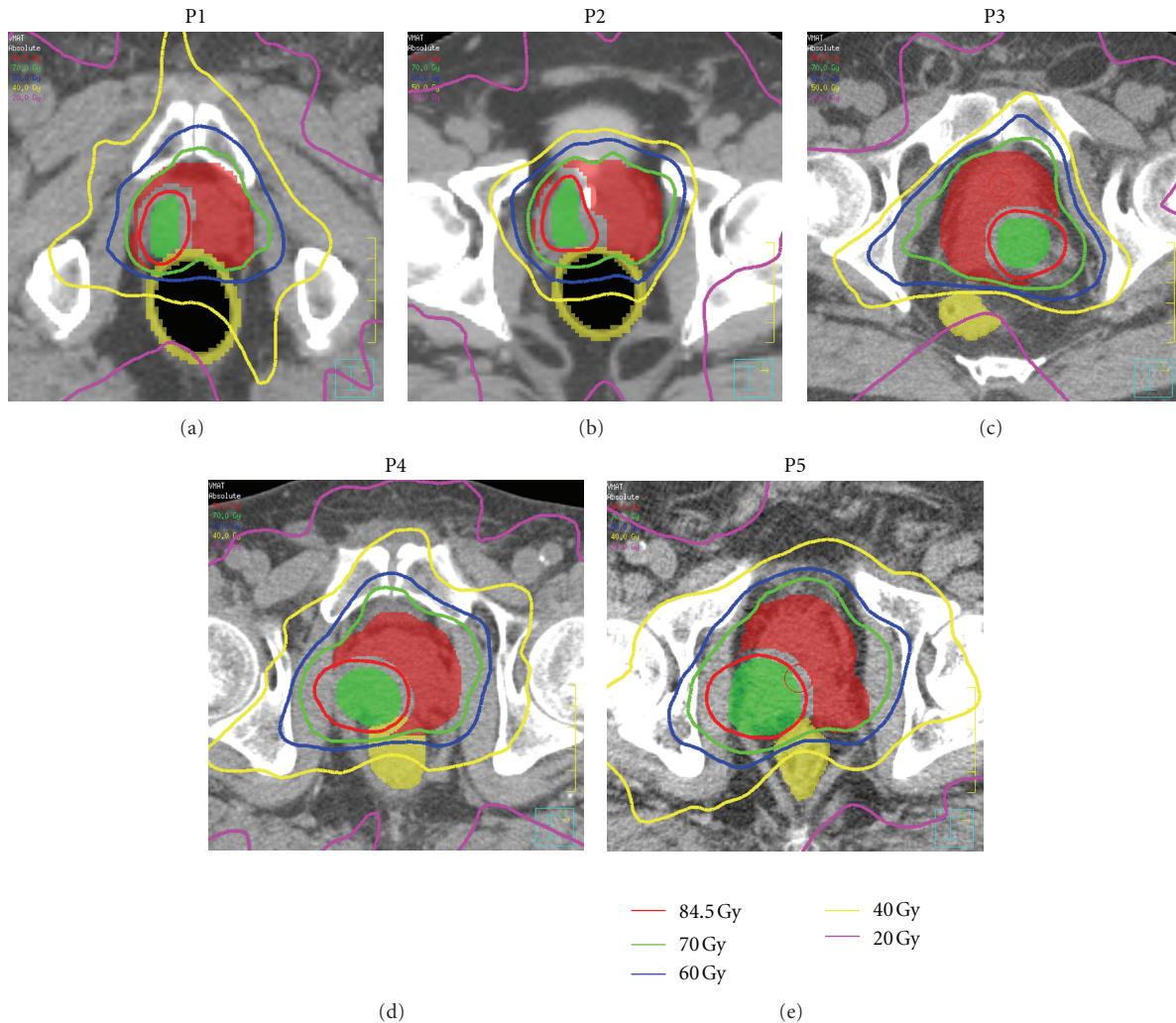


FIGURE 1: Isodose lines for the five patients. PTV-H is the green colorwash, PTV-R is the red colorwash and the rectum is the yellow colorwash. P1 and P2 each had a rectal balloon; P3, P4, and P5 had no balloon.

rate set to be discretely variable from 0 to 300 MU/min. The final gantry spacing was 4° , and the maximum delivery time was 120 seconds. Physical dose optimization objectives were created based on the ideal dose distribution derived from the biological optimization. Two steps of 40 iterations were performed. Dose calculation based on a $2 \times 2 \times 2 \text{ mm}^3$ dose grid was then performed using the adaptive convolution dose algorithm. The rationale for the two-step optimization process was to allow the optimizer to create an “ideal” set of fluence maps, which would adhere to the optimization objectives as close as possible, before using this “ideal” dose distribution as the basis for the deliverable SmartArc optimization. That is, the initial biological optimization allows one to obtain the highest boost dose possible to the sub-tumor volume without violating the normal tissue constraints on the normal tissue volumes.

The plans were transferred to Computational Environment for Radiotherapy Research (CERR, University of Washington in St. Louis) for analysis [14]. For all plans, the following metrics were calculated: EUD of the PTV-H and PTV-R and the difference between these values ΔEUD ,

percentage volume of the rectum receiving 25 Gy, 50 Gy, and 70 Gy, the rectal NTCP (calculated using the QUANTEC values for \geq grade 2 rectal bleeding of $D_{50} = 76.9 \text{ Gy}$, $m = 0.13$, and $n = 0.09$), the bladder volume receiving 55 Gy, and the maximum bladder dose. The maximum bladder dose was taken as the dose 1 cc of the bladder receiving the highest dose. EUD was calculated using Equation 8 in [15] with an SF_2 of 0.48.

In addition to the plan quality analysis, one treatment plan was selected for delivery quality assurance on an Elekta Infinity linear accelerator. The treatment plan for patient 3 was calculated on a kVCT of the Delta4 phantom (Scandidos, Uppsala, Sweden). The plan was delivered and the dose was measured in the phantom. Comparison of the delivered dose with the planned dose was performed using the 2D gamma metric with 3%/3 mm criteria.

3. Results

The dose distributions and metrics were compared for the five patients. Figure 1 shows the isodose lines for the five

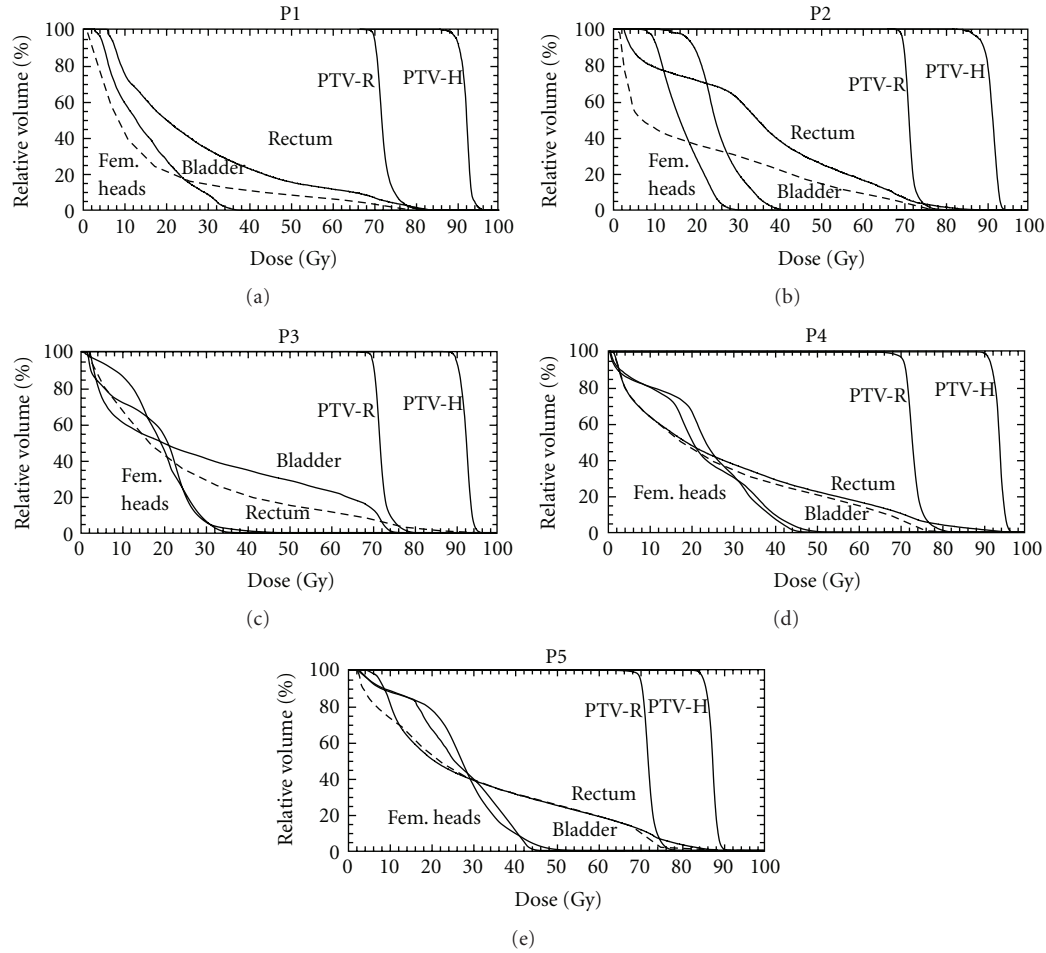


FIGURE 2: DVHs for the five patients. The bladder line is dashed.

TABLE 2: Dosimetric metrics for the target and OAR structures.

Patient	PTV-H EUD (Gy)	PTV-R EUD (Gy)	Δ EUD	Rectum			Bladder		
				V50 Gy (%)	V70 Gy (%)	V75.6 Gy (%)	NTCP (%)	V55 Gy (%)	Max (Gy)
P1	92.8	72.9	19.9	17.2	8.7	5.2	11.1	7.4	78.7
P2	92.2	72.5	19.7	26.5	7.5	3.2	8.2	11.8	74.5
P3	93.3	72.9	20.3	15.3	7.5	3.8	9.9	26.0	74.9
P4	94.8	74.2	20.6	22.8	11.0	6.2	20.0	17.5	75.6
P5	88.3	73.1	15.2	25.4	12.3	6.3	13.0	23.0	74.1

patients, showing that sufficient modulation was achieved with one arc to conform the boost dose to the PTV-H volume with limited coverage of the rectal volume with the boost dose. Figure 2 shows the DVHs for the five patients for both the PTVs and the OARs.

The dosimetric metrics are presented in Table 2. The PTV-H targets received EUDs of between 88.34 Gy and 94.75 Gy; however, these had an upper dosimetric limit placed on them during optimization, without which dose volume histograms (DVHs) would exceed 100 Gy. Subtumor boosting allowed an increase in EUD to the high-risk PTV of between 15.22 Gy and 20.55 Gy over the dose the PTV-R received.

The rectal DVH values for all patients met the V50 Gy < 30% objective presented by Mohan et al. for the 2.5 Gy \times 28 fractions regime [16]. Due to the increased doses per fraction used in this planning study, the maximum rectal dose objective of 74 Gy used by Mohan et al. was not considered [16]. Instead, the volumes receiving 75.6 Gy were analysed as per the 86.4 Gy treatment regime reported by Zelefsky et al. [17]. All patients easily met this treatment objective of V75.6 Gy < 30%, with the maximum being 6.3% (patient 5). The rectal NTCP values for \geq grade 2 rectal bleeding range from 8.2% to 20.0%. The bladder DVH values all met the V55 Gy < 30% specified by Mohan et al. [16]. There was no discernible dosimetric difference between the

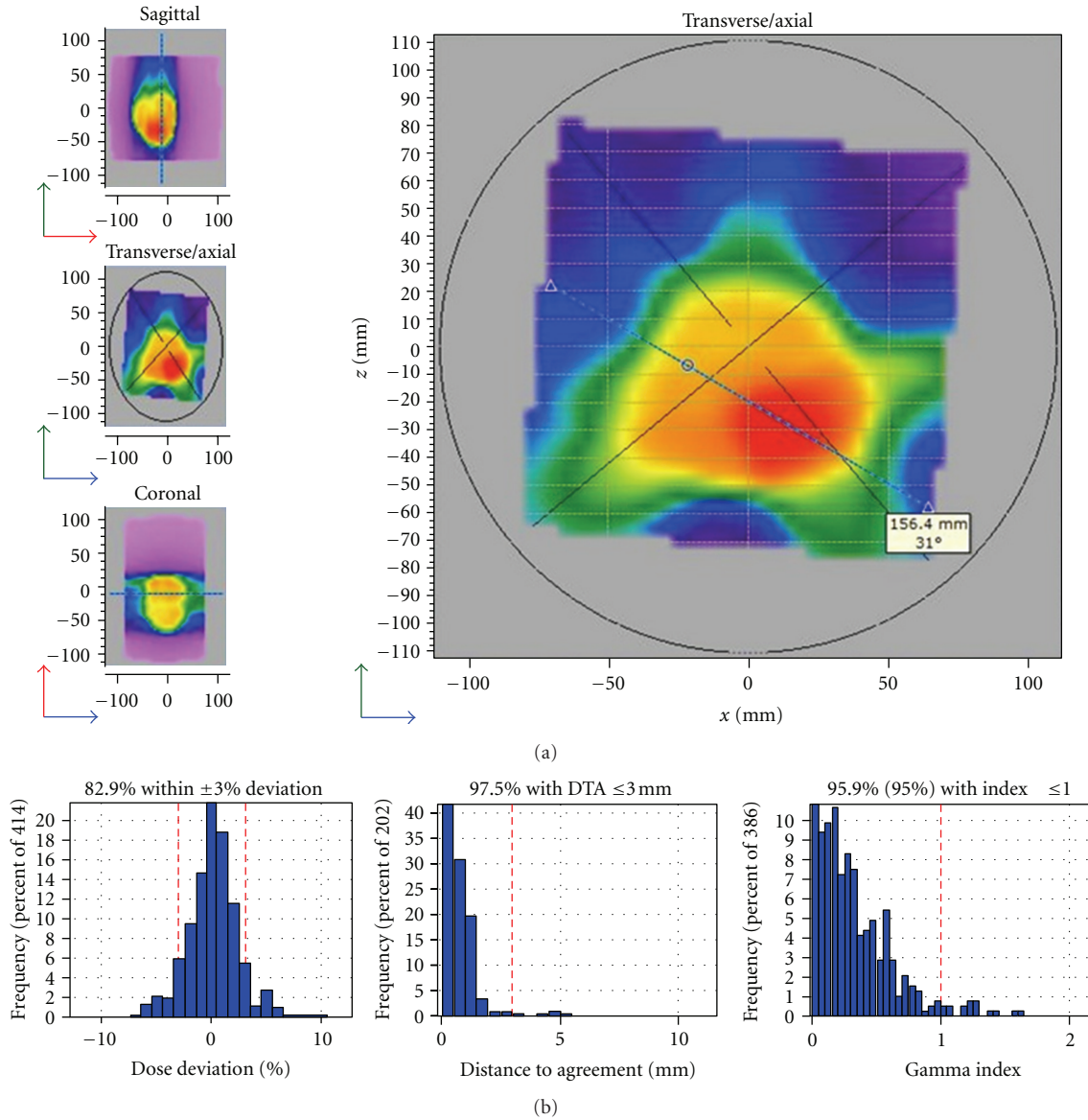


FIGURE 3: VMAT delivery QA for patient 3. (a) shows the axial distribution obtained by delivering a risk adaptive VMAT plan to the Delta4 phantom. (b) shows the respective distributions for the dose deviation, distance to agreement, and gamma index found for this plan.

two patients with balloons and the three patients without balloons.

The measured dose in the Delta4 phantom was compared with the planned dose for the treatment plan selected for delivery. Using a gamma criteria of 3%/3 mm, 95.9% of all points passed (cf. Figure 3(b)).

4. Discussion

The capability of VMAT for achieving sufficient modulation for prostate radiotherapy with simultaneous integrated boost has been investigated in this study. Despite the more complex target geometry, one treatment arc was sufficient to meet treatment objectives. This allows one to take advantage of

advanced imaging techniques such as MRI and PET to identify subregions in the heterogeneous tumor environment and efficiently escalate the dose to selected volumes. It should be noted that this technique could potentially be applied to other treatment sites where simultaneous integrated boosting could be advantageous. %

Despite the large differences in the rectal anatomy between patients with a rectal balloon and patients without a rectal balloon, there was very little difference in the planned rectal dose between patients with and without a rectal balloon. However, due to the high doses delivered to the PTV-H volume, which is often in the posterior lobe of the prostate, adjacent to the rectum, any small changes in prostate or rectal position, size or shape could lead to large

differences between the planned and delivered doses. As a result, use of a rectal balloon would be beneficial due to the improved setup reproducibility and consistency of the rectal size and shape provided by the use of a rectal balloon.

Although contoured, the bladder and femoral head structures were not used for optimization due to their having very little impact on the optimization result. That is to say, optimization on these structures was not required to obtain the low bladder and femoral head doses observed here. This is likely a consequence of the combination of delivery technique, where the dose is delivered from all angles which spreads out the dose distribution, minimizing the dose delivered to each critical structure, and the optimization using the normal structure, which has the effect of steepening the dose gradient outside of the target volume.

The prostate dose in the presented plans was limited by treating the PTV-H and PTV-R as target volumes but the whole PTV as a normal tissue structure. This is akin to the method for optimizing target dose based on the EUD function presented by Wu et al. [18], who treated the target volume as both a target and a normal tissue structure to improve the homogeneity of the dose distribution. The result of our target optimization method was that the dose to the PTV-H was boosted to an EUD of 88–95 Gy whilst still maintaining an EUD between 72.5 Gy and 74.2 Gy to the PTV-R. This limits the dose to the urethra and rectum to doses less than that allowed in the MSKCCC dose escalation trial. [17] Our current method differs from that presented by Kim and Tomé [3], who did not limit the dose on the prostate and as such observed a more heterogeneous target dose. The dose to the normal structures using the VMAT technique was less than that achieved by Kim and Tomé [3] who used a static gantry angle IMRT technique. The current method also used two NTCP objectives on the rectum (as opposed to one in Kim and Tomé [3]) to reduce the rectal volumes receiving both high and mid-low doses. This is also a contributing factor to the reduced rectal doses observed in the current study.

5. Conclusions

We have shown that biologically optimized VMAT plans can be derived from a risk-adaptive sub-tumor dose escalation strategy for prostate cancer. A single arc provides sufficient modulation to achieve dose escalation to a high-risk subvolume of the prostate of up to a Δ EUD of 20.3 Gy above the gEUD of the remainder of the prostate. This was achieved without violating rectal NTCP constraints, allowing for efficient delivery of risk-adaptive prostate radiotherapy.

Acknowledgment

The authors would like to thank Dr. Edward T. Bender for assistance with plan delivery and Delta4 measurement.

References

[1] Y. Kim and W. A. Tomé, “Is it beneficial to selectively boost high-risk tumor subvolumes? A comparison of selectively

boosting high-risk tumor subvolumes versus homogeneous dose escalation of the entire tumor based on equivalent EUD plans,” *Acta Oncologica*, vol. 47, no. 5, pp. 906–916, 2008.

- [2] W. A. Tomé and J. F. Fowler, “Selective boosting of tumor subvolumes,” *International Journal of Radiation Oncology Biology Physics*, vol. 48, no. 2, pp. 593–599, 2000.
- [3] Y. Kim and W. A. Tomé, “Risk-adaptive optimization: selective boosting of high-risk tumor subvolumes,” *International Journal of Radiation Oncology Biology Physics*, vol. 66, no. 5, pp. 1528–1542, 2006.
- [4] Y. Kim and W. A. Tomé, “On voxel based iso-tumor-control probability and iso-complication maps for selective boosting and selective avoidance intensity-modulated radiotherapy,” *Imaging Decisions MRI*, vol. 12, no. 1, pp. 42–50, 2008.
- [5] Y. Kim and W. A. Tomé, “On the impact of functional imaging accuracy on selective boosting IMRT,” *Physica Medica*, vol. 25, no. 1, pp. 12–24, 2009.
- [6] N. Hardcastle, W. A. Tomé, K. Foo, A. Miller, M. Carolan, and P. Metcalfe, “Comparison of Prostate IMRT and VMAT Biologically Optimised Treatment Plans,” *Medical Dosimetry*, vol. 36, no. 3, pp. 292–298, 2011.
- [7] D. Palma, E. Vollans, K. James et al., “Volumetric modulated arc therapy for delivery of prostate radiotherapy: comparison with intensity-modulated radiotherapy and three-dimensional conformal radiotherapy,” *International Journal of Radiation Oncology Biology Physics*, vol. 72, no. 4, pp. 996–1001, 2008.
- [8] P. Zhang, L. Happersett, M. Hunt, A. Jackson, M. Zelefsky, and G. Mageras, “Volumetric modulated arc therapy: planning and evaluation for prostate cancer cases,” *International Journal of Radiation Oncology Biology Physics*, vol. 76, no. 5, pp. 1456–1462, 2010.
- [9] I. B. Mihaylov, M. Fatyga, K. Bzdusek, K. Gardner, and E. G. Moros, “Biological optimization in volumetric modulated arc radiotherapy for prostate carcinoma,” *International Journal of Radiation Oncology, Biology, Physics*, vol. 82, no. 3, pp. 1292–1298, 2012.
- [10] D. Jolly, D. Alahakone, and J. Meyer, “A RapidArc planning strategy for prostate with simultaneous integrated boost,” *Journal of Applied Clinical Medical Physics*, vol. 12, no. 1, pp. 35–49, 2011.
- [11] V. S. Khoo and D. P. Dearnaley, “Question of dose, fractionation and technique: ingredients for testing hypofractionation in prostate cancer—the CHHiP trial,” *Clinical Oncology*, vol. 20, no. 1, pp. 12–14, 2008.
- [12] J. M. Michalski, H. Gay, A. Jackson, S. L. Tucker, and J. O. Deasy, “Radiation dose-volume effects in radiation-induced rectal injury,” *International Journal of Radiation Oncology Biology Physics*, vol. 76, no. 3, pp. S123–S129, 2010.
- [13] S. L. Tucker, L. Dong, R. Cheung et al., “Comparison of rectal dose-wall histogram versus dose-volume histogram for modeling the incidence of late rectal bleeding after radiotherapy,” *International Journal of Radiation Oncology Biology Physics*, vol. 60, no. 5, pp. 1589–1601, 2004.
- [14] J. O. Deasy, A. I. Blanco, and V. H. Clark, “CERR: a computational environment for radiotherapy research,” *Medical Physics*, vol. 30, no. 5, pp. 979–985, 2003.
- [15] A. Niemierko, “Reporting and analyzing dose distributions: a concept of equivalent uniform dose,” *Medical Physics*, vol. 24, no. 1, pp. 103–110, 1997.
- [16] D. S. Mohan, P. A. Kupelian, and T. R. Willoughby, “Short-course intensity-modulated radiotherapy for localized prostate cancer with daily transabdominal ultrasound localization of the prostate gland,” *International Journal of*

Radiation Oncology Biology Physics, vol. 46, no. 3, pp. 575–580, 2000.

- [17] M. J. Zelefsky, Z. Fuks, and S. A. Leibel, “Intensity -modulated radiation therapy for prostate cancer,” *Seminars in Radiation Oncology*, vol. 12, no. 3, pp. 229–237, 2002.
- [18] Q. Wu, R. Mohan, A. Niemierko, and R. Schmidt-Ullrich, “Optimization of intensity-modulated radiotherapy plans based on the equivalent uniform dose,” *International Journal of Radiation Oncology Biology Physics*, vol. 52, no. 1, pp. 224–235, 2002.

Research Article

The HYP-RT Hypoxic Tumour Radiotherapy Algorithm and Accelerated Repopulation Dose per Fraction Study

W. M. Harriss-Phillips,^{1,2} E. Bezak,^{1,2} and E. Yeoh^{1,3}

¹ School of Chemistry and Physics, University of Adelaide, Adelaide, SA 5005, Australia

² Department of Medical Physics, Royal Adelaide Hospital, Adelaide, SA 5000, Australia

³ Department of Radiation Oncology, Royal Adelaide Hospital, Adelaide, SA 5000, Australia

Correspondence should be addressed to W. M. Harriss-Phillips, wendy.harriss@health.sa.gov.au

Received 16 February 2012; Accepted 11 April 2012

Academic Editor: Loredana Marcu

Copyright © 2012 W. M. Harriss-Phillips et al. This is an open access article distributed under the Creative Commons Attribution License, which permits unrestricted use, distribution, and reproduction in any medium, provided the original work is properly cited.

The HYP-RT model simulates hypoxic tumour growth for head and neck cancer as well as radiotherapy and the effects of accelerated repopulation and reoxygenation. This report outlines algorithm design, parameterisation and the impact of accelerated repopulation on the increase in dose/fraction needed to control the extra cell propagation during accelerated repopulation. Cell kill probabilities are based on Linear Quadratic theory, with oxygenation levels and proliferative capacity influencing cell death. Hypoxia is modelled through oxygen level allocation based on pO₂ histograms. Accelerated repopulation is modelled by increasing the stem cell symmetrical division probability, while the process of reoxygenation utilises randomised pO₂ increments to the cell population after each treatment fraction. Propagation of 10⁸ tumour cells requires 5–30 minutes. Controlling the extra cell growth induced by accelerated repopulation requires a dose/fraction increase of 0.5–1.0 Gy, in agreement with published reports. The average reoxygenation pO₂ increment of 3 mmHg per fraction results in full tumour reoxygenation after shrinkage to approximately 1 mm. HYP-RT is a computationally efficient model simulating tumour growth and radiotherapy, incorporating accelerated repopulation and reoxygenation. It may be used to explore cell kill outcomes during radiotherapy while varying key radiobiological and tumour specific parameters, such as the degree of hypoxia.

1. Introduction

Multiple studies have shown that hypoxia decreases cellular sensitivity to ionising radiation in living tissue. Consequently, there is an increase in radioresistance of hypoxic tumour cells following single or multifraction radiotherapy compared to oxic cells. Approximately 70% of locally advanced head and neck squamous cell carcinomas (HNSCC) have been reported to exhibit hypoxic regions, with median oxygen levels having a significant influence patient prognosis [1–3]. Reports from HNSCC clinical trials and experimental work commonly express hypoxia as the percentage of cells in the tumour having pO₂ values less than 10, 5, or 2.5 mmHg, which is often very high (>50%) [4, 5]. In contrast, the average pO₂ for healthy epithelial cells is approximately 40 mmHg [5].

Tumour hypoxia occurs when the diffusion of oxygen from the surrounding tissue becomes insufficient in a nonvascularised tumour mass. It has been shown that tumours can grow up to a diameter of 1 to 2 mm without an independent blood supply [6, 7], after which neovascularisation is necessary for sustained growth. However, the new blood vessels may be chaotic in nature and possess faults such as holes and shunts. Consequently, an unstable and insufficient oxygen supply may develop causing tumour hypoxia. However, when a tumour is treated with fractionated radiotherapy, oxygen levels may begin to increase again during the process of tumour shrinkage, a phenomenon named reoxygenation (ROx).

In aggressive tumours of epithelial origin such as HNSCC, cellular repopulation after trauma such high-dose irradiation, occurs through cell division of the surviving cell

population. This repopulation can occur at an increased rate, a phenomenon named accelerated repopulation (AR). AR can have a detrimental impact on radiotherapy outcome, especially if the total treatment time is relatively long [8]. Multiple published HNSCC clinical trial reports conclude that the onset time of AR, or the so-called kick-off time, is between 2 and 5 weeks [8–12] after the start of treatment.

As a supplement to clinical trials, Monte Carlo (MC) models can provide treatment response predictions which are (i) readily obtained and low in cost, (ii) reproducible, (iii) have the ability to account for the statistical nature of cellular kinetics and radiotherapy physics, and (iv) tumour specific depending on the data input into the model. MC methods and modern computing technology now make it possible to simulate the progression of individual tumour cells throughout the growth and treatment of a tumour approaching clinical sizes.

The first reported computer model to employ MC methods was named CELLSIM by Donaghey and coworkers, published in the early 1980s [13]. One of the first models to include cellular-based stochastic methods as well as oxygen and nutrient diffusion factors came from work led by Dutching in the early 1980s and into the following decade [14–17]. Using their approach, a tumour up to 1 mm in diameter could be simulated and then treated with radiotherapy. Recent reports regarding stochastic hypoxic tumour modelling over that past two decades have come from work by group leaders such as Kocher, Titz, Borkenstein, and Stamatakos [18–24], in which the modelling of individual cells and hypoxia-related parameters have been applied.

The *HYP-RT* model reported on here is based on the biological proliferative hierarchy of epithelial tissue to simulate oxic as well as hypoxic head and neck squamous cell carcinoma evolution. Cell division is tracked throughout growth and fractionated radiotherapy. *HYP-RT* takes into account the reoxygenation process of hypoxic tumours and the increased proliferation caused by accelerated repopulation. Stem cell symmetrical division is applied as the sole mechanism of AR, that is, the division of a stem cell into two daughter stem cells, based on reports of the dominance of this mechanism over other mechanisms such as cell cycle time shortening [8, 25]. A nonspatial approach in this probabilistic model means that cells are considered randomly placed within the tumour which is a justified approach considering that hypoxic tumour cells have been shown in multiple studies to be spatially irregular down to the submillimeter level, for example, in immunohistochemistry studies [26]. Compared to other models in the literature, *HYP-RT* has the benefits of fast computation, a high cell number, simple oxygenation data input in the form of a pO_2 histogram, and the simulation of the combined effects of AR and ROx.

The aim of the current modelling work was to extend the previous hypoxic tumour growth algorithm [27] and simulate conventionally fractionated radiotherapy. Improving the cell data storage and random cell selection aspects of the algorithm was also a goal, so that a full simulation could be completed in less than one hour. It was also important to model a sufficient cell number to surpass the approximate

avascular exponential growth phase (10^6 cells [28]) and reach a cell number approaching clinical levels, that is, 10^8 - 10^9 cells, while achieving statistically stable results ($\leq 5\%$).

This report outlines the methodology of the radiotherapy effect algorithm and discusses the key parameters of the model. Focus is placed on the ROx and AR modules of the algorithm and the effects of varying related parameters during simulations. The model is validated for the oxic tumour case through a comparison with linear quadratic (LQ) theory. The current work builds on a previous detailed description of the original hypoxic tumour growth algorithm [27] and the recently published conventional radiotherapy model outcomes [29] using the default parameters defined in the current report. In the following sections, modelling methods and algorithm design are detailed, along with the validation of modelling AR by means of increasing the stem cell symmetrical division probability and the consequential rise in dose per fraction needed to control the extra cell growth.

2. Methods

2.1. The Tumour Growth Algorithm. Carcinogenesis is initiated through cell division of a single oxic stem cell. Cell proliferation and subsequent tumour progression have been modelled by the continual division of cells into one or two viable daughter cells, with attributes allocated and saved to computer memory in an object vector array referred to as the *cellarray*. The current data storage method differs from the two dimensional array methods previously reported. Methods were modified to allow for more efficient data storage that is 100% memory efficient at the time of tumour growth completion and enhanced efficiency relating to random sampling procedures.

In the model, each element in the *cellarray* represents one cell *object* containing all cellular attributes as well as a *pointer* value indicating the position of the next chronological cell due to divide (the *linked list* method). MC methods are implemented to allow the random nature of the cellular kinetics and the effects of radiation treatment to be simulated using probability distributions. Cellular parameters, such as cell cycle time (CCT) and the cell type, resulting from mother cell division and the differentiation process, are allocated based on random number generation using uniform, normal, or exponential probability distributions and the Ziggurat random number generator [36].

Stem cells (S) first pass through the G0 quiescence phase with an exponential probability of duration and then enter the cell cycle. These cells are considered clonogenic and infinitely proliferating; however they may differentiate upon division or enter state of quiescence induced by low oxygenation. Other types of cells in the model include transit amplifying cells that cycle for a limited number of generations (*T* cells), differentiating cells (*D1* and *D2* cells), as well as fully differentiated cells (*D3* cells). Stem cells may divide into *S*, *T*, or *D1* cells, while transit cells may divide into *D1* or *D2* cells. In normal epithelium, the *D1* cells correspond to those created in the basal layer, while *D2* to those created

TABLE 1: Default parameter values and ranges available in the tumour growth algorithm.

Parameter	Default	References	Comments
<i>Cell total</i>	10^8	N/A	The fully grown tumour cell limit.
<i>Spercent</i> , symmetrical stem cell division probability (%)	3%	N/A	This parameter was set to produce a 1% total stem cell population in the tumour.
Low oxygen limit for cell cycle arrest (mmHg)	1 mmHg	[43, 44]	At this pO_2 level hypoxia-induced quiescence may be initiated.
Percentage of cells exiting the cell cycle (with $pO_2 < 1$ mmHg) (%)	50%	N/A	The total number of hypoxia-induced quiescent cells (< 1 mmHg) = 3% using this parameter value, in line with the pO_2 histogram used.
Tumour cell number threshold for hypoxia	10^6	[6, 7, 28, 45]	Hypoxia is modelled after the cell number is reached by allocating pO_2 from the modelled pO_2 histogram.
Hypoxic cell half life due to necrosis: $pO_2 < 1$ mmHg (days)	4 days	[46, 47]	Due to the 4- to 10-day hypoxic cell lifetime in human colon carcinoma spheroids, and 2 days in xenograft HNSCC.

above the basal layer. The percentages of each cell type in the model were verified as biologically plausible based on experiment epithelial tissue reports and other modelling studies [37–39].

The parameter *Spercent* controls symmetrical stem cell division and represents the probability of a stem cell dividing into two daughter stems cells. This parameter was assigned a default value of 3.0%, which was based on achieving a total stem cell population of approximately 1% [27], a differentiated cell population of approximately 85% [37, 38], and an average tumour doubling time of 50 days [40]. Note that doubling times for tumour of differing oxygenation levels fell within a 35- to 65-day range.

Due to the high percentage (85%) of noncycling cells required to ensure suitable tumour growth rates, the modelled tumours may be roughly equated to mid- to well-differentiated HNSCC disease. This is in contrast to poorly differentiated tumours. However, this distinction is difficult to quantify. The modelling of tumours exhibiting specific levels of differentiation was not a goal of the current work, nor was the interplay between the number of differentiated cells and tumour oxygenation status.

The oxygenation of *oxic* tumours utilises a uniform pO_2 distribution, ranging from 5 to 100 mmHg. These pO_2 limits were set due to 5 mmHg often being used in published clinical trial reports as a hypoxic threshold and due to 100 mmHg [41] being the highest value measured experimentally in HNSCC Eppendorf studies. To model a biologically relevant range of tumour cell pO_2 values for head and tumours, normalised data from Eppendorf studies [5, 41, 42] were implemented using a log-normal function and a random number algorithm written by J. Filliben (1982).

Tumour growth parameters values were set using biological data from the literature (e.g., oxygen distribution). If this was not possible, the model was used to explore the relative effects of certain parameters on other variables and parameters during the growth and treatment process (e.g., ROx increment size during radiotherapy). Key growth-related parameters and associated references are presented in Table 1.

TABLE 2: Tumour oxygenation histogram data for the three modelled oxygenation levels, indicating the modelled percentage of cells in four commonly reported pO_2 ranges.

pO_2 range (mmHg)	Oxic (%)	Moderately hypoxic (%)	Severely hypoxic (%)
0 to 2	2.1	7.3	9.4
0 to 5	5.2	22.1	33.2
0 to 10	10.4	45.6	54.5
0 to 20	20.8	65.4	69.6

To implement tumour hypoxia, a pO_2 probability distribution is used to allocate values to daughter cells. For a mother cell producing only one cell, the mother cell pO_2 is passed to the daughter cell. When two daughter cells are generated, one cell is randomly chosen to retain the mother cell pO_2 and the other receives a new pO_2 value from the distribution.

The first hypoxic pO_2 distribution modelled is named moderate hypoxia. A second pO_2 distribution representing a tumour with more severe hypoxia is also modelled. The severe hypoxia pO_2 distribution is generated to achieve a relatively high number of cells in the low pO_2 range (< 10 mmHg) compared to moderate hypoxia and is tested in the model for the impact on tumour growth rate. Distributions with a higher ($> 3\%$) percentage of cells below 1 mmHg result in tumours that are too hypoxic and result in tumour shrinkage instead of growth. Both pO_2 distributions along with published data are shown in Figure 1(a). Numeric histogram data for published versus modelled percentages of cells in different pO_2 ranges are presented in Figure 1(b) and Table 2.

Cellular pO_2 influences CCT [43, 48], implemented using an exponential function to slow the cell cycle with decreasing pO_2 . To account for the effects cell quiescence due to very low oxygenation, a threshold value of 1.0 mmHg is applied. These quiescent cells then die with a half life value of 4 days unless subsequently reoxygenated. As some cells have

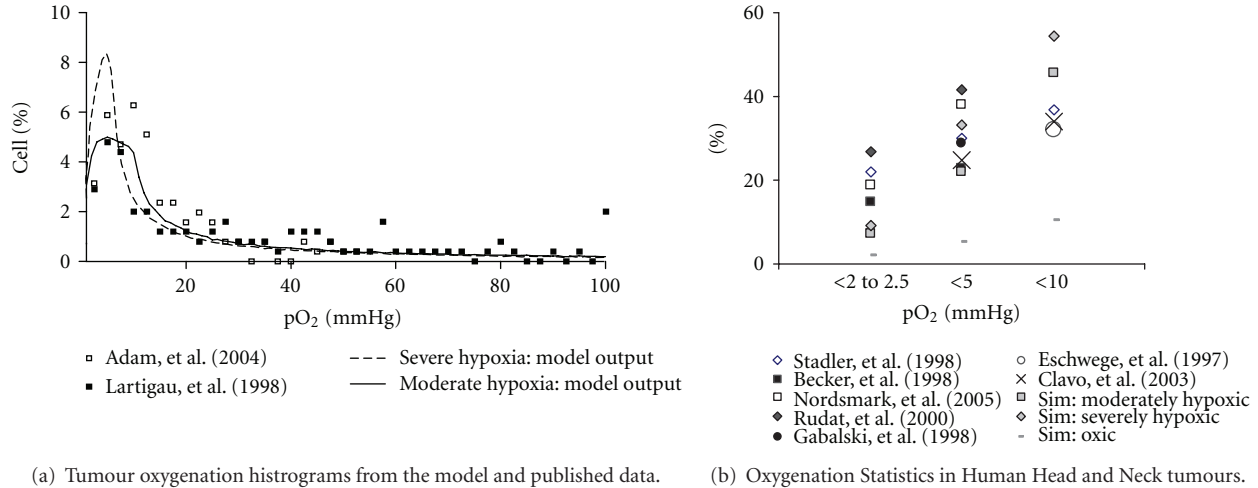


FIGURE 1: The distribution of tumour oxygen levels used (a) to simulate moderate and severe tumour and (b) in simulations (sim) compared to published data for three oxygenation ranges [4, 30–35]. The distributions in (a) represent the pO_2 histogram outputs from the model using a log-normal random number generator.

been shown experimentally to continue cycling even at very low oxygenation levels through anaerobic metabolism, only a percentage of cells with pO_2 of less than 1 mmHg are made quiescent. The percentage for this parameter was determined by trial and error and ensuring that the total population of cells with this very low oxygenation corresponded with the log-normal pO_2 distribution at the 0 to 1 mmHg level (3%).

An analysis of the growth algorithm was performed to analyse the effects of the symmetrical stem cell division probability (*Spercent*) on tumour growth rate (doubling time, T_D) and total growth time. This was carried out for oxic and hypoxic tumours, with the cell types in the population being validated. All of the current modelling work was programmed in the FORTRAN95 programming language within the Microsoft Visual Studio framework (2003).

2.2. The Radiotherapy Algorithm. The radiotherapy algorithm was developed to simulate the effects of fractionated therapy, assuming that a uniform dose is delivered to all cells. LQ theory is used to define the average cycling cell survival probability using the standard surviving fraction (SF) equation based on alpha and beta parameters. This is calculated for each cell individually for each dose fraction in the schedule. For example, using alpha and beta values of 0.3 and 0.03, respectively ($\alpha/\beta = 10$ Gy), and a standard 2 Gy per day treatment schedule, the SF value is 48.7%. However, this calculation is adjusted for the individual cell based on the cellular pO_2 . The adjustment is based on the oxygen enhancement ratio (OER) (1), which is implemented in the program by normalising the OER curve to a maximum value of one at 60 mmHg [49]:

$$\text{OER} = \frac{1 + 0.81(pO_2^{0.616})}{(1 + 0.324 pO_2^{0.616})}. \quad (1)$$

For each fraction, all cells in the *cellarray* are chronologically assessed to determine if they will survive or die. Figure 2 represents the relationship between (a) OER and pO_2 (mmHg) and (b) probability of lethality and pO_2 (mmHg) used in the model. Note that the effect of the actual dose being delivered is not shown in Figure 2, only the influence of pO_2 on cell death when a specific dose per fraction is applied [50, 51].

To model the gradual rise in tumour oxygenation during treatment, pO_2 increments (3 mmHg) are distributed to the cell population at set time intervals. During reoxygenation events, a percentage of cells have their pO_2 values increased by one or more pO_2 increments, that is, by 0, 3, 6, 9, or 12 mmHg. Events are set to occur a few hours after each treatment fraction (default value of 4 hours [44]). The number of cells randomly chosen to receive the various increases in pO_2 is based on Binomial theory (2):

$$P_k = \binom{n}{k} p^k (1-p)^{n-k}, \quad (2)$$

where n is the total number of oxygen increments (equal to the number of cells in the population at the current time), k is the number of pO_2 increments applied to a cell, and P_k is the probability of a cell receiving a $k \times 3$ mmHg increase in pO_2 . The probability of five or more increments is below 0.5% and regarded as negligible.

Default parameters in the ROx algorithm were set through observation of the rate at which hypoxia-induced quiescent cells were brought back into the cell cycle and the rate of change of the resulting pO_2 histograms from the cycling cell population. Oxygen increment size was set by default to ensure that tumours shrink to between 10^5 and 10^6 cells (1 mm in diameter) with a final pO_2 histogram resembling a uniform *oxic* distribution with all pO_2 values ≥ 5 mmHg.

Cells assigned to quiescence due to hypoxia ($pO_2 < 1$ mmHg) have a probability of having their pO_2 levels

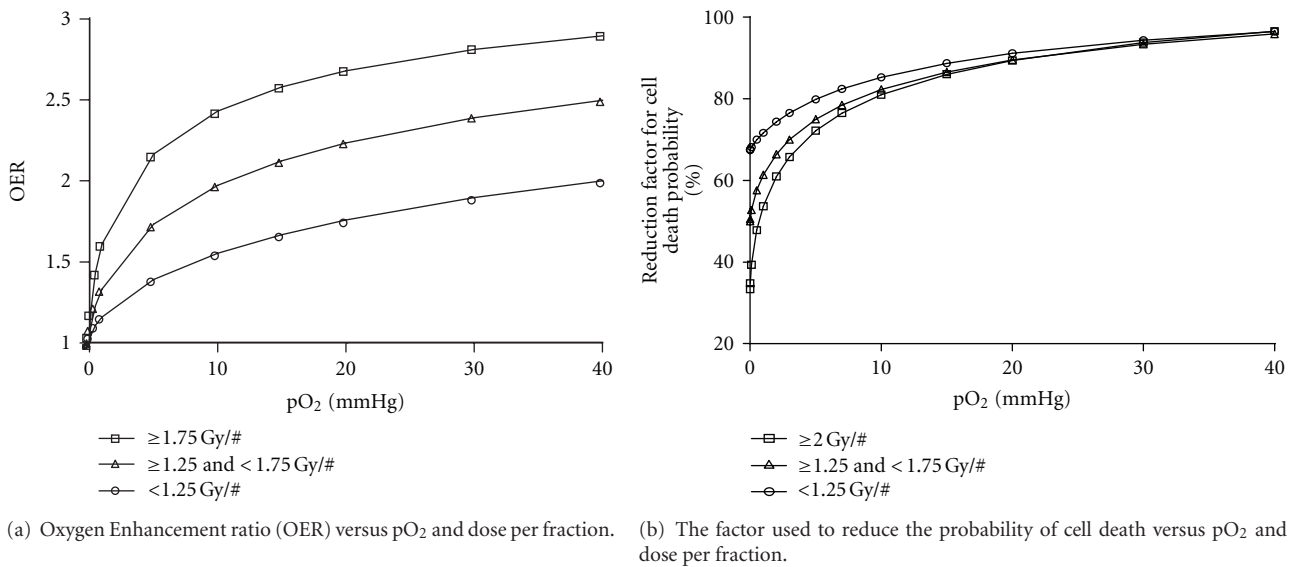


FIGURE 2: (a) Oxygen Enhancement Ratio (OER) curves implemented in the model for adjusting the radiosensitivity of cells during radiotherapy, based on cellular pO₂ and dose per fraction, and (b) conversion of the OER curves into a probability of cell death factor, through OER curve normalisation.

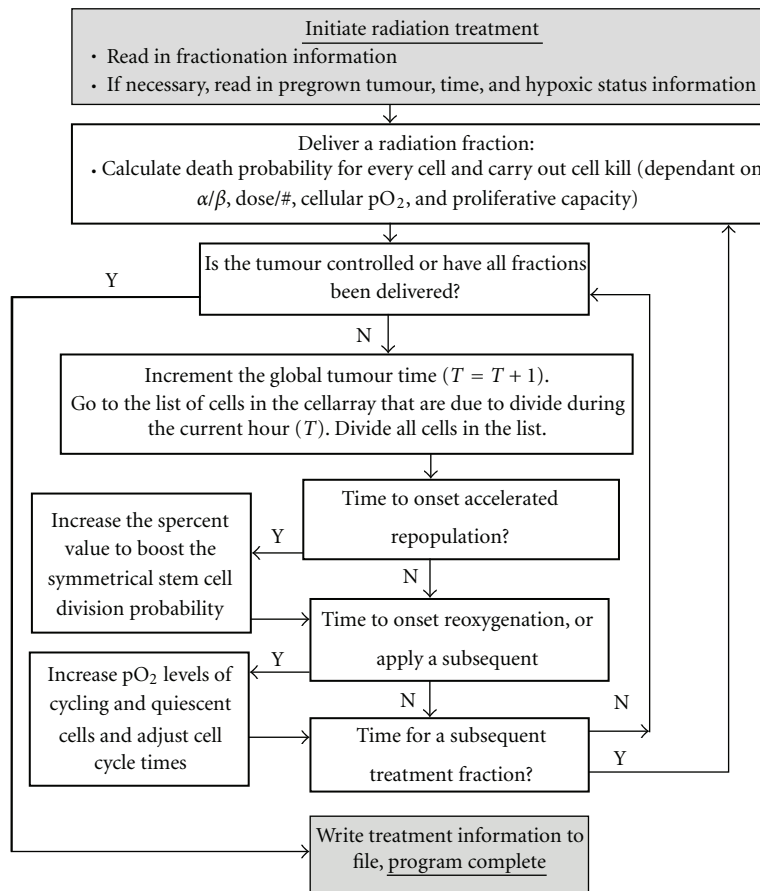


FIGURE 3: A flow diagram of the fractionated radiotherapy algorithm, where initiation of treatment is followed by continual cell proliferation between dose fractions.

TABLE 3: A list of model parameters used in the fractionated radiotherapy algorithm.

Parameter	Default	References	Comments
Accelerated repopulation (AR)—time of onset after initialisation during RT (weeks)	No onset	[8, 10–12, 25, 53–55]	The number of weeks into RT that AR is onset, 2–4 weeks observed in literature; however 0 week onset has been made possible for modelling microscopic response in a small tumour system.
Reoxygenation (ROx)—time of onset after initialisation during RT (weeks)	No onset	N/A	An extremely variable parameter and open to user input.
Time of ROx after a particular RT fraction (weeks)	4 hours	[44]	
<i>AR boost factor</i>	$\times 10$	[23, 25, 40]	The factor applied to increase the symmetrical stem cell division probability during AR.
ROx-induced incremental increases in pO_2 (mmHg)	3 mmHg	N/A	The pO_2 increment size during randomised reoxygenation after an RT fraction (linearly SF dependent), set to obtain full oxygenation by ~ 1 to 2 mm tumour diameter.
ROx percentage of the very low oxygenated cell population (%)	60%	N/A	The percentage of hypoxia-induced quiescent cells brought back into the cell cycle upon ROx after an RT fraction (linearly SF dependent), set to obtain full oxygenation when the tumour has reduced to 10^5 to 10^6 cells (from 10^8 initial cells).
Alpha (LQ model) Gy^{-1}	0.3	[56, 57]	Used in SF calculations (linear quadratic equation).
Beta (LQ model) Gy^{-2}	0.03		Used in SF calculations (linear quadratic equation).
Noncycling cell radiosensitivity compared to oxic cycling cells	0.5	[58, 59]	Factor for the decreased radiosensitivity of noncycling cells, based on the likely increase in resistance of cells in resting phase (transit cells and stems cells however assumed to be equally radiosensitive in tumour cells).

increased using a parameter to control the percentage of cells to be retrieved from the quiescent group and reentered into the *cellarray* that stores the cycling cells.

Accelerated repopulation is modelled by increasing the *Spercent* variable by a multiplicative factor (the *AR boost factor*) to simulate rapid tumour regrowth. As the range of possible onset times of AR varies in literature reports, a range of 0 to 3 weeks is analysed. This time range covers the possibility of immediate cell response as well as the latest onset time to have effect on total dose outcomes in the model.

The default *AR boost factor* is based on a study of the extradose required to kill the cells that exist due to AR. When simulating no AR effects in oxic tumours 30×2 Gy (6 weeks of treatment) is required to control a tumour, therefore for all AR- and ROx-related simulations the effects of AR are calculated using 6 weeks at the iso-effect total treatment time. The duration of treatment for total cell kill was then compared to the 6-week standard time and the extradose per fraction required calculated for each simulation. Note that

the extradose per fraction applies only during the weeks in which AR is occurring. The extra dose per fraction, d , is calculated using standard biological equivalent dose theory (3):

$$BED = nd \left(1 + \frac{d\alpha}{\beta} \right), \quad (3)$$

where BED is the total dose required from simulations to kill all cells after onset of AR, $\alpha/\beta = 10$ Gy, and n is the number of fractions for which AR is applied [52]. The default irradiation schedule used in the treatment module for this work is the conventional 2 Gy per day, 5 day per week dose schedule. Figure 3 outlines the flow of the radiotherapy algorithm. The key parameters utilised in the model to simulate ROx and AR during radiotherapy are outlined in Table 3.

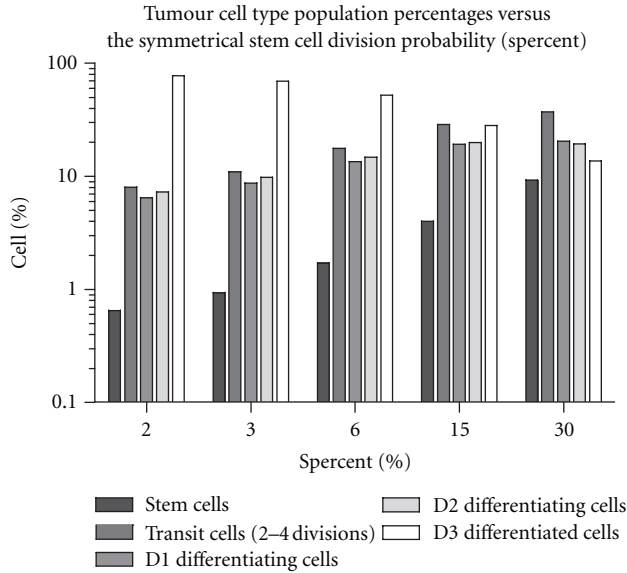


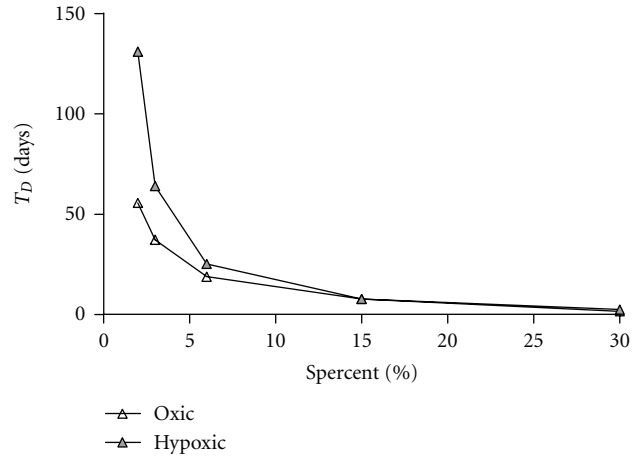
FIGURE 4: The average percentage of cell types within simulated tumours of 10^8 cells, where (a) the symmetrical stem cell division probability parameter, *Spercent*, has been varied from 2 to 30% (standard deviation $<1\%$).

3. Results

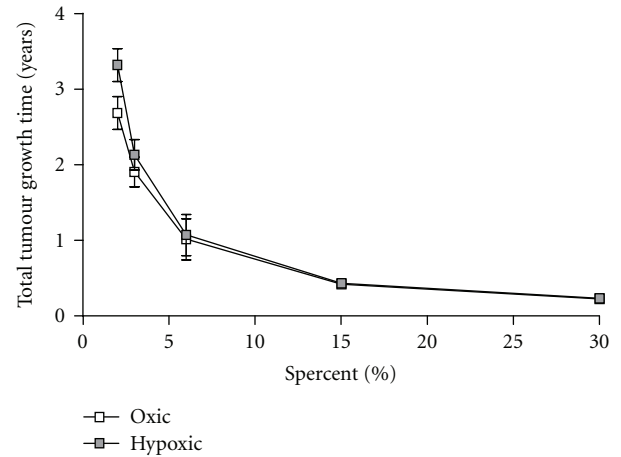
All tumour growth simulation results apply to 10^8 cell virtual tumours. The results summarise the impact of the *Spercent* parameter on growth rate and cell types percentage and verify that the modelling of hypoxia does not change the cell population structure, as intended. Treatment results relate to verification of the default *AR boost factor* for different AR onset times for both oxic and hypoxic tumours. Hypoxic tumour results are also presented for simulations varying the hypoxia-induced quiescent cell death half-life. Note that it may be possible for tumour cell of any proliferative capacity to avoid radiation cell kill due to hypoxia and become reoxygenated after treatment, contributing to local tumour recurrence. Moreover, hypoxia may cause mutations in the tumour cell population including dedifferentiation which may result in more aggressive tumour growth [60, 61]. Consequently, although survival of only the stem cells is traditionally considered to result in treatment failure, the number of fractions required to kill all stem, transit, and first-generation differentiating cells is presented.

Hypoxic tumour radiotherapy results use the moderately hypoxic pO_2 distribution shown in Figure 1(a). Severely hypoxic tumours with a higher number of cells in the 0 to 10 mmHg range were also modelled, but results did not differ significantly from moderately hypoxic results. This issue will be investigated in future work to discern the necessary change in the shape of the pO_2 curve (peak width and peak height) required to obtain statistically different outcomes for very hypoxic tumours.

3.1. *Tumour Growth Analysis and Algorithm Efficiency.* The constituent tumour cell population and the dependence of



(a) Oxic vs. moderately hypoxic tumour doubling time (T_D) versus the symmetrical stem cell division probability (*Spercent*).



(b) Oxic vs. moderately hypoxic tumour total growth time (10^8 cells) versus the symmetrical stem cell division probability (*Spercent*).

FIGURE 5: (a) The doubling time (T_D), and (b) the total tumour growth times, versus the symmetrical stem cell division probability (*Spercent*) ranging from 2 to 30% for oxic and moderately hypoxic simulations of tumour growth up to 10^8 cells. In Figure (a) the size of the error bars are negligible.

cell type percentage on the *Spercent* parameter are shown in Figure 4. The default value used for the *Spercent* parameter (3%) results in a distribution of cell types that closely match literature reports and a realistic statistically stable tumour growth rate after 10^4 cells [38, 40, 62]. The tumour growth characteristics for oxic and hypoxic tumours are displayed in Figures 5(a) and 5(b). These tumour growth times (for a small 0.5 to 1.0 cm diameter tumour mass) agree with reported values of T_D for head and neck cancers [40]. Note that hypoxia-related parameters are set to maintain the distribution of cell types in the tumour throughout growth. Experimental data relating to how the cell percentages change when tumours are in a hypoxic state is difficult to obtain; therefore this effect has not been considered.

The *linked list* method of data storage allows for flexible and efficient cell data storage and enables 10^8 cells to be

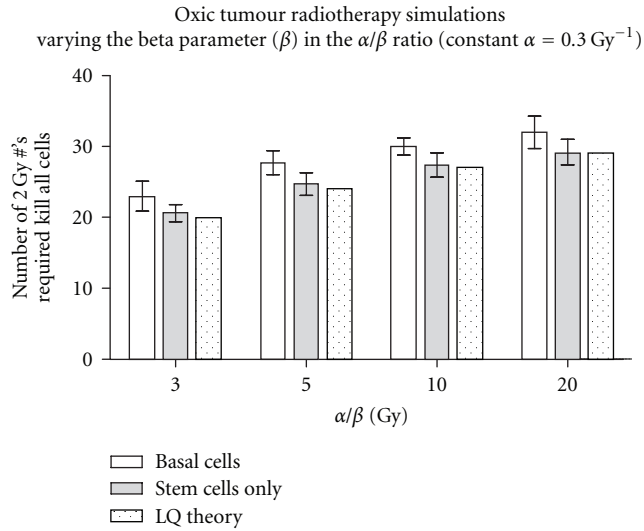


FIGURE 6: Comparison of the number of 2 Gy fractions required in the HYP-RT model to kill all basal or all stem cells compared to the linear quadratic (LQ) model (the first fraction that achieves <1.000 cells remaining), for oxic tumour conventional radiotherapy.

propagated on a standard off-the-shelf computer. For oxic tumour growth simulations the average computation time is now less than fifteen minutes. For hypoxic tumours this may be extended up to thirty minutes. Total tumour growth times increase for hypoxic tumours due to the extracellular death and therefore a longer time was required to propagate cells up to an equivalent tumour volume. Treatment-related parameters, especially the *Spercent* and *AR boost factor*, also alter the computation time because of their impact on stem cell exponential growth and the reduction in (non-cycling) cells.

3.2. The Dependence of Cell Kill on the Alpha/Beta Ratio. The default α/β value in the model is 10 Gy. However, results for a range of α/β values help to verify that the model predicts the same level of cell kill as LQ theory for oxic tumours (Figure 6). In the comparison, α values were held constant (0.3 Gy^{-1}) while the beta value was varied (from 0.1 to 0.015 Gy^{-2}), producing α/β values in the range of 3 to 20 Gy. For this analysis basal cell elimination as well as the elimination of stem cells only is considered. The stem cell simulation results are in good agreement with the LQ model, while results involving the cell kill of all basal cells are on average 2 to 3 fractions higher.

3.3. Oxic Tumour Radiotherapy. A factor is used in HYP-RT to increase the stem cell symmetrical division probability to model accelerated repopulation (the AR boost factor). To determine the most plausible AR boost factor, the onset times of AR are varied from 3% to 15% and from 0 to 3 weeks, respectively, and the consequential extra dose per fraction is required to account for the extracellular growth calculated (Figure 7). Note that the increases in doses per fraction

shown in Figure 7 apply during the period of AR only therefore the week of AR onset is not a critical parameter.

An *AR boost factor* value of 10 results in an extra dose between 0.5 and 0.8 Gy per fraction, which is consistent with clinical trial reports [8, 63, 64]. An *AR boost factor* less than 10 increases the dose per fraction by 0.3 Gy or less, while an *AR boost factor* more than 10 results in an extra dose per fraction above 1.0 Gy. An *AR boost factor* of 10 was intuitively expected to impact on tumour response in a biologically plausible manner, as there have been reported increases in tumour growth rate of up to 10 times (reducing the potential doubling time (T_{pot}) from approximately 10 to 20 days down to as low as 2 days [8, 65], approaching the stem cell division time.

An *AR boost factor* of 10 decreases the tumour doubling time after the onset of AR; for example, for moderately hypoxic tumours the tumour doubling time decreases from 65 days down to 4.4 days after the onset of AR. Similarly for oxic tumours, doubling times decrease from 37 days down to 3.7 days after the onset of AR (all standard deviation errors <1 day). For moderately hypoxic tumours these doubling times have good agreement with HNSCC published data [8].

3.4. Hypoxic Tumour Radiotherapy. Interfraction pO_2 histograms for a reoxygenating tumour are shown in Figure 8. ROx events are initiated in simulations after the first dose fraction in this example, with full ROx occurring by fraction 11. The model smoothly moves the peak of the histogram curve to the right-hand side, to higher average pO_2 levels, simulating gradual ROx in the tumour, as desired.

Cells exhibiting very low oxygenation ($\text{pO}_2 < 1 \text{ mmHg}$) levels enter a hypoxia-induced quiescent state. The modelled half-life of cells in this state does not impact significantly on the number of fractions required to control the tumour; however it does alter the timing of full ROx. Figure 9 shows the impact of the hypoxic cell half life on cell kill and full ROx timing when varied from 2 to 6 days.

The timing of ROx applied after completion of each fraction of conventional therapy was analysed for the impact on the total dose required to kill all cells. No significant difference was found between applying ROx either 4 or 23 hours (just preceding the next daily fraction) after a fraction. This result is expected since only conventional treatments were simulated in this study, with 24 hours between fractions. However, for future simulation work involving alternate schedules (hyperfractionated schedules with less than 2 Gy per fraction), this may change since ROx may occur during or after the next, same day fraction.

The effects of AR on the dose per fraction required to maintain total treatment times for hypoxic tumours were also studied. During these calculations, 8 weeks is used for the standard treatment time, as this is the treatment time required in hypoxic tumour simulations with no AR considered. The increase in dose per fraction (above the standard 2.0 Gy) is 0.5 to 0.9 Gy using an *AR boost factor* of 10 (Figure 10), closely matching oxic tumour results. The dose per fraction required during AR to control the extracellular growth is relatively consistent for different AR onset times

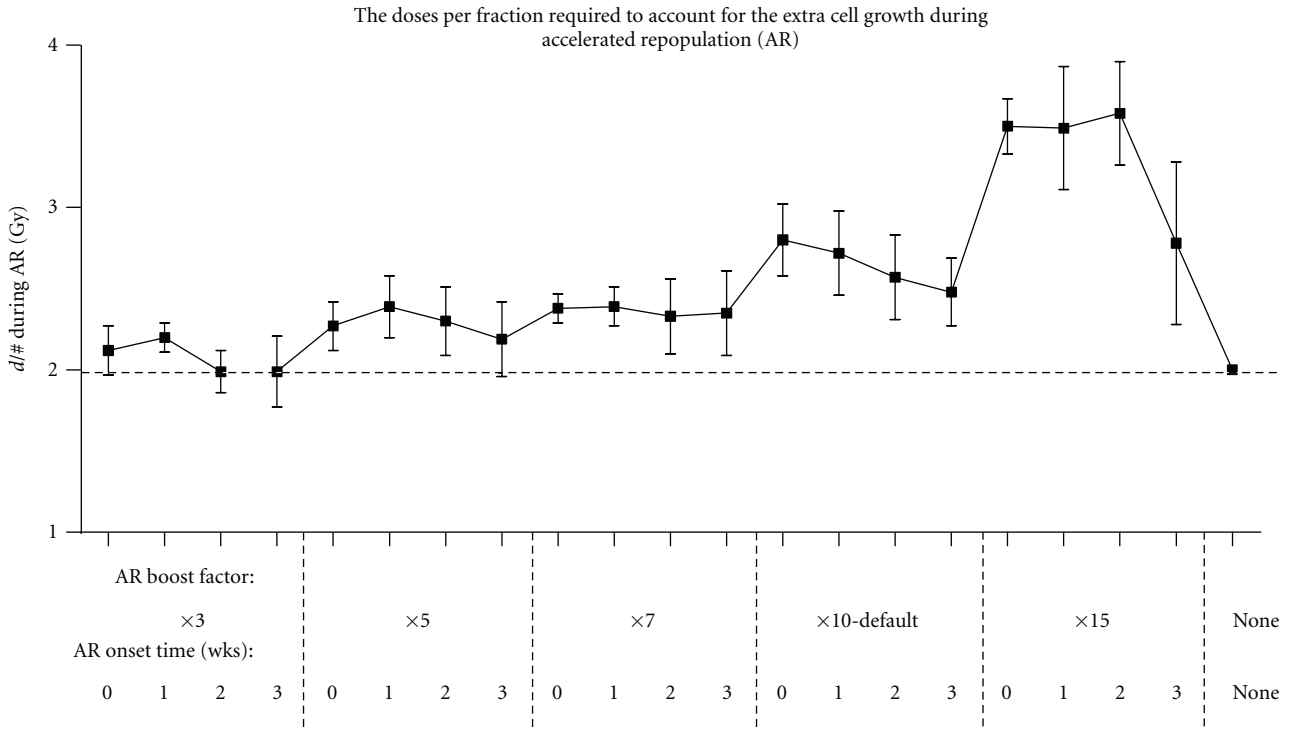


FIGURE 7: The increase in dose per fraction ($d/\#$) required during conventional radiotherapy of oxic tumours to account for accelerated repopulation (AR), assuming a fixed total treatment time of 6 weeks and the increase in $d/\#$ coinciding with the onset of AR.

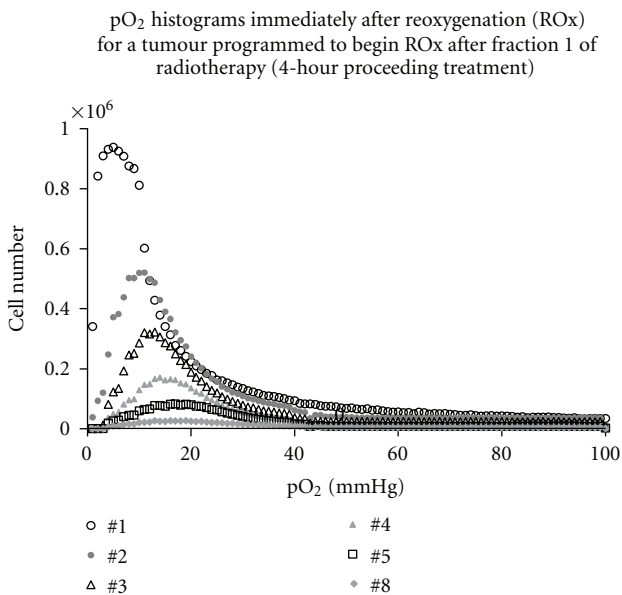


FIGURE 8: Oxygenation (pO_2) histograms after each fraction of simulated conventional radiotherapy, ranging from fractions 1 to 8 of a moderately hypoxic tumour. In this example, treatment is initiated when the tumour population has reached 10^8 cells and hypoxic quiescent cells are reoxygenated above 1 mmHg by fraction number 11 (5×10^6 cells) and above 5 mmHg by fraction 20 (5×10^5 cells).

(as it is in the oxic tumour study), because the dose increase only applies *after* AR onset. With ROx simultaneously considered, the dose per fraction reduces slightly but is still approximately an extra 0.5 Gy per fraction.

An *AR boost factor* of 10 is considered the most valid value for this parameter based not only on the dose per fraction study but also according to the decrease in tumour doubling times predicted by the model; for example, the tumour doubling time reduced to 1 to 5 days after onset of AR compared with 35 to 65 days before onset of AR, with the range depending on oxygenation status.

These results also indicate that the onset time of AR is likely to be ≤ 2 weeks if ROx occurs at ≤ 2 weeks. However, the onset time of AR could be >2 weeks if ROx also occurs late or not at all (based on dose per fraction increases within 0.5 to 1.0 Gy). Note that in all text and figures, error bars represent standard deviations based on nine simulations per parameter set. The statistical software package Prism 5 (v5.02, *GraphPad Software Inc.*) and Microsoft Excel 2003 were used in the analysis of the data.

4. Discussion

Onset times of ROx may be varied in the model from zero (immediately after treatment initiation) to three weeks. Immediate ROx is biologically possible because of the reduced demand of oxygen arising from the death of the

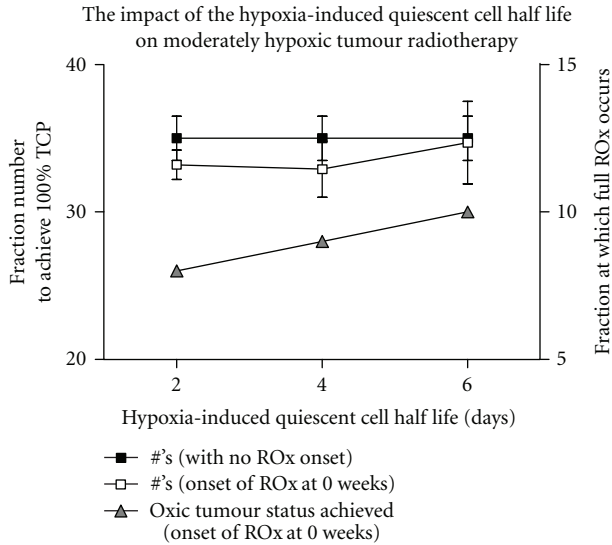


FIGURE 9: A comparison of the average number of conventional radiotherapy fractions with simulated reoxygenation (ROx) with no accelerated repopulation, required for cell kill of moderately hypoxic tumours when varying the half life of hypoxic quiescent cells.

first lethally hit cells (some hours after the first fraction). Variability of onset of ROx occurs because of other considerations such as the structure of the vascular and supporting tissues of the tumour and the dynamics of dead cell clearance from the tumour mass. All of these factors are likely to vary among patients, making the prediction of onset time of ROx for a particular tumour especially challenging. The timing of ROx events after each treatment fraction does not impact on the final cell kill results for the simulated conventional treatments in this study beyond the statistical error of the algorithm. The impact was not expected to be significant because all ROx events were programmed to occur before the next daily fraction.

ROx is ideally modelled continuously throughout tumour shrinkage. Modelling increases to cellular pO_2 levels at every hour of the radiotherapy regimen is computationally exhaustive; therefore as a compromise, ROx events are modelled after every daily dose fraction. Ideally, modelling of ROx would also be based on human pre- and midtreatment tumour oxygenation assay or imaging data, for example, PET, CT, MRI, or US imaging methods; however such data is not readily available for every patient. In the future more data of this kind may become available through research efforts including stratification of patients in clinical trials investigating tumour oxygenation dynamics. Trial outcomes would be very useful for radiobiological modelling of tumour treatment response; however they may never be able to predict individual tumour oxygenation behavior for a specific patient. At this stage, the model can provide quantitative information about the relative importance of hypoxia and reoxygenation during radiotherapy. Results highlight the need to pursue research into techniques for noninvasively and efficiently collecting individual tumour data for input into oxygenation specific models.

Modelling the onset time of AR as early as zero weeks is based on the hypothesis that the microscopic response of tumour cell injury may start after the first radiative damage event. This somewhat contradicts reports based on clinical trial data of AR onset or kick-off times in the order of 2 to 5 weeks [8, 9, 11, 55, 65]. However, these reports are based on large patient averages of total treatment time effects and results of which are not necessarily representative of when AR is initiated at the microscopic level. Like ROx, AR onset times are likely to vary from patient to patient; thus for this study a range of onset times of 0 to 3 weeks is used.

Due to the complexity of biological factors required in the model, it was necessary to make a number of assumptions/limitations. The reduction of the cell cycle time as an AR mechanism has been shown to have a significant but relatively small effect on tumour response; however this was not modelled. It is likely that a number of these mechanisms are induced together and are more significant if used in combination [8, 25, 65, 66]. Abortive division of sterilised stem cells (rather than differentiating) may also contribute to repopulation of tissue after irradiation [67]. However, these effects are not as well understood, with limited studies in the literature.

The radiotherapy effect algorithm does not take into account repair of radiation-induced cell damage; however the modelling of cellular repair will be considered in future work. Spatial information of the tumour cells was not taken into account; however this was not a hindrance to the current results which are concerned with homogeneous dose delivery. For future spatial dose delivery application, such as IMRT or dose painting, the modelling of specific hypoxic subvolumes of hypoxia will be a necessary addition to the model.

HYP-RT modelling methods vary from other recent stochastic hypoxia and radiotherapy modelling methods, involving individual cells or cell groups [20, 24, 68], because the tumour oxygenation data required is simple and easily input in the form of a pO_2 histogram. The pO_2 histogram may also be manipulated during tumour growth (or treatment) if required to model dynamic oxygenation effects.

Current issues with this model and other models of this kind include the requirement of data gained through methods that are invasive for the patient; however this is improving as imaging techniques and associated marker drugs are being researched and trialled.

Possible current uses for the model include the study of cellular kinetic mechanisms and observations of (i) the relative differences in total doses required when AR and ROx are onset at various times, (ii) the differences in the total doses required for tumours of varying oxygenation levels, and (iii) the prediction of the effects of treatment breaks on the extradose required to compensate for the break.

5. Conclusion

Due to the complexities and dynamic nature of tumour oxygen and reoxygenation during radiotherapy, MC methods remain the most comprehensive and simplistic way of

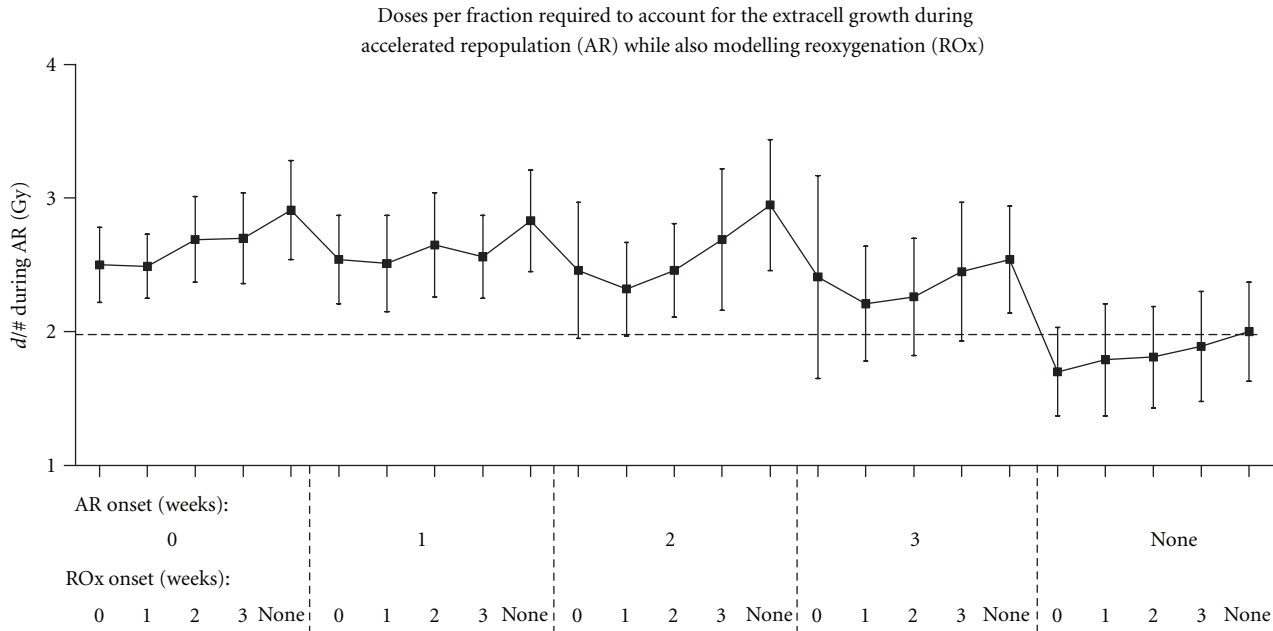


FIGURE 10: The increase in dose per fraction ($d/\#$) required during conventional radiotherapy of moderately hypoxic tumours to account for accelerated repopulation (AR), assuming a fixed total treatment time of 8 weeks and the increase in $d/\#$ coinciding with the onset of AR, for various onset times of AR and ROx.

incorporating hypoxia into a tumour model. The *HYP-RT* model builds upon previous tumour growth modelling work and is capable of modelling radiation cell kill for tumours comprised of up to 10^8 individual cells. Computational and temporal efficiency has been improved compared to previous model versions, with better use of memory space and more efficient selection and allocation of randomised parameters. Simulations of tumour growth and radiotherapy treatment can be performed in approximately thirty minutes or less. The way in which tumour hypoxia has been modelled is simple yet specific, enabling individual tumour data input in the form of a pretreatment pO_2 histogram.

The reoxygenation algorithm provides a method of gradually altering the initially hypoxic tumour oxygenation histogram throughout treatment, to model the process of oxygenation increase for a hypoxic tumour. The accelerated repopulation algorithm provides a method of increasing the cell propagation rate, using a parameter that increases the symmetrical stem cell division probability, with a factor of ten found to be most suitable value based on a study involving the increase in dose per fraction required to kill the extracell growth during conventional radiotherapy.

Future aims include efficiently modelling 10^9 cell virtual tumours to provide an even larger individual cell-based model and the conversion of the code into the more modern C++ programming language. The model has already been used to explore the conventional radiotherapy schedule for hypoxic tumours [29] and will be reported on in the near future regarding alternate radiation regimens for tumours of different oxygenation levels.

Acknowledgments

The authors would like to thank Dr. Loredana Marcu and Dr. Damien Phillips, for theoretical radiobiology and code development assistance during this work.

References

- [1] D. M. Brizel, R. K. Dodge, R. W. Clough, and M. W. Dewhirst, "Oxygenation of head and neck cancer: changes during radiotherapy and impact on treatment outcome," *Radiotherapy and Oncology*, vol. 53, no. 2, pp. 113–117, 1999.
- [2] M. Nordmark and J. Overgaard, "Tumor hypoxia is independent of hemoglobin and prognostic for loco-regional tumor control after primary radiotherapy in advanced head and neck cancer," *Acta Oncologica*, vol. 43, no. 4, pp. 396–403, 2004.
- [3] P. Stadler, A. Becker, H. J. Feldmann et al., "Influence of the hypoxic subvolume on the survival of patients with head and neck cancer," *International Journal of Radiation Oncology Biology Physics*, vol. 44, no. 4, pp. 749–754, 1999.
- [4] M. Nordmark, S. M. Bentzen, V. Rudat et al., "Prognostic value of tumor oxygenation in 397 head and neck tumors after primary radiation therapy. An international multi-center study," *Radiotherapy and Oncology*, vol. 77, no. 1, pp. 18–24, 2005.
- [5] M. F. Adam, E. C. Gabalski, D. A. Bloch et al., "Tissue oxygen distribution in head and neck cancer patients," *Head & Neck*, vol. 21, no. 2, pp. 146–53, 1999.
- [6] C. J. Conti, "Vascular endothelial growth factor: regulation in the mouse skin carcinogenesis model and use in antiangiogenesis cancer therapy," *Oncologist*, vol. 7, supplement 3, pp. 4–11, 2002.

- [7] J. A. Stanley, W. U. Shipley, and G. G. Steel, "Influence of tumour size on hypoxic fraction and therapeutic sensitivity of Lewis lung tumour," *British Journal of Cancer*, vol. 36, no. 1, pp. 105–113, 1977.
- [8] H. R. Withers, J. M. G. Taylor, and B. Maciejewski, "The hazard of accelerated tumor clonogen repopulation during radiotherapy," *Acta Oncologica*, vol. 27, no. 2, pp. 131–146, 1988.
- [9] D. J. Brenner, "Accelerated repopulation during radiotherapy: quantitative evidence for delayed onset," *Radiation Oncology Investigations*, vol. 1, no. 3, pp. 167–172, 1993.
- [10] B. Maciejewski, H. R. Withers, J. M. G. Taylor, and A. Hliniak, "Dose fractionation and regeneration in radiotherapy for cancer of the oral cavity and oropharynx: tumor dose-response and repopulation," *International Journal of Radiation Oncology Biology Physics*, vol. 16, no. 3, pp. 831–843, 1989.
- [11] L. J. Peters and H. R. Withers, "Applying radiobiological principles to combined modality treatment of head and neck cancer—the time factor," *International Journal of Radiation Oncology Biology Physics*, vol. 39, no. 4, pp. 831–836, 1997.
- [12] K. R. Trott, "The mechanisms of acceleration of repopulation in squamous epithelia during daily irradiation," *Acta Oncologica*, vol. 38, no. 2, pp. 153–157, 1999.
- [13] C. E. Donaghey, "CELLSIM and CELLGROW: tools for cell kinetic modeling," *ISA Transactions*, vol. 22, no. 4, pp. 21–24, 1983.
- [14] W. Duchting, T. Ginsberg, and W. Ulmer, "Modeling of radiogenic responses induced by fractionated irradiation in malignant and normal tissue," *Stem Cells*, vol. 13, supplement 1, pp. 301–306, 1995.
- [15] W. Duchting, W. Ulmer, R. Lehrig, T. Ginsberg, and E. Dedeleit, "Computer simulation and modelling of tumor spheroid growth and their relevance for optimization of fractionated radiotherapy," *Strahlentherapie und Onkologie*, vol. 168, no. 6, pp. 354–360, 1992.
- [16] W. Duchting and T. Vogelsaenger, "Three-dimensional pattern generation applied to spheroidal tumor growth in a nutrient medium," *International Journal of Bio-Medical Computing*, vol. 12, no. 5, pp. 377–392, 1981.
- [17] W. Duchting and Vogelsaenger Th., "Recent progress in modelling and simulation of three-dimensional tumor growth and treatment," *BioSystems*, vol. 18, no. 1, pp. 79–91, 1985.
- [18] K. Borkenstein, S. Levegrün, and P. Peschke, "Modeling and computer simulations of tumor growth and tumor response to radiotherapy," *Radiation Research*, vol. 162, no. 1, pp. 71–83, 2004.
- [19] D. D. Dionysiou, G. S. Stamatakos, N. K. Uzunoglu, K. S. Nikita, and A. Marioli, "A four-dimensional simulation model of tumour response to radiotherapy in vivo: parametric validation considering radiosensitivity, genetic profile and fractionation," *Journal of Theoretical Biology*, vol. 230, no. 1, pp. 1–20, 2004.
- [20] C. Harting, P. Peschke, K. Borkenstein, and C. P. Karger, "Single-cell-based computer simulation of the oxygen-dependent tumour response to irradiation," *Physics in Medicine and Biology*, vol. 52, no. 16, pp. 4775–4789, 2007.
- [21] M. Kocher, H. Treuer, J. Voges, M. Hoevens, V. Sturm, and R. P. Müller, "Computer simulation of cytotoxic and vascular effects of radiosurgery in solid and necrotic brain metastases," *Radiotherapy and Oncology*, vol. 54, no. 2, pp. 149–156, 2000.
- [22] G. S. Stamatakos, E. I. Zacharaki, M. I. Makropoulou et al., "Modeling tumor growth and irradiation response in vitro—a combination of high-performance computing and web-based technologies including VRML visualization," *IEEE Transactions on Information Technology in Biomedicine*, vol. 5, no. 4, pp. 279–289, 2001.
- [23] L. Marcu, T. van Doorn, S. Zavgorodni, and I. Olver, "Growth of a virtual tumour using probabilistic methods of cell generation," *Australasian Physical and Engineering Sciences in Medicine*, vol. 25, no. 4, pp. 155–161, 2002.
- [24] B. Titz and R. Jeraj, "An imaging-based tumour growth and treatment response model: investigating the effect of tumour oxygenation on radiation therapy response," *Physics in Medicine and Biology*, vol. 53, no. 17, pp. 4471–4488, 2008.
- [25] L. Marcu, T. van Doorn, and I. Olver, "Modelling of post-irradiation accelerated repopulation in squamous cell carcinomas," *Physics in Medicine and Biology*, vol. 49, no. 16, pp. 3767–3779, 2004.
- [26] A. S. E. Ljungkvist, J. Bussink, J. H. A. M. Kaanders, N. E. Wiedenmann, R. Vlasman, and A. J. Van Der Kogel, "Dynamics of hypoxia, proliferation and apoptosis after irradiation in a murine tumor model," *Radiation Research*, vol. 165, no. 3, pp. 326–336, 2006.
- [27] W. M. Tuckwell, E. K. Bezak, E. Yeoh, and L. Marcu, "Efficient Monte Carlo modelling of individual tumour cell propagation for hypoxic head and neck cancer," *Physics in Medicine and Biology*, vol. 53, no. 17, pp. 4489–4507, 2008.
- [28] D. L. S. McElwain, R. Callcott, and L. E. Morris, "A model of vascular compression in solid tumours," *Journal of Theoretical Biology*, vol. 78, no. 3, pp. 405–415, 1979.
- [29] W. M. Harriss-Phillips, E. Bezak, and E. K. Yeoh, "Monte Carlo radiotherapy simulations of accelerated repopulation and reoxygenation for hypoxic head and neck cancer," *British Journal of Radiology*, vol. 84, no. 1006, pp. 903–918, 2011.
- [30] A. Becker, G. Hänsgen, M. Blocking, C. Weigel, C. Lautenschläger, and J. Dunst, "Oxygenation of squamous cell carcinoma of the head and neck: comparison of primary tumors, neck node metastases, and normal tissue," *International Journal of Radiation Oncology Biology Physics*, vol. 42, no. 1, pp. 35–41, 1998.
- [31] B. Clavo, J. L. Pérez, L. López et al., "Influence of haemoglobin concentration and peripheral muscle pO₂ on tumour oxygenation in advanced head and neck tumours," *Radiotherapy and Oncology*, vol. 66, no. 1, pp. 71–74, 2003.
- [32] F. Eschwege, J. Bourhis, T. Girinski et al., "Predictive assays of radiation response in patients with head and neck squamous cell carcinoma: a review of the Institute Gustave Roussy experience," *International Journal of Radiation Oncology Biology Physics*, vol. 39, no. 4, pp. 849–853, 1997.
- [33] E. C. Gabalski, M. Adam, H. Pinto, J. M. Brown, D. A. Bloch, and D. J. Terris, "Pretreatment and midtreatment measurement of Oxygen tension levels in head and neck cancers," *Laryngoscope*, vol. 108, no. 12, pp. 1856–1860, 1998.
- [34] V. Rudat, B. Vanselow, P. Wollensack et al., "Repeatability and prognostic impact of the pretreatment pO₂ histography in patients with advanced head and neck cancer," *Radiotherapy and Oncology*, vol. 57, no. 1, pp. 31–37, 2000.
- [35] P. Stadler, H. J. Feldmann, C. Creighton, R. Kau, and M. Molls, "Changes in tumor oxygenation during combined treatment with split- course radiotherapy and chemotherapy in patients with head and neck cancer," *Radiotherapy and Oncology*, vol. 48, no. 2, pp. 157–164, 1998.
- [36] G. Marsaglia and W. W. Tsang, "The ziggurat method for generating random variables," *Journal of Statistical Software*, vol. 5, no. 8, pp. 1–7, 2000.

- [37] N. Wright and M. Alison, *The Biology of Epithelial Cell Populations*, vol. 2, Oxford University Press and Clarendon Press, Oxford, UK, 1984.
- [38] E. Aarnaes, B. Kirkhus, and O. P. F. Clausen, "Mathematical model analysis of mouse epidermal cell kinetics measured by bivariate DNA/anti-bromodeoxyuridine flow cytometry and continuous [3H]-thymidine labelling," *Cell and Tissue Kinetics*, vol. 23, no. 5, pp. 409–424, 1990.
- [39] C. S. Potten, "Cell cycles in cell hierarchies," *International Journal of Radiation Biology & Related Studies in Physics*, vol. 49, no. 2, pp. 257–278, 1986.
- [40] G. G. Steel, *Basic Clinical Radiobiology*, Hodder Arnold, UK, 2002.
- [41] E. Lartigau, A. Lusinchi, P. Weeger et al., "Variations in tumour oxygen tension (pO₂) during accelerated radiotherapy of head and neck carcinoma," *European Journal of Cancer*, vol. 34, no. 6, pp. 856–861, 1998.
- [42] J. M. Brown, "The hypoxic cell: a target for selective cancer therapy—eighteenth Bruce F. Cain Memorial Award Lecture," *Cancer Research*, vol. 59, no. 23, pp. 5863–5870, 1999.
- [43] T. Alarcón, H. M. Byrne, and P. K. Maini, "A mathematical model of the effects of hypoxia on the cell-cycle of normal and cancer cells," *Journal of Theoretical Biology*, vol. 229, no. 3, pp. 395–411, 2004.
- [44] A. S. E. Ljungkvist, J. Bussink, P. F. J. W. Rijken, J. H. A. M. Kaanders, A. J. van der Kogel, and J. Denekamp, "Vascular architecture, hypoxia, and proliferation in first-generation xenografts of human head-and-neck squamous cell carcinomas," *International Journal of Radiation Oncology Biology Physics*, vol. 54, no. 1, pp. 215–228, 2002.
- [45] C. W. S. Chin, A. J. E. Foss, A. Stevens, and J. Lowe, "Differences in the vascular patterns of basal and squamous cell skin carcinomas explain their differences in clinical behaviour," *Journal of Pathology*, vol. 200, no. 3, pp. 308–313, 2003.
- [46] R. E. Durand and E. Sham, "The lifetime of hypoxic human tumor cells," *International Journal of Radiation Oncology Biology Physics*, vol. 42, no. 4, pp. 711–715, 1998.
- [47] A. S. E. Ljungkvist, J. Bussink, J. H. A. M. Kaanders et al., "Hypoxic cell turnover in different solid tumor lines," *International Journal of Radiation Oncology Biology Physics*, vol. 62, no. 4, pp. 1157–1168, 2005.
- [48] L. Webster, R. J. Hodgkiss, and G. D. Wilson, "Cell cycle distribution of hypoxia and progression of hypoxic tumour cells in vivo," *British Journal of Cancer*, vol. 77, no. 2, pp. 227–234, 1998.
- [49] J. P. Kirkpatrick, L. I. Cárdenas-Navia, and M. W. Dewhirst, "Predicting the effect of temporal variations in PO₂ on tumor radiosensitivity," *International Journal of Radiation Oncology Biology Physics*, vol. 59, no. 3, pp. 822–833, 2004.
- [50] J. Denekamp, A. Daşu, A. Waites, and B. Littbrand, "Hyperfractionation as an effective way of overcoming radioreistance," *International Journal of Radiation Oncology Biology Physics*, vol. 42, no. 4, pp. 705–709, 1998.
- [51] A. Daşu and J. Denekamp, "Superfractionation as a potential hypoxic cell radiosensitizer: prediction of an optimum dose per fraction," *International Journal of Radiation Oncology Biology Physics*, vol. 43, no. 5, pp. 1083–1094, 1999.
- [52] R. G. Dale and B. Jones, *Radiobiological Modelling in Radiation Oncology*, The British Institute of Radiology, London, UK, 2007.
- [53] K. R. Trott and J. Kummermehr, "Rapid repopulation in radiotherapy: a debate on mechanism. Accelerated repopulation in tumours and normal tissues," *Radiotherapy and Oncology*, vol. 22, no. 3, pp. 159–160, 1991.
- [54] J. Kummermehr, W. Dörr, and K. R. Trott, "Kinetics of accelerated repopulation in normal and malignant squamous epithelia during fractionated radiotherapy," *BJR Supplement*, vol. 24, pp. 193–199, 1992.
- [55] C. H. J. Terhaard, H. B. Kal, and G. J. Hordijk, "Why to start the concomitant boost in accelerated radiotherapy for advanced laryngeal cancer in week 3," *International Journal of Radiation Oncology Biology Physics*, vol. 62, no. 1, pp. 62–69, 2005.
- [56] M. Stuschke and H. D. Thames, "Hyperfractionated radiotherapy of human tumors: overview of the randomized clinical trials," *International Journal of Radiation Oncology Biology Physics*, vol. 37, no. 2, pp. 259–267, 1997.
- [57] J. C. Horiot, A. C. Begg, R. Le Fur et al., "Present status of EORTC trials of hyperfractionated and accelerated radiotherapy on head and neck carcinoma," *Recent Results in Cancer Research*, vol. 134, pp. 111–119, 1994.
- [58] E. J. Hall and A. G. Garcia, *Radiobiology for the Radiologist*, Lippincott Williams and Wilkins, Philadelphia, Pa, USA, 2006.
- [59] C. S. Potten, "The cell kinetic mechanism for radiation-induced cellular depletion of epithelial tissue based on hierarchical differences in radiosensitivity," *International Journal of Radiation Biology*, vol. 40, no. 2, pp. 217–225, 1981.
- [60] R. P. Hill, "Tumor progression: potential role of unstable genomic changes," *Cancer and Metastasis Reviews*, vol. 9, no. 2, pp. 137–147, 1990.
- [61] J. A. Royds, S. K. Dower, E. E. Qvarnstrom, and C. E. Lewis, "Response of tumour cells to hypoxia: role of p53 and NFκB," *Journal of Clinical Pathology*, vol. 51, no. 2, pp. 55–61, 1998.
- [62] E. Aarnaes, O. P. F. Clausen, B. Kirkhus, and P. De Angelis, "Heterogeneity in the mouse epidermal cell cycle analysed by computer simulations," *Cell Proliferation*, vol. 26, no. 3, pp. 205–219, 1993.
- [63] C. I. Armpilia, R. G. Dale, and B. Jones, "Determination of the optimum dose per fraction in fractionated radiotherapy when there is delayed onset of tumour repopulation during treatment," *British Journal of Radiology*, vol. 77, no. 921, pp. 765–767, 2004.
- [64] J. F. Fowler and P. M. Harari, "Confirmation of improved local-regional control with altered fractionation in head and neck cancer," *International Journal of Radiation Oncology Biology Physics*, vol. 48, no. 1, pp. 3–6, 2000.
- [65] A. C. Begg, I. Hofland, and J. Kummermehr, "Tumour cell repopulation during fractionated radiotherapy: correlation between flow cytometric and radiobiological data in three murine tumours," *European Journal of Cancer*, vol. 27, no. 5, pp. 537–543, 1991.
- [66] J. F. Fowler, "Rapid repopulation in radiotherapy: a debate on mechanism. The phantom of tumor treatment—continually rapid proliferation unmasked," *Radiotherapy and Oncology*, vol. 22, no. 3, pp. 156–158, 1991.
- [67] W. Dörr, "Three A's of repopulation during fractionated irradiation of squamous epithelia: asymmetry loss, Acceleration of stem-cell divisions and Abortive divisions," *International Journal of Radiation Biology*, vol. 72, no. 6, pp. 635–643, 1997.
- [68] D. D. Dionysiou, G. S. Stamatakos, D. Gintides, N. Uzunoglu, and K. Kyriaki, "Critical parameters determining standard radiotherapy treatment outcome for glioblastoma multiforme: a computer simulation," *The Open Biomedical Engineering Journal*, vol. 2, pp. 43–51, 2008.

Research Article

In Silico Nanodosimetry: New Insights into Nontargeted Biological Responses to Radiation

Zdenka Kuncic,¹ Hilary L. Byrne,¹ Aimee L. McNamara,¹ Susanna Guatelli,² Westa Domanova,^{1,3} and Sébastien Incerti⁴

¹ School of Physics, University of Sydney, Sydney, NSW 2006, Australia

² Centre for Medical Radiation Physics, University of Wollongong, Wollongong, NSW 2522, Australia

³ Department of Physics, Technical University of Munich, 85748 Garching, Germany

⁴ Université Bordeaux 1, CNRS/IN2P3, Centre d'Etudes Nucléaires de Bordeaux-Gradignan, 33175 Gradignan, France

Correspondence should be addressed to Zdenka Kuncic, zdenka.kuncic@sydney.edu.au

Received 21 February 2012; Accepted 2 April 2012

Academic Editor: Eva Bezak

Copyright © 2012 Zdenka Kuncic et al. This is an open access article distributed under the Creative Commons Attribution License, which permits unrestricted use, distribution, and reproduction in any medium, provided the original work is properly cited.

The long-held view that radiation-induced biological damage must be initiated in the cell nucleus, either on or near DNA itself, is being confronted by mounting evidence to suggest otherwise. While the efficacy of cell death may be determined by radiation damage to nuclear DNA, a plethora of less deterministic biological responses has been observed when DNA is not targeted. These so-called nontargeted responses cannot be understood in the framework of DNA-centric radiobiological models; what is needed are new physically motivated models that address the damage-sensing signalling pathways triggered by the production of reactive free radicals. To this end, we have conducted a series of *in silico* experiments aimed at elucidating the underlying physical processes responsible for nontargeted biological responses to radiation. Our simulation studies implement new results on very low-energy electromagnetic interactions in liquid water (applicable down to nanoscales) and we also consider a realistic simulation of extranuclear microbeam irradiation of a cell. Our results support the idea that organelles with important functional roles, such as mitochondria and lysosomes, as well as membranes, are viable targets for ionizations and excitations, and their chemical composition and density are critical to determining the free radical yield and ensuing biological responses.

1. Introduction

The theory of radiation interactions with matter, established over the course of the last century by celebrated physicists such as Bohr [1], Bethe [2], Bethe and Heitler [3], and Fano [4], now underpins a vast range of cutting-edge technologies and applications, from high-energy particle detectors for the Large Hadron Collider, to atmospheric, space and astrophysics, to electron-beam lithography and materials analysis techniques (e.g., electron microscopy, X-ray spectroscopy). For medical applications, such as imaging and radiation therapy, electromagnetic interactions that take place in living biological systems are of paramount importance because collisions can excite and ionize the constituent molecules, leading to impaired biological function. When this occurring inside a cell nucleus, there is an increased likelihood of damaging DNA and compromising the cell's viability [5].

The physical and chemical mechanisms of radiation-induced nuclear DNA damage (i.e., strand breaks and other lesions resulting from interactions on or near DNA) have been generally well understood for several decades [6] and an extensive body of literature now exists on radiobiology [7–11]. Radiation target theory [9], in particular, has provided a successful framework for achieving the fundamental aim of radiation therapy, which is to maximise tumour cell kill while sparing normal cells, assuming that initial damage to nuclear DNA is central to the killing of a cell by reproductive cell death (i.e., mitosis inhibited by loss of large amounts of genetic material). But when electromagnetic interactions occur primarily outside the nucleus, the ensuing biological damage is poorly understood [12].

Compelling evidence for such nontargeted damage is now emerging from the increasing incidence of secondary

malignancies among cancer survivors treated with radiotherapy, attributed to the unavoidable exposure of healthy tissue to low-dose radiation [13–15]. At low doses, radiation can miss nuclear DNA altogether because of the small relative volume it occupies in the cell. If damaged cells that would normally be eliminated instead escape apoptosis and undergo cell cycle division, carcinogenesis may develop due to the survival and proliferation of cells with accumulating damage or mutations. Molecular signalling pathways that disrupt cellular tissue homeostasis can give rise to both acute and late effects in normal tissue following radiotherapy [16]. Indeed, there is growing concern in particular over the low-dose radiation bath into which relatively large volumes of normal tissue are immersed in modern conformal radiotherapy delivery techniques. An increasing number of radiotherapy studies are now paying more attention to normal cells surrounding irradiated tumours [17]. However, quantitative, physically motivated models are lacking in the literature, primarily because the DNA-centric approach of classical radiobiology is no longer valid at low doses. For this reason, models predicting normal tissue complications have had limited success in describing clinically observed normal tissue reactions [18].

Further independent evidence demonstrating the limitations of the existing DNA-target paradigm for radiation-induced damage has emerged from cell irradiation experiments using microbeams, which deliver a focused beam of low-energy (typically tens of keV) radiation to spatially localised regions in a cell up to several microns away from the nucleus. These experiments provide new insights into the complex biological pathways triggered by extranuclear radiation energy deposition and resulting damage to cytoplasmic structures such as lysosomes, membranes, and mitochondria (Figure 1). Several newly recognised responses, collectively referred to as nontargeted responses, are manifested by effects such as mutagenesis (stable mutations in cell progeny), genomic instability (unstable effects caused by changes in genetic information), bystander effect (responses in neighbouring, unirradiated cells), changes in gene expression, and even adaptive responses [12, 19–24]. These effects are markedly different from the mechanistic response to DNA-targeted radiation; nontargeted responses are not directly related to the amount of energy deposited in or near the nuclear DNA of the cells traversed by the radiation. The microbeam results suggest instead that nontargeted biological responses are determined by cell's entire state, including all proteins and macromolecules in its cytoplasm, some of which may cause functional damage when released from lysosomes and mitochondria, while structural membrane damage can potentially also affect intra- and intercellular signalling pathways.

Low-energy electrons are the most abundant product of radiation interactions, and their collisions with surrounding molecules are primarily responsible for initiating the sequence of biochemical events that leads to radiation-induced damage in biological systems [25]. Much of our present understanding of radiation-induced biological damage on subcellular scales (down to nanometric volumes) stems from microdosimetry and nanodosimetry studies.

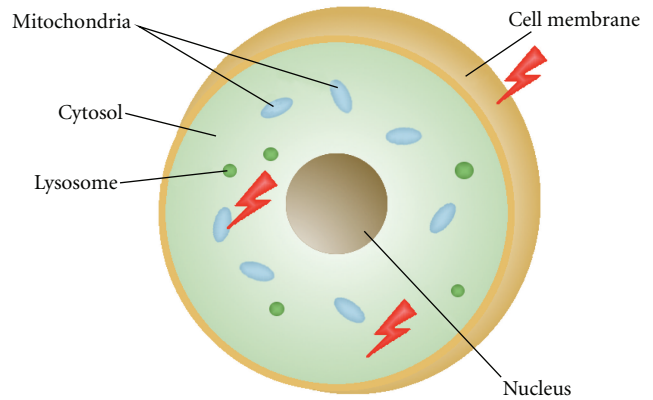


FIGURE 1: Schematic illustration of a cell, showing potentially important extranuclear targets that have been implicated in triggering complex damage signalling pathways induced by radiation (shown in red).

A significant limitation of experimental studies, however, is that single particle detection methods rely on gas counters, which are a poor approximation to biological tissue. Nevertheless, significant progress has been made in understanding DNA damage by measuring ionization cluster-size distributions and particle tracks [26–29]. Monte Carlo (MC) simulations provide an alternate method for advancing our understanding of radiation-induced DNA damage and many independent MC models have been developed for determining DNA strand break yields by simulating electron track structure and ionization clusters in nanometric volumes or simple DNA models [30–35]. To date, however, no MC simulations have investigated the biological damage observed as nontargeted responses resulting from extranuclear irradiation.

In this paper, we briefly report *in silico* nanodosimetry studies which aim to reveal new insights into radiation-induced biological damage beyond nuclear DNA. Our simulation studies consider primary particles of different types (electrons, protons, and alphas), since nontargeted effects have been observed for radiation types of different linear energy transfer (LET) [21]. Section 2 presents the theoretical background and the MC computational approach relevant to modelling low-energy electromagnetic interactions on subcellular scales. We present and discuss our preliminary results in Section 3, and conclusions are given in Section 4.

2. Theoretical Background and Computational Approach

At energies below a few keV, which are relevant for electron scattering on subcellular scales, the wave properties of the incident electrons become increasingly important. Thus, the probability of inelastic scattering of incident electrons must be derived from electrodynamics rather than mechanics. Scattering cross-sections need to be derived for liquid water, which is the main constituent of biological tissue.

The Geant4 software toolkit provides state-of-the-art capability in depth and scope of Monte Carlo based approaches to modelling radiation interactions in biological systems; new models for low-energy electromagnetic cross-sections for liquid water are available for nanodosimetry and electron track structure simulations.

2.1. Low-Energy Electromagnetic Interactions. In the classical treatment of inelastic scattering of low-energy electrons [36, 37], the stopping power is the retarding force experienced by the incident electron due to the polarization field induced in the medium through which it propagates. The electron energy loss and momentum transfer are determined by the dielectric function ϵ , which describes the electromagnetic response of the medium to the disturbance caused by the incident electron. The corresponding differential cross-section for inelastic electron scattering can be expressed in terms of the inverse mean free path Λ :

$$\frac{d^2\Lambda}{dq dE} = \frac{1}{\pi a_0 q T} \text{Im} \left[\frac{-1}{\epsilon(\mathbf{q}, E)} \right], \quad (1)$$

where T and E are the electron energy before and after scattering, respectively, $\hbar\mathbf{q}$ is the momentum transfer, and $a_0 = \hbar^2/e^2 m_e$ is the Bohr radius. For electron energies large compared with atomic energies, the valence electrons can be regarded as approximately free. Using the electron plasma dielectric response for ϵ in (1) gives a solution consistent with the standard Bethe-Bloch stopping power derived from nonrelativistic quantum mechanics [36].

In the quantum treatment of inelastic electron scattering, the differential cross-section can be written as [2, 38, 39]

$$d\sigma = \frac{m_e q}{4\pi\hbar^2 T} |T_{fi}|^2 \delta(E + E_n - E_0) dq dE, \quad (2)$$

where E_0 and E_n are the energies of the atom before and after scattering, respectively, and T_{fi} is the transition matrix for transitions between initial and final states of the electron-atom system. The calculation of T_{fi} in the first Born approximation using an appropriate Coulomb interaction potential [38] yields

$$d\sigma = 4\pi \frac{dq}{a_0 q T} |\langle n|d|0\rangle|^2 \delta(E + E_n - E_0) dE, \quad (3)$$

where d is the matrix element of the atom's dipole moment due to the space density distribution of its electrons. The sum over all final states n gives the following relation for the polarizability of the atom: $\text{Im}[\epsilon^{-1}] \approx 4\pi N \sum_n |\mathbf{d}_{0n}|^2 \delta(E + E_n - E_0)$, where N is the number of atoms per unit volume. The relation $\Lambda = N\sigma$ then recovers (1) [36, 38, 40].

The probability of inelastic scattering of low-energy electrons, as described by (1), requires determination of $\epsilon(\mathbf{q}, E)$, which has proven challenging for biological tissue. Valence electrons in soft-condensed matter cannot be regarded as free or nearly free, as they are in metals and other conductors, so the commonly used Lindhard dielectric function for an electron plasma is a poor approximation to the collective response of bound molecular electrons. Furthermore, the

effective intermolecular potential in the condensed phase acts as a screen on the polarization field induced by an incident electron, and collective plasma excitations can delocalize energy deposition. The problem is further compounded by the lack of direct measurement data due to the inherent practical difficulties in conducting scattering experiments with condensed molecular targets. Although experimental data to date is only available in the optical limit (zero momentum transfer), they have nevertheless enabled improved semiempirical dielectric models to be derived and extended into the finite momentum transfer domain, $q > 0$ (i.e., finite scattering angles; e.g., [41, 42], and references therein). An alternative approach to modelling low-energy inelastic electron scattering is to use the method of partial wave expansion, which is relevant at low energies, where the Born plane wave approximation breaks down. When the incident electron energy becomes comparable to the binding energy of atomic electrons, scattering can no longer be considered a small perturbation to the system and the free electron wavefunction (i.e., a plane wave) can no longer be assumed. Champion [43] has derived new theoretical results using the partial wave approach to describe ionization of molecular water by low-energy electrons.

2.2. Geant4. Geant4 is an open-source software toolkit developed for general-purpose Monte Carlo radiation transport simulations [44, 45]. Its object-oriented structure and approach has enabled an impressive scope of applications, ranging from high-energy particle physics and astrophysics, to medical physics and imaging. The medical applications, in particular, are growing rapidly and are becoming more versatile; Geant4 models have been developed for radiotherapy scenarios (e.g., brachytherapy, medical linear accelerator beams, hadrontherapy, internal and radionuclide dosimetry), imaging techniques (e.g., CT, emission tomography, electronic portal imaging), and also for micro- and nanodosimetry studies, including electron track structure down to nanometric length scales. Microbeam cell irradiation experiments can also be modeled with Geant4.

In addition to the standard interaction cross-section databases for atomic collisions (i.e., NIST), Geant4 also provides additional low-energy electromagnetic classes with several choices of cross-section model data (e.g., Livermore, Penelope), including the new Geant4-DNA module (<http://geant4-dna.org/>), which can explicitly model all interaction events as discrete processes [46]. This extension has been specifically designed for radiobiology and nanodosimetry applications and includes implementation of a semiempirical Born model (c.f., Section 2.1) for ionization and excitation of liquid water by electrons, protons, and alphas (and a few other ions) valid for energies down to eV scales [42]. New developments currently underway include the capability to model key radiation chemistry processes such as water radiolysis.

We have been using Geant4 to develop a suite of *in silico* experiments designed to give us a better understanding of the physical processes underlying biological responses to radiation damage that occurs outside the cell nucleus. Biological damage, both structural and functional, is initiated

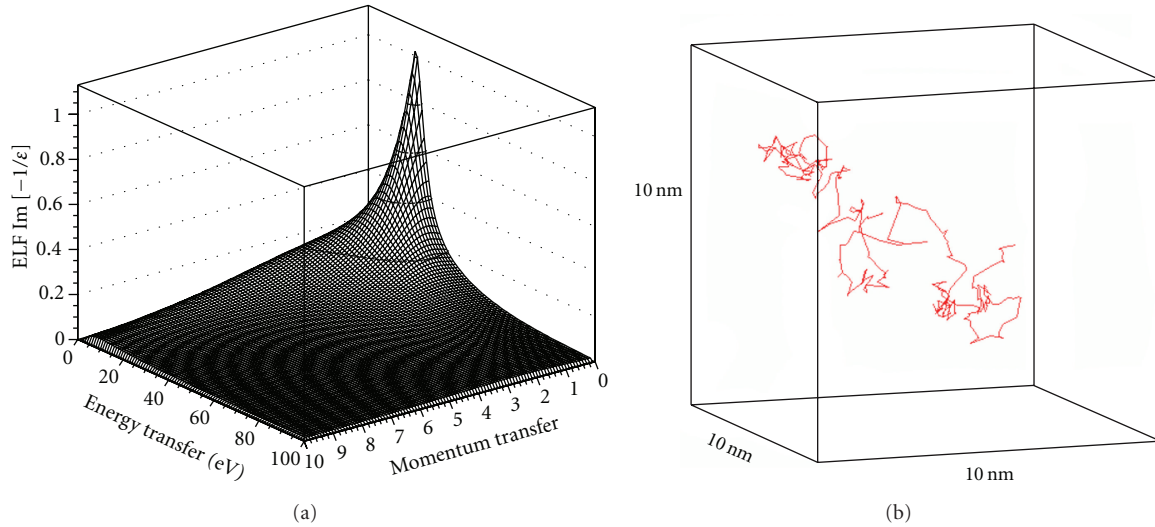


FIGURE 2: (a) Energy loss function (ELF) for low-energy electrons (c.f. (1)) in liquid water plotted as a function of energy and momentum transfer (the so-called “Bethe ridge”). (b) Corresponding track of a 100 eV electron in a 10 nm cube of liquid water.

by ionizations which produce the free radicals that have been implicated in intra- and intercellular signalling. Our models represent the first simulation studies aimed at directly addressing nontargeted biological responses triggered by radiation damage beyond nuclear DNA.

3. Results and Discussion

Here, we present preliminary results of three separate studies: (1) electron track structure on nanometric scales in liquid water using the Geant4-DNA semiempirical models for excitations and ionizations of low-energy electrons, (2) the spatial distribution of clustered ionization events resulting from the traversal of protons and photons through a sub-cellular scale volume of water, and (3) simulation of a microbeam cell irradiation experiment, showing localized energy deposition and ionization distributions in a realistic cell model when only the cytoplasm is irradiated by an alpha particle beam.

3.1. Nanometric Electron Tracks. Figure 2 shows plots of the energy loss function (ELF), $\text{Im}[-1/\epsilon(\mathbf{q}, E)]$, for low-energy electrons (c.f. (1)), and the corresponding electron track structure resulting from an electron with an initial energy of 100 eV in a 10 nm cube of liquid water. The electron ELF plotted in the energy-momentum plane, referred to as the “Bethe ridge,” has been calculated for liquid water using semiempirical models for inelastic scattering [41, 42] based on those implemented in Geant4-DNA. The electron track structure has been simulated using the models for elastic and inelastic electron scattering available in Geant4-DNA (the Champion and Born models, resp.). A quantitative evaluation of these models has been presented by Incerti et al [46]. The Bethe ridge plot exhibits a prominent peak at ≈ 21 eV, which is close to the plasma frequency of water, as has

been noted in previous studies [41, 42]. It should be noted, however, that other inelastic channels, such as collective excitations and autoionization [47, 48], are not taken into account in this ELF. Collective excitations include plasmon-like resonances that can delocalize energy deposition away from the electron track. Autoionization is the process by which water molecules, in the liquid phase, undergo spontaneous decay. When excited by an incident electron, $(\text{H}_2\text{O})_2$ molecules dissociate rapidly, producing secondary electrons and H_2O^+ ions [49, 50]. How these additional energy loss processes might change the shape of the Bethe ridge is not clear and more theoretical work is needed.

3.2. Ionization Cluster Distribution. In this study, we used Geant4 (version 9.4) to model monoenergetic proton and X-ray pencil beams incident on a liquid water cube, of length 40 mm, to investigate the distribution of ionization clusters and relative biological effectiveness of these different forms of radiation. The photon interactions were modelled with the low-energy electromagnetic package (based on the Livermore data libraries), including processes for the photoelectric effect, Compton scattering, Rayleigh scattering, and pair production. In the case of protons, the standard electromagnetic package models were used to model ionization and multiple scattering for protons with $E \geq 10$ MeV. In both cases, protons and electrons with energies < 200 MeV and < 10 keV, respectively, were transported in the water medium down to a few eV, using the Geant4-DNA model extensions. The processes for electron ionization, excitation, and elastic scattering (the Champion elastic model) were included and the lower energy limit for the excitation and elastic scattering models was set to 8.23 eV [51]. The physics processes of the low-energy protons (< 10 MeV) included charge decrease, excitation, and ionization [52, 53]. The simulation produced the number of ionizations in voxels of a few nanometers in

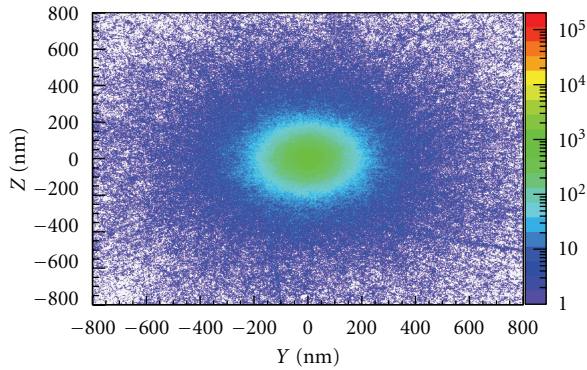


FIGURE 3: Cluster distribution of 200 MeV monoenergetic pencil beam protons in liquid water, showing the number of ionizations per 2×2 nm voxel at a depth of 0.25 mm.

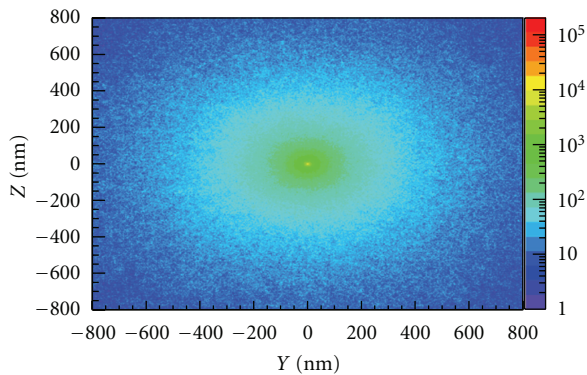


FIGURE 4: Cluster distribution of 100 keV monoenergetic pencil beam photons in liquid water, showing the number of ionizations per 2×2 nm voxel at a depth of 20 mm.

size at different points along the particle trajectory (cluster size distribution).

Figures 3 and 4 show the cluster ionization distribution of incident 200 MeV pencil beam protons and incident 100 keV pencil beam photons, respectively. The total number of each particle type was chosen to give approximately the same dose deposited in the water phantom. The number of ionizations occurring within nanometric voxels (the cluster size distribution), with dimension 2×2 nm, is shown at two different depths in the water phantom: 0.25 mm for protons and 20 mm for photons. In each case, the plots show the ionization clustering on the YZ plane. The incident pencil beam is directed along the x -axis and the colourbar shows the number of ionizations per voxel. For 200 MeV protons, the depth of 0.25 mm is well before the Bragg peak, but a large number of ionizations are still evident and are concentrated around the beam (c.f. Figure 3). Photons on the other hand show very few ionizations at the same depth. At 20 mm depth, however, the number of ionizations in the vicinity of the beam is comparable to that produced by protons at 0.25 mm depth and although more scattering produces a broader spread of ionizations away from the beam, the cluster distribution around the beam axis is remarkably

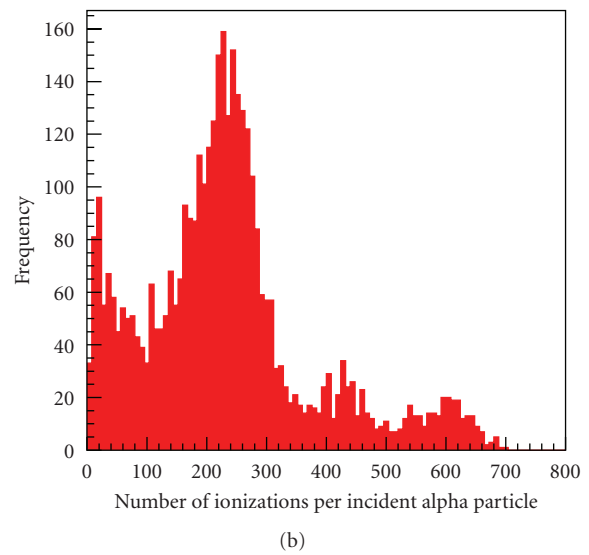
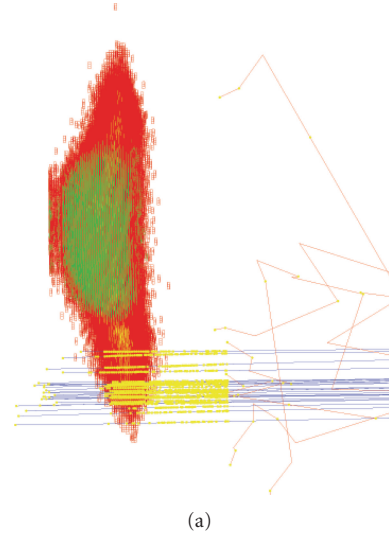


FIGURE 5: (a) Geant4 visualization of a microbeam cell irradiation simulation, showing a 5 micron beam of 3 MeV alpha particles (blue lines, incident from the right) targeting the cytoplasm (red) and avoiding the nucleus (green). (b) corresponding histogram of ionizations in the cytoplasm per incident particle for 10^4 incident alphas.

similar. This suggests that 100 keV photons have a similar potential to cause biological damage as 200 MeV protons.

3.3. Microbeam Cell Irradiation. Figure 5 shows a visualization of our microbeam cell irradiation simulation and the corresponding histogram of ionizations per incident particle in the cytoplasm. The simulation was based on the microbeam example in Geant4 (version 9.4), which is modelled on a cellular irradiation beamline facility configured to deliver a beam of 3 MeV alpha particles focussed down to $5 \mu\text{m}$ in diameter. The cell geometry is a voxelized 3D model based on a human keratinocyte cell line. See Incerti et al. [54] for more details.

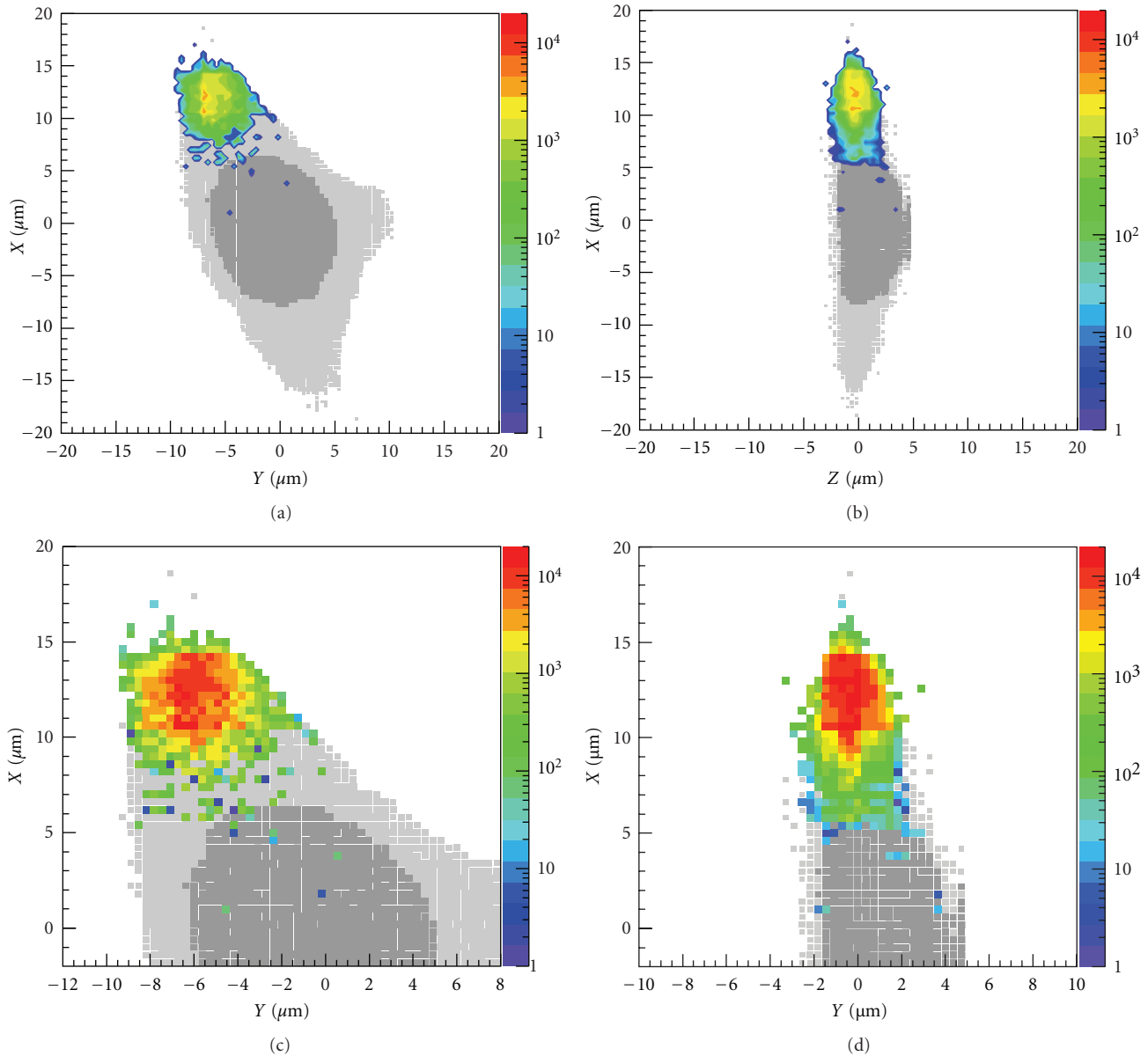


FIGURE 6: Top row: 2D projection of mean energy deposit (in eV) per voxel in the microbeam irradiated cell, showing the cross-sectional plane (left) and the longitudinal plane (right). Bottom row: corresponding distribution of number of ionizations in the cytoplasm. All plots were calculated for 10^4 incident alpha particles.

In our simulation, the beam was displaced off-centre, so only the cytoplasm was irradiated and not the nucleus. We used the Livermore physics processes, rather than Geant-DNA, since this allowed us to investigate the effect of chemical composition (the Geant4-DNA processes are only available for liquid water). The Livermore processes are valid down to 250 eV, corresponding to a physical scale-size ~ 30 nm. The cell cytoplasm and nucleus were based on a realistic chemical composition with a density of 1 g cm^{-3} . The mass-fraction constituents of the cytoplasm were oxygen ($\approx 58\%$), carbon ($\approx 20\%$), hydrogen ($\approx 9\%$), nitrogen ($\approx 8.5\%$), and phosphorus ($\approx 4.5\%$). The primary mass-fraction constituents of the nuclear material were oxygen

($\approx 74.5\%$) and hydrogen ($\approx 11\%$), with lower amounts of carbon ($\approx 9\%$), nitrogen ($\approx 3\%$), and phosphorus ($\approx 2.5\%$) compared to the cytoplasm [55]. In addition, a number of localized overdensities (10 g cm^{-3}) with the same material content as the nucleus were also distributed throughout the cytoplasm. These substructures, which could represent organelles, affect the ionization histogram (Figure 5) by reducing the average number of ionizations per event. This can be attributed to the combined effects of chemical composition and density. Despite the higher oxygen content of the substructure targets, the lower relative amounts of high atomic number elements such as carbon and nitrogen, with respect to the rest of the cytoplasm, results in an overall

lower mean excitation energy and an increased probability of ionization. The higher density of the substructures increases the number of ionizations per incident alpha particle. The material density affects the overall frequency of ionizations. This result demonstrates the importance of chemical composition and density in determining the probability of ionization events and hence, production of free radical species in a real cell and subcellular structures such as organelles, membranes, as well as macromolecules and other proteins.

Figure 6 shows the 2D projection of mean energy deposition per voxel and ionization events in the microbeam cell irradiation simulation. The average specific energy deposited per event is 0.08 J kg^{-1} . The spatial distribution of mean energy deposition is clearly correlated with the ionization distribution in the cytoplasm. Both distributions are localized but exhibit spreading around the $5 \mu\text{m}$ beam due to scattered secondary electrons. In particular, a finite number of ionizations is also found to occur along the cell and nuclear membranes, where structural damage can impair membrane-mediated inter- and intracellular signalling (i.e., via binding of ligands, diffusion of molecules through gap junctions). Within the cytoplasm, ionizations that occur in the organelles can affect the release of proteins and macromolecules, leading to functional damage. Realistic physical models for these organelles, including their spatial distribution in the cell, molecular composition, density, and size, are needed to better quantify the probability of ionizations.

A limitation of the current model is that it employs interaction probabilities based on atomic rather than molecular collisions. This means that it is not currently possible to simulate the direct production of key free radical species such as hydroxyl radicals (OH^\cdot) and superoxide anions (O_2^\cdot) which are implicated in intra- and intercellular signalling. However, a preliminary model for simulating radiolysis of molecular water and diffusion of free radical species has been implemented in the latest release of Geant4 (version 9.5). We note that the steep gradient in number density of ionizations evident in Figure 6 suggests rapid diffusion of radiolytic products across regions of the cell. We aim to explore this in future work.

4. Conclusions

We have presented a summary of preliminary results from a series of simulation studies investigating nontargeted responses to radiation using Geant4. Our study on low-energy electromagnetic interactions demonstrates that secondary electrons, with energies well below 100 eV, can ionize and excite liquid water on nanometric scales. More theoretical work is needed, however, to enable modelling of collective excitations and autoionization of molecular water and other molecules such as lipids which are relevant for membrane-mediated signalling. Such modelling would enable more quantitative evaluation of the likelihood of cellular dysfunction, lysis, or death resulting from primary damage to membranes and membrane-bound organelles (e.g., lysosomes, mitochondria) throughout the cell.

We also investigated the role of ionization clustering on nanoscales in liquid water without assuming *a priori*

a nuclear DNA target. Our results demonstrate that low-energy photons can generate clustered ionization distributions similar to that produced by protons, suggesting a similar potential to cause biological damage. This has important implications for situations such as radiotherapy, where secondary low-energy photons are produced in abundance and can readily reach normal tissue surrounding a tumor.

Our simulation study on extranuclear microbeam irradiation of a realistic cell demonstrates the importance of chemical composition and density of cellular substructures in determining the level of radiation damage by ionizations. Although it is not yet possible to explicitly simulate within Geant4 the production of molecular free radical species that have been implicated in signalling, the spatial distribution of ionization events outside the nucleus is suggestive of the possible structural and functional damage that would trigger damage-response signalling by the cell. In future work, we plan to take advantage of the ongoing developments in Geant4, particularly the developing capability to model water radiolysis and diffusion of free radicals.

References

- [1] N. Bohr, "On the decrease of velocity of swiftly moving electrified particles in passing through matter," *Philosophical Magazine*, vol. 25, p. 10, 1915.
- [2] H. Bethe, "Zur theorie des durchgangs schneller korpuskularstrahlen durch materie," *Annalen der Physik*, vol. 5, p. 325, 1930.
- [3] H. Bethe and W. Heitler, "On the stopping of fast particles and on the creation of positive electrons," *Proceedings of the Royal Society of London A*, vol. 146, p. 83, 1934.
- [4] U. Fano, "Atomic theory of electromagnetic interactions in dense materials," *Physical Review*, vol. 103, no. 5, pp. 1202–1218, 1956.
- [5] D. T. Goodhead, "The initial physical damage produced by ionizing radiations," *International Journal of Radiation Biology*, vol. 56, no. 5, pp. 623–634, 1989.
- [6] J. W. Harper and S. J. Elledge, "The DNA damage response: ten years after," *Molecular Cell*, vol. 28, no. 5, pp. 739–745, 2007.
- [7] D. E. Lea, *The Action of Radiation on Living Cells*, Cambridge University Press, London, UK, 1946.
- [8] M. M. Elkind and H. Sutton, "X-ray damage and recovery in mammalian cells in culture," *Nature*, vol. 184, no. 4695, pp. 1293–1295, 1959.
- [9] T. R. Munro and C. W. Gilbert, "The relation between tumour lethal doses and the radiosensitivity of tumour cells," *The British journal of radiology*, vol. 34, pp. 246–251, 1961.
- [10] A. M. Kellerer and H. H. Rossi, "The theory of dual radiation action," *Current Topics in Radiation Research*, vol. 8, p. 85, 1972.
- [11] K. H. Chadwick and H. P. Leenhouts, *The Molecular Theory of Radiation Biology*, Springer, Berlin, 1981.
- [12] K. M. Prise, G. Schettino, M. Folkard, and K. D. Held, "New insights on cell death from radiation exposure," *Lancet Oncology*, vol. 6, no. 7, pp. 520–528, 2005.
- [13] M. Tubiana, "Can we reduce the incidence of second primary malignancies occurring after radiotherapy? A critical review," *Radiotherapy and Oncology*, vol. 91, no. 1, pp. 4–15, 2009.
- [14] R. Takam, E. Bezak, and E. E. Yeoh, "Risk of second primary cancer following prostate cancer radiotherapy: DVH analysis

- using the competitive risk model,” *Physics in Medicine and Biology*, vol. 54, no. 3, pp. 611–625, 2009.
- [15] W. D. Newhauser and M. Durante, “Assessing the risk of second malignancies after modern radiotherapy,” *Nature Reviews Cancer*, vol. 11, no. 6, pp. 438–448, 2011.
- [16] H. P. Rodemann and M. A. Blaese, “Responses of normal cells to ionizing radiation,” *Seminars in Radiation Oncology*, vol. 17, no. 2, pp. 81–88, 2007.
- [17] X. G. Xu, B. Bednarz, and H. Paganetti, “A review of dosimetry studies on external-beam radiation treatment with respect to second cancer induction,” *Physics in Medicine and Biology*, vol. 53, no. 13, pp. R193–R241, 2008.
- [18] J. W. Denham, Q. J. Walker, D. S. Lamb et al., “Mucosal regeneration during radiotherapy,” *Radiotherapy and Oncology*, vol. 41, no. 2, pp. 109–118, 1996.
- [19] L.-J. Wu, G. Randers-Pehrson, A. Xu et al., “Targeted cytoplasmic irradiation with alpha particles induces mutations in mammalian cells,” *Proceedings of the National Academy of Sciences of the United States of America*, vol. 96, no. 9, pp. 4959–4964, 1999.
- [20] C. Shao, M. Folkard, B. D. Michael, and K. M. Prise, “Targeted cytoplasmic irradiation induces bystander responses,” *Proceedings of the National Academy of Sciences of the United States of America*, vol. 101, no. 37, pp. 13495–13500, 2004.
- [21] K. M. Prise and J. M. O’Sullivan, “Radiation-induced bystander signalling in cancer therapy,” *Nature Reviews Cancer*, vol. 9, no. 5, pp. 351–360, 2009.
- [22] D. Averbeck, “Non-targeted effects as a paradigm breaking evidence,” *Mutation Research*, vol. 687, no. 1–2, pp. 7–12, 2010.
- [23] E. G. Wright, “Manifestations and mechanisms of non-targeted effects of ionizing radiation,” *Mutation Research*, vol. 687, no. 1–2, pp. 28–33, 2010.
- [24] G. Schettino, S. T. Al Rashid, and K. M. Prise, “Radiation microbeams as spatial and temporal probes of subcellular and tissue response,” *Mutation Research*, vol. 704, no. 1–3, pp. 68–77, 2010.
- [25] H. Nikjoo and L. Lindborg, “RBE of low energy electrons and photons,” *Physics in Medicine and Biology*, vol. 55, no. 10, pp. R65–R109, 2010.
- [26] D. T. Goodhead, “An assessment of the role of microdosimetry in radiobiology,” *Radiation Research*, vol. 91, no. 1, pp. 45–76, 1982.
- [27] B. Grosswendt, “Recent advances of nanodosimetry,” *Radiation Protection Dosimetry*, vol. 110, no. 1–4, pp. 789–799, 2004.
- [28] R. W. Schulte, “Nanodosimetry: principle and current status,” in *Proceedings of the AIP Conference*, vol. 1345, p. 249, 2011.
- [29] H. Nettelbeck and H. Rabus, “Nanodosimetry: the missing link between radiobiology and radiation physics?” *Radiation Measurements*, vol. 48, p. 893, 2011.
- [30] H. Nikjoo, D. Emfietzoglou, R. Watanabe, and S. Uehara, “Can Monte Carlo track structure codes reveal reaction mechanism in DNA damage and improve radiation therapy?” *Radiation Physics and Chemistry*, vol. 77, no. 10–12, pp. 1270–1279, 2008.
- [31] D. J. Brenner and J. F. Ward, “Constraints on energy deposition and target size of multiply damaged sites associated with DNA double-strand breaks,” *International Journal of Radiation Biology*, vol. 61, no. 6, pp. 737–748, 1992.
- [32] D. T. Goodhead, “Initial events in the cellular effects of ionizing radiations: clustered damage in DNA,” *International Journal of Radiation Biology*, vol. 65, no. 1, pp. 7–17, 1994.
- [33] H. Nikjoo, P. O’Neill, D. T. Goodhead, and M. Terrissol, “Computational modelling of low-energy electron-induced DNA damage by early physical and chemical events,” *International Journal of Radiation Biology*, vol. 71, no. 5, pp. 467–483, 1997.
- [34] M. A. Bernal, C. E. Dealmeida, C. Sampaio, S. Incerti, C. Champion, and P. Nieminen, “The invariance of the total direct DNA strand break yield,” *Medical Physics*, vol. 38, no. 7, pp. 4147–4153, 2011.
- [35] A. L. McNamara, S. Guatelli, D. A. Prokopovich, M. I. Reinhard, and A. B. Rosenfeld, “A comparison of x-ray and proton beam low energy secondary electron track structures using the low energy models of Geant4,” *International Journal of Radiation Biology*, vol. 88, no. 1–2, pp. 164–170, 2012.
- [36] L. D. Landau, L. P. Pitaevskii, and E. P. Lifshitz, *Electrodynamics of Continuous Media*, Oxford, Pergamon, Greece, 2nd edition, 1984.
- [37] R. H. Ritchie, “Energy losses by swift charged particles in the bulk and at the surface of condensed matter,” *Nuclear Instruments and Methods In Physics Research*, vol. 198, no. 1, pp. 81–91, 1982.
- [38] L. D. Landau and E. P. Lifshitz, *Quantum Mechanics—Non-Relativistic Theory*, Oxford, Pergamon, Greece, 3rd edition, 1977.
- [39] U. Fano, “Penetration of protons, alpha particles and mesons,” *Annual Review of Nuclear and Particle Science*, vol. 13, p. 1, 1963.
- [40] V. B. Berestetskii, L. P. Pitaevskii, and E. P. Lifshitz, *Quantum Electrodynamics*, Butterworth-Heinemann, Oxford, UK, 2nd edition, 1982.
- [41] M. Dingfelder, R. H. Ritchie, J. E. Turner, W. Friedland, H. G. Paretzke, and R. N. Hamm, “Comparisons of calculations with PARTRAC and NOREC: transport of electrons in liquid water,” *Radiation Research*, vol. 169, no. 5, pp. 584–594, 2008.
- [42] D. Emfietzoglou and H. Nikjoo, “Accurate electron inelastic cross sections and stopping powers for liquid water over the 0.1–10 keV range based on an improved dielectric description of the Bethe surface,” *Radiation Research*, vol. 167, no. 1, pp. 110–120, 2007.
- [43] C. Champion, “Electron impact ionization of liquid and gaseous water: a single-center partial-wave approach,” *Physics in Medicine and Biology*, vol. 55, no. 1, pp. 11–32, 2010.
- [44] S. Agostinelli et al., “Geant4—a simulation toolkit,” *Nuclear Instruments and Methods in Physics Research A*, vol. 506, p. 250, 2003.
- [45] J. Allison et al., “Geant4 developments and applications,” *IEEE Transactions on Nuclear Science*, vol. 53, p. 270, 2006.
- [46] S. Incerti, A. Ivanchenko, M. Karamitros et al., “Comparison of GEANT4 very low energy cross section models with experimental data in water,” *Medical Physics*, vol. 37, no. 9, pp. 4692–4708, 2010.
- [47] C. D. Wilson, C. A. Dukes, and R. A. Baragiola, “Search for the plasmon in condensed water,” *Physical Review B*, vol. 63, no. 12, Article ID 121101, pp. 1–4, 2001.
- [48] P. L. Geissler, C. Dellago, D. Chandler, J. Hutter, and M. Parrinello, “Autoionization in liquid water,” *Science*, vol. 291, no. 5511, pp. 2121–2124, 2001.
- [49] T. Jahnke et al., “Ultrafast energy transfer between water molecules,” *Nature Physics*, vol. 6, p. 139, 2010.
- [50] M. Mucke, M. Braune, S. Barth et al., “A hitherto unrecognized source of low-energy electrons in water,” *Nature Physics*, vol. 6, no. 2, pp. 143–146, 2010.
- [51] C. Champion, S. Incerti, H. Aouchiche, and D. Oubaziz, “A free-parameter theoretical model for describing the electron elastic scattering in water in the Geant4 toolkit,” *Radiation Physics and Chemistry*, vol. 78, no. 9, pp. 745–750, 2009.

- [52] S. Chauvie, Z. Francis, S. Guatelli et al., “Geant4 physics processes for microdosimetry simulation: design foundation and implementation of the first set of models,” *IEEE Transactions on Nuclear Science*, vol. 54, no. 6, pp. 2619–2628, 2007.
- [53] S. Chauvie, S. Incerti, P. Moretto, M. G. Pia, and H. Seznec, “Microdosimetry in high-resolution cellular phantoms using the very low energy electromagnetic extension of the Geant4 toolkit,” in *Proceedings of the IEEE Nuclear Science Symposium and Medical Imaging Conference (NSS-MIC '07)*, pp. 2086–2088, November 2007.
- [54] S. Incerti, H. Seznec, M. Simon, P. Barberet, C. Habchi, and P. Moretto, “Monte Carlo dosimetry for targeted irradiation of individual cells using a microbeam facility,” *Radiation Protection Dosimetry*, vol. 133, no. 1, pp. 2–11, 2009.
- [55] J.-P. Alard, V. Bodez, A. Tchirkov et al., “Simulations of neutron interactions at the single-cell level,” *Radiation Research*, vol. 158, no. 5, pp. 650–656, 2002.